



# A NUMERICAL INVESTIGATION INTO THE STRESS MEMORY EFFECT IN ROCKS

by  
Vadim Louchnikov

A thesis submitted in fulfilment of the requirements for the degree of  
Master of Engineering Science (Geomechanics)

The University of Adelaide  
Faculty of Engineering, Computer & Mathematical Sciences  
School of Petroleum Engineering

2004



## **DISCLAIMER**

*This thesis contains no material which has been accepted for the award of any other degree or diploma in any university and that, to the best of my knowledge and belief, contains no material previously published or written by another person, except where due reference is made in the text of the thesis. I consent to the thesis being made available for photocopying and load if accepted for the award of the degree.*

*Vadim Louchnikov*

## **ACKNOWLEDGEMENT**

I wish to express my gratitude to my supervisors **Dr Suzanne Hunt** and **Dr Tony Meyers** for their generous supply of ideas, suggestions and criticism, without which this work would not have been possible. I would like to thank my wife **Irina** for her encouragement and support throughout the course of this study.

## ABSTRACT

Reliable and inexpensive methods of in-situ stress measurement have been sought for more than 40 years. A number of non-destructive core-based methods of in-situ stress determination are currently available, among which Deformation Rate Analysis (DRA) and Acoustic Emissions (AE) method have the most promising potential due to their ability to measure stress as opposed to strain, which is measured by strain recovery techniques. The DRA and AE method are similar in their utilisation of a phenomenon termed *Kaiser effect* in the case of AE and *deformation memory effect* in the case of DRA. The KE/DME is defined as a recollection of a maximum stress a rock core had been subjected prior to its retrieval from the in-situ environment. The physical nature of this phenomenon has not however been universally established. In this study, interaction of microcracks as the most probable cause of the KE/DME, was investigated. To reproduce the damage that occurs to rock at the micro level, a discrete element modelling code was required, which enabled dynamic failure propagation to be modelled. Commercially available code *PFC<sup>2D</sup>* was found to be suitable for this purpose due to its ability to explicitly model mechanical damage in rocks. The numerical model was based on a real prototype – a sandstone rock core, which had also been previously subjected to the DRA. Although the bulk of the numerical tests were conducted on intact rock models, it was found that changes in the lithology and introduction of discontinuities did not have significant effect on the DME. Influence of the confining stress on the DME was confirmed. It was assumed that only the highest historical stress could be determined reliably using the DRA technique. The ability of the numerical model to reproduce the DME was validated. The link between the DME and development of microcracks was established. The results of the study encourage further use of the code for understanding the micromechanical behaviour of rocks under loading.

**Key words:** deformation rate analysis, acoustic emissions, Kaiser effect, deformation memory effect, in-situ stress, discrete element modelling, numerical simulation, particle flow code.

The overall research work comprised the present thesis and three publications:

- 2003 Hunt SP, Meyers AG and Louchnikov V. 'Modelling the Kaiser effect and deformation rate analysis in sandstone using the discrete element method', *Computers and Geotechnics J.*, v.30(7), pp.611-621.
- 2003 Hunt SP, Meyers AG, Louchnikov V and Oliver KJ. 'Use of the DRA technique, porosimetry and numerical modelling for estimating the maximum in-situ stress in anisotropic rock core', in *Proc. of 10th Int. Congress on Rock Mechanics*, Johannesburg, South Africa, September 2003.
- 2004 Louchnikov V, Meyers AG and Hunt SP. 'The use of Particle Flow Code for investigating the stress memory effect in rocks', paper accepted for publication at *2nd Int. Symposium on Numerical Modelling in Micromechanics via Particle Methods*, Kyoto, Japan, October 2004.

# CONTENTS

1	INTRODUCTION.....	1
1.1	General.....	1
1.2	In-situ stress and its constituents.....	2
1.3	First-order estimate of in-situ stress.....	3
1.4	Stress measurement techniques.....	6
1.5	Stress memory effects.....	6
1.6	Research objectives.....	7
2	CORE-BASED STRESS MEASUREMENT METHODS.....	9
2.1	General.....	9
2.2	Anelastic strain recovery.....	9
2.3	Differential strain analysis.....	10
2.4	Acoustic emissions.....	11
2.5	Deformation rate analysis.....	12
2.6	Summary.....	15
3	KAISER EFFECT AND DEFORMATION MEMORY EFFECT: THEORETICAL BACKGROUND.....	16
3.1	Brittle rock behaviour under deviatoric compression.....	16
3.2	Micromechanics of rock damage.....	19
4	PHYSICAL PROTOTYPE.....	24
5	NUMERICAL MODELLING.....	28
5.1	Numerical modelling in rock mechanics.....	28
5.2	Discrete element method: $PFC^{2D}$ .....	28
5.2.1	General formulation.....	28
5.2.2	Definition of microcracks in $PFC$ .....	33
5.2.3	Modelling strategy.....	34
5.3	Development of synthetic specimens.....	35
5.3.1	Intact rock model.....	35
5.3.2	Fine-grained model.....	40
5.3.3	Complex lithology model.....	43
5.3.4	Discontinuous rock model.....	45

5.4	Modelling deformation memory effect.....	47
5.4.1	Intact rock model.....	47
5.4.2	Fine-grained model and complex lithology models .....	54
5.4.3	Discontinuous rock model.....	58
5.4.4	Effect of joint orientation.....	60
5.4.5	Effect of confining stress.....	61
6	DISCUSSION.....	72
7	CONCLUSIONS.....	77
	REFERENCES.....	79
APPENDICES		
	Appendix 1. Glossary.....	85
	Appendix 2. Detailed modelling processes .....	90
	A2.1 Conventions.....	90
	A2.2 Specimen-genesis codes.....	90
	A2.3 Cyclic test subroutines: all models.....	103
	A2.4 Effect of joint orientation.....	109
	A2.5 Effect of confining stress.....	143

# 1 INTRODUCTION

## 1.1 General

Knowledge of the in-situ stress tensor is a key element in the process of design of any underground excavation. No matter what type of a rock failure occurs, it is ultimately related to the stress change around the rock mass. The importance of the stress data has been recognised in all industries involved in subsurface development: mining, oil and construction. Stress is a fundamental component in a typical design of an underground excavation as illustrated in Figure 1.1. In the mining industry information on the in-situ stress is necessary at many stages of mine planning: when deciding on the appropriate layout of development openings, when designing ground support, when establishing an efficient stoping sequence, etc. In the oil industry stress data are required for understanding the natural and induced fluid flow, reservoir drainage pattern, well integrity and flooding strategies for enhanced recovery. Selecting the optimal bearing for directional drilling so as to avoid wellbore instability depends primarily on the magnitude and orientation of the in-situ stresses. In the civil industry in-situ stress is one of the main input parameters for making decisions on dimensions, orientation and shape of tunnels and underground caverns. Knowledge of the initial state of stress is also a legislative requirement: no underground excavations can be approved unless a risk assessment has been conducted and doing so will involve assessing the influence of in-situ stress on the stability of the excavation.

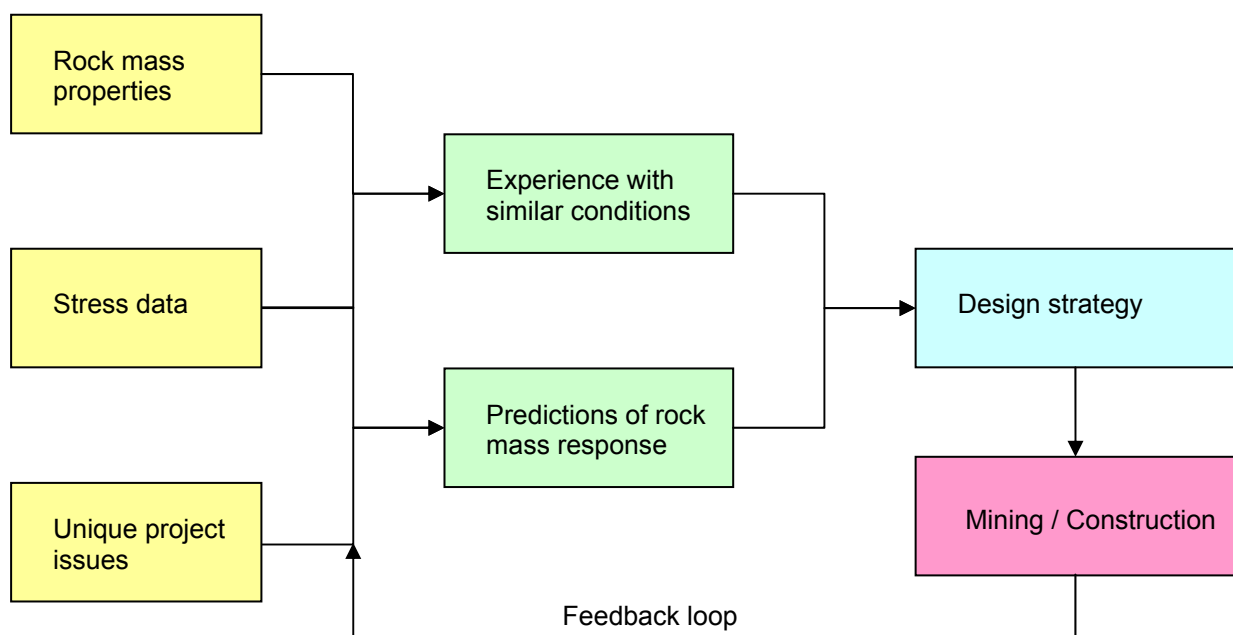


Figure 1.1. Design strategy of an underground excavation in rock (after Martin et al., 2003).

## 1.2 In-situ stress and its constituents

The weight of the overlying rock mass was recognised for more than a century as a primary source of stress around underground openings. Heim (1878) in his study on the mechanics of tectonic events introduced a *hydrostatic stress field theory*, postulating that the rocks in the earth crust are in the state of hydrostatic stress, similar to the stress state in liquids. This theory was later modified to a *lithostatic stress field theory*, which assumes the rocks in the crust are in the state of isotropic state:

$$\sigma_H = \sigma_h = \sigma_v \equiv P_c \quad (1.1)$$

where  $\sigma_H$  and  $\sigma_h$  are the maximum and minimum components of the horizontal stress,  $\sigma_v$  is the vertical stress and  $P_c$  is the confining pressure. For many years the design of underground excavations was based predominantly on this assumption, since no stress measurement methods were available to disprove this theory. The lithostatic stress field theory was later replaced by the *uniaxial strain* model (Terzaghi & Richart, 1952). This concept suggests that because rocks are confined at depth, the horizontal expansion is restricted by adjacent rock, so that ideally the principal strains  $\varepsilon_1 \neq 0$ ,  $\varepsilon_2 = \varepsilon_3 = 0$ , thus making the horizontal stress a function of the weight of the overburden and the Poisson's ratio only:

$$\sigma_H = \sigma_h = \rho g Z \frac{\nu}{1-\nu} \quad (1.2)$$

where  $\rho$  is the integrated rock density of the overburden,  $g$  is the gravitational acceleration,  $\nu$  is the Poisson's ratio and  $Z$  is the depth at the point of interest. From Eq.1.2 it is evident, the major principal stress is the vertical stress (if  $\nu = 0.25$  then  $\sigma_H = \sigma_h = 0.33\sigma_v$ ). While this estimation was often sufficient for underground design purposes, it was noticed that the horizontal stresses frequently exceeded the vertical overburden pressure. Wegener (1915) stated that 'under the immediate impression of the congruence of the Atlantic coasts' large horizontal forces were imposed of the land mass. His *continental drift* hypothesis connected all orogenic and tectonic events with large horizontal movements in the earth crust. This theory was further developed by Hast (1958), who found that the horizontal stresses often exceeded the overlying rock mass pressure by 1.3 to 1.5 times and in extreme cases up to 8 times. He explained this phenomenon by 'bending stresses' in the earth crust due to uplift forces in the Scandinavian Peninsula. For many years the continental drift theory was not developed further. It was not until the 1960s, on the basis of new evidence from marine research, that Wegener's theory begun to gradually find acceptance. Relatively recent works by Dewey (1972), James (1973), McKenzie & Sclater

(1973), Courtillot & Vink (1983) further corroborated and verified the plate tectonics hypothesis by contributing substantial evidence about the driving forces between continents.

Although the lithostatic stress field theory and the uniaxial strain model are still sometimes being used today, it has been universally recognised that tectonic forces have significant effect on in-situ stresses and for this reason need to be considered in the design of underground excavations. It is however difficult to determine the influence of the tectonic forces quantitatively.

### 1.3 First-order estimate of in-situ stress

To take into account action of tectonic forces, Sheorey (1994) developed an *elasto-static thermal model* which accounted for the crust curvature, changes in density, elastic constants and coefficients of thermal expansion. He suggested the following relationship for the horizontal-to-vertical stress ratio  $k$ :

$$k = 0.25 + 7E_h \left( 0.001 + \frac{1}{Z} \right) \quad (1.3)$$

where  $E_h$  is the Young's modulus of the rock mass measured horizontally (GPa),  $Z$  is the depth at the point of interest (m).

This equation is presented in Figure 1.2 plotted for different values of  $E_h$ .

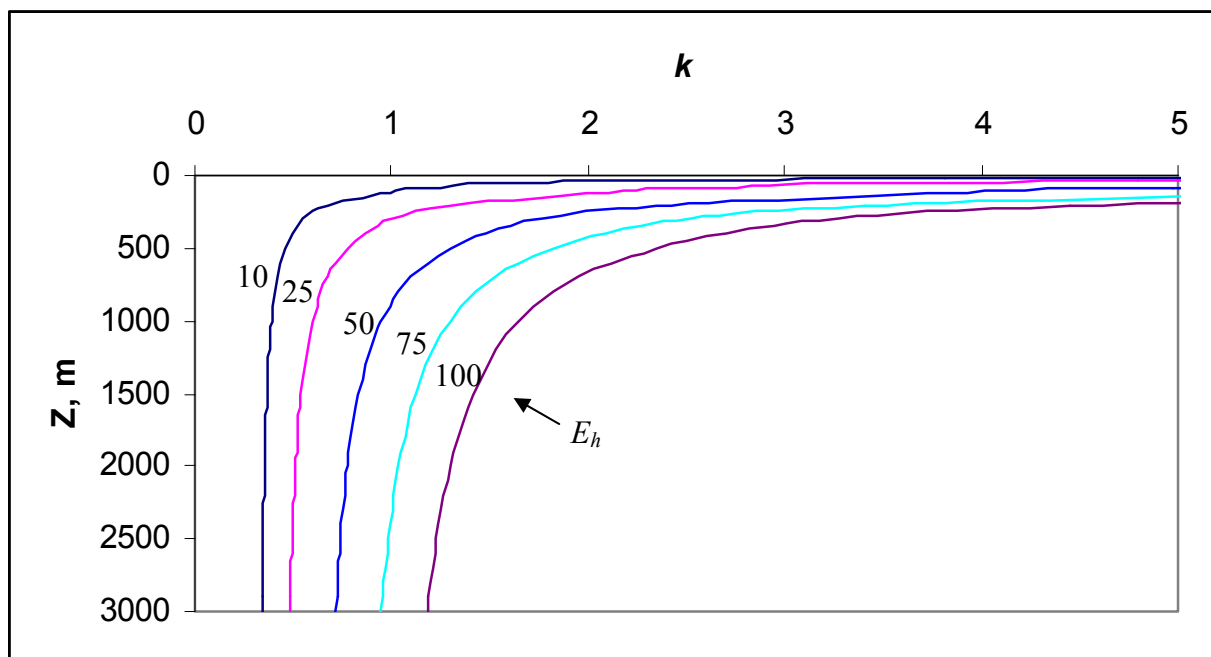
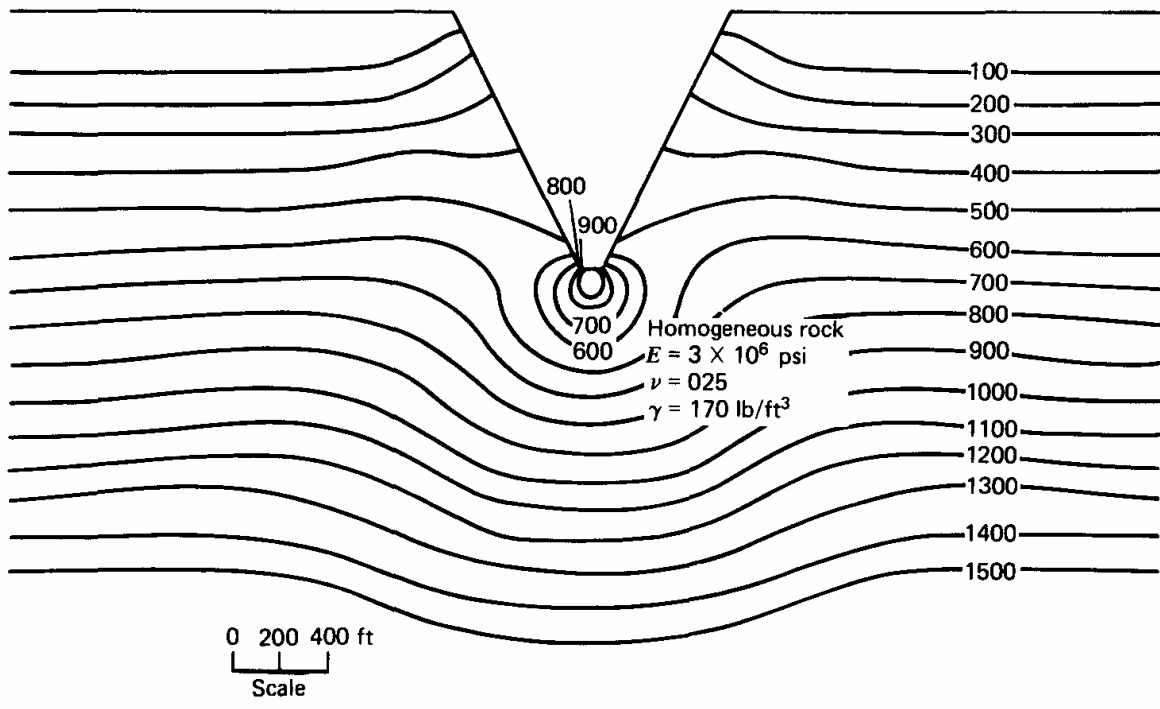


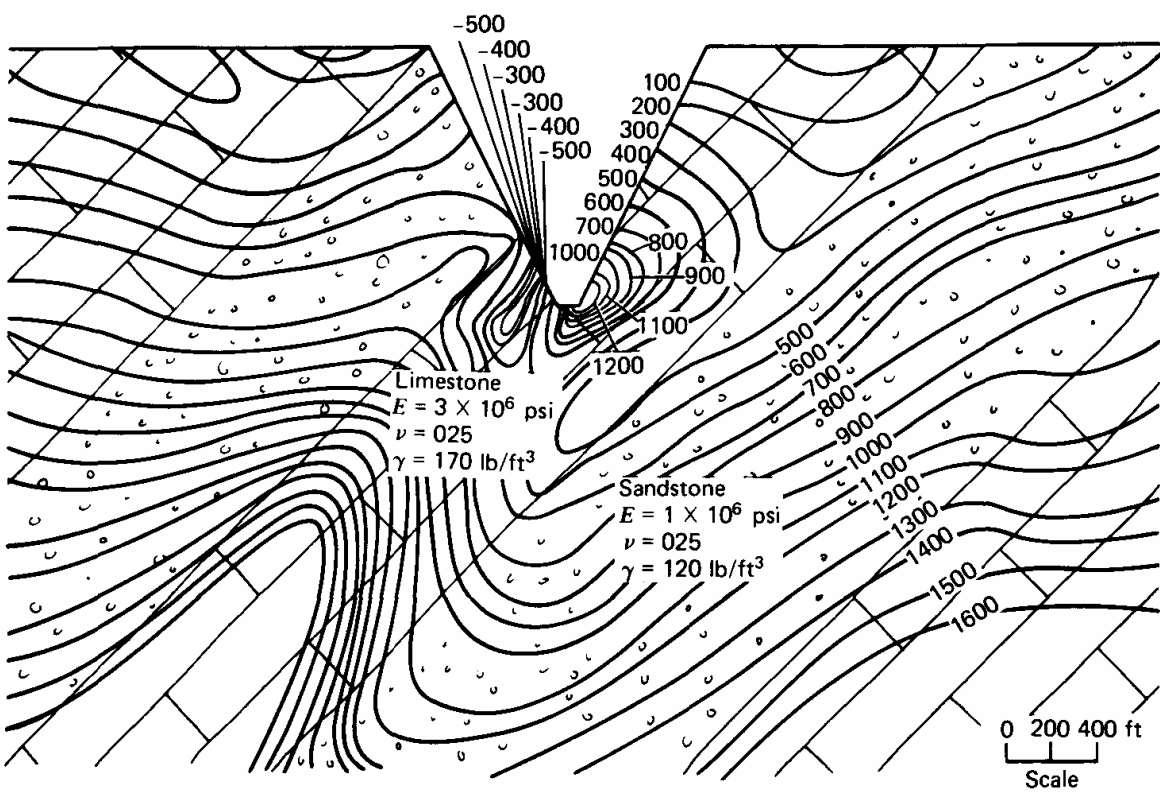
Figure 1.2. Horizontal-to-vertical stress ratio at different horizontally measured Young's modulus (after Sheorey, 1994).

Sheorey's theory suggests that it is a relatively straightforward exercise to estimate the value of the in-situ stress. However it fails to recognise that rock masses are heterogeneous and discontinuous; characteristics that complicate the task of estimating the in-situ stresses acting at a point. Changes in topography also have considerable influence on stress behaviour, in particular for shallow excavations. For example, Figure 1.3 shows stress contours below a valley: 1.3a – the stress model predicted for a homogeneous rock mass, 1.3b – stress distribution for an actual sedimentary sequence. The stress magnitude and orientation change significantly for the heterogeneous material. Stiffer and denser limestone experiences higher stress concentrations while stresses are reduced around the more deformable sandstone. As a result of these influences, in-situ stress can only be estimated using the technique described above (i.e. a closed form solution) in uniform formations for a homogeneous rock mass, or where accurate data on the stress tensor is only required as a mean value perhaps for a large scale (km's) application. In most engineering cases measurement of the in-situ stresses will be required.

In recent years numerical modelling techniques have been developed to help understand and explain observations in complex stress regimes and for prediction of stress away from local points of measurement. Major discontinuities at rock density contrasts, such as faults and mappable seismic horizons, can greatly affect both the magnitude and orientation of the principal stress components. The effect of such heterogeneities contained within the rock mass has been the subject of many field observations (Martin & Chandler, 1993, Barton & Zoback, 1994). Several numerical techniques have been proposed for modelling stress and strain in a heterogeneous rock mass. The general applicability of these methods was reviewed by Jing & Hudson (2002) and Jing (2003). The modelling techniques to be reliably used require validation of the in-situ stress data from actual sites and hence do not preclude the need for site based stress information.



(a)



(b)

Figure 1.3. Comparison of maximum shear stresses beneath valleys in: (a) homogeneous and (b) heterogeneous formations (from Goodman, 1980). The stress units are psi.

## 1.4 Stress measurement techniques

Stresses in rock have been measured since the 1930s and several techniques are currently available. All stress measurement methods can be broadly divided into three principal groups:

1. Indicative methods
2. Field-based methods
3. Core-based methods

The first category is strictly speaking not ‘stress measurement’, but rather ‘stress estimation’ methods e.g. borehole breakouts and core diskings. These techniques can however be referred to as stress measurement, as there is ongoing experimental work being conducted on quantification of the stresses observed from these phenomena (e.g. Hamison & Lee, 1995, Te Kamp et al, 1995).

The second group of techniques involves methods that disturb the in-situ rock conditions by inducing strains or by opening pre-existing cracks. These include e.g.

- Borehole relief methods (overcoring and borehole slotting)
- Hydraulic methods (hydraulic fracturing and hydraulic tests on pre-existing fractures)

These methods allow direct stress (strain) measurement.

The third category encompasses various laboratory tests performed on drill cores:

- Strain recovery methods (anelastic strain recovery and differential strain curve analysis)
- Kaiser effect methods (acoustic emissions and deformation rate analysis)

These methods are referred to as *indirect stress measurement techniques* as they do not measure stresses (strains) directly in the field but rather from core taken from the field and tested in a laboratory. The methods of this group take advantage of a phenomenon, colloquially termed the *stress memory effect*.

## 1.5 Stress memory effects

Discovery of the stress memory effect in solid materials is attributed to Josef Kaiser, a German engineer and scientist. Kaiser (1950), while studying acoustic emissions (AE) emanating from metals under compressive loading, noticed a sudden onset of AE from a specimen once the loading surpassed the level of stress applied to the metal during a previous test. This phenomenon has been since referred to as the *Kaiser effect* (KE). Experiments on the KE in geo-

materials were pioneered by Goodman (1963), who observed similar onset of AE in rocks under compressive loading. There was little research into the effect reported subsequently until Kanagawa et al. (1976) realised the potential for the KE to be applied to the evaluation of in-situ stress by testing a cored sample of rock taken from the formation of interest. Afterwards the effect has been extensively researched by many practitioners including Kurita & Fujii (1979), Holcomb & Costin (1986), Hughson & Crawford (1987), Friedel & Thill (1990), Momeyez & Hassani (1992), Pestman et al. (2002) and others.

The Kaiser effect is not the only rock stress memory phenomenon. Others include:

- *deformation memory effect* (Yamamoto et al., 1990)
- *ultrasonic memory effect and electric memory effect* (Fujii & Hamano, 1977)
- *ion emission memory effect* (Reed & McDowell, 1994)
- *mercury withdrawal rate effect* (Vavra et al., 1992).

The Kaiser effect and deformation memory effect (DME) have the most potential for the practical estimation of in-situ stresses, while the other methods tend to be less developed. It is believed that the KE and DME have similar physical bases involving anelastic deformation processes.

Although the KE/DME have been extensively reported on, there is still a lack of understanding as to the physical nature of the phenomena. One of the most convincing explanations is based on microcrack theory, which, in brief, can be interpreted as follows (after Holcomb, 1993 and Li, 1996). A rock is damaged at a micro level as a result of being placed under stress. This stress creates an extensive network of microcracks. If the stress is removed and then reapplied, the rock does not undergo nucleation of new microcracks until the load level exceeds the previously applied stress. At this stress the rock begins experiencing a sudden increase in the number of new microcracks, which is accompanied by a sharp onset of acoustic emissions.

## **1.6 Research objectives**

This study is aimed at investigating the DME using a numerical modelling code. The main objectives are:

- Examination of the ability of a numerical model to replicate the DME;
- Verification of the link between the DME and the microfracture character of rock deformation.

Despite the ever-growing research activities into the KE/DME, there are still many unanswered questions relating to the accurate application of the stress measurement techniques based on these phenomena. The present study is intended to provide answers to many of the following questions:

- There is disagreement as to whether laboratory and geologically applied triaxial stresses produce a KE/DME estimate which provides a measure of axial or deviatoric stress magnitudes. How relevant are these results to geologically applied stress regimes?
- Does the KE/DME provide the present-day or historical maximum in-situ geological stress?
- What is the influence of the confining stress on the KE/DME? If it does have an affect on the quality of stress estimation, then the stress measurement based on the KE/DME might be limited to a certain range of depths.
- What is the influence of the variations in the material properties on the KE/DME?
- How sensitive is the KE/DME to the pore-water pressure?
- How is the KE/DME affected by the degree of porosity?
- Can the KE-based methods be applied to the intact rock only or to the jointed samples as well? How is the KE/DME affected by the orientation of discontinuities?
- The KE/DME appears to be obscured over time, with the measurable retention period being described as the *Kaiser effect retention span* (KERS). What are the limitations on the time elapsed from coring?
- Is the KE/DME affected by the coring-induced damage?
- Can the analysis procedure be developed to improve accuracy of results?

To address the research objectives, a number of numerical models of a sandstone specimen were analysed. The base model was reproduced from an actual sandstone core. More complex models were generated as derivatives of the base prototype.

## **2 CORE-BASED STRESS MEASUREMENT METHODS**

### **2.1 General**

Although some of the stress measurement techniques, like hydraulic fracturing and overcoring, found wide acceptance in the industry, they can offer acceptable accuracy only under ideal conditions (Ljunggren et al, 2003). Due to a number of limitations, summarised in Table 2.1, there are no overall clear advantages of these methods over the core-based techniques, which whilst providing similar degree of accuracy, have prospective to be carried out routinely and at low cost.

The core-based methods involve determination of the in-situ stresses from tests on oriented drill cores in a laboratory. These techniques are based on the straining microcracks induced during coring. The population and orientation of these microcracks are assumed to be a direct function of the in-situ stress. A dominant population of microcracks, oriented in a preferential direction, is interpreted to indicate the orientation of the maximum principal stress. As a precaution, errors may be considerable when other microcracks, in addition to those induced during coring, are present; for example, microfractures induced during core handling and preparation or naturally present fractures. These errors are minimised by using more than one laboratory method for determining the in-situ stresses and by comparing the results obtained from the tests with field observations (e.g. orientation of breakouts, characteristic modes of failure in underground openings, diskings, etc.). This category of stress measurement methods can be broken into two sub-groups:

1. Strain recovery methods (anelastic strain recovery, differential strain analysis)
2. Stress memory effect methods (acoustic emissions, deformation rate analysis)

### **2.2 Anelastic strain recovery**

For the anelastic strain recovery (ASR) method the magnitudes and directions of the in-situ principal stresses can be inferred from the magnitudes and directions of the in-situ principal strains. The method involves monitoring time-dependent strain relaxation of freshly-cut oriented core. Previous studies on this technique are presented e.g. by Warpinski & Teufel (1989), Wolter & Berckhemer (1989), Yassir et al. (1998).

The principle behind the method is that during the coring process a core undergoes differential relaxation. At the start of coring, the stresses on the core wall drop from their original in-situ values to the drilling fluid pressure. Once the coring is completed, strain recovery continues. During the drill trip time, the stresses and the fluid pressure decrease. Once the core is retrieved at the surface, the strains within it are continuously monitored in six different directions; three orthogonal parallel and perpendicular to the core axis and three at 45° to these orientations. The total measured strains include an instantaneous elastic component and an anelastic component. The anelastic (time-dependent) component may occur over a matter of ten to more than one hundred hours. Due to the finite time for tripping and instrumentation of the core, the strain measurements do not detect the initial elastic recovery and part of the anelastic relaxation. A data transformation is then used to determine the magnitudes and directions of the principal strains. From these values, the applicable stresses are then estimated by incorporating a viscoelastic constitutive relationship.

### **2.3 Differential strain analysis**

The concept of differential strain analysis (DSA) is similar to ASR; to determine the principal strain directions and to infer the orientation of the in-situ principal stress (e.g. Strickland & Ren, 1980, Sakaguchi et al., 2002).

The core is strain gauged in three dimensions so that directional deformation can be measured. The core is then hydrostatically loaded to beyond the stress it was subjected to in-situ. During loading, the deformation in any direction is proportional to the dilation that took place in that direction during core removal. Microfractures created by stress relief close first. Continued loading causes deformation that is primarily a function of the intrinsic mechanical properties of the rock. By differentiating between intrinsic behaviour, at high hydrostatic pressure, and induced behaviour (by the presence of open microfractures), the directional strain input due to microfractures can be determined. In an isotropic rock, the direction of the maximum principal strain corresponds to a direction perpendicular to the strike of the orientation with the maximum microfracture density and indicates the direction of the maximum in-situ principal strain.

The derivation of principal stress magnitudes from laboratory measured principal strains is difficult. In an idealised case, the following theoretical approach can be used to assess these values. If the principal strains are known, stress directions and magnitudes can be inferred from elastic relations. A requirement, therefore, is to determine the elastic properties in the principal

strain directions. A first-order approach to this task is to infer these properties from directional bulk compressibilities, determined from individual strain gauges during the DSA testing. Knowing the directionally dependent material properties, transformation from strain to stress can be performed. One basic assumption used in this calculation is that the stress and strain have a non-hysteretic relationship; that is, the amount of stress required to open microcracks is the same as that required to close them. The transformation yields a ratio ( $\sigma_1:\sigma_2:\sigma_3$ ). If there is one independent measure of in-situ stress (for example, a micro-hydraulic fracturing stress measurement, a pre-treatment shutdown, or a density log integrated to the surface), magnitudes may be attached to this ratio.

Several important assumptions are used to idealise the stress-strain relationships and to obtain the inferred principal strains and stresses i.e.

- All of the microcracks are generated during unloading due to the release of in-situ stresses, and are aligned with the directions of these stresses;
- For an isotropic material, the principal strain ratios can be used to infer the in-situ stress magnitudes provided that an independent in-situ stress measurement of one of the principal stresses is available;
- For an orthotropic (and hence including transversely isotropic) material, the orientations of the orthotropy are assumed to coincide with the directions of the principal strains. It is further assumed that the stress magnitudes required to close the microcracks are the same as those magnitudes that generated and opened the microcracks.

## 2.4 Acoustic emissions

Acoustic emissions method is based on the Kaiser effect. The method involves drilling several small cores from a larger core recovered from the region at which the in-situ stress details are required. The orientations of the small cores are based on the in-situ orientation of the larger core. After appropriate sample preparation, acoustic sensors are attached to the small cores and uniaxial compression tests are performed on them. AE emanated from the rock are monitored during the test. The intensiveness of AE is low until the loading exceeds the previously experienced maximum in-situ stress when there is a sharp increase in the gradient of the ‘AE cumulative count vs. axial stress’ curve (Figure 2.1). The distinctive inflection point is often referred to as the *take-off point*. If a sufficient number of tests are conducted on the small cores, the full 3D in-situ stress tensor can be obtained.

A number of researchers (e.g. Kanagawa et al. (1976), Momayez & Hassani (1992), Zhang et al. (1996), Seto & Villaescusa (1999), Qin et al. (1999)) reported varying degrees of success in application of the AE technique for the measurement of in-situ stress. At present, the method finds increasing interest among the Australian mining companies in its practical application to the in-situ stress measurement (e.g. Villaescusa & Li, 2004).

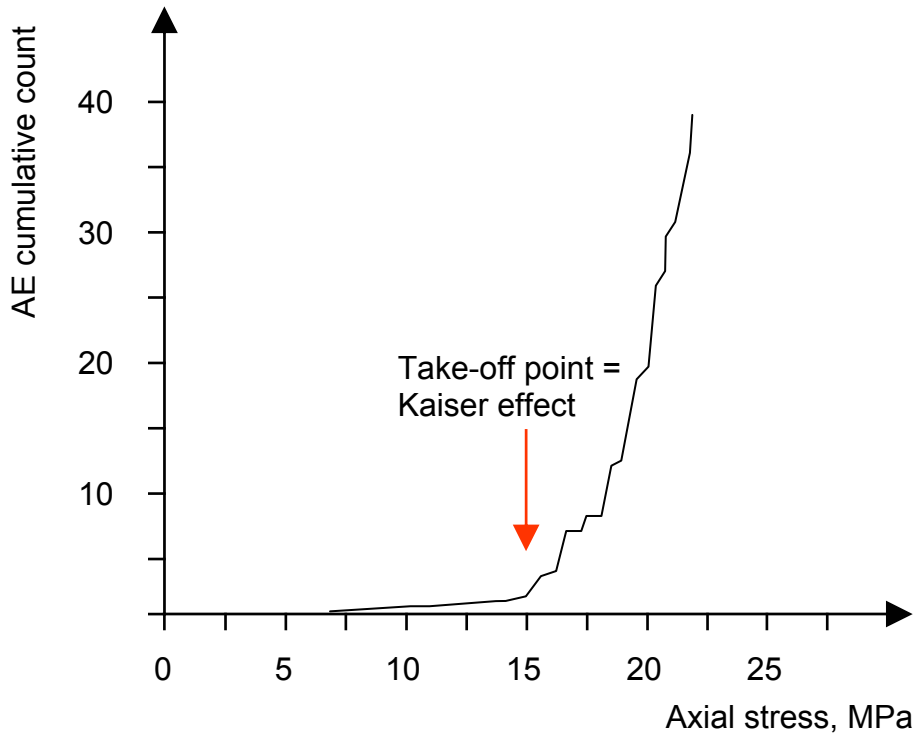


Figure 2.1. Typical graph of AE cumulative counts vs. axial stress illustrating Kaiser effect.

## 2.5 Deformation rate analysis

The deformation rate analysis (DRA) method is based on the deformation memory effect. Similar to the AE method, secondary cores are drilled from an oriented parent core, prepared and subjected to uniaxial compression. However, instead of recording AE, the process involves monitoring changes in strains detected by a number of strain gauges bonded to the core as the specimen undergoes cyclic compressive loading. The concept of the method is that there is change in the stress-strain behaviour once the loading exceeds the previously applied maximum stress. The process involves loading the specimen above the maximum in-situ stress, then unloading it, and repeating the cycle one more time (Figure 2.2). The strain difference between the two loading curves, correlated with the same value of stress, is plotted in terms of the axial stress. The basic formulation of the DRA method is expressed by the *strain difference function*:

$$\Delta\varepsilon_{i,j}(\sigma) = \varepsilon_j(\sigma) - \varepsilon_i(\sigma); \quad j > i \quad (2.1)$$

where  $\varepsilon_i$  is the axial strain in the core under  $i^{th}$  loading,  $\varepsilon_j$  is the axial strain in the core under  $j^{th}$  loading,  $\sigma$  is the applied stress corresponding to both strains.

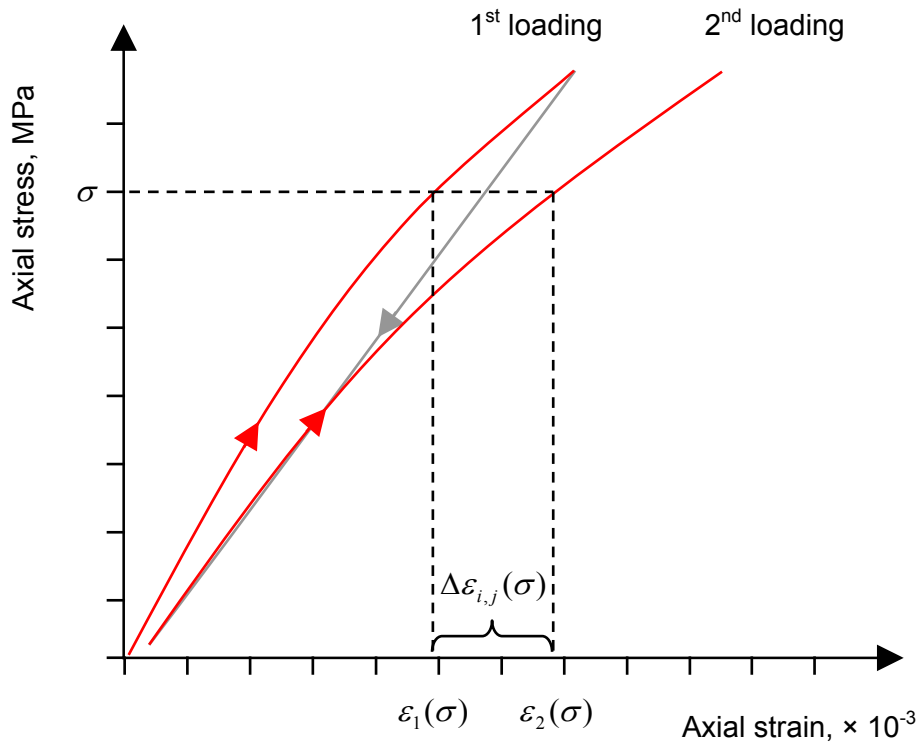


Figure 2.2. Differential rate analysis principle

All tests in the current study are based on the DRA technique. An axial stress, termed henceforth as a *pre-load* (simulating major principal in-situ stress) is applied to a core. The core is then subjected to two re-loading cycles (Figure 2.3). This procedure will hereafter be referred to as the *load-reload-reload* or LRR test.

Yamamoto et al. (1990) experimentally demonstrated that the curve in the ‘differential strain vs. stress’ plot changes gradient when it passes the value of the pre-load (Figure 2.4).

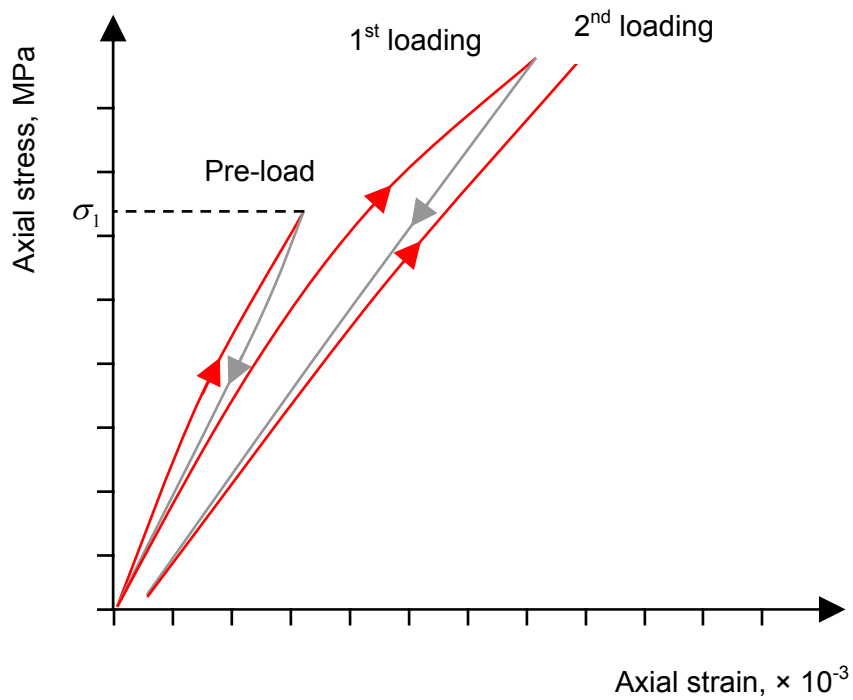


Figure 2.3. LRR test, general principle.

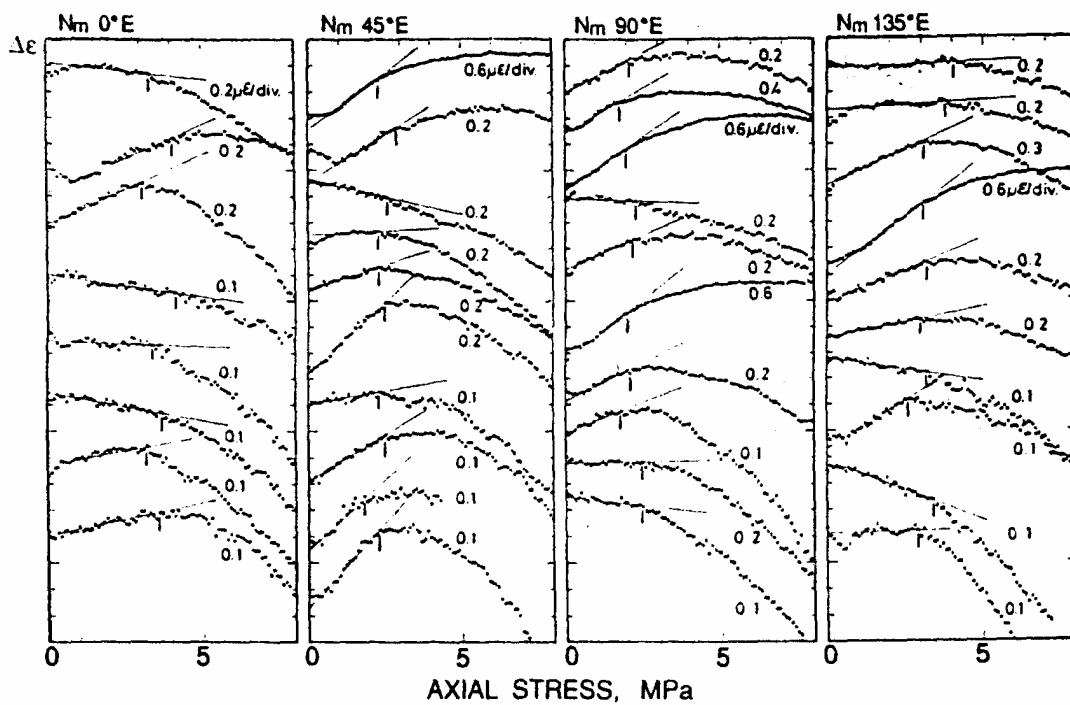


Figure 2.4. Illustration of DME: curve bending point (marked with a tick) was read as maximum in-situ stress experienced by a specimen in a particular direction. For each of four orientations eight cores were studied: each curve represents a different specimen (from Yamamoto et al., 1990).

## 2.6 Summary

In brief, all core-based methods of stress measurement described in this chapter are listed in Table 2.1. For comparison purposes, the conventional techniques are also presented. The advantages, limitations and conditions for the application of each method are discussed.

*Table 2.1. Stress measurement methods (adopted and modified from Ljunggren et al., 2003).*

<b>Method</b>	<b>2D/3D</b>	<b>Advantages</b>	<b>Limitations</b>	<b>Application</b>
Borehole breakouts	2D	Stress information obtained at an early stage. Stress orientation is obvious.	Stress magnitude can be only roughly assumed.	Occurs mostly in deep holes.
Core diskings	2D	By-product information obtained at the drilling stage.	Orientation can be relatively accurate, magnitude – rough estimation.	Estimation of stress at an early stage.
Overcoring	2D/3D	Most developed technique in both theory and practice	Scattering due to small rock volume. Requires drill rig. Problems with proper cell installation.	Can be used for stress measurement at depths down to 1000m.
Borehole slotting	2D	Does not require overcoring. Instrument is fully recoverable. Quick.	Borehole must be dry. Stress parallel to borehole axis must be known.	Used in boreholes at shallow depths.
Hydraulic fracturing	2D	Measurement in existing boreholes. Quick. Low data scatter in results.	Involves large expensive equipment. Limited to vertical holes.	Suitable at early stages, when no u/g access exists.
Hydraulic tests on pre-existing fractures (HTPF)	2D/3D	Measurement in existing boreholes. Suitable for highly stressed environment.	Time consuming. Requires existing fractures in the hole with varying orientations.	Used when overcoring and hydraulic fracturing fail.
ASR, DSA	2D/3D	Suitable for great depths.	Complicated measurements at micro-scale. Results might be not representative due to small volumes. Sensitive to a number of factors.	Estimation of stresses at large depth.
AE, DRA	2D/3D	Simple and of low cost.	Relatively low reliability. Requires further research.	Can be routinely applied for any conditions. Rough stress estimation.

### 3 KAISER EFFECT AND DEFORMATION MEMORY EFFECT: THEORETICAL BACKGROUND

#### 3.1 Brittle rock behaviour under deviatoric compression

To numerically model the behaviour of rock under compressive stress, the stress-strain characteristics of typical rock should be understood. These characteristics are defined in the stress-strain curve which generally encompasses two phases of rock deformation: pre-failure and post-failure. When a rock is subjected to a compressive load, it can be described as undergoing four stages of deformation (Figure 3.1):

1. *Quasi-elastic deformation.* If the stress is relieved, the specimen returns to its original shape and size. The stress-strain curve is linear and obeys Hooke's law.
2. *Elasto-plastic deformation.* Once the elastic limiting stress  $\sigma_e$  is exceeded, the specimen only partially returns to its original shape if the load is removed.
3. *Plastic flow.* Stress does not increase between the failure stress  $\sigma_f$ , which under the uniaxial stress conditions is equal to the rock UCS  $\sigma_c$ , and disintegrating stage stress  $\sigma_d$ , while strain rate remains high.
4. *Disintegration.* If the loading is continued, one or more fractures develop and the material eventually fails with the stress value rapidly decreasing to the remnant stress  $\sigma_r$  (equal to the rock residual strength).

The brittleness of a rock is determined by its behaviour between the failure stress and the disintegration stress. Short intervals characterise brittle materials while ductile rocks are those that have a long plastic flow interval.

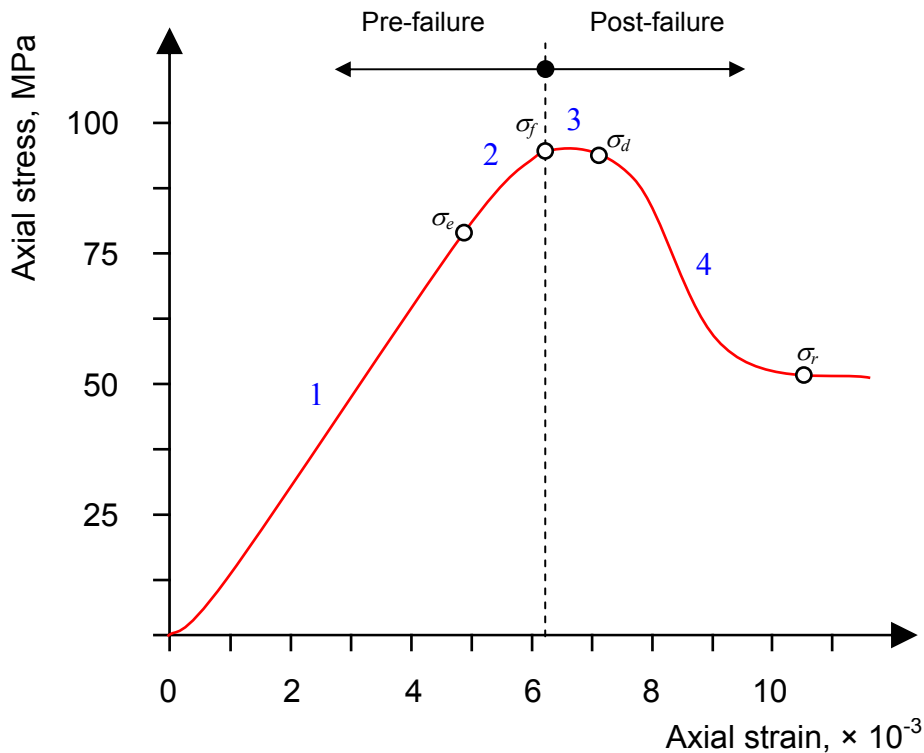


Figure 3.1. A typical stress-strain diagram of a rock specimen under uniaxial compression.

The anelastic deformation of brittle rocks has been widely explained by nucleation and growth of microcracks (e.g. Kranz, 1983). Based on laboratory studies involving the stress-strain behaviour of brittle rock, the failure process can be broken down into a number of stages characterised by changes in the measured axial and lateral strain response recorded during uniaxial (or polyaxial) compression tests (Fig. 3.2). These stages include:

- I. Crack closure.
- II. Linear elastic deformation.
- III. Crack initiation and stable crack growth.
- IV. Crack damage and unstable crack growth.
- V. Failure and post peak behaviour.

Crack closure occurs at the beginning of loading when existing cracks, orientated at a favourable angle to the applied load, close. During crack closure, the stress-strain response is non-linear (concaving upwards), indicating an increasing stiffness. Once the majority of existing cracks have closed, linear elastic deformation takes place (point A), which involves pore deformation and grain compression. The stress level of about  $0.3-0.4\sigma_c$  (point B, crack initiation stress  $\sigma_{ci}$ ) is characterised by nucleation of new microcracks at the most stressed points inside the rock, generally around the sample mid-section (Goodman, 1980). This process is followed by the

stable growth of microcracks in the direction normal to the minor principal stress. The stability of the crack growth means that with each increment in the applied load they grow to a finite length and then cease growing. After the loading reaches the elasto-plastic stage (point C, crack damage stress  $\sigma_{cd}$ ), cracks begin growing uncontrollably (unstable growth) until they encounter another crack, pore, or a free space. Thus a network of jointed cracks is created. With increasing load, the coalescing cracks form a rupture surface, commonly termed a *failure plane* (point D, failure stress  $\sigma_f$ ). The post-failure behaviour involves macrocracking by interconnection of microcracks (between points D and E) and following frictional sliding of the rock material on macrocracks (from point E).

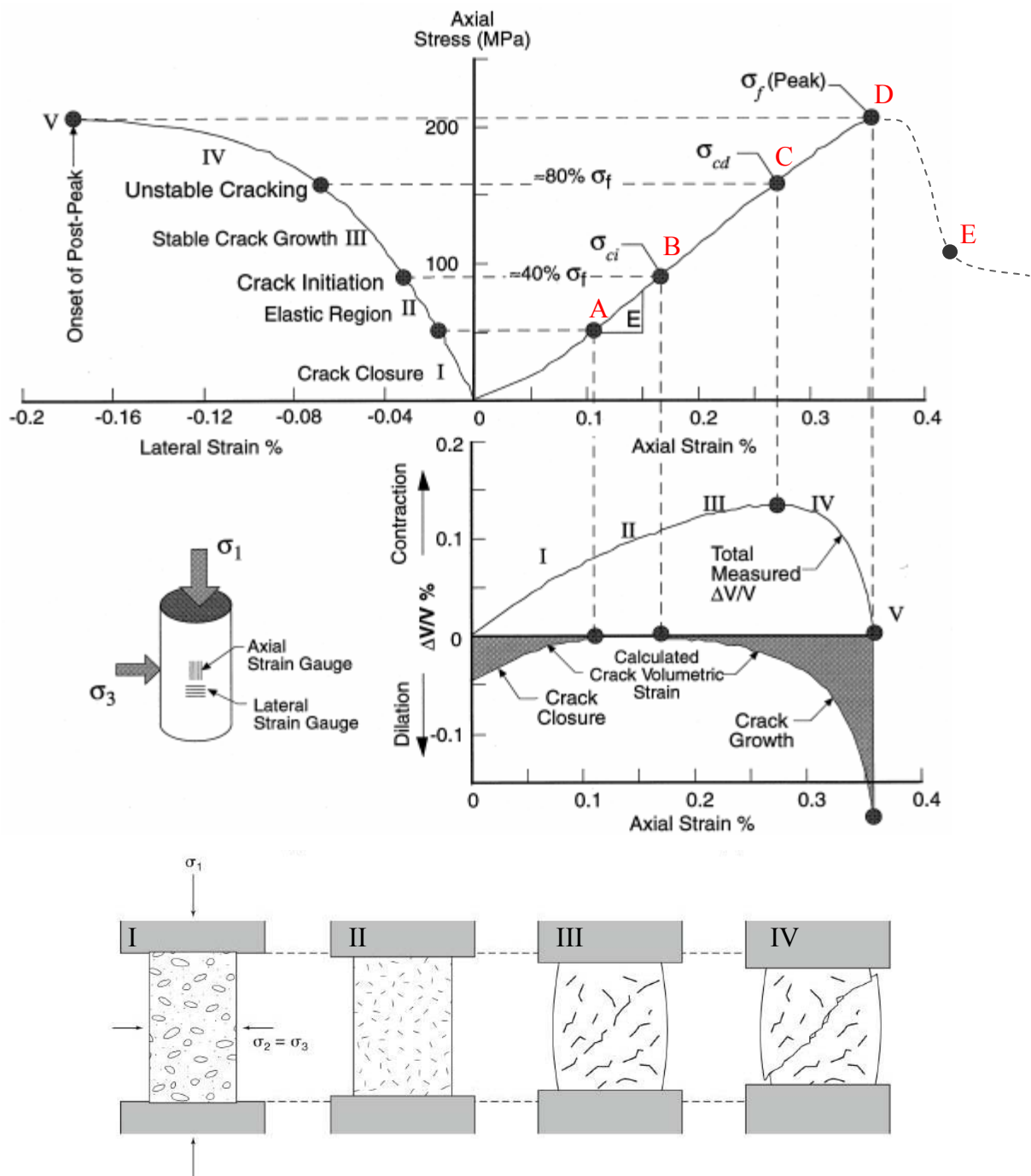


Figure 3.2. Stages of crack development (after Martin & Chandler, 1994).

### 3.2 Micromechanics of rock damage

Modern linear elastic fracture mechanics is largely based on Griffith's model of fracture (Jaeger & Cook, 1979). Griffith (1924) developed a theory capturing the essential physical processes of crack propagation in brittle materials, providing an energy-based failure criterion for uniaxial tensile rupture, which states that the critical stress required for crack propagation in a brittle material is given by:

$$\sigma_c = \sqrt{\frac{2E\gamma_s}{\pi a}} \quad (3.1)$$

where  $E$  is the material's Young's modulus,  $\gamma_s$  is the specific energy (the energy per unit area required to create two free surfaces),  $a$  is the half length of an internal crack. The theory is based on an assumption that the macrofracture occurs as a result of the development and growth of *branching cracks*, the microcracks nucleating at the sharp ends of pre-existing cracks and flaws, under the action of applied stresses. Over time, Griffith's theory has undergone significant improvement by numerous studies on fracture in various materials; however the fundamental idea of considering existing microcracks as nucleation sites for branching cracks has not changed. Yet the mechanics of microcrack development are not completely understood, for the reason that it is difficult to observe the crack formation. Only the basics of this process will be introduced here, as it is not the purpose of this research to analyse the microfracturing process in great detail. It is however necessary to understand the broad principles to place the subsequent research into context.

Two types of microcracks are differentiated by their position in the rock matrix:

1. *Inter-crystal/grain cracks*, involve a fracture propagating between crystal boundaries when the shear strength on a grain exceeds the inter-granular strength of the cement material (Figure 3.3a).
2. *Intra-crystal/grain cracks*, involve a fracture splitting the grains (Figure 3.3b). This type of fracture generally requires much higher specific energy than that for inter-crystalline cracks to develop.

In the case of sedimentary rocks, sandstone in particular, the predominant type of microfracturing is inter-crystal/grain, as the precipitated silica cement and clays filling the pore spaces are significantly weaker than the quartz grains.

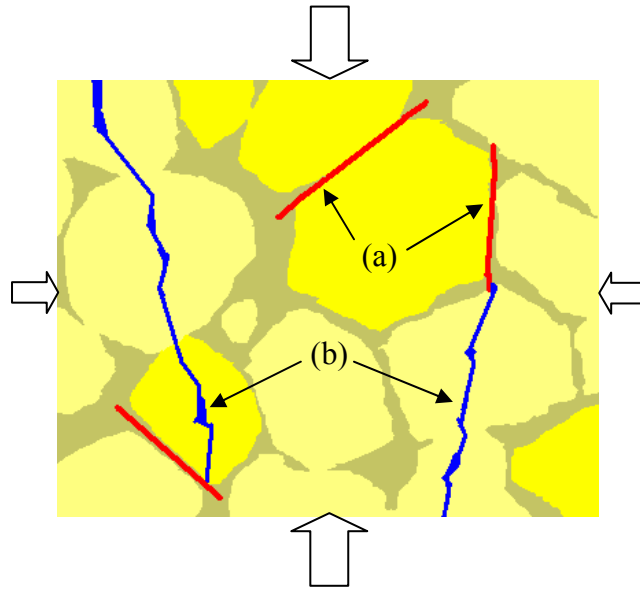


Figure 3.3. Two types of microcracks: (a) inter-crystal/grain; (b) intra-crystal/grain.

Pre-existing microcracks can be oriented in any direction and, upon loading, this orientation will influence their mechanical behaviour. The particular type of behaviour can define two types of microcracks:

- *Shear cracks*: inclined to the direction of applied differential load (Figure 3.4a). The surfaces of these cracks undergo frictional sliding under applied load.
- *Tensile cracks*: oriented parallel or normal to the direction of the applied differential load (Figure 3.4b). These cracks experience closure (normal cracks) or opening (parallel cracks) under the load.

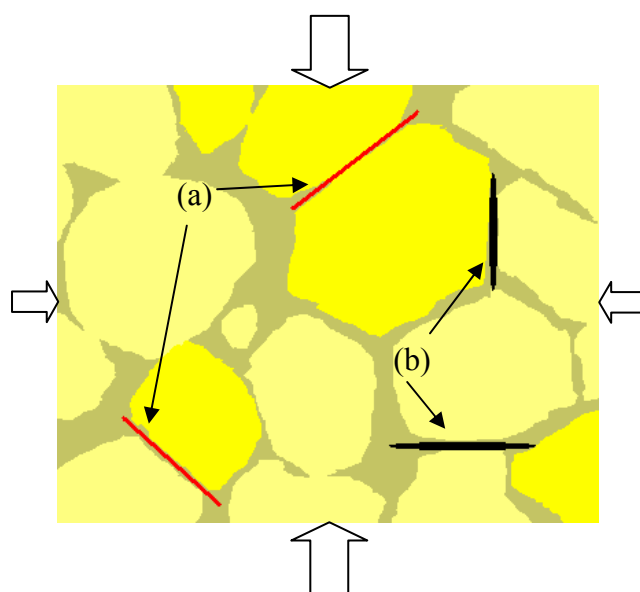


Figure 3.4. Microcracks distinguished by their orientation to differential stress: (a) shear cracks; (b) tensile cracks.

Tensile axial cracks may be one of three types (Brace & Byerlee, 1967), depending on the mechanism of their formation:

1. *Isolated axial crack*, Figure 3.4b;
2. *Junction crack*, Figure 3.5a;
3. *Wing crack*, Figure 3.5b.

Isolated axial cracks are formed along cleavages within grains or along grain boundaries. The mechanism of junction and wing cracks formation and propagation is as follows. Consider pre-existing shear microcracks in a rock specimen (Figure 3.5).

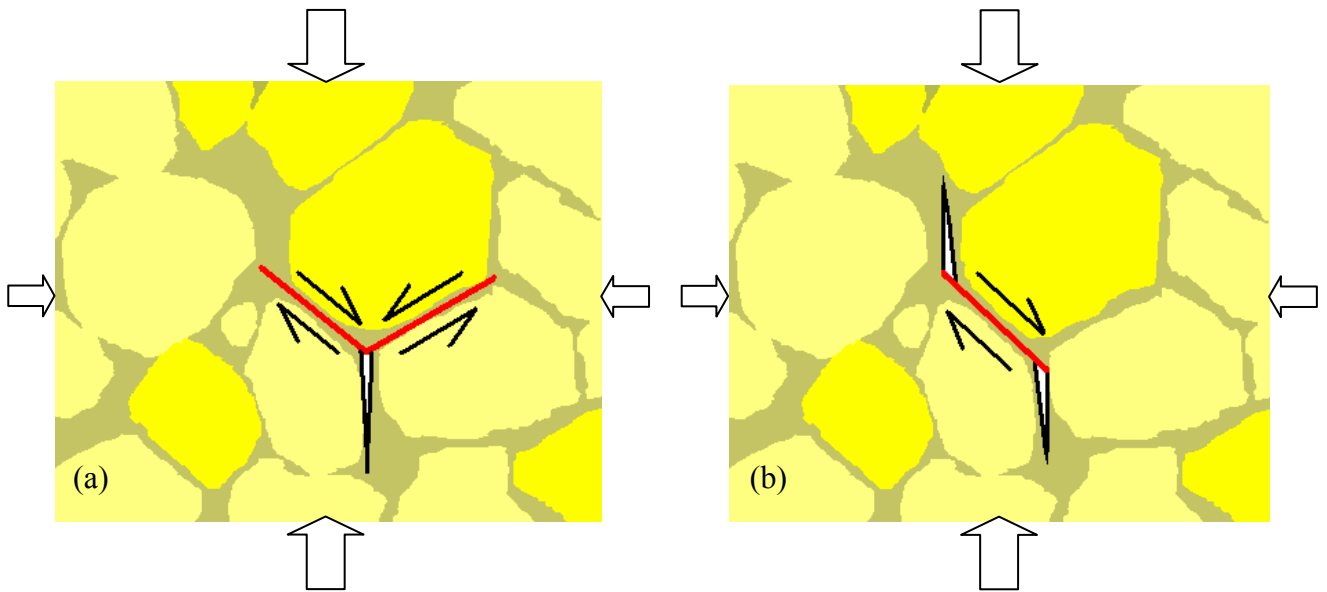


Figure 3.5. Frictional sliding and formation of tensile: (a) junction crack; (b) wing cracks

Under application of a differential load the crack experiences shear stress  $\tau$  acting along its surfaces. This stress can be withstood only up to a certain critical value  $\tau_c$  i.e.:

$$\tau_c = S_0 + \mu\sigma \quad (3.2)$$

where  $S_0$  is the shear strength of the closed crack,  $\mu$  is the coefficient of friction and  $\sigma$  is the stress acting normal to the crack surface. Once the shear stress is greater than  $\tau_c$ , the crack surfaces slide relative to each other. If the shear stress is high enough, the crack will fail at its tips (Griffith's theory). This leads to the opening of a tensile junction crack or wing cracks which are oriented in the direction of the applied maximum stress,  $\sigma_1$ . As a result, the rock will experience dilatancy i.e. anelastic increase in volume. If the specimen is unloaded, some cracks will close or slide back; however some displacement will be irrecoverable, causing anelastic hysteresis  $\Delta\varepsilon$  in the stress-strain diagram (Figure 3.6).

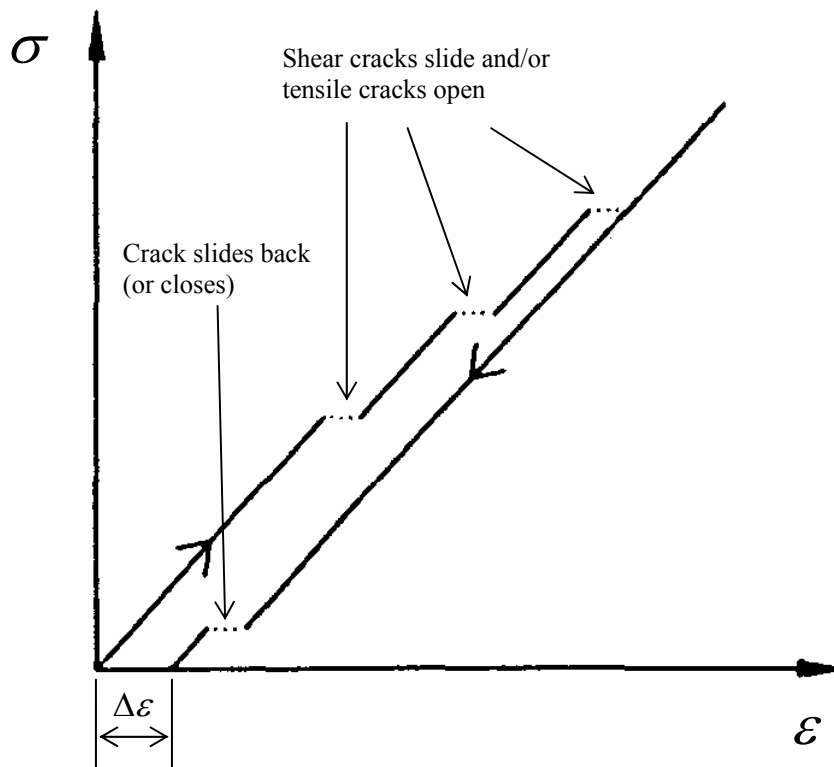


Figure 3.6. Hysteresis  $\Delta\varepsilon$  resulted from irrecoverable sliding and/or opening of microcracks (after Fjær et al., 1992).

Many researchers of the KE/DME (e.g. Stevens & Holcomb (1980), Costin (1983), Stuart et al. (1993), Li & Nordlund (1993), Barr & Hunt (1999)) agree that the mechanism responsible for the phenomenon is based on the microcrack rock deformation. They propose that the damage in the specimen accumulated by the formation of microcracks (in the anelastic region) while applying the pre-load stress under laboratory conditions is irreversible. Hence, consecutive reloading does not produce any notable damage in the specimen until the stress reaches the value of the previously applied load, as most induced under this stress regime microcracks have already been formed. With continuing application of the compressive stress, past the pre-load value, the specimen again begins to experience microcrack nucleation and growth. Thus it can be said the damage in the rock sample caused by the pre-load has been memorised in the form of a network of microcracks (irreversible damage). Initially nucleating then growing, these cracks produce microseismic waves (acoustic signals) caused by the energy release, predominantly from the breakage of the interparticle bonds. This action accounts for the onset of AE at the moment the stress increases beyond the maximum in-situ stress the rock has previously experienced. The cumulative count of AE is directly proportional to the number of microcracks accumulated in a sample during the uniaxial compression.

Utilisation of the DME by the DRA technique can be explained as follows. In purely elastic material, strain is considered to be reversible. In elasto-plastic materials such as rocks, there are two strain components present: elastic, which is reversible, and inelastic, which is not. The reversible components of strain are cancelled in the strain difference function (Eq. 2.1). The development of new tensile and shear cracks results in irreversible rock damage, thus the differential strain from two consecutive loading cycles will have a non-zero value. This phenomenon is particularly apparent once the axial stress exceeds the previously applied maximum stress, since this stage of loading, as discussed above, is characterised by the onset of irrecoverable microcracks. Strain rate in two cyclic reloading curves is expected to be similar up to the pre-load value, as not many new microcracks will be formed. The strain difference function is either horizontal or gently increases to the pre-load (Figures 2.4 and 3.7). After surpassing the pre-load, the differential strain decreases as the strain hardening effect occurs in the subsequent reloading cycle.

The microcrack-based nature of the DME as a primary underlying principle of the phenomenon is assumed throughout this study. The aim of this research is to develop a model that numerically validates the physical occurrence of the KE/DME. The numerical model is based on the behaviour of sandstone discussed in the next section.

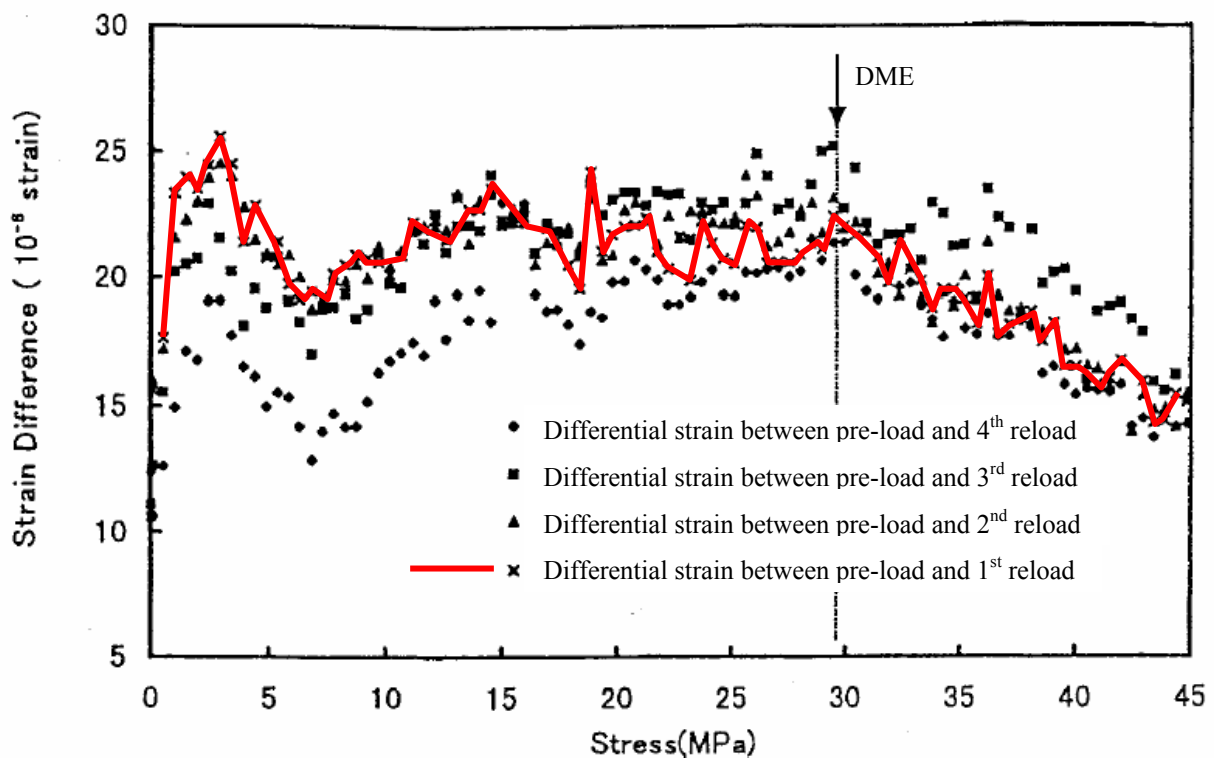


Figure 3.7. Strain difference function for a granite specimen subjected previously to axial stress of 31.5 MPa under confining pressure of 15 MPa (from Seto et al., 1999).

## 4 PHYSICAL PROTOTYPE

A 61-mm diameter core of coarse-grained sandstone was chosen as a physical prototype for the numerical model, Figure 4.1. The thin section in Figure 4.2 shows the core to be comprised approximately of 40% quartz, 40% feldspar with the remainder being opaques and fine-grained cements. The specimen is well-cemented and compacted with an average grain size of approximately 0.25 mm. There is no bedding observed in the sample. The bulk density of the rock is  $2,397 \text{ kg/m}^3$ , its uniaxial compressive strength is 82.1 MPa and the Young's modulus is 14.3 GPa. In this work, the core is referred to as 'Specimen #3', after Oliver (2001) who performed the actual tests on it.



*Figure 4.1. Physical prototype, Specimen #3.*

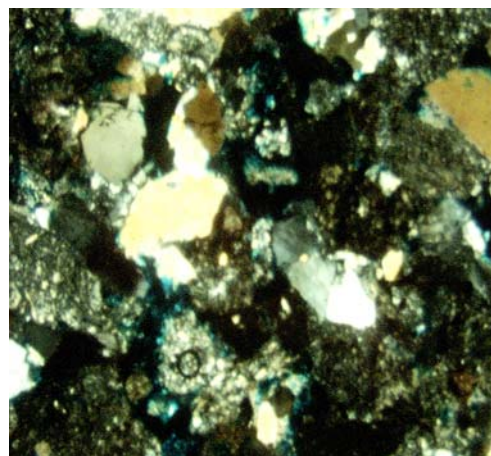


*Figure 4.2. Thin section of Specimen #3 under polarised light.*

The core was tested as follows (Meyers et al., 2002). Diametrically opposing strain gauges were used to monitor axial strain during loading. Each gauge was wired to form one of four ‘arms’ of a full Wheatstone bridge. Two strain gauges attached to another core acted as ‘dummy’ gauges in the other two arms of the bridge. The axial load on the core was monitored with a Shaevitz pressure transducer connected into the hydraulic line of the loading machine. The out-of-balance voltage from the bridge and the output from the transducer were amplified using two high-resolution Sanei DC strain amplifiers (Model 6M91). The voltages from the amplifiers were input into separate channels of a 16-bit A/D converter. The digital output was logged with a data logger. An LRR test was performed on the core for three different stress values. The first cycle steadily applied a pre-load at a rate of 0.2 kN/s, which was intended to simulate an in-situ stress. The pre-load was selected to induce a stress in the core greater than that to which the core had recently been subjected to in-situ (estimated from the overburden load). The pre-load was maintained within a tolerance of  $\pm 1\%$  for one hour; the duration considered sufficient to induce a ‘stress memory’ into the core. The load was then removed rapidly to simulate the stress relief that occurs with overcoring. The second and third cycles involved slowly loading the core up to a stress of about 15-20% higher than pre-load. The transducers were logged during the re-loading cycles and all data was stored in spreadsheet format.

Details of the stresses applied during the tests are listed in Table 4.1. The strain difference function was performed on two re-loading cycles (Figure 4.3). Trend lines were fitted to each curve to assist with the determination of inflection points.

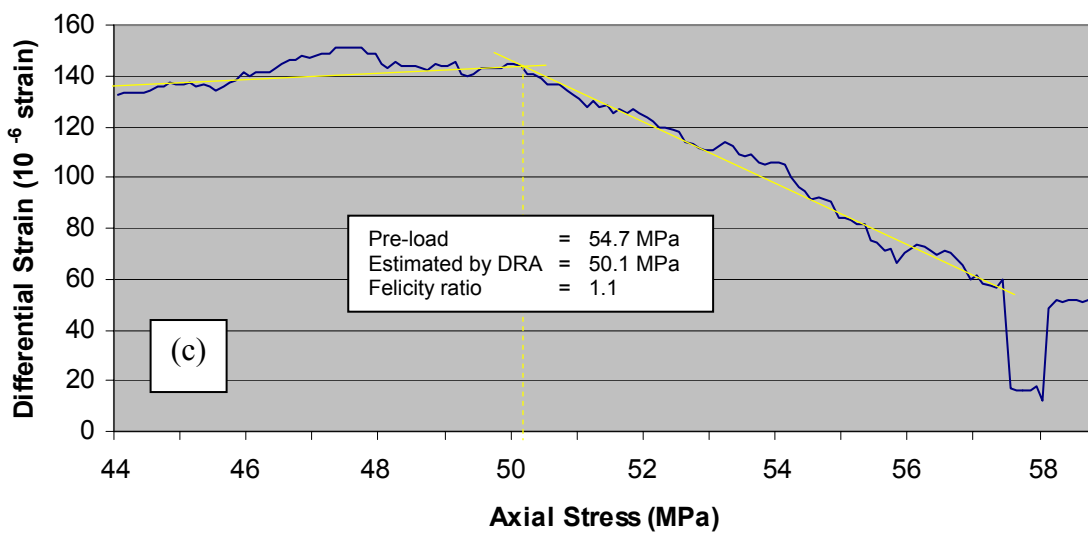
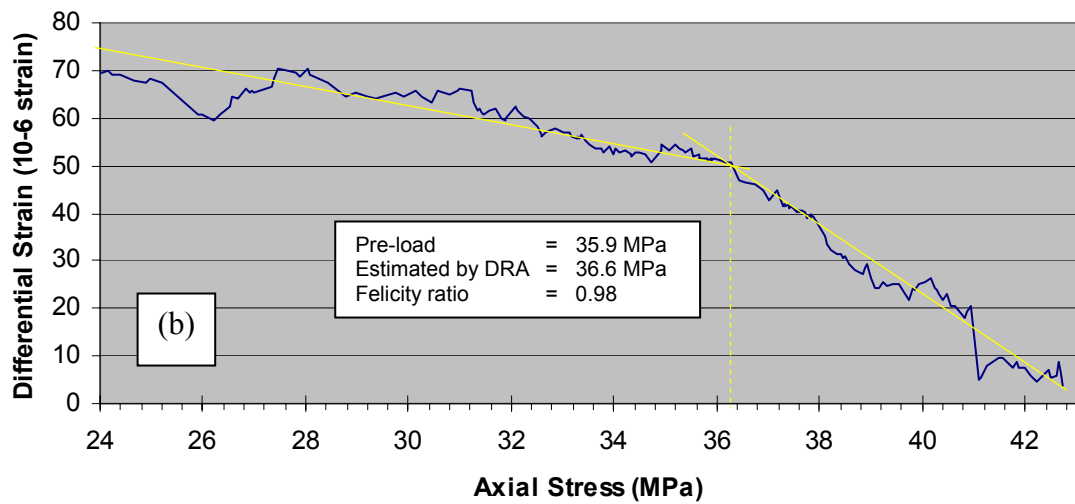
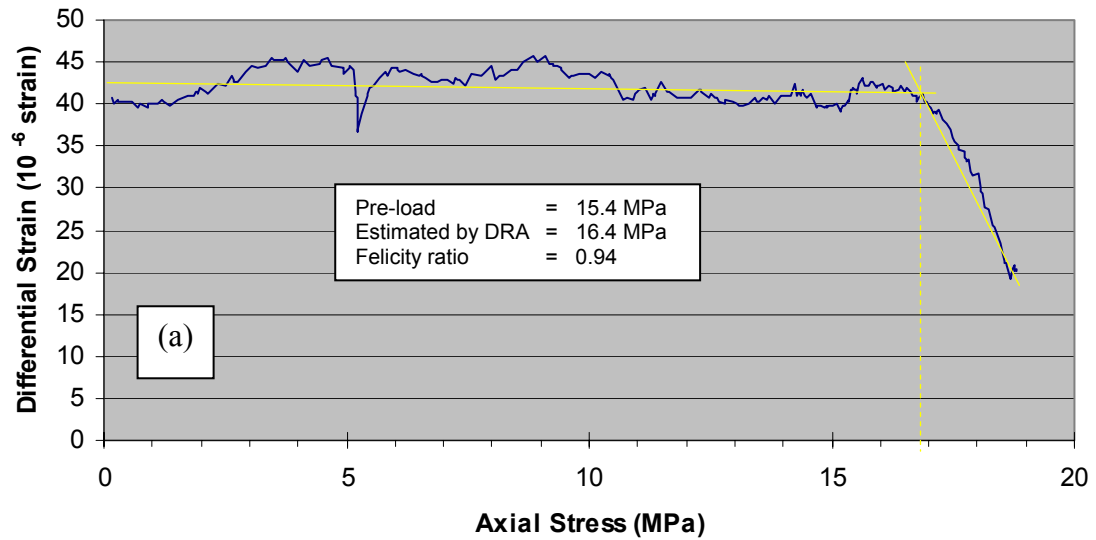


Figure 4.3. Strain difference function at various pre-loads: (a) 15.4 MPa; (b) 35.9 MPa; (c) 54.7 MPa.

Table 4.1. Axial loads applied in LRR tests on Specimen #3.

Cycle number	Applied load, MPa		
1 (pre-load)	15.4 <sup>1</sup>	35.9	54.7
2 and 3 (reloads)	18.8	42.8	59.9

The axial stress at each inflection point, which indicates the DME, is listed in Table 4.2. The ratio between the stress at the inflection point and the pre-load stress is referred to as the *Felicity ratio* (FR). A ratio of 1 indicates the values fully coincide. The ratios determined for each pre-load are presented in Table 4.2. The results suggest that the stress at which the DME occurred was similar to the pre-load.

Table 4.2. Results of LRR tests on Specimen #3.

<b>Inflection point (DME), MPa</b>	16.4	36.6	50.1
<b>FR</b>	0.94	0.98	1.10

---

<sup>1</sup> In this work, all induced pre-load values are denoted by red font.

## 5 NUMERICAL MODELLING

### 5.1 Numerical modelling in rock mechanics

In general, two methodologies are used to model the characteristics and behaviour of rock masses: continuous and discontinuous.

In continuous modelling, the rock mass is modelled as a continuum with infinite degrees of freedom. Its behaviour is described by differential equations located at points within the area defined by the extent of the rock mass under consideration. This area is sub-divided into a finite number of elements, sub-domains, which have finite degrees of freedom. Displacements and positions of an element are interpolated from discrete nodal values. For every element, the partial differential equations governing the motion of material points in the continuum are formulated, which produces a discrete system of differential equations. The sub-domains are required to satisfy the governing differential equations as well as to ensure continuity of solution at the interface with neighbouring elements.

The discontinuous modelling technique, generally referred to as the discrete element method (DEM), involves representing the rock mass as a finite number of elements. Each element is free to rotate and translate. The behaviour of an element is governed by the laws of motion. The method is based on an explicit solution scheme, in which the approximate solution for displacement  $u_{i+1}$  at time  $t+1$  is determined in terms of known values of  $u_i$  at the previous time level  $t$ . The explicit solution permits step-by-step evaluation of displacement and does not require resolution of a series of differential equations. It is the efficiency of this system that endears it to modelling discontinua, a characteristic that makes it the modelling method of choice for this study.

### 5.2 Discrete element method: $PFC^{2D}$

#### 5.2.1 General formulation

The discrete element approach derives from models of microscopic crystals, in which the crystal is considered to be made up of a closely packed lattice of particles interacting according to Hooke's law. Cundall and Strack (1979) used a similar approach to model discontinuous rock using the DEM technique. In this technique, particles representing grains of rock interact through both radial and shear forces. Although the DEM was originally developed for modelling rocks, it

has been widely used for reconstruction of mechanical behaviour of other granular materials, such as grains, powders, soils, ice etc.

Sandstone is particularly well suited for DEM modelling as the material effectively comprises an assemblage of quartz grains interbonded by silica cements (Figure 5.1). This feature can be idealised by a collection of spherical (in a 3D code) or circular (in a 2D code) particles bonded to each other (Figure 5.2). The process of a DEM model conception can be envisaged as a natural physical process. The modelling is implemented in the algorithm by simulating the physical processes governing sedimentation and compaction of sandstone under the action of gravity, inter-granular contact forces and friction forces between unbonded grains.

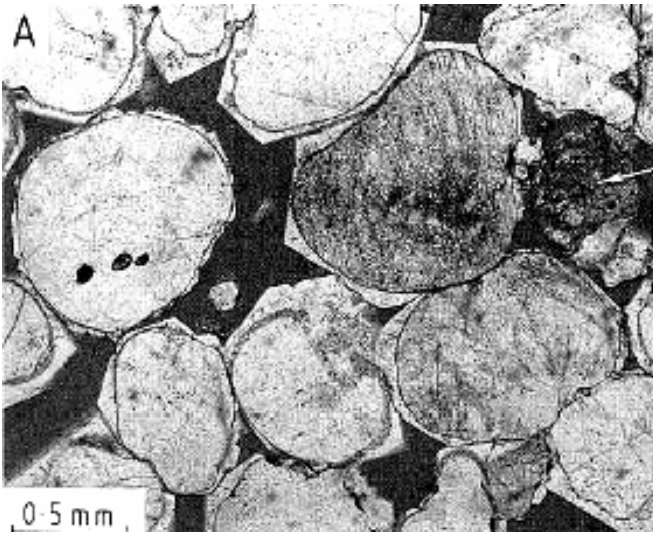


Figure 5.1. Typical sandstone texture: quartz grains imbedded into the silica matrix (from Jin et al., 2003).

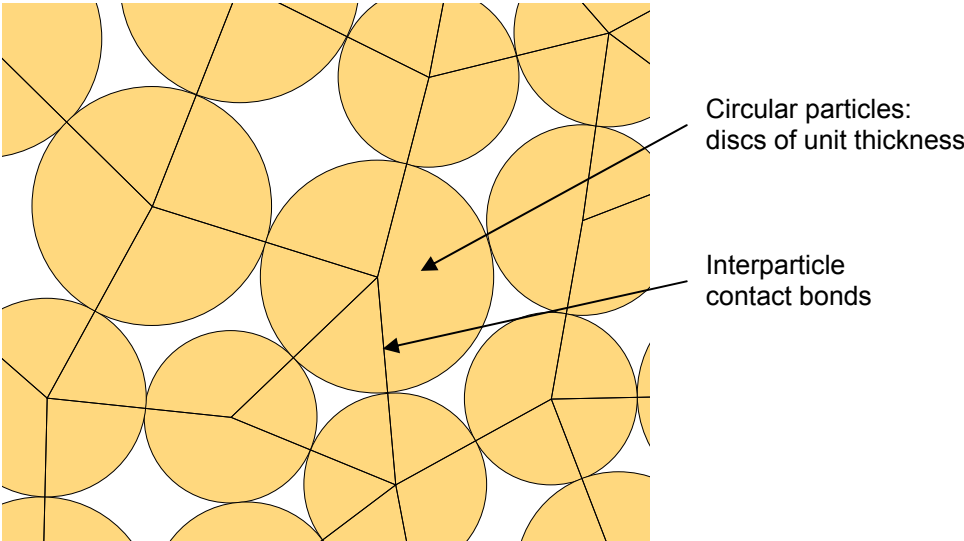


Figure 5.2. Representation of sandstone texture in a 2-dimensional DEM model: arbitrary sized circular particles jointed by contact bonds.

In this research, Particle Flow Code –  $PFC^{2D}$ , a formulation of the discrete element method developed by Itasca Consulting Group (Itasca, 1999), was chosen for modelling the DME in a sandstone specimen. The decision has been made for the following reasons. The code:

- simulates movements and interaction of discrete bodies;
- provides fully dynamic real-time simulation;
- recognises new contacts automatically;
- provides tools for measuring forces between particles and stresses at any point;
- allows complete detachment between particles and as such simulates modelling of microcracks.

A typical two-dimensional  $PFC^{2D}$  model represents an assemblage of arbitrary sized circular discs of unit thickness (Figure 5.2). The dynamic simulation principle is based upon solution of Newton's laws of motion for each particle in the assembly. The force system can be either in equilibrium or such as to cause particles to flow. For solid materials, such as rocks, more complex behaviour is modelled by the introduction of contact bonds representing inter-particle forces. Local deformations between particles in the bonded models are initiated by bond breakage. The contact bonds are assigned shear and tensile strength values. When the tensile strength is exceeded, the bond breaks and the tensile strength becomes zero. When the shear strength is exceeded, the shear force is set to a residual value that depends on the compressive normal force at the contact and the coefficient of friction, thus resulting in frictional sliding.

In addition to circular particles (referred to as *balls* in the  $PFC$  terminology), there is an element in a particle flow model called a *wall*. Walls allow for the application of velocity boundary conditions to the model, which exert external forces on the particles.

Some important assumptions are required for the solution (Itasca, 1999):

- the particles are represented as rigid discs;
- particle contacts occur at a point.

Particle overlap is permitted at the contacts (soft-contact approach), but these overlaps are small relative to the particle size.

The calculation cycle is a time-stepping process, where Newton's second law and force-displacement law are applied to each contact repeatedly, as illustrated by the diagram in Figure 5.3.

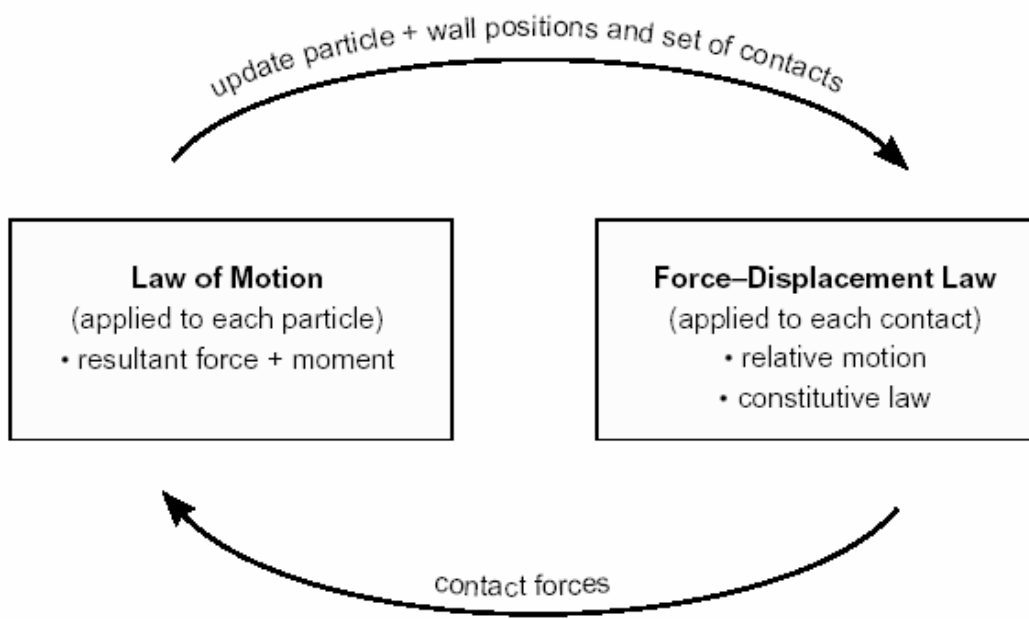


Figure 5.3. Calculation cycle in PFC (from Itasca, 1999).

At the start of each time step (termed a *cycle*), the particle contacts are updated from the known ball and wall coordinates. The force-displacement law is applied first, to update the contact forces acting at each contact location. Then, the law of motion is applied to each particle to calculate its velocity. During simulation, both processes run in parallel.

The solution process begins by determining the unit normals of the contacts; refer to Figure 5.4 (after Itasca, 1999):

$$n_i = \frac{x_i^{[B]} - x_i^{[A]}}{d} \quad (5.1)$$

where  $n_i$  is the unit normal,  $x_i^{[A]}$  and  $x_i^{[B]}$  are the location of centres of balls A and B, and  $d$  is the distance between the ball centres.

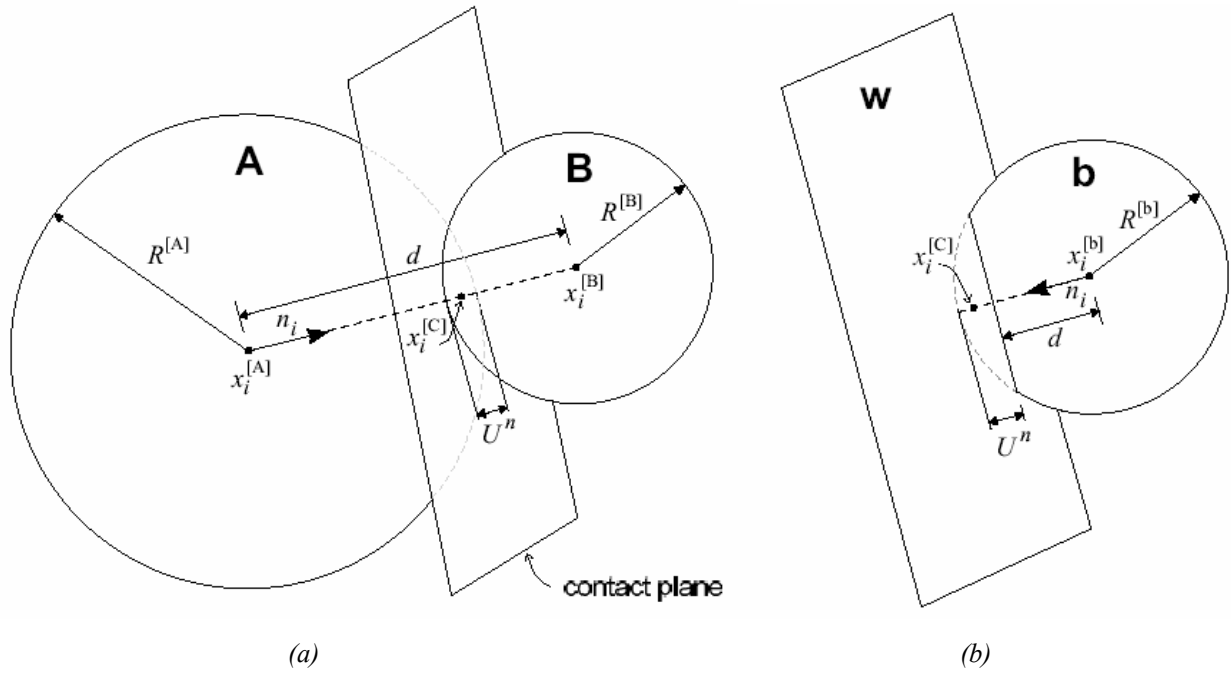


Figure 5.4. Schematic diagram of: (a) ball-ball contact; (b) ball-wall contact (from Itasca, 1999).

The overlap at contacts, a relative contact displacement in the normal direction, is determined as:

$$U^n = \begin{cases} R^{[A]} + R^{[B]} - d, & \text{(ball-ball)} \\ R^{[b]} - d, & \text{(ball-wall)} \end{cases} \quad (5.2)$$

where  $R^{[\Phi]}$  is the radius of the ball  $\Phi$ .

The location of the contact point is then calculated as:

$$x_i^{[C]} = \begin{cases} x_i^{[A]} + \left( R^{[A]} - \frac{1}{2} U^n \right) n_i, & \text{(ball-ball)} \\ x_i^{[b]} + \left( R^{[b]} - \frac{1}{2} U^n \right) n_i, & \text{(ball-wall)} \end{cases} \quad (5.3)$$

Having determined the contact location, velocities can be calculated. The motion of a particle is described in terms of the translational motion of a point in the particle and the rotational motion of the particle (Note, there is only one rotational degree of freedom in two-dimensional particles):

$$F_i = m(\ddot{x}_i - g_i) \quad \text{(translational motion)} \quad (5.4)$$

$$M_3 = 0.5mR^2\dot{\omega}_3 \quad \text{(rotational motion)} \quad (5.5)$$

where  $F_i$  is the resultant force acting on the particle,  $m$  is the mass of the particle,  $\ddot{x}_i$  is the particle acceleration,  $g_i$  is the gravitational acceleration,  $M_3$  is the resultant moment acting on the particle,  $\dot{\omega}_3$  is the angular acceleration of the particle about the out-of-plane axis.

The equations of motion are then integrated involving a time-step  $\Delta t$  :

$$\begin{aligned}\ddot{x}_i^{(t)} &= \frac{1}{\Delta t} \left( \dot{x}_i^{(t+\Delta t/2)} - \dot{x}_i^{(t-\Delta t/2)} \right) \\ \ddot{\omega}_3^{(t)} &= \frac{1}{\Delta t} \left( \omega_3^{(t+\Delta t/2)} - \omega_3^{(t-\Delta t/2)} \right)\end{aligned}\quad (5.6)$$

$$\begin{aligned}\dot{x}_i^{(t+\Delta t/2)} &= \dot{x}_i^{(t-\Delta t/2)} + \left( \frac{F_i^{(t)}}{m} + g_i \right) \Delta t \\ \omega_3^{(t+\Delta t/2)} &= \omega_3^{(t-\Delta t/2)} + \left( \frac{M_3^{(t)}}{0.5mR^2} \right) \Delta t\end{aligned}\quad (5.7)$$

The velocities are then used to update the position of the particle centre:

$$x_i^{(t+\Delta t)} = x_i^{(t)} + \dot{x}_i^{(t+\Delta t/2)} \Delta t \quad (5.8)$$

The critical value of the time step for a stable solution is calculated based on simplified mass-spring system logic (Itasca, 1999):

$$t_{crit} = \begin{cases} \sqrt{\frac{m}{k^{tran}}} & \text{(translational motion)} \\ \sqrt{\frac{0.5mR^2}{k^{rot}}} & \text{(rotational motion)} \end{cases} \quad (5.9)$$

where  $k^{tran}$  and  $k^{rot}$  are the translational and rotational stiffnesses.

### 5.2.2 Definition of microcracks in PFC

The capability of the *PFC* material to reproduce damage in the solid rock is attributed to its ability to generate compression induced tensile cracks. The mechanism of the microcrack formation, as it is implemented in the code, is illustrated in Figure 5.5. Each broken bond is analogous to the formation of a microcrack.

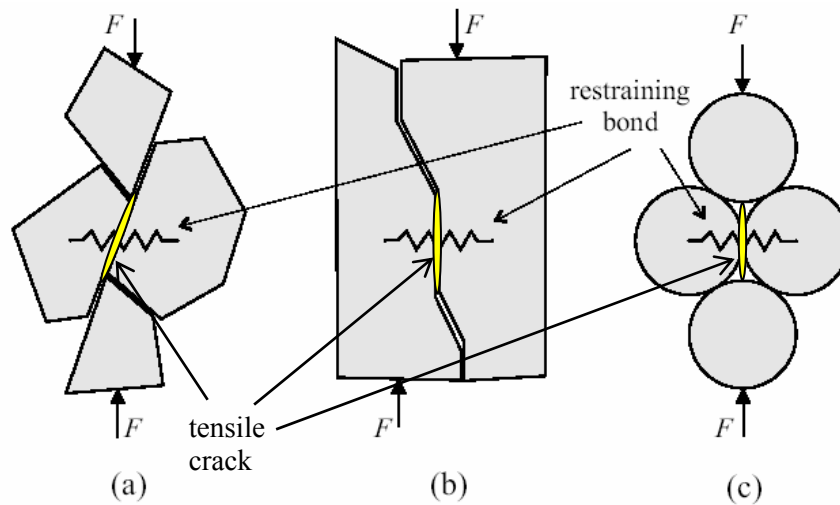


Figure 5.5. Mechanism of tensile crack formation: (a) and (b) in a physical rock material; (c) idealised representation in a DEM environment (after Itasca, 1999).

Fracture development in a *PFC* model occurs naturally through evolution of localised microfractures into a sample macro failure: after a bond breaks, stress is globally redistributed causing more cracks to form nearby.

A microcrack in a *PFC* model is assumed to be a cylinder with its axis lying in the modelling plane (Figure 5.6). The size and location of the cylinder are determined by the sizes and positions of two parent particles and defined by the radius, thickness, unit normal and the cylinder centroid. The cylinder thickness is determined as:

$$t_c = d - (R^{[A]} + R^{[B]}) \quad (5.10)$$

where  $d$  is the distance between particle centres,  $R^{[A]}$  and  $R^{[B]}$  are the particles radii. The cylinder centroid is located at:

$$x_i = x_i^{[A]} + (R^{[A]} + 0.5t_c)n_i \quad (5.11)$$

where  $n_i$  is the unit normal from  $x_i^{[A]}$  to  $x_i^{[B]}$ .

The cylinder radius is given by:

$$R_c = R^{[A]} + (R^{[B]} - R^{[A]}) \left( \frac{R^{[A]} + 0.5t_c}{d} \right) \quad (5.12)$$

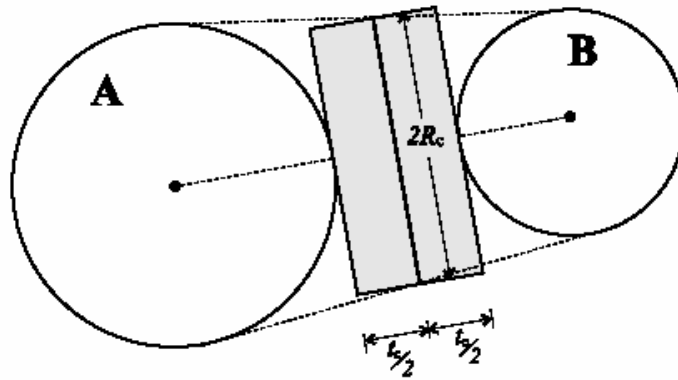


Figure 5.6. Representation of a microcrack in PFC (from Itasca, 1999).

### 5.2.3 Modelling strategy

The process of the numerical modelling of the DME comprised the following stages:

1. Generating the initial base model assembly;
2. Calibrating the model to match the mechanical properties of the real rock;
3. Conducting compressive cyclic tests;
4. Transferring test data into spreadsheets, obtaining the DME characteristic points;
5. Analysing results.

The overall modelling strategy is represented in Figure 5.7. Initially the DME tests were conducted on an intact rock model consisting of a homogenous material. Then a number of more complex models were created: complex lithology model and discontinuous rock model. Subsequently, the synthetic specimens were subjected to the uniaxial and biaxial compressive tests. To simplify analysis during the experiment only one variable in each test series was modified between tests.

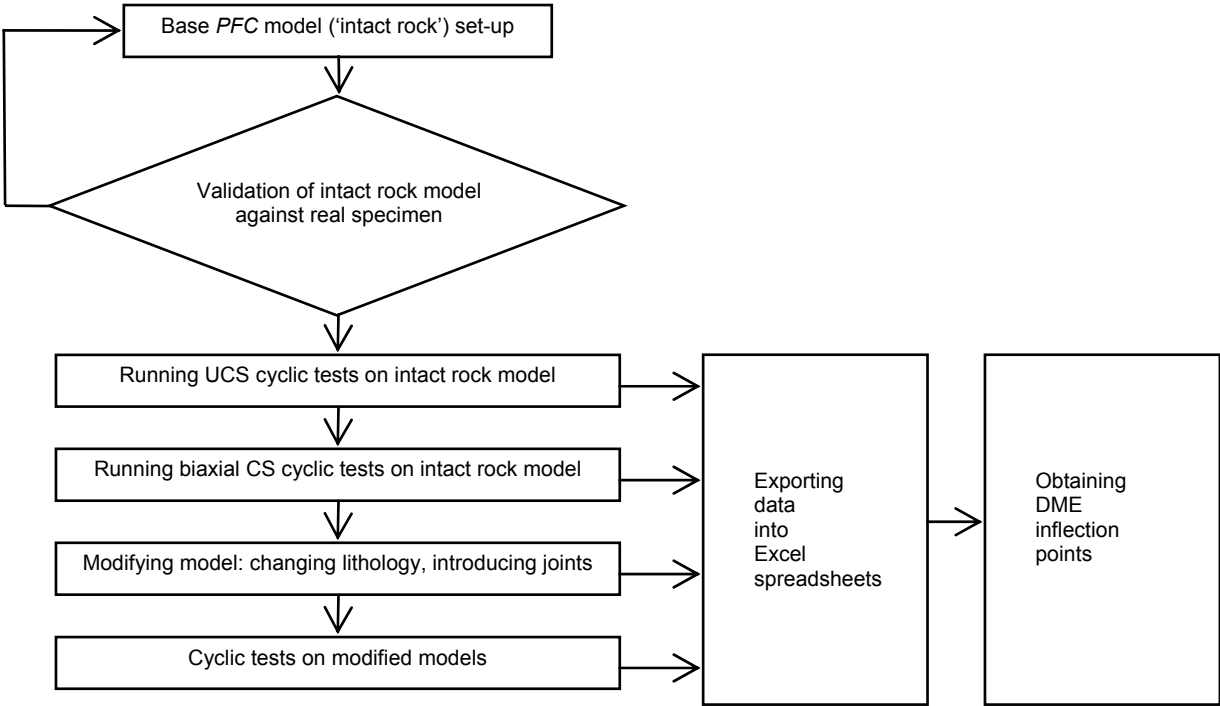


Figure 5.7. Modelling strategy.

### 5.3 Development of synthetic specimens

#### 5.3.1 Intact rock model

The process involved in generating a model is illustrated in Figure 5.8. The steps in the flowchart are logical, similar to those that occur in a natural environment. Initial assembly of a simulated rock sample was implemented by a process involving the generation of walls and particles (Figure 5.9). The base model represented an ‘intact rock’ replica of the physical Specimen #3. This model was created in two stages. In the first stage, the synthetic specimen was assembled with arbitrarily assigned deformability and strength parameters. The second stage involved applying the uniaxial compressive load to the assembly followed by a number of iterative modifications of microparameters to obtain realistic behaviour of the model, i.e. the model must have rock-distinctive stress-strain response as well as failure mode<sup>2</sup>.

<sup>2</sup> All subroutines used for the numerical modelling of the DME are presented in Appendix 2.

Figure 5.9 illustrates the final model. Contact bonds between the particles are represented by a line connecting particle centres. Each particle has at least three contact bonds to ensure the stability of the assembly. The network of interparticle contact forces is presented in Figure 5.10.

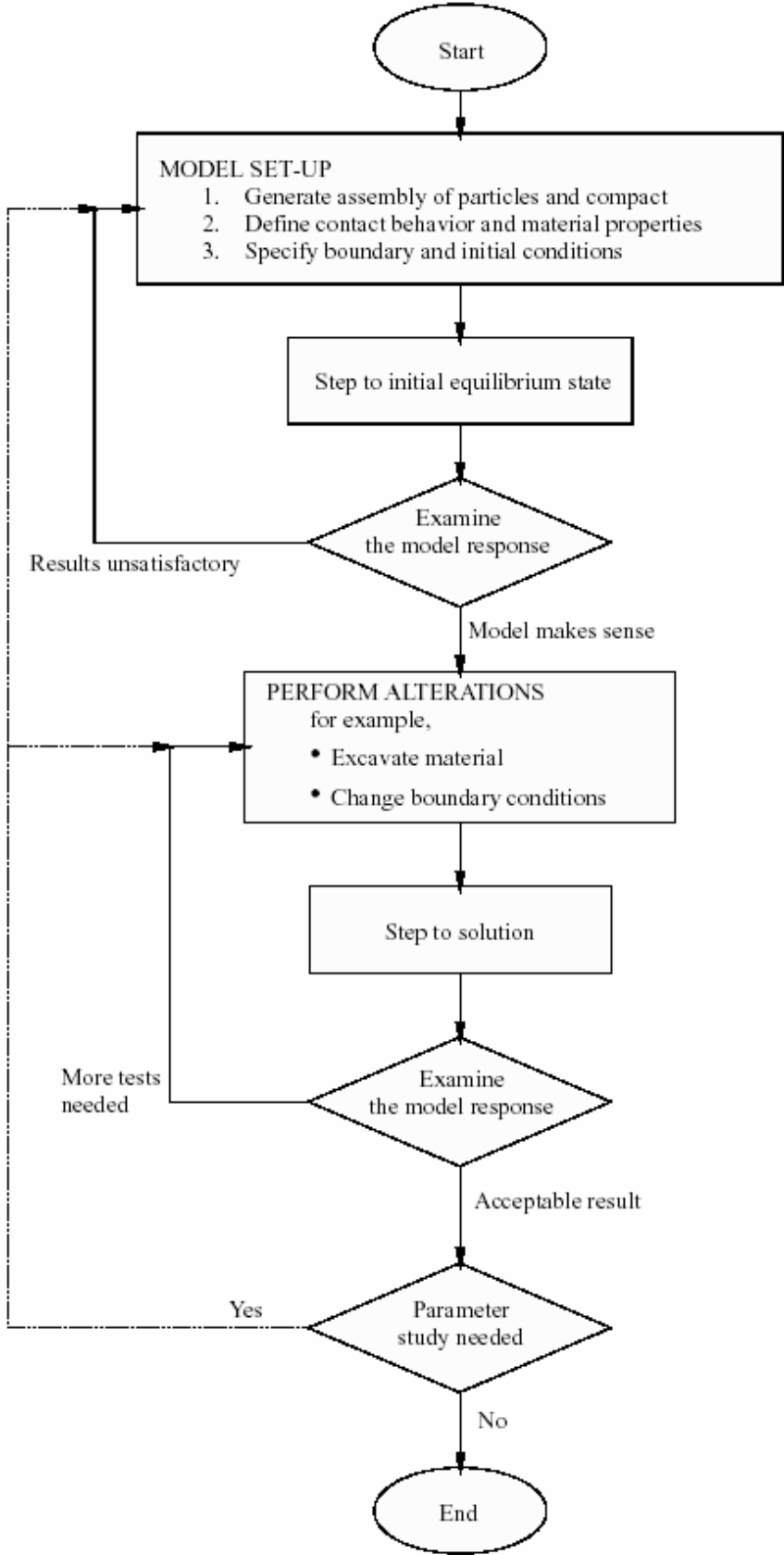


Figure 5.8. General solution procedure (from Itasca, 1999).

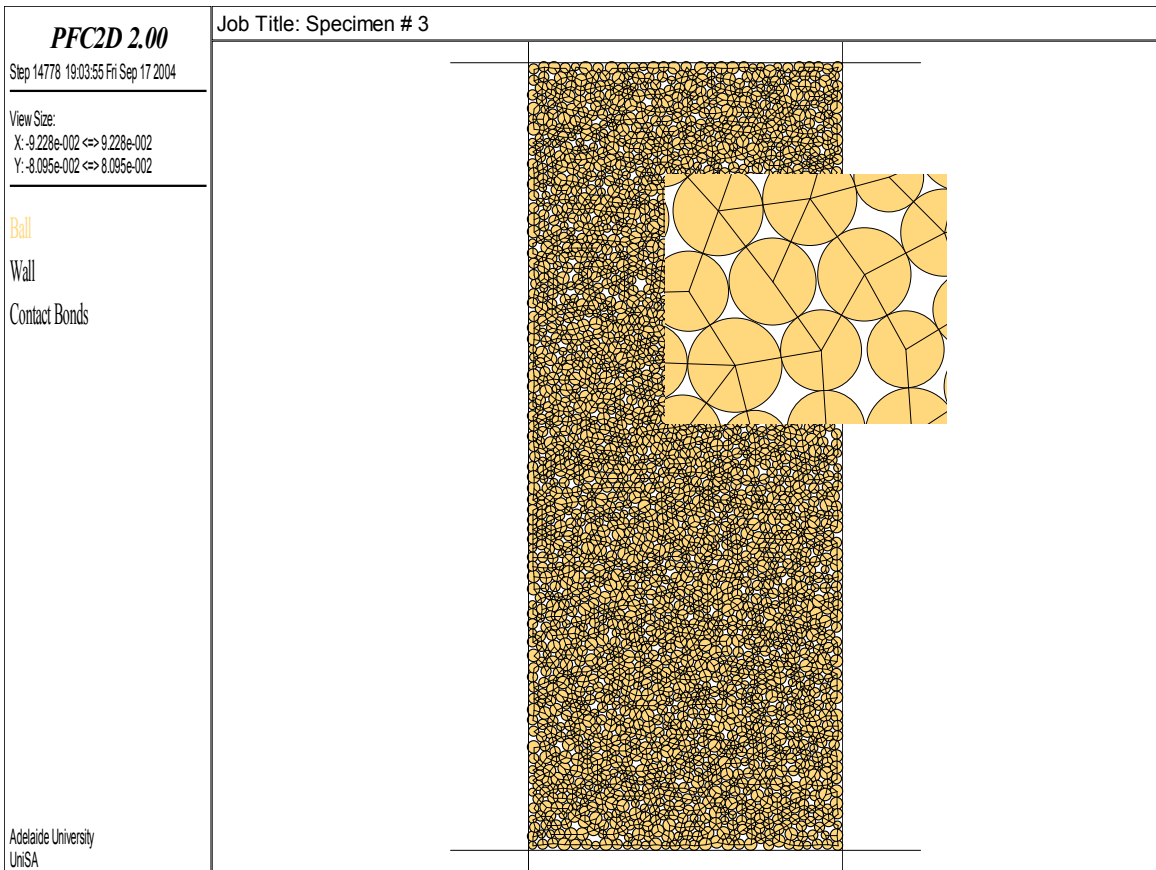


Figure 5.9. Assembled model. Close-up shows interparticle contact bonds.

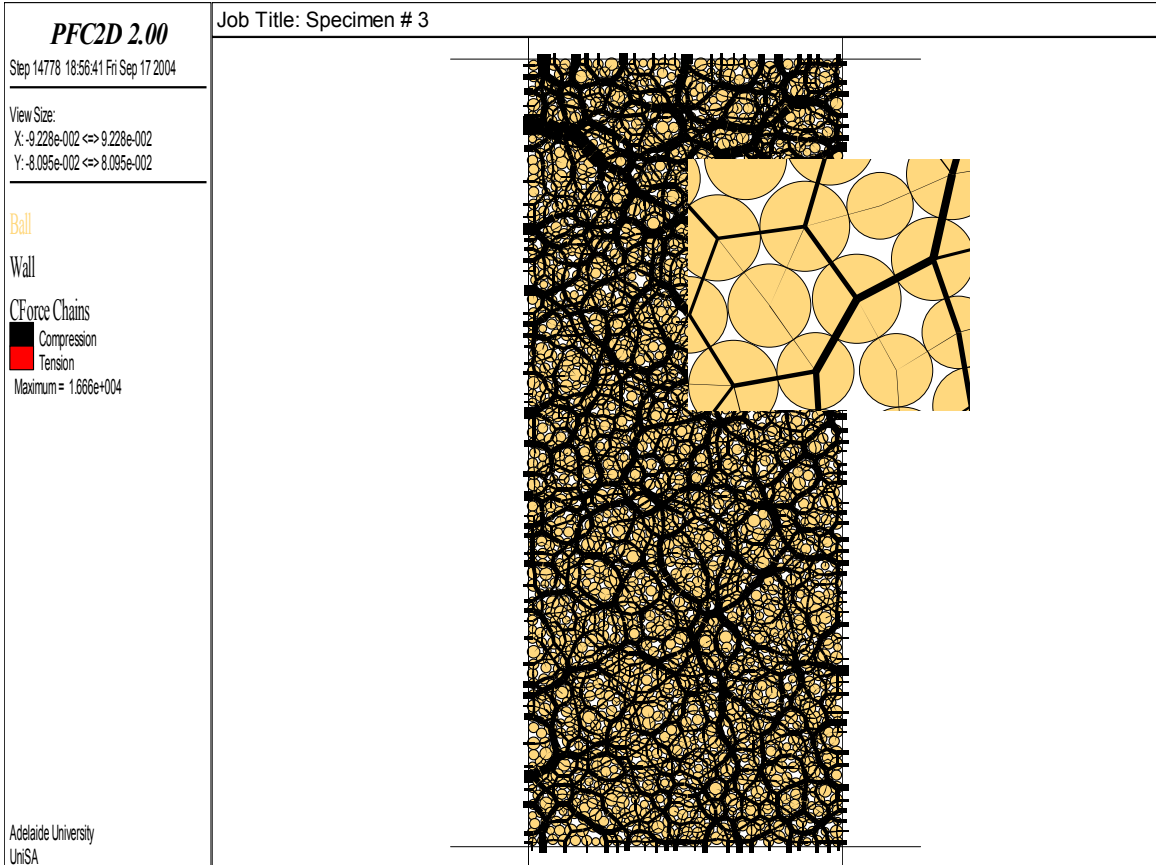


Figure 5.10. Contact forces between particles. The line thickness is proportional to the force magnitude.

The model consisted of 2,505 round particles ranging in size from 0.8 to 1.2 mm. This size is not associated with the grain size of a real specimen (mean 0.25 mm) as the macroresponse of the replicated model is independent of particle size (Itasca, 1999). Decreasing the ball sizes increases the number of particles, which unnecessarily complicates the model and results in an increased computational time.

The biaxial compressive test set-up is presented in Figure 5.11. The specimen is loaded by moving the top and bottom horizontal walls (referred to as ‘platens’) whereas the lateral walls, controlled by a servo-mechanism algorithm, maintain the constant confining pressure on the specimen. In the case of a uniaxial compressive test, the confining stress is assigned a very low value and vertical walls are made negligibly ‘soft’ relative to the ball stiffness.

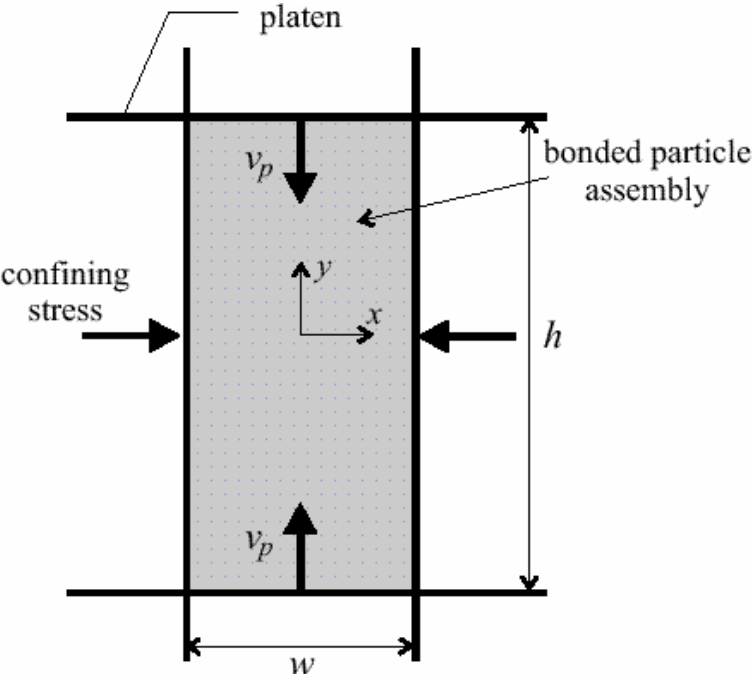


Figure 5.11. Biaxial test principle in PFC environment (from Itasca, 1999).

Table 5.1 lists the macroscopic properties of the synthetic material as well as the properties of the physical prototype. Although every effort was made to obtain an accurate match of the properties of the two materials, the minor discrepancies could not be overcome. The stress-strain diagram of the modelled rock is presented in Figure 5.12.

Table 5.1. Parametric comparison of real specimen and its numerical replica.

Material	Density (kg/m <sup>3</sup> )	UCS (MPa)	Young’s modulus (GPa)	Poisson’s ratio
Real sandstone	2397	83.1	14.3	0.23
Intact rock model	2397	85.1	14.2	0.21

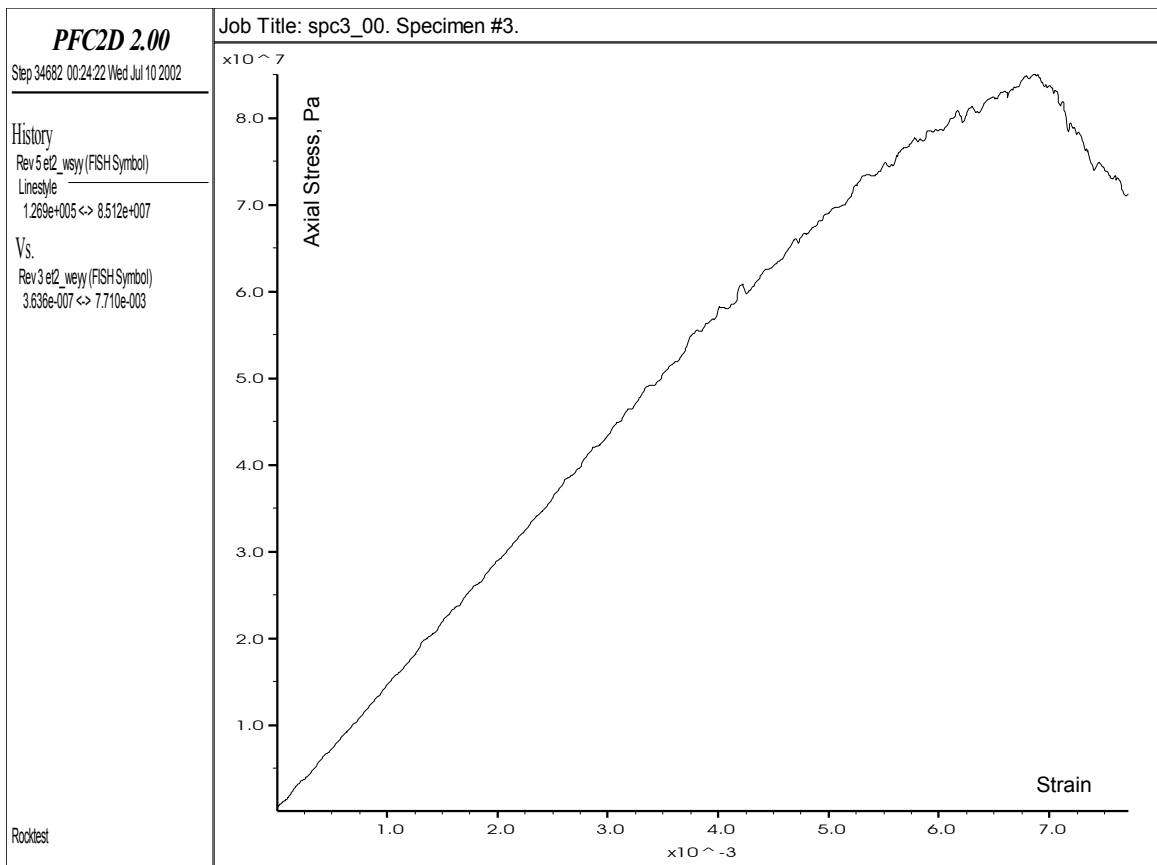


Figure 5.12. Intact rock model: stress-strain diagram.

Specimen failure can be observed by obtaining a view of microcracks in the core, superimposed on the view of particle displacement vectors (Figure 5.13a). Figure 5.13b represents the same specimen failed at the confining stress of 20 MPa in a biaxial test. In both cases, the main failure planes occur at about  $30^\circ$  to the direction of maximum principal stress, a typical orientation for the plane of maximum shear stress within an actual physical sample undergoing similar loading conditions.

Once the model was complete and the mechanical properties of the physical and the numerical specimens were similar, it was concluded that the stress-strain characteristics of the model closely resembled those of the real rock. The modelling process was then progressed to the main stage of the analysis, i.e. replicating the DME.

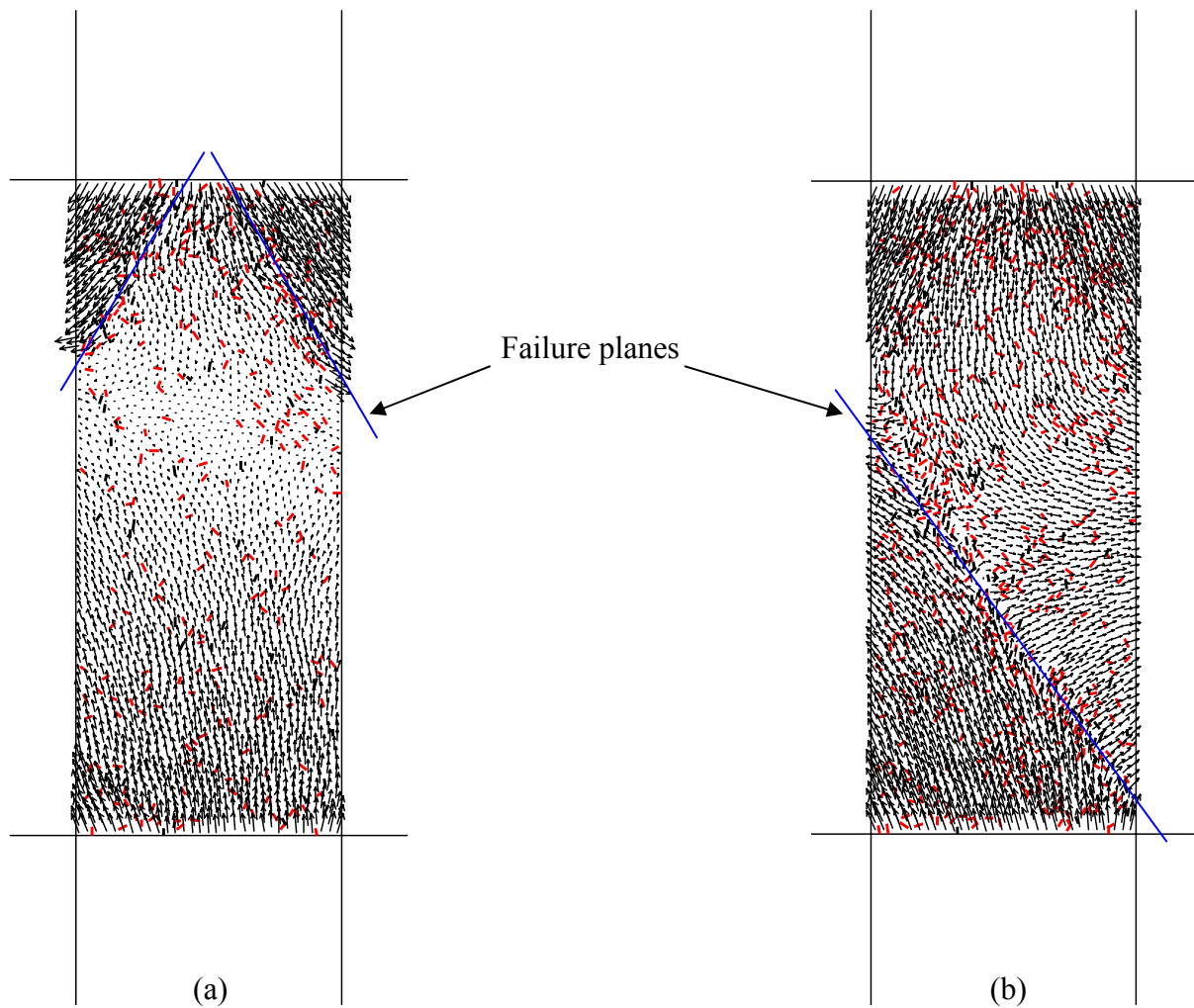


Figure 5.13. Cracks and displacement vectors in the model after failure under: (a) uniaxial compressive test; (b) biaxial compressive test with confining stress of 20 MPa. Shear cracks are denoted by red colour, tensile cracks by black.

### 5.3.2 Fine-grained model

Microcracks in a *PFC* model are formed at locations of interparticle bonds; hence their number depends on the number of particles constituting the model. In this study, it was assumed that a fine-grained model would provide more apparent DME inflection points. After analysing a number of trial models, it was found that the specimens with very fine particles required significant computational time to bring the model to the state of force equilibrium. On the basis of the results obtained from these trials, it was considered reasonable to use a model with 6,415 particles, Figure 5.14. The state of the sample at failure is presented in Figures 5.15-5.17.

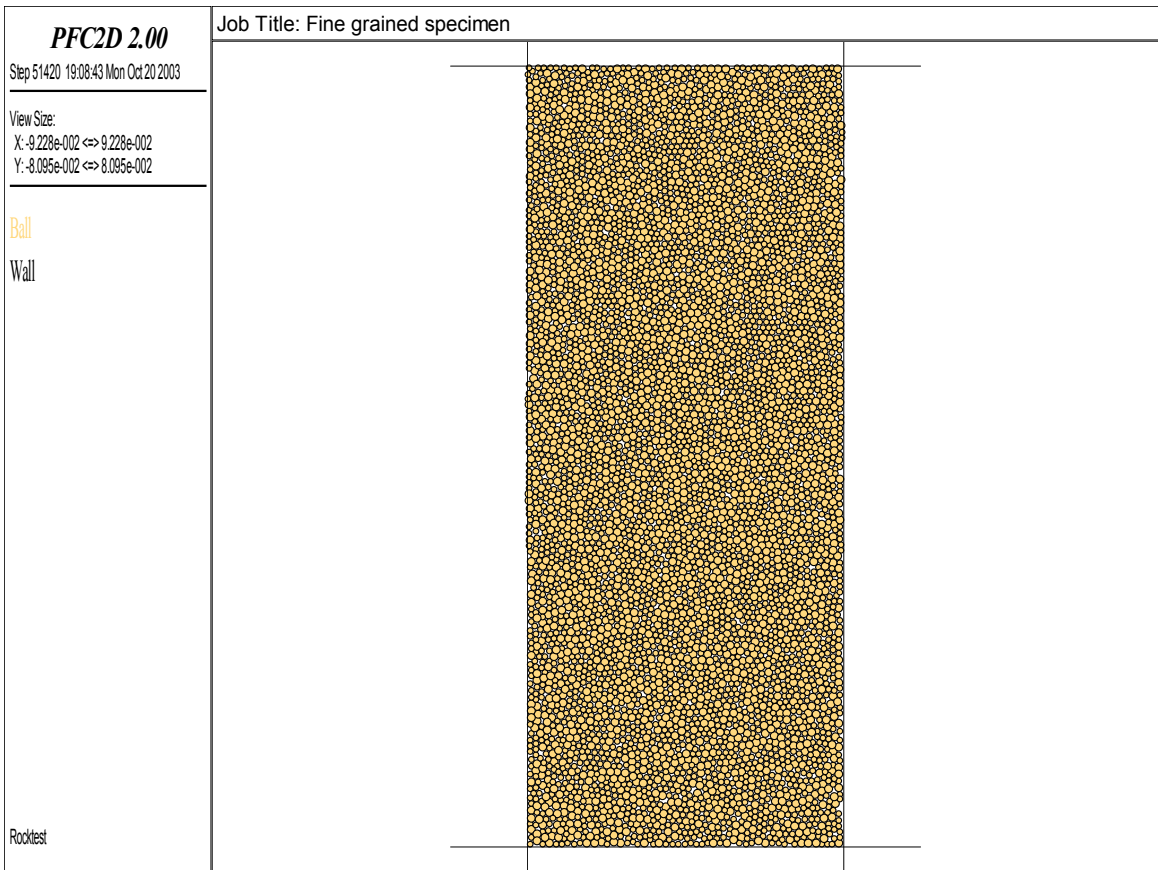


Figure 5.14. Fine-grained model consisting of 6,415 particles.

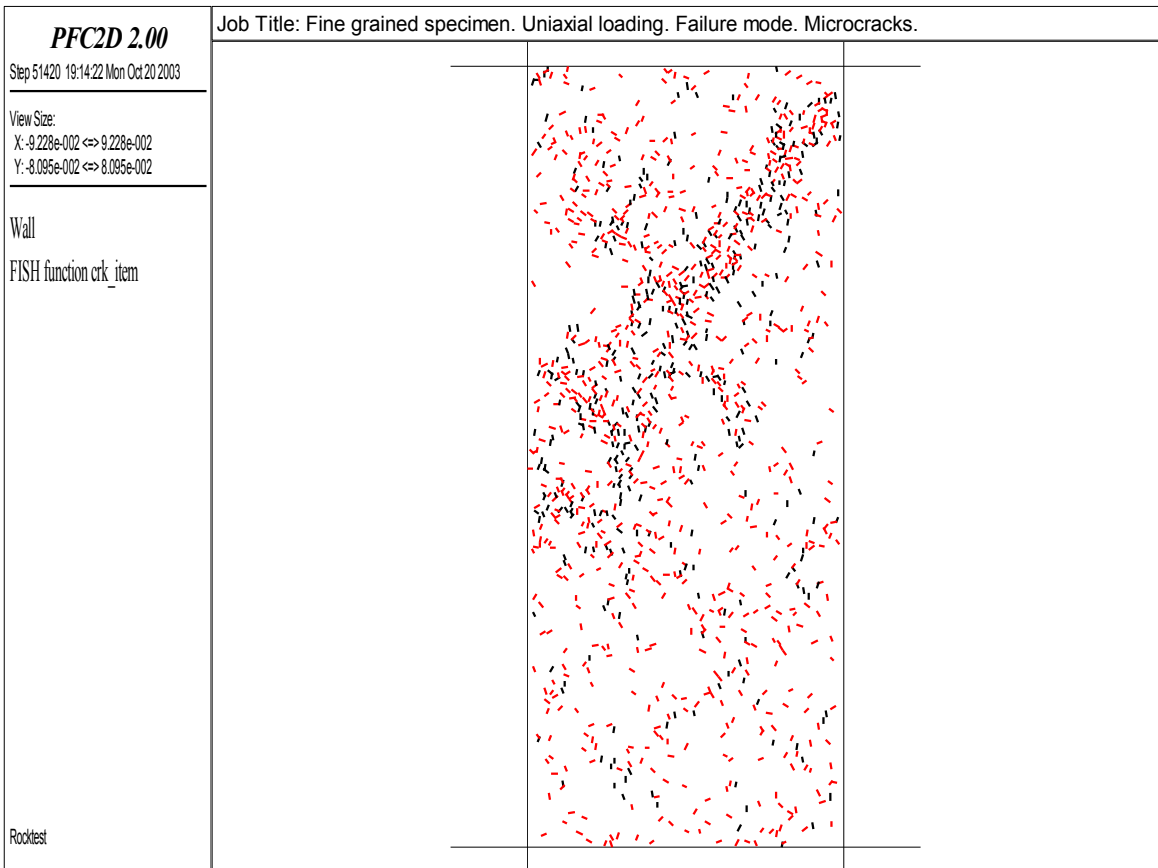


Figure 5.15. Fine-grained model: microcrack network at failure.

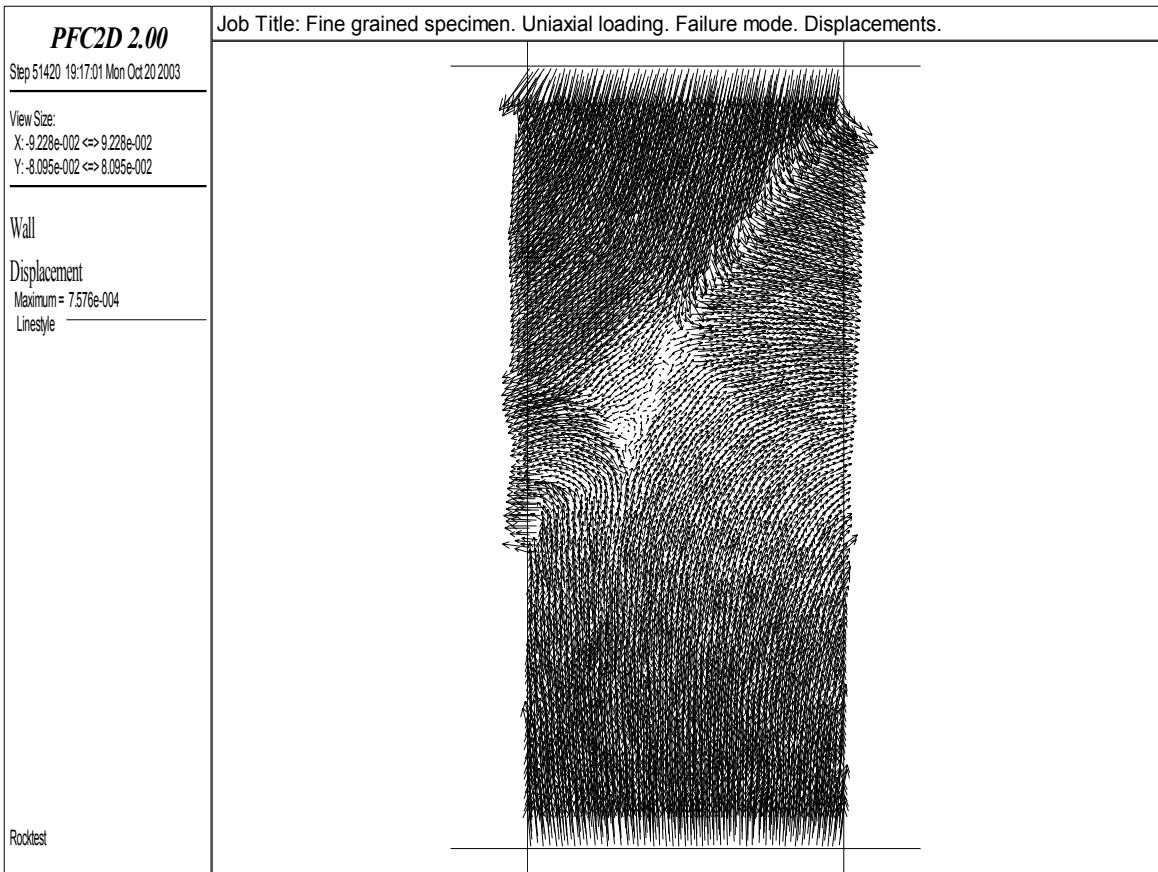


Figure 5.16. Fine-grained model: displacement vectors at failure.

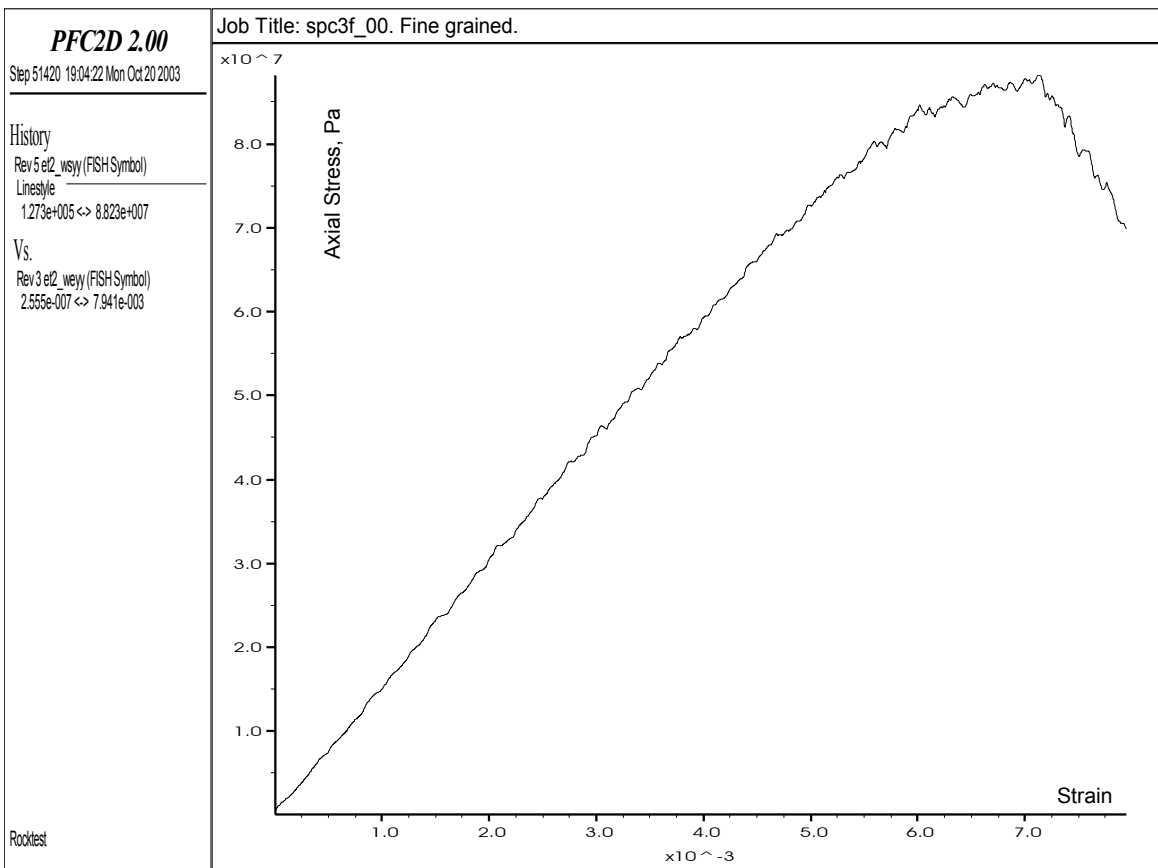


Figure 5.17. Fine-grained model: stress-strain diagram.

### 5.3.3 Complex lithology model

Rocks are rarely homogeneous; lithology can vary even at the scale of a cored specimen. To investigate the influence of the heterogeneity on the DME, a model was created using two materials of different bond strengths (Figure 5.18). The model had contact bonds in the middle section of the specimen that were weaker by two orders of magnitude than in the top and bottom sections. The friction between particles in this region was also reduced. The bond strengths and coefficients of friction were chosen arbitrarily, under the condition that both parameters had to be lower than those in the outer regions of the model. Detailed data on the model properties are presented in Appendix 2, Code 2.7. The model at failure is represented by Figures 5.19 and 5.20.

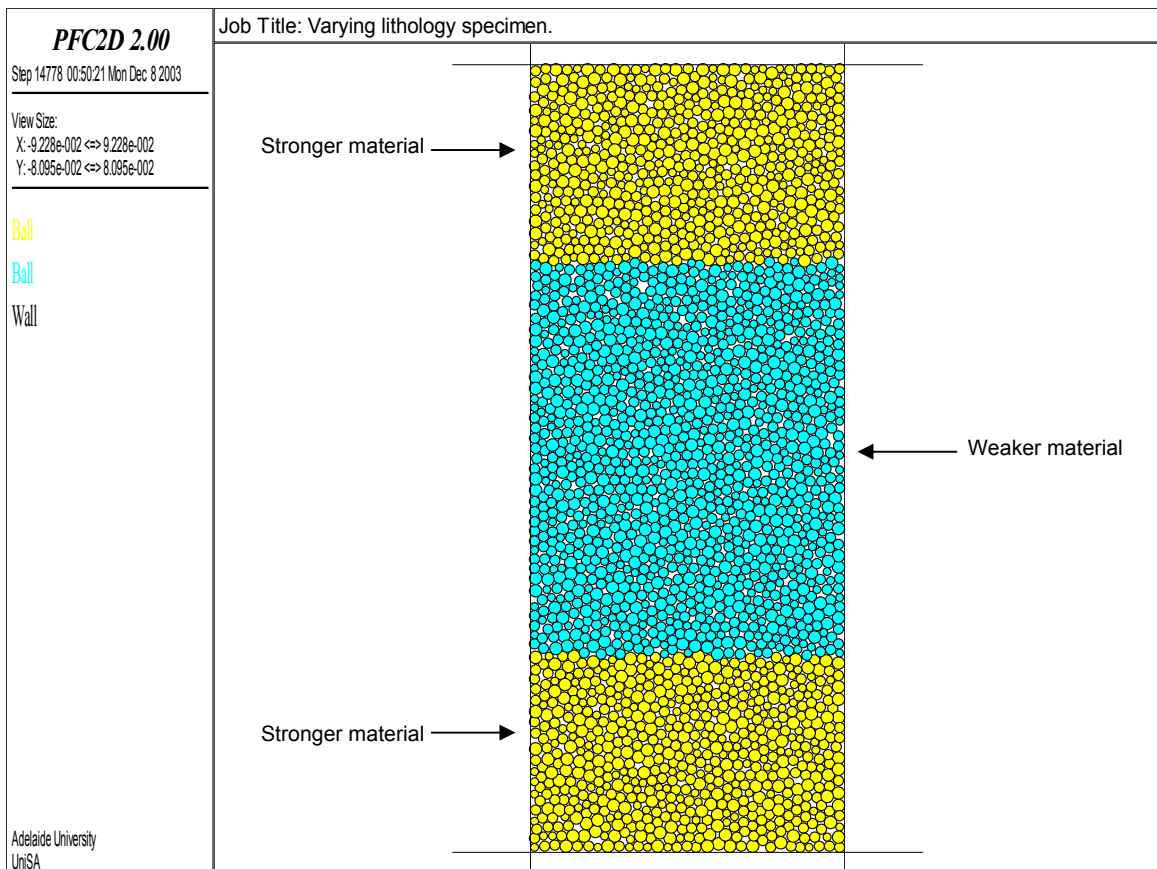


Figure 5.18. Complex lithology model.

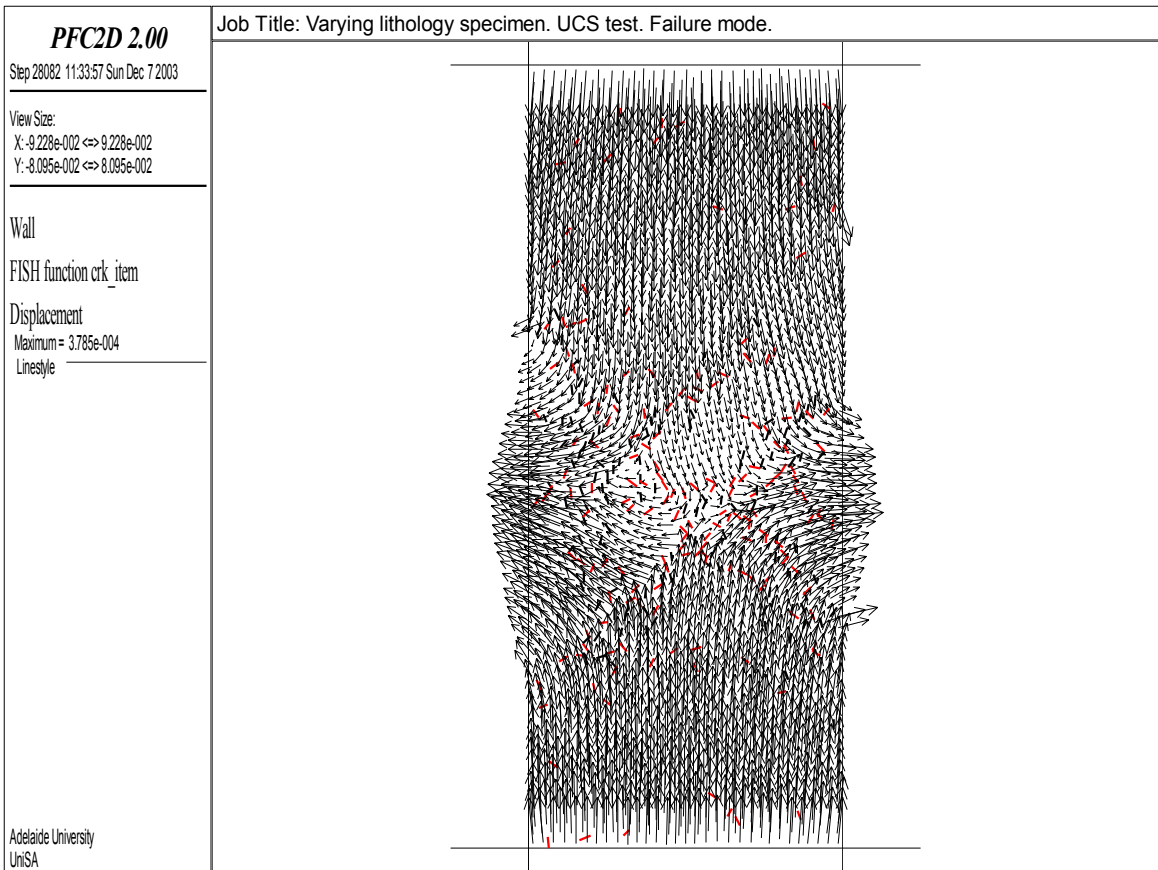


Figure 5.19. Complex lithology model: microcrack network and particle displacement vectors at failure.

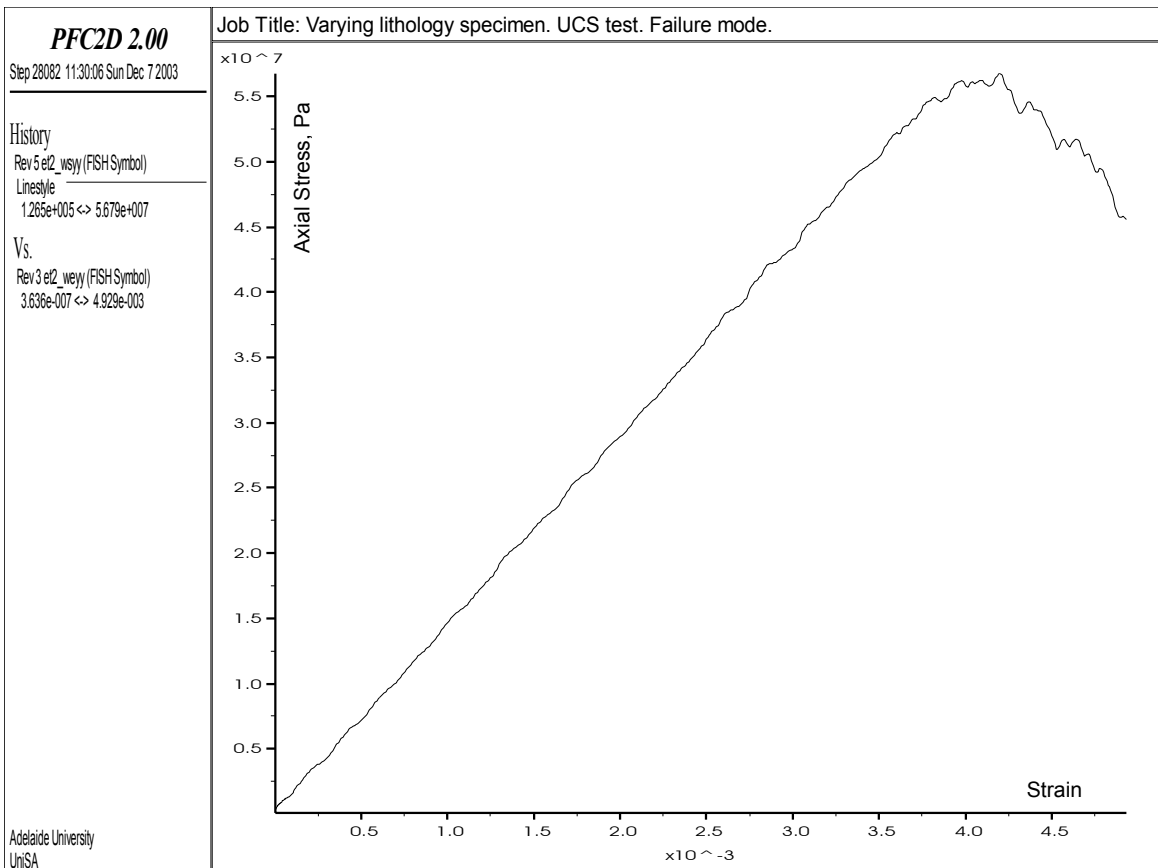


Figure 5.20. Complex lithology model: stress-strain diagram.

### 5.3.4 Discontinuous rock model

As well as being heterogeneous, rocks are often also intersected by discontinuities. Two sets of these were introduced into the intact rock model as shown in Figure 5.21. The bond strength between particles adjacent to the discontinuities was defined as being weaker than that of the ‘intact rock’. The friction on the joint planes was also assigned a lower value. Similar to the case with the complex lithology specimen, both properties were assigned randomly. Detailed data on the model properties are presented in Appendix 2, Code 2.9. Different ball colours in Figure 5.21 are introduced for illustrative purposes only, as the properties of all particles were defined as being the same. The model at failure is illustrated in Figures 5.22 and 5.23.

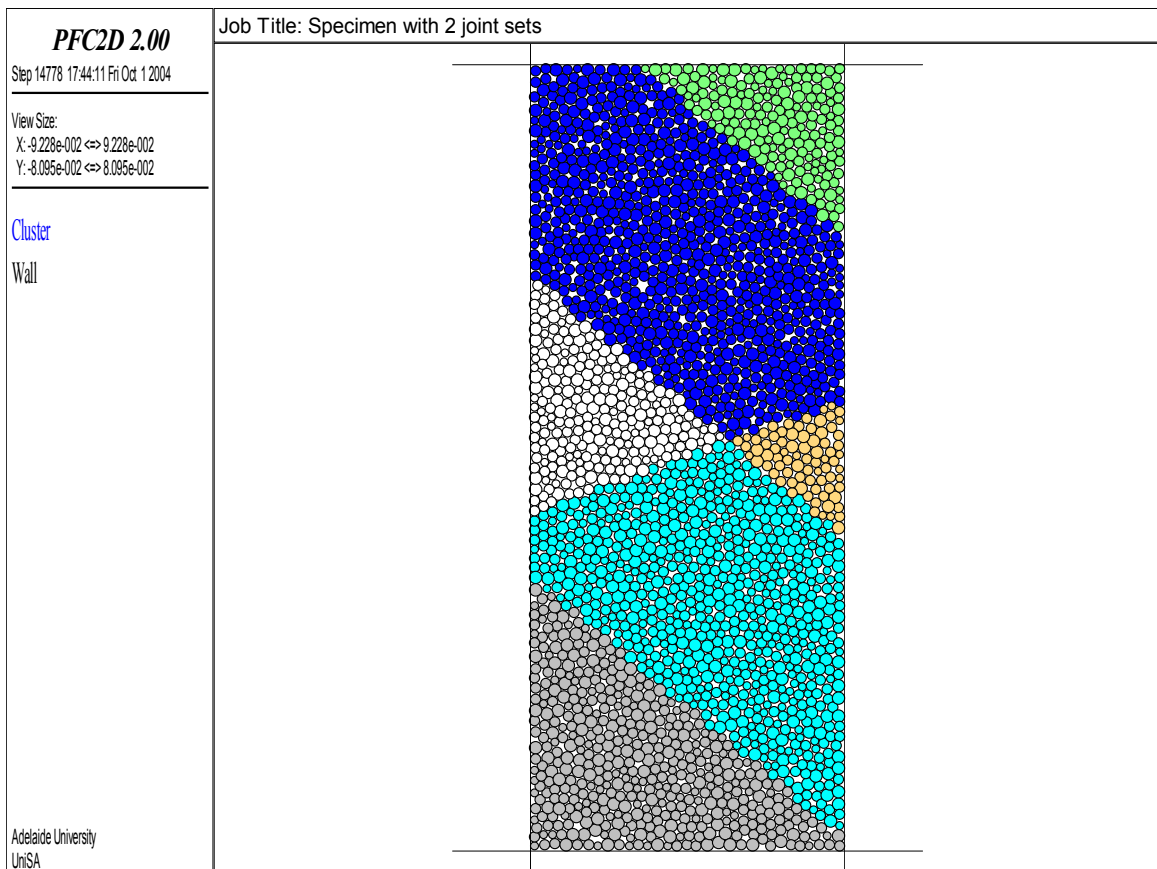


Figure 5.21. Discontinuous rock specimen with two joint sets.

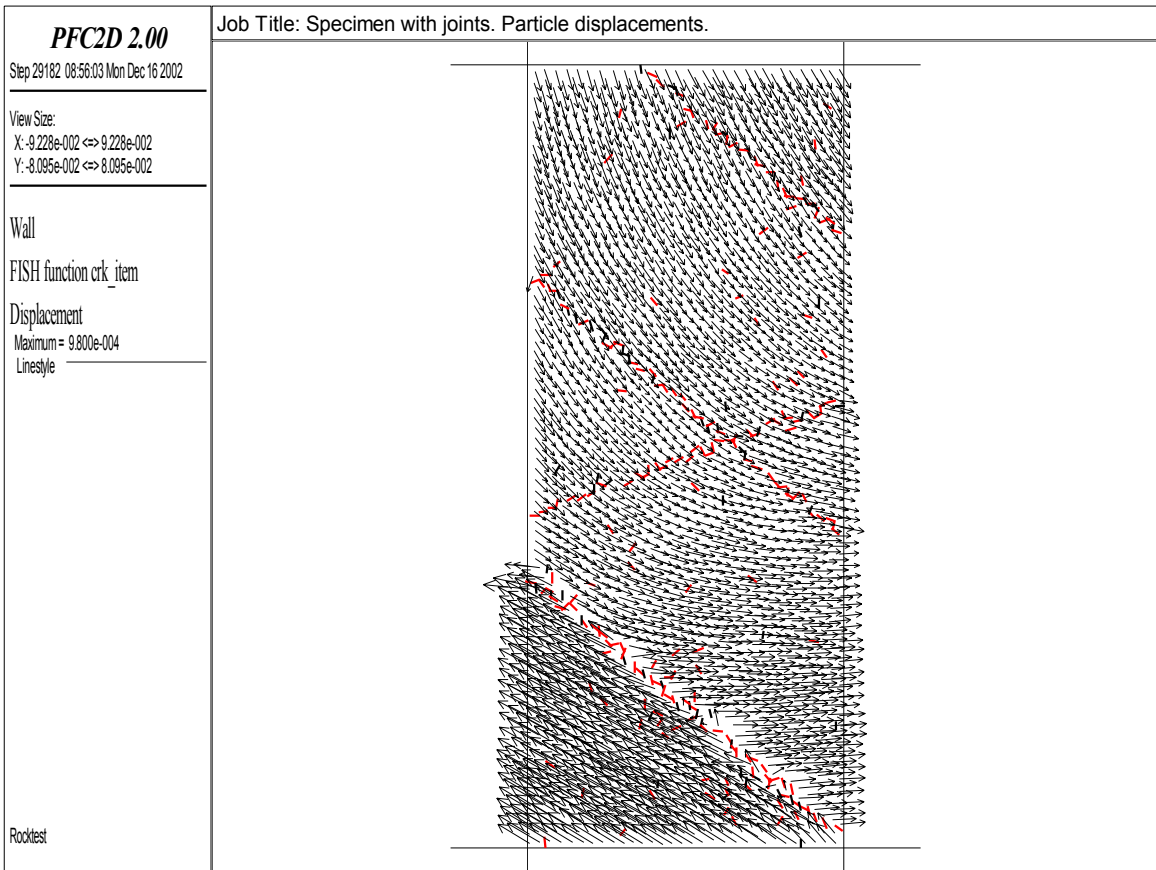


Figure 5.22. Discontinuous rock model: microcrack network and particle displacement vectors at failure.

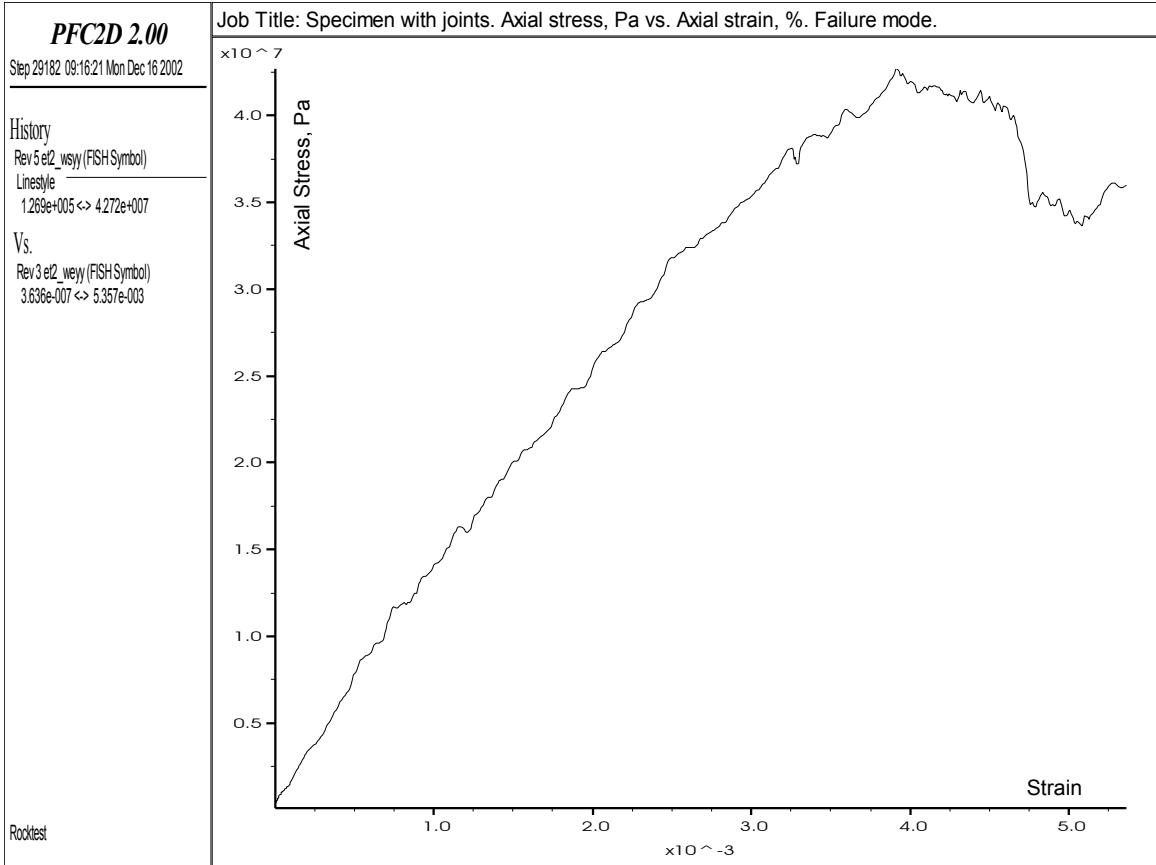


Figure 5.23. Discontinuous rock model: stress-strain diagram.

## 5.4 Modelling deformation memory effect

### 5.4.1 Intact rock model

There are various parameters that can be obtained from a *PFC* log file after simulating a compression test<sup>3</sup>. One parameter of interest is the crack initiation stress  $\sigma_{ci}$ . In testing real rocks, the crack initiation stress is the stress at which the crack volumetric strain indicates that the rock is beginning to dilate (the crack volumetric strain is defined as the difference between the elastic volumetric strains and the total volumetric strains). However, in *PFC*<sup>2D</sup>, this parameter represents different behaviour, as volumetric strains cannot be confidently determined in a two-dimensional code. Peculiar to *PFC*<sup>2D</sup>, the crack initiation stress is defined as the axial stress at which a certain number of microcracks have formed, which is a fraction of the total number of cracks in a failed specimen. In the present study, the crack initiation stress fraction was selected to be 2%. In the case of the intact rock model, this stress was determined as 11.5 MPa = 0.13 $\sigma_c$  (Appendix 2, Code A2.5)<sup>4</sup>. If an LRR test was run at the pre-load below this value, the DME would not be detected, as the deformation in the specimen in the region  $0 < \sigma < \sigma_{ci}$  would be assumed to be perfectly elastic, i.e. the strain is fully recoverable. If the pre-load was applied above  $\sigma_{ci}$ , a certain number of cracks would be permanently created. This logic was confirmed by running LRR tests in the regions  $0 < \sigma < \sigma_{ci}$  and  $\sigma > \sigma_{ci}$ .

Similar to the tests on physical specimen, the pre-load on the synthetic core was applied in four tests at progressively increasing values: one in the elastic region and three in the anelastic region. It has to be noted that when coring real rocks, the in-situ stresses acting on the core are relieved almost instantaneously. In this study, however, for simplicity, the unloading of the pre-load was conducted at the same rate as the loading (platens velocity = 0.2 m/s; see Appendix 2, Table A2.3 and Code A2.3 for details). It was decided to use the same platen acceleration algorithm provided by the code developers in all numerical simulations, regardless of whether it was pre-, un- or re-loading. Hence such an unloading regime does not correctly simulate the coring process. Nevertheless, it was considered, this simplification would not have considerable effect on the essence of the DME. In the simulation of the biaxial tests, however, an effort was made to simulate the unloading process more realistically by instantaneous removal of the confining stress. It is intended to address the loading/unloading rate issue in future research, when testing a 3D model.

---

<sup>3</sup> Log files for all models are presented in Appendix 2.

<sup>4</sup> Note: a typical crack initiation stress for real rocks is 0.3-0.4 $\sigma_c$  (refer to Figure 3.2, Chapter 3).

The driver files for all tests are listed in Appendix 2, Codes A2.11 to A2.14. The applied stress values are presented in Table 5.2. The pre-load stresses were chosen to be of the same magnitudes as those in the case of the physical specimen (refer to Table 4.1). The stress-strain diagrams of the cyclic tests are shown in Figures 5.24 to 5.27. Each plot contains two microcrack snapshots: one made at the moment of the pre-load and the other at the completion of the test.

Table 5.2. Axial stress values applied in LRR tests on intact rock model.

Cycle No.	Applied stress, MPa			
1 (pre-load)	6.0	15.4	35.9	54.7
2 & 3 (reloads)	9.7	26.2	55.2	73.6

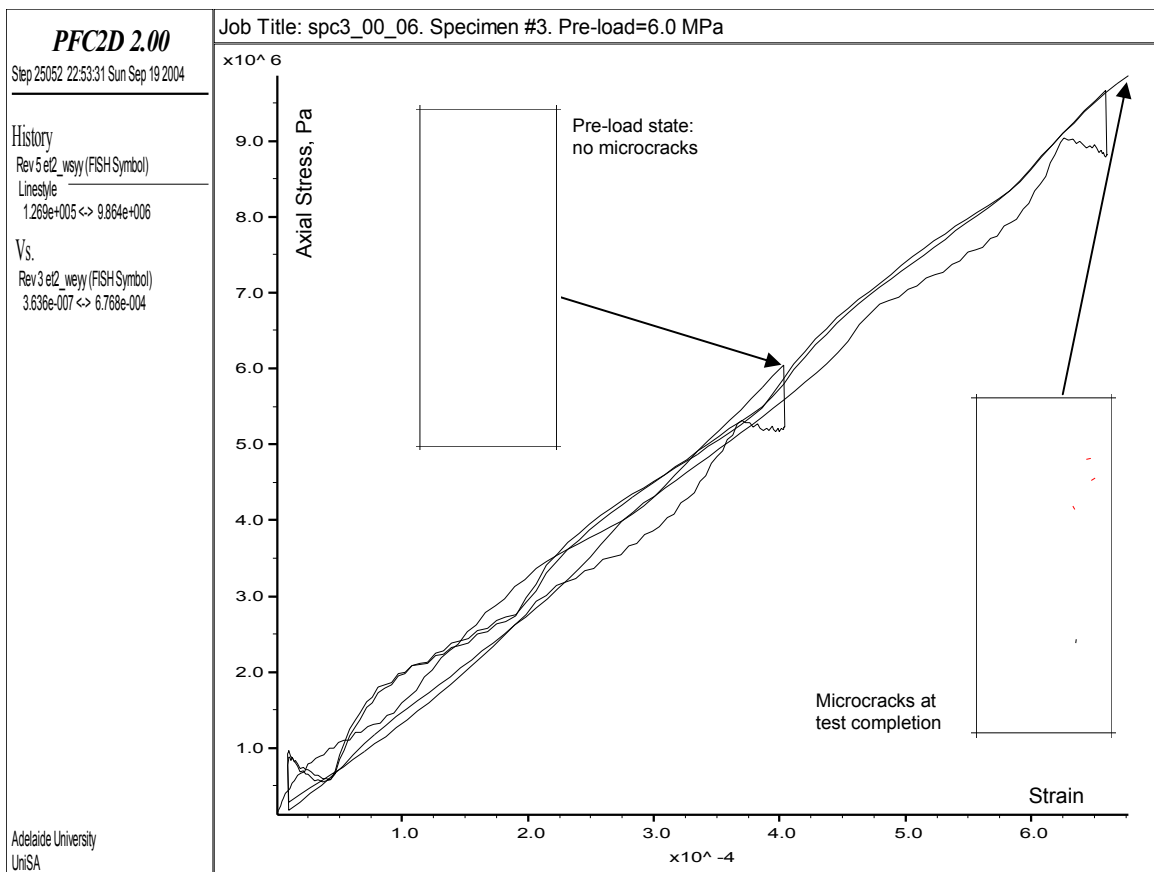


Figure 5.24. LRR test on intact rock model at 6.0 MPa pre-load.

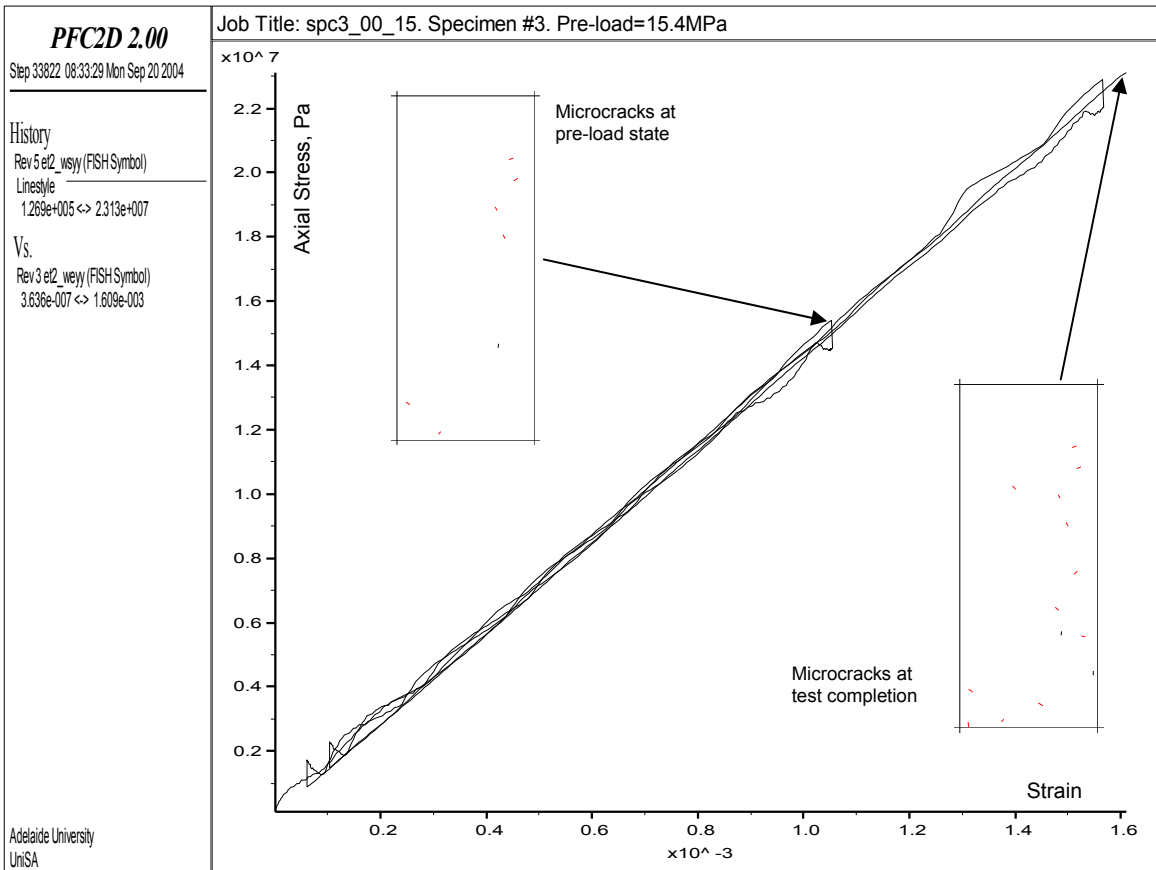


Figure 5.25. LRR test on intact rock model at 15.4 MPa pre-load.

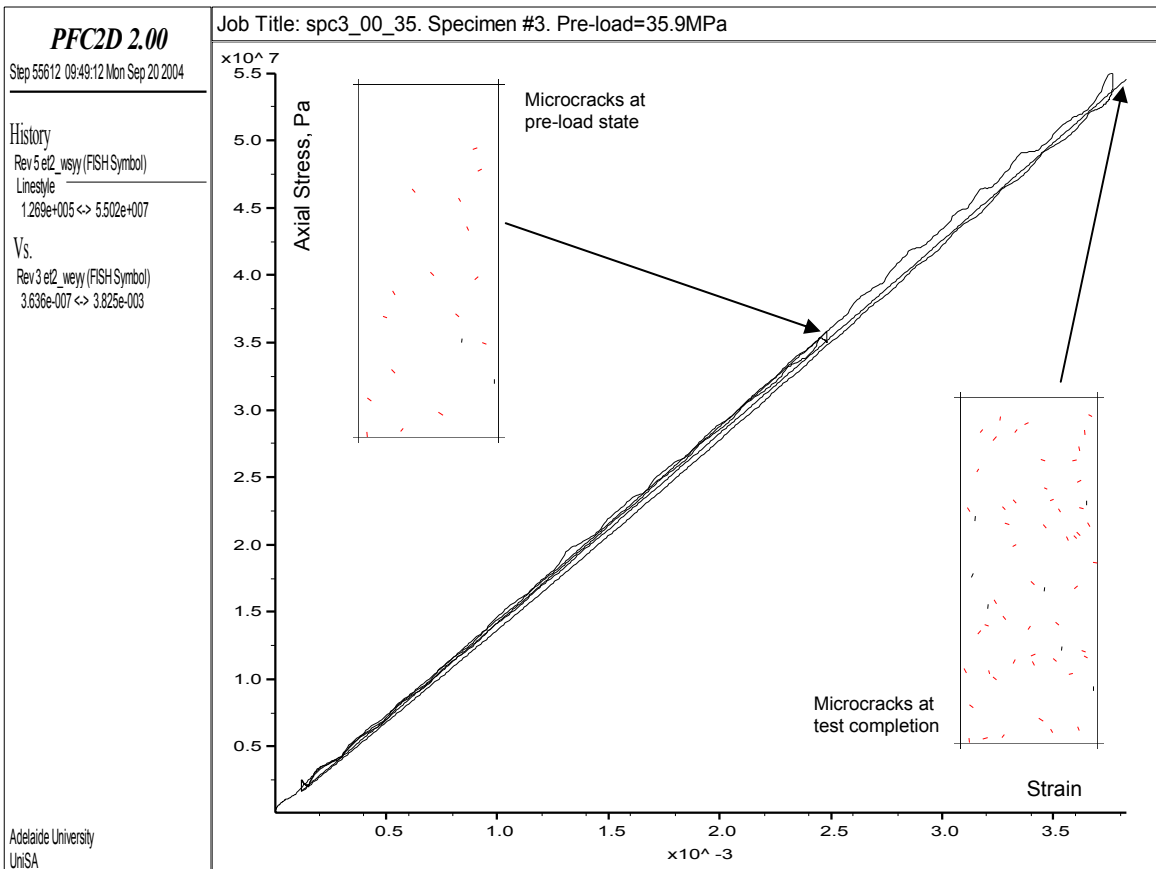


Figure 5.26. LRR test on intact rock model at 35.9 MPa pre-load.

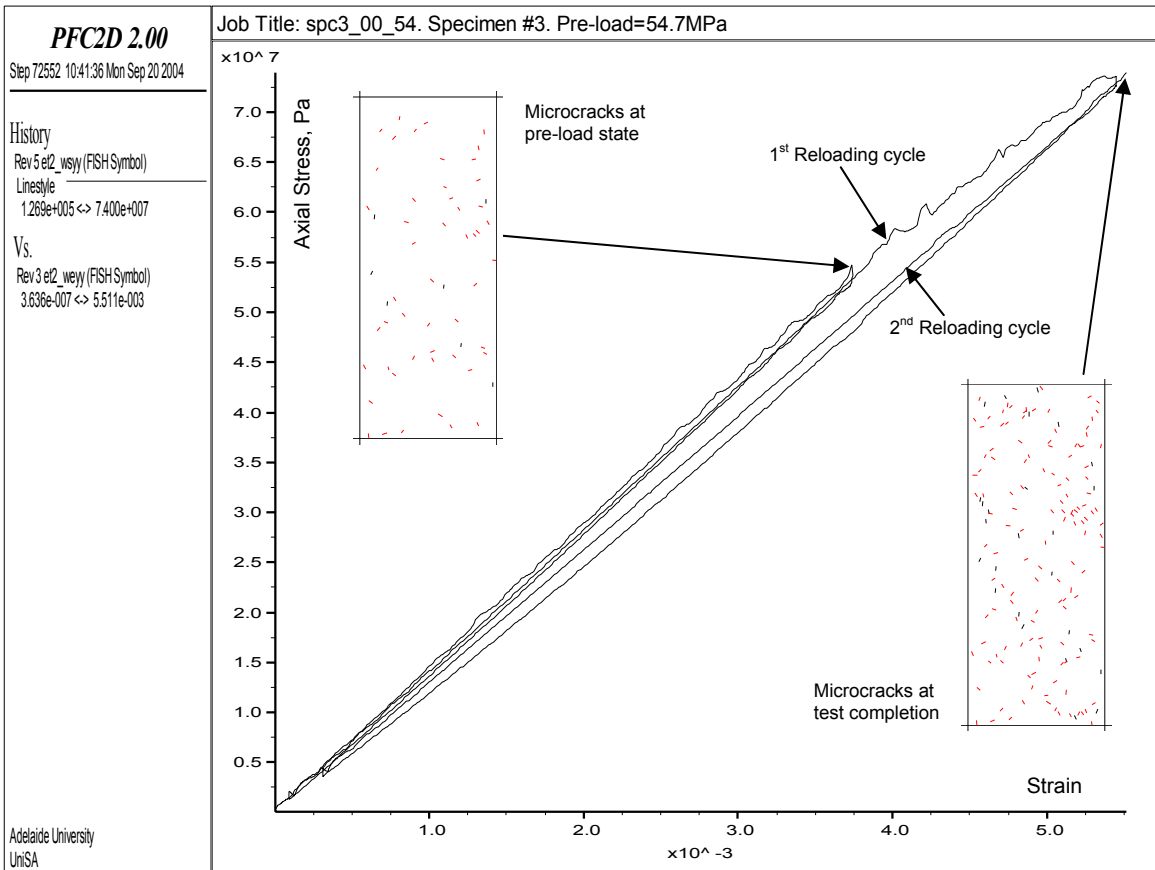


Figure 5.27. LRR test on intact rock model at 54.7 MPa pre-load.

Deformation rate analysis utilising Eq.2.1 was carried out for each test. The detailed procedure of the data processing required to do so is described in Appendix 2. Results of the DRA are presented in Figure 5.28.

As mentioned above, based on the DRA concept, it was expected that the DME response would not be apparent from an LRR test conducted in the purely elastic region. This behaviour is demonstrated in Figure 5.28a, which plots the differential strain versus axial load for the pre-load of 6 MPa (which is less than the crack initiation stress). The differential strain is constant (equals zero) throughout the entire test. This behaviour is different in the following three LRR tests carried out in the anelastic region at the pre-loads listed in Table 5.2. In each case a distinctive ‘memory kick’ can be observed (Figures 5.28b to 5.28d) corresponding correctly to a stress similar to the pre-load value. Trend lines have been added, which enable accurate determination of the characteristic points. These points and the Felicity ratios are listed in Table 5.3. Alongside each plot in Figure 5.28 is a sample microcrack snapshot, which was recorded at the peak of each pre-loading cycle.

There are two distinctive inflection points in the DRA curve in Figures 5.28b-d. The first point is related to a positive gradient and the second to a negative gradient of the curve. It is postulated, the first characteristic point equates to the DME, as it is associated with the stress applicable to the pre-load in each test (Table 5.3). Following the first inflection point, the gradient declines, which suggests that the strain difference between the two reloading cycles decreases with continuing application of load. This behaviour is clearly visible in Figure 5.27 where the gap between the 1<sup>st</sup> and 2<sup>nd</sup> reloading cycles narrows after surpassing the pre-load. This trend is not so obvious in Figures 5.25 and 5.26; the reason being that it is difficult to detect the difference which is measured in tens of microns.

*Table 5.3. Results of LRR tests on intact rock model.*

Pre-load, MPa	15.4	35.9	54.7
Inflection point, MPa	17.4	36.5	54.7
FR	0.89	0.98	1.0

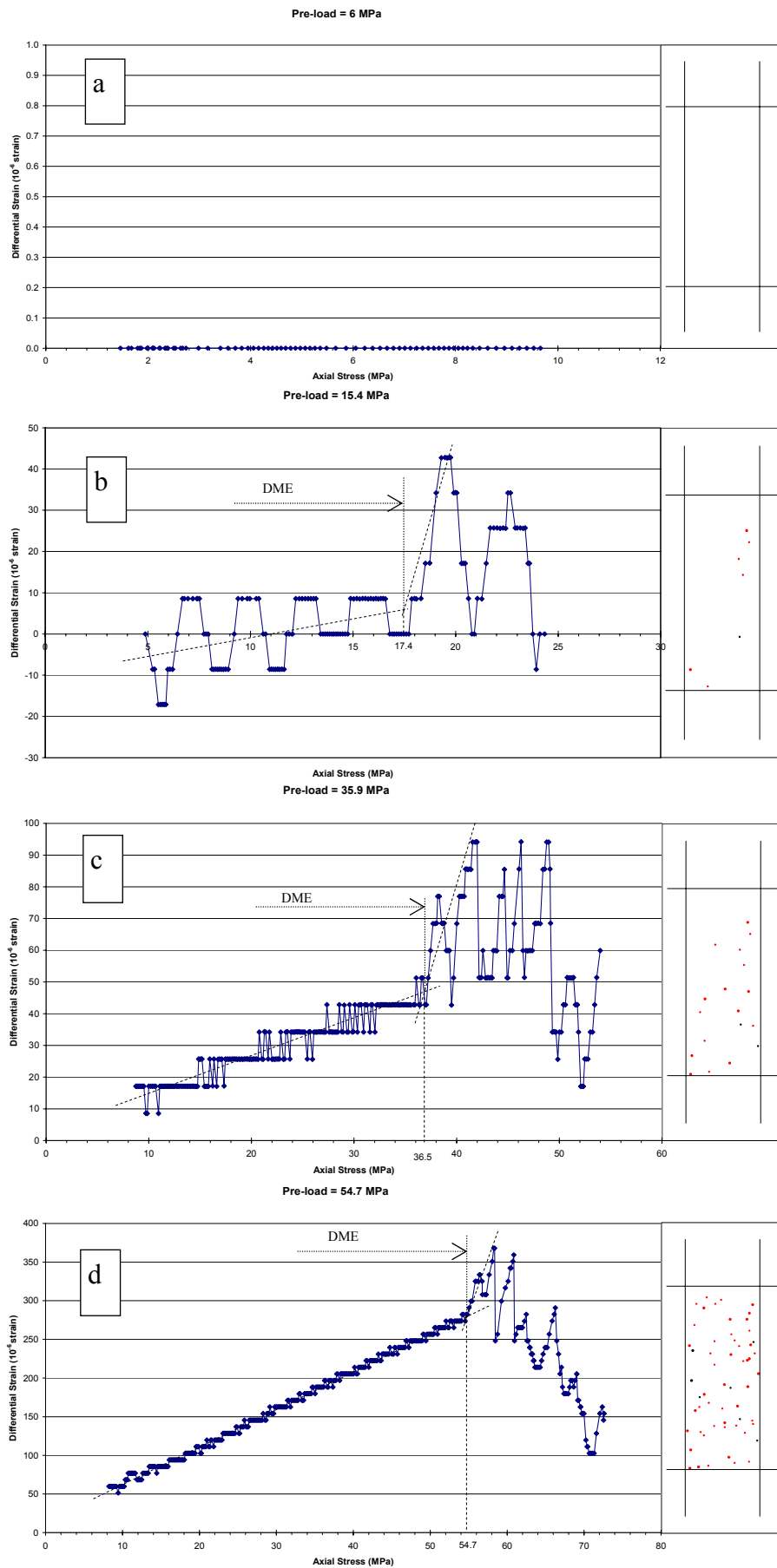


Figure 5.28. DRA curves and microcrack snapshots for different pre-load values: (a) 6.0 MPa; (b) 15.4 MPa; (c) 35.9 MPa; (d) 54.7 MPa.

Demonstration of the DME in the numerical model can also be verified by monitoring the cumulative number of microcracks and the friction energy in the model. The histories of these parameters were recorded in each test during the 1<sup>st</sup> reloading cycle and are shown in Figures 5.29 and 5.30. Felicity ratios calculated for the DME determined from these graphs indicate that in all tests the pre-load values were determined accurately (Table 5.4).

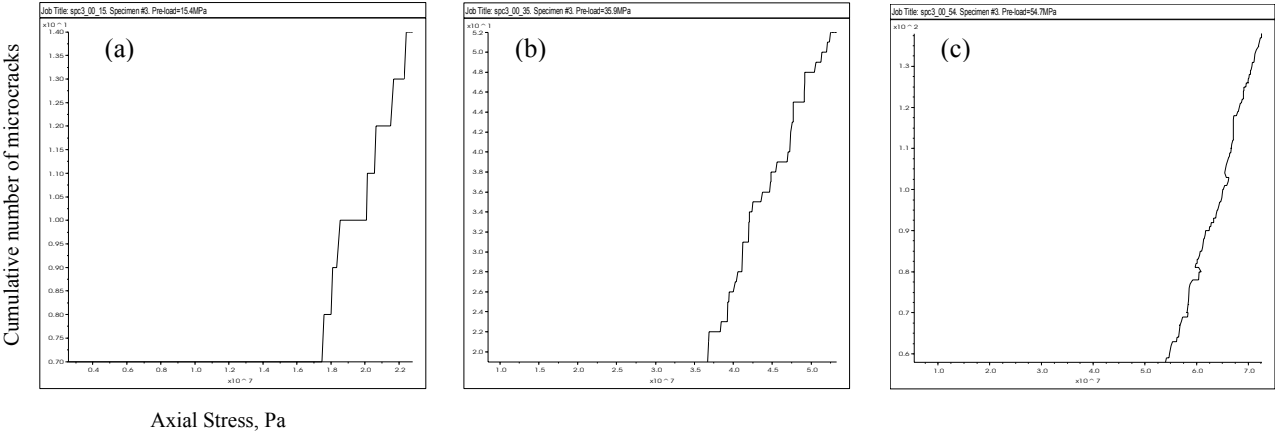


Figure 5.29. Cumulative number of microcracks in the model vs. axial stress for different pre-load values: (a) 15.4 MPa; (b) 35.9 MPa; (c) 54.7 MPa.

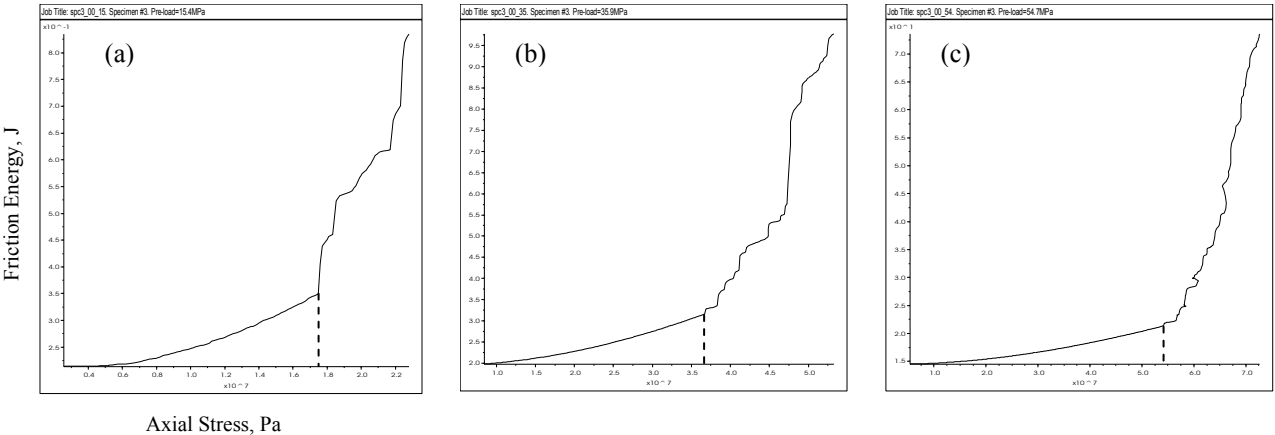


Figure 5.30. Friction energy vs. axial stress for different pre-load values: (a) 15.4 MPa; (b) 35.9 MPa; (c) 54.7 MPa.

Table 5.4. Pre-load values determined from cumulative number of microcracks and friction energy.

Pre-load stress, MPa	15.4	35.9	54.7
DME from cum. No. of microcracks, MPa	17.5	36.9	54.3
FR	0.88	0.97	1.01
DME from friction energy, MPa	17.5	36.7	54.1
FR	0.88	0.98	1.01

### 5.4.2 Fine-grained and complex lithology models

Similar to the ‘intact rock’, LRR tests were conducted on the fine-grained and the complex lithology models. The DRA technique provided a well defined inflection point in each case, closely corresponding to the pre-load values. Detailed results are presented in Figures 5.31 to 5.36 and Tables 5.5 and 5.6.

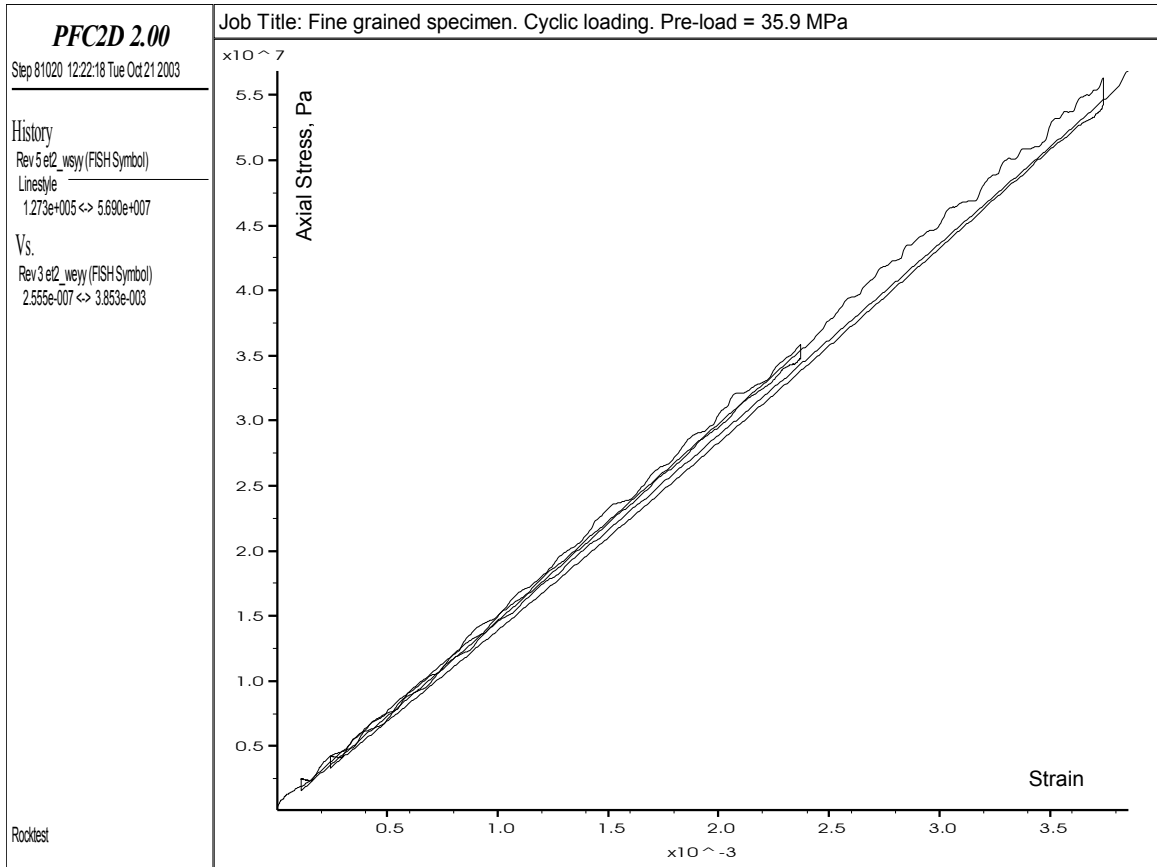


Figure 5.31. LRR test on fine-grained model at 35.9 MPa pre-load.

Fine grained specimen. Pre-load = 35.9 MPa. Uniaxial cyclic test.

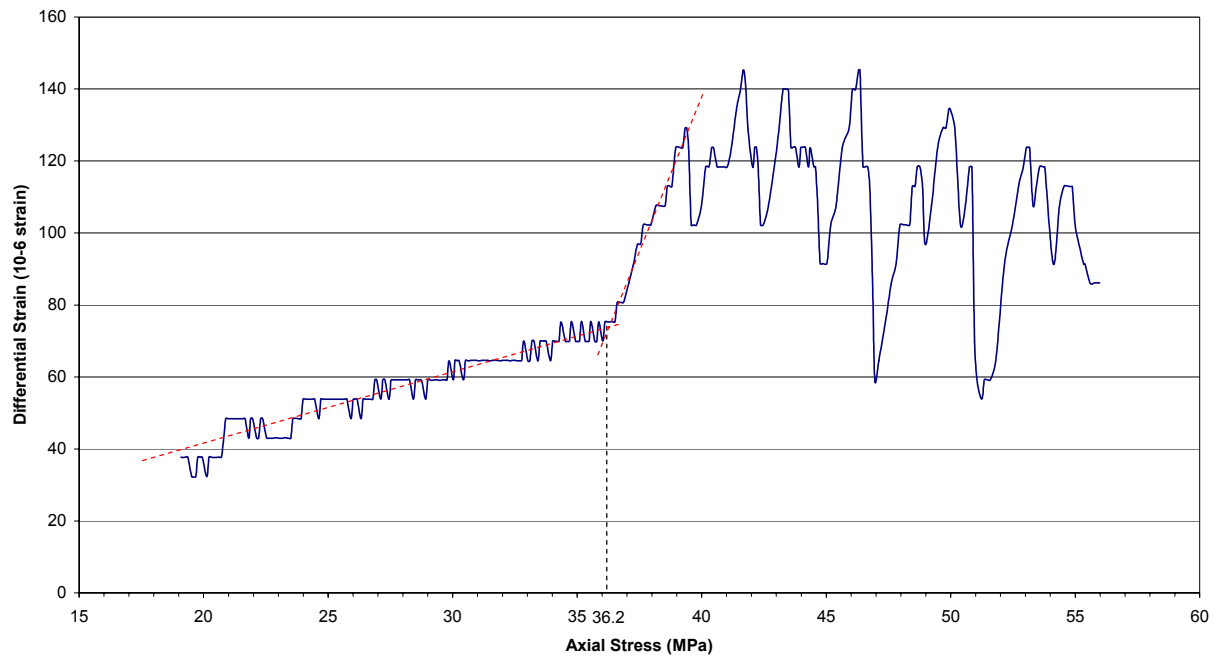


Figure 5.32. DRA curve from LRR test on fine-grained model at 35.9 MPa pre-load.

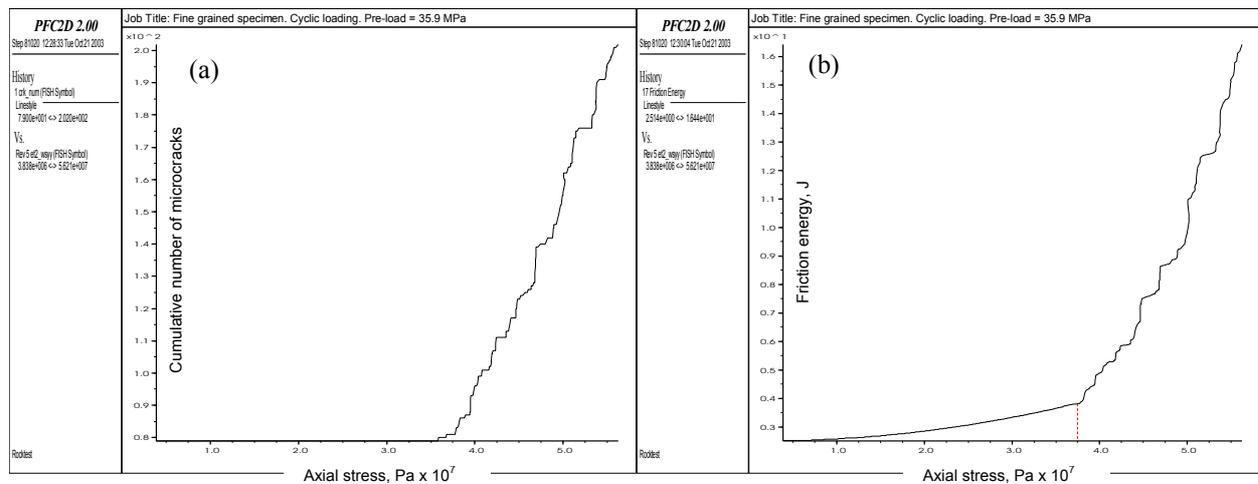


Figure 5.33. Fine-grained model at 35.9 MPa pre-load: (a) cumulative number of microcracks; (b) friction energy.

Table 5.5. Result of LRR test on fine-grained model.

Pre-load stress, MPa	35.9
DME from DRA curve, MPa	36.2
FR	0.99
DME from cum. No. of microcracks, MPa	35.8
FR	1.00
DME from friction energy, MPa	38.0
FR	0.94

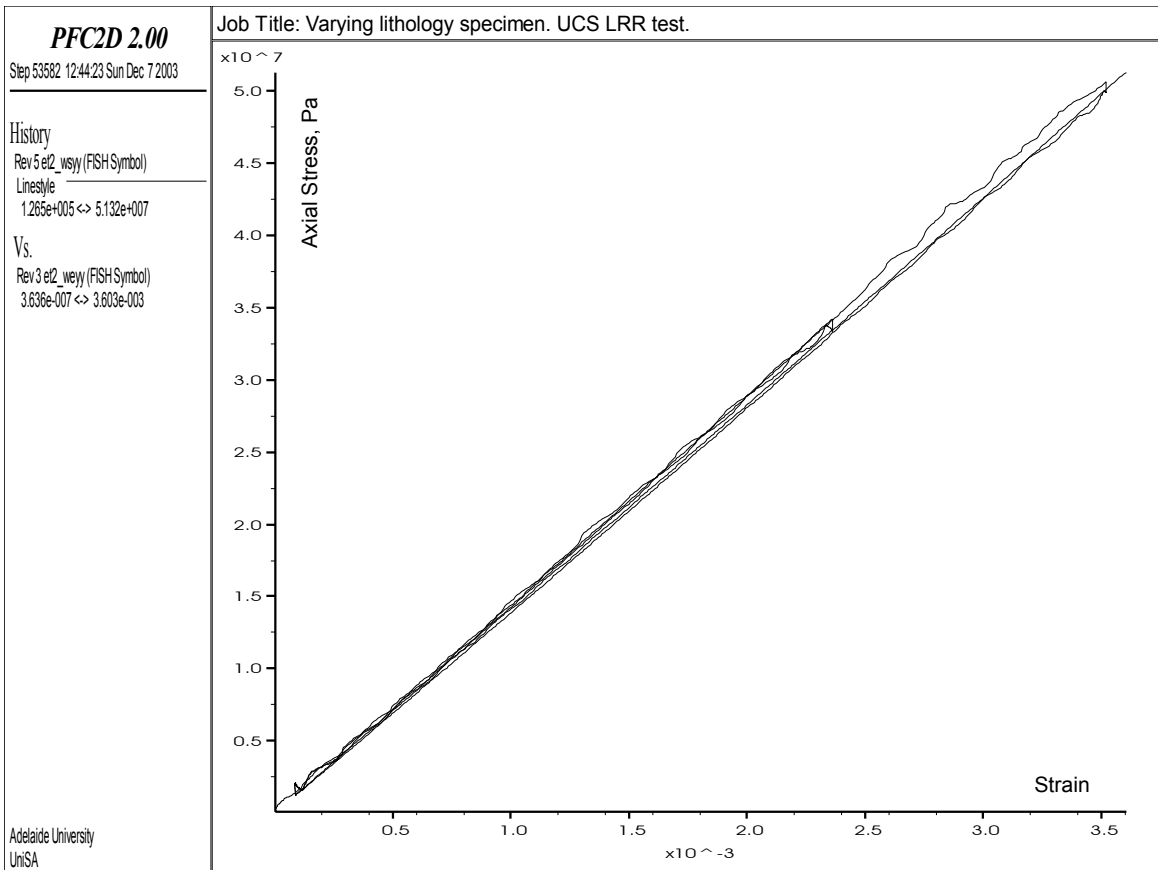


Figure 5.34. LRR test on complex lithology model at 34.2 MPa pre-load.

Varying lithology sample. Pre-load = 34.2 MPa. Uniaxial cyclic test.

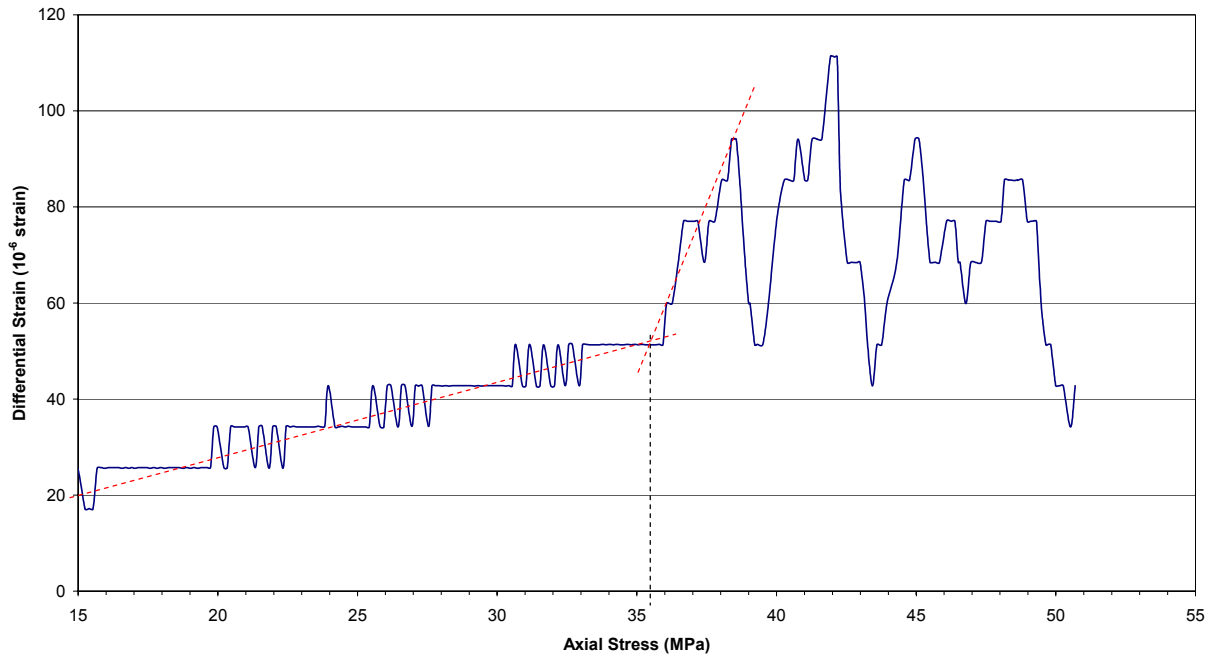


Figure 5.35. DRA curve from LRR test on complex lithology model at 34.2 MPa pre-load.

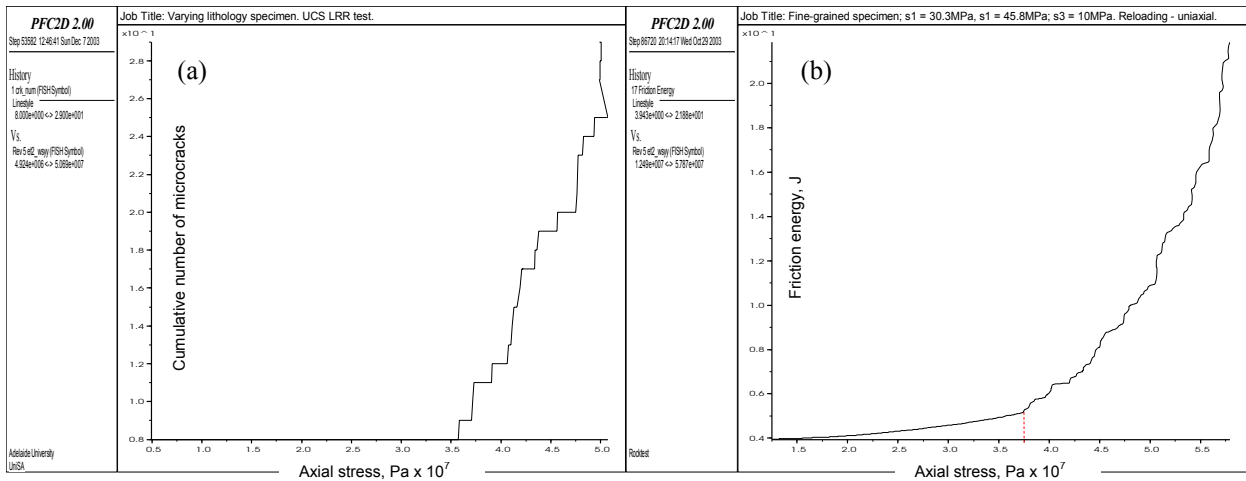


Figure 5.36. Complex lithology model at 34.2 MPa pre-load: (a) cumulative number of microcracks; (b) friction energy.

Table 5.6. Result of LRR test on complex lithology model.

Pre-load stress, MPa	34.2
DME from DRA curve, MPa	35.5
FR	0.96
DME from cum. No. of microcracks, MPa	35.7
FR	0.96
DME from friction energy, MPa	37.5
FR	0.91

### 5.4.3 Discontinuous rock model

Results of an LRR test on the discontinuous rock model are presented in Figures 5.37 to 5.39 and Table 5.7. The deformations in this model (Figure 5.37) are notably greater than in the models discussed earlier. This is due to the significantly weaker bonds between particles on the discontinuity plane, which resulted in a greater number of microcracks (Figure 5.39a) leading to greater deformations in the simulated specimen.

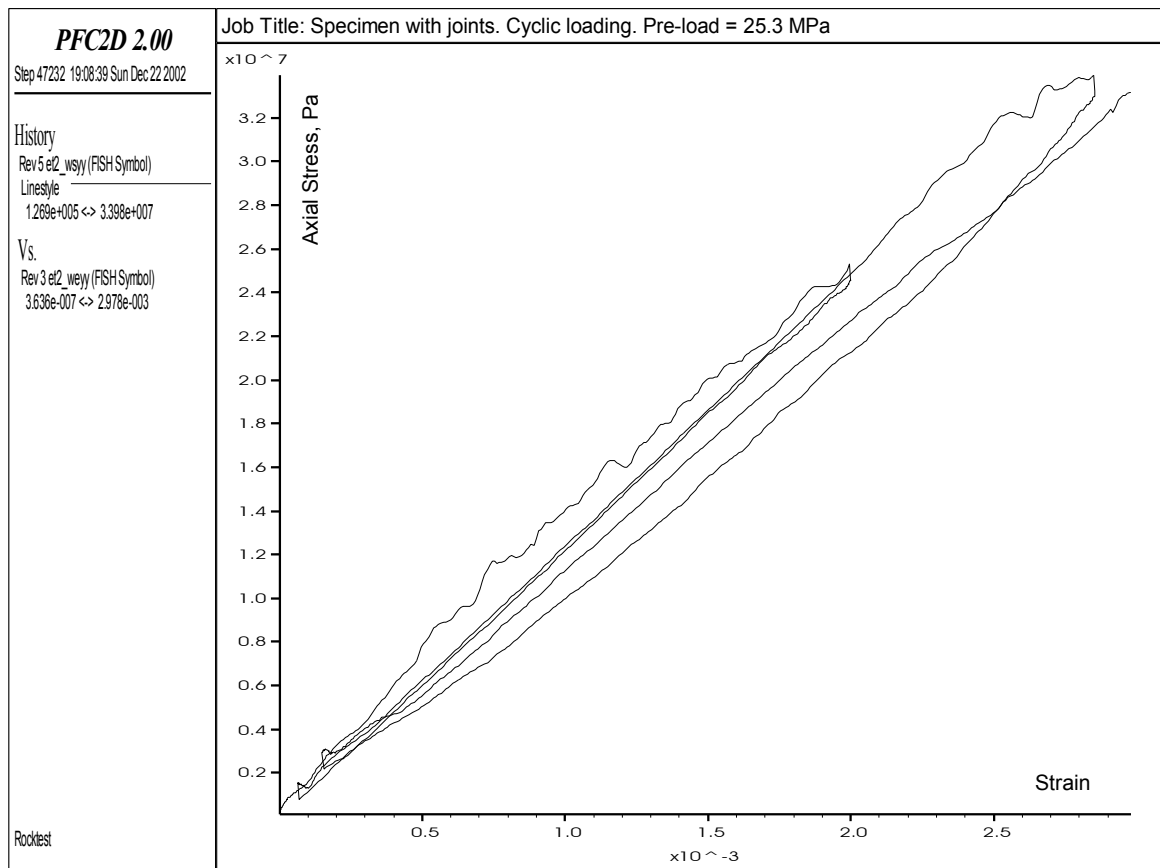


Figure 5.37. LRR test on discontinuous rock model at 25.3 MPa pre-load.

Specimen with joints. Pre-load = 25.3 MPa.

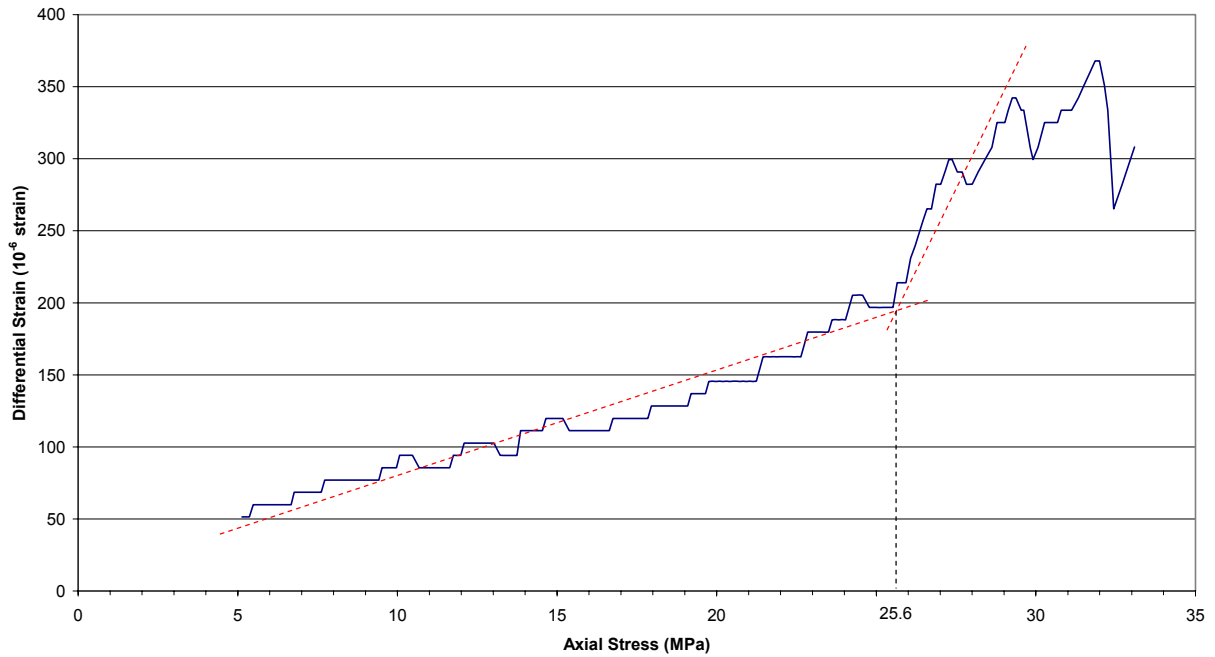


Figure 5.38. DRA curve from LRR test on discontinuous rock model at 25.3 MPa pre-load.

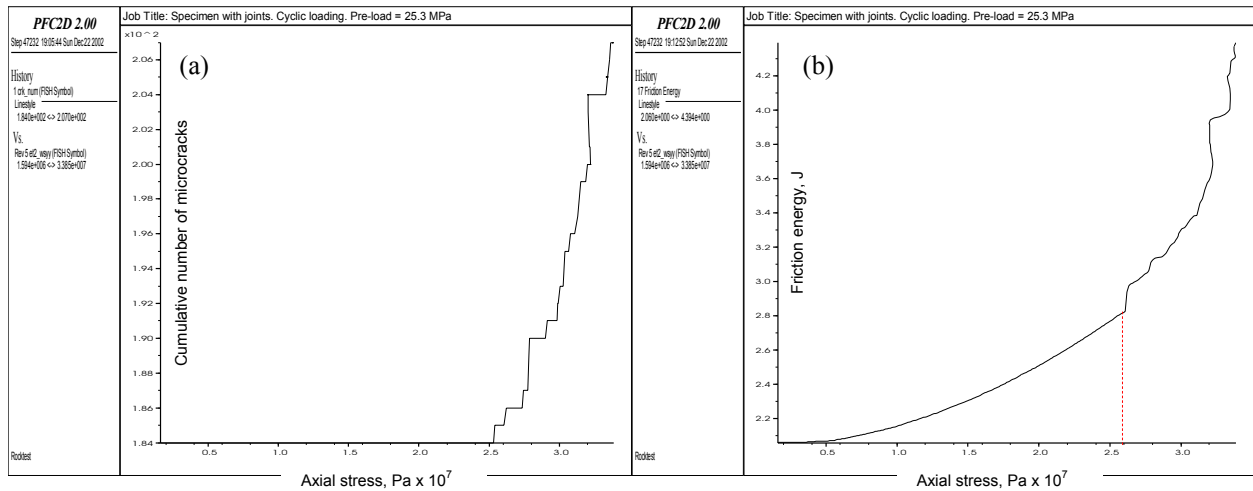


Figure 5.39. Discontinuous rock model at 25.3 MPa pre-load: (a) cumulative number of microcracks; (b) friction energy.

Table 5.7. Result of LRR test on discontinuous rock model.

Pre-load stress, MPa	25.3
DME from DRA curve, MPa	25.6
FR	0.99
DME from cum. No. of microcracks, MPa	25.2
FR	1.00
DME from friction energy, MPa	26.0
FR	0.97

#### 5.4.4 Effect of joint orientation

Having established the fact that the presence of discontinuities did not have a significant effect on the DME, the influence of their orientation on the DME was investigated. It is well known that discontinuous rocks display strength anisotropy; the compressive strength of a rock being sensitive to the orientation of any discontinuity that intersects it. Figure 5.40 illustrates the general representation of such anisotropy.

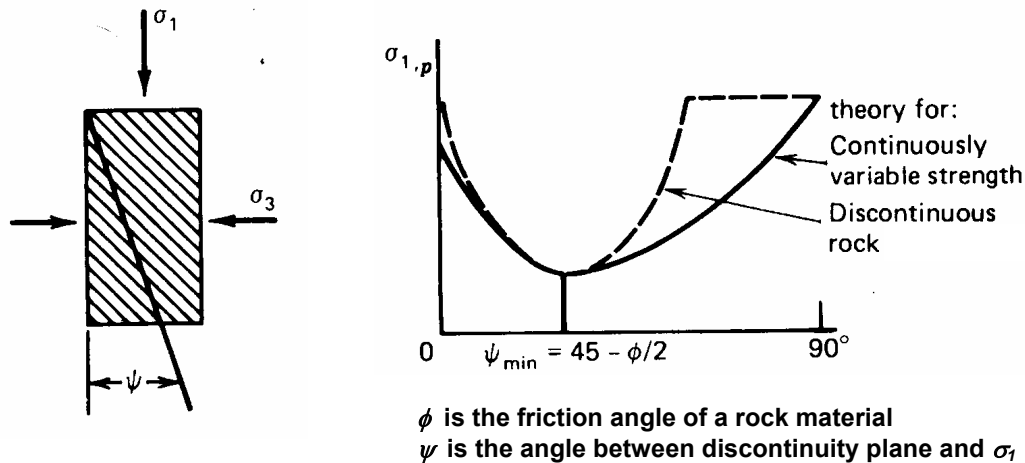


Figure 5.40. Influence of discontinuity orientation on rock strength (from Goodman, 1980).

It is proposed that the DME is similarly influenced by the orientation of a discontinuity. Eight numerical models were created, in which a single discontinuity intersected the model at various angles to the axial load (Figure 5.41). All other material properties remained unchanged from those assigned in previous models.

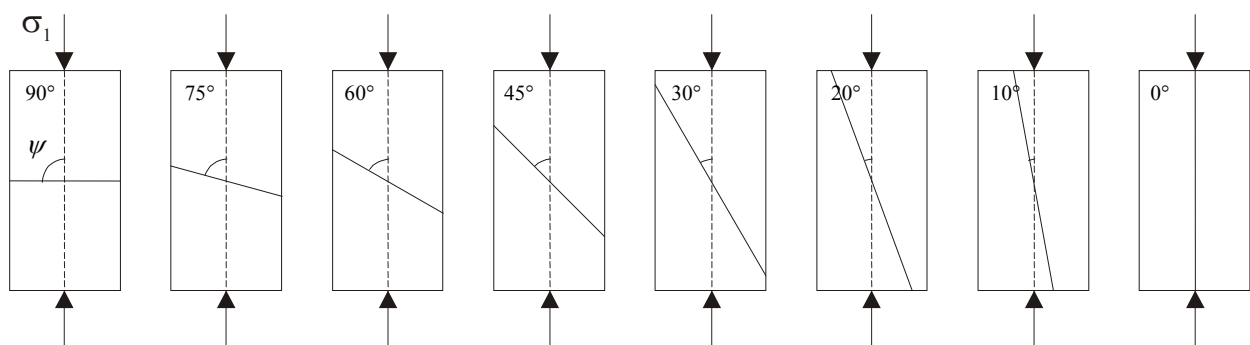


Figure 5.41. Series of models with a single discontinuity at variable orientation.

The microparameters of the discontinuities were assigned values similar to the discontinuous rock model studied in Section 5.3.4. Details on the modelling processes are given in Appendix 2. Results of the UCS and uniaxial LRR tests on all models are presented in Figures A2.11 to A2.27 and Tables A2.5 to A2.13 of Appendix 2.

In Figure 5.42, the model strength (which is equal to the maximum axial stress at failure) is plotted versus the discontinuity plane angle. It is obvious; the jointed model displayed the characteristics of strength anisotropy. There is a distinct similarity between this result and that for real discontinuous rock (refer to Figure 5.40). FR values plotted on the same graph followed the trend of the strength anisotropy indicating the occurrence of the DME anisotropy. The results are further discussed in Chapter 6.

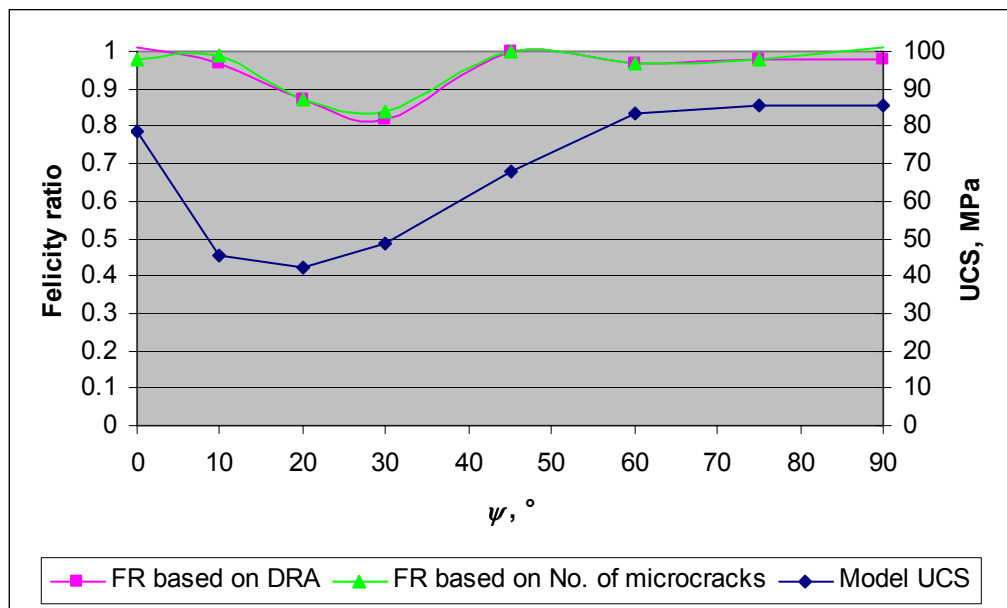


Figure 5.59. Strength anisotropy / DME anisotropy of the model with a single joint.

#### 5.4.5 Effect of confining stress

Several researchers have examined the effect of confining stress on the KE/DME. Holcomb (1983) and Hughson & Crawford (1987) found that the stress required for KE detection increased at higher confining stress, whereas Wang et al. (1999) found that the KE decreased as confining stress increased. Kanagawa et al. (1976), Momayez & Hassani (1992) and Seto et al. (1996) found that confining stress had virtually no influence on the KE/DME.

The next stage of the research aimed to address these apparent inconsistencies by attempting to answer the following questions:

- Is the DME affected by the confining stress?
- Which stress is detected by the DME: absolute maximum or differential/deviatoric?
- What stress can be determined by the DME: maximum historical (paleo-stress) or the latest historical (present-day) stress?

Since  $PFC^{2D}$  is a two-dimensional code, the models could only be tested under biaxial stress conditions. In a typical test, a model was biaxially loaded to a pre-determined value. The confining stress was then instantaneously removed to simulate the process of rock coring. Two successive uniaxial reloading cycles were then applied. A number of these tests were carried out on models of intact rock and fine-grained rock under various stress conditions. The testing program, detailed in Table 5.17, comprised the following stages:

1. LRR tests on the intact rock model. Three tests were conducted with a progressively increasing value of the confining stress.
2. LRR tests on the fine-grained model. Two tests were conducted under stresses similar to those applied in the previous series of tests.

The principal stresses were assigned their magnitudes reasonably typical of the virgin stress tensor at many Australian underground mines. In all LRR tests, the intention was to keep the pre-load at approximately the same value, in this case around 36 MPa.

3. LLRR (*load-load-reload-reload*) tests on the intact rock model. The tests aimed to investigate the ‘paleo- or present-day stress’ question. The specimen was pre-loaded twice under biaxial stress conditions. In the first test a progressively increasing load was applied in consecutive pre-loads. In the second test a progressively decreasing load was applied.
4. LLRR tests on the fine-grained specimen. The modelling was similar to that used for the LLRR tests on the intact rock model.

The test results are presented in Figures 5.60 to 5.68. The cyclic stress-strain diagrams are given in Appendix 2. The DRA results are discussed in Chapter 6.

Table 5.17. Programme for tests under biaxial stress conditions.

Stage	Test No.	Model	$\sigma_1'$ , MPa (1 <sup>st</sup> pre-load)	$\sigma_1''$ , MPa (2 <sup>nd</sup> pre-load)	$\sigma_3$ , MPa	$\sigma_1/\sigma_3$
1	1	Intact rock	35.6	N/A	12	2.94
	2	Intact rock	35.9	N/A	20	1.79
	3	Intact rock	35.9	N/A	28	1.28
2	4	Fine-grained	35.6	N/A	12	2.94
	5	Fine-grained	35.6	N/A	20	1.79
3	6	Intact rock	26.1	35.4	12	N/A
	7	Intact rock	35.4	26.0	12	N/A
4	8	Fine-grained	26.5	36.2	12	N/A
	9	Fine-grained	36.4	26.9	12	N/A

Intact rock specimen:  $s_1 = 35.6$  MPa,  $s_3 = 12.0$  MPa.

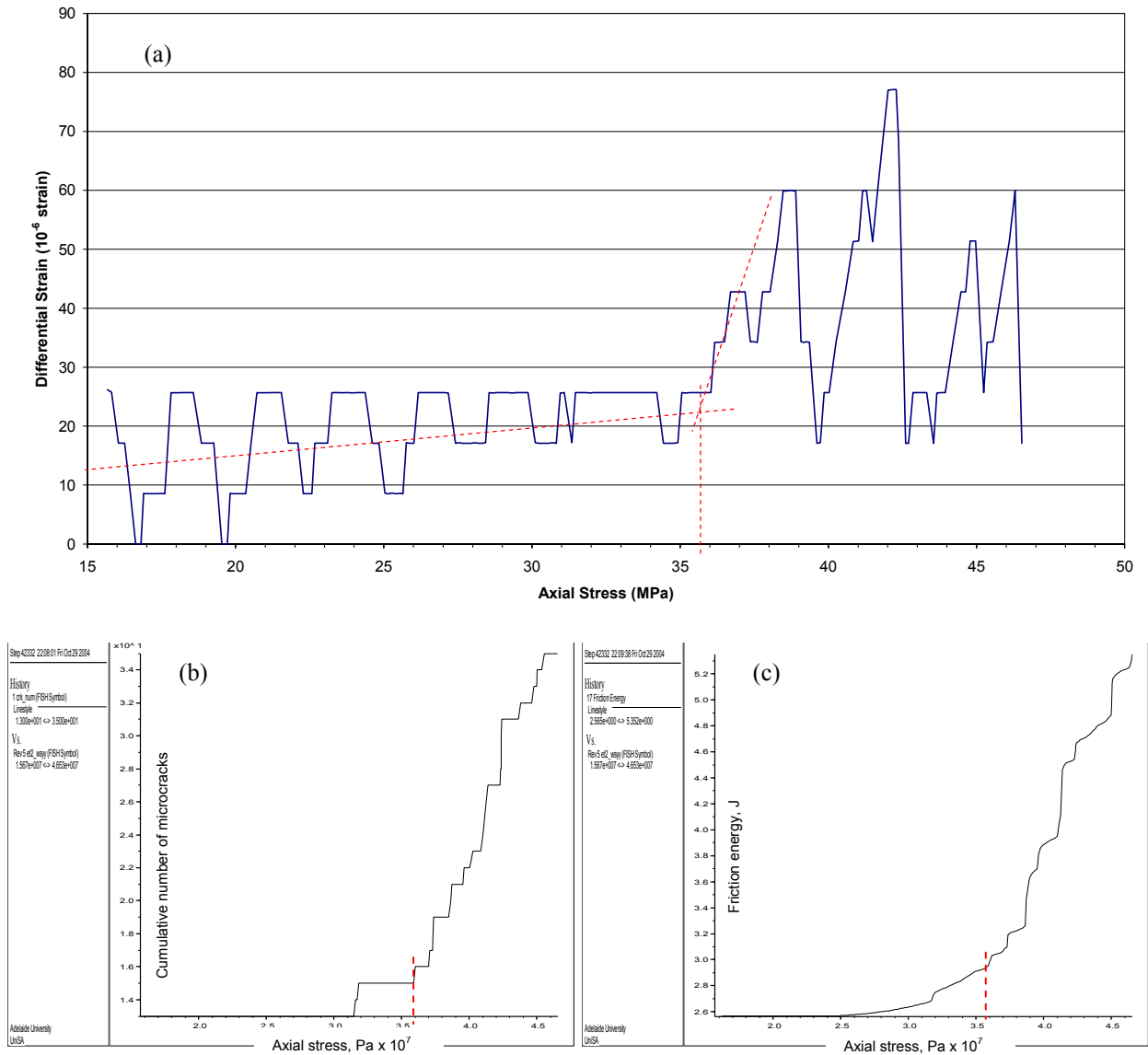


Figure 5.60. Test No.1: (a) DRA curve; (b) cumulative number of microcracks; (c) friction energy.

Table 5.18. Results of Test No.1.

Pre-load stress, MPa	35.6
DME from DRA curve, MPa	35.6
FR	1.00
DME from cum. No. of microcracks, MPa	35.8
FR	0.99
DME from friction energy, MPa	35.8
FR	0.99

Intact rock specimen:  $s_1 = 35.9$  MPa,  $s_3 = 20.0$  MPa.

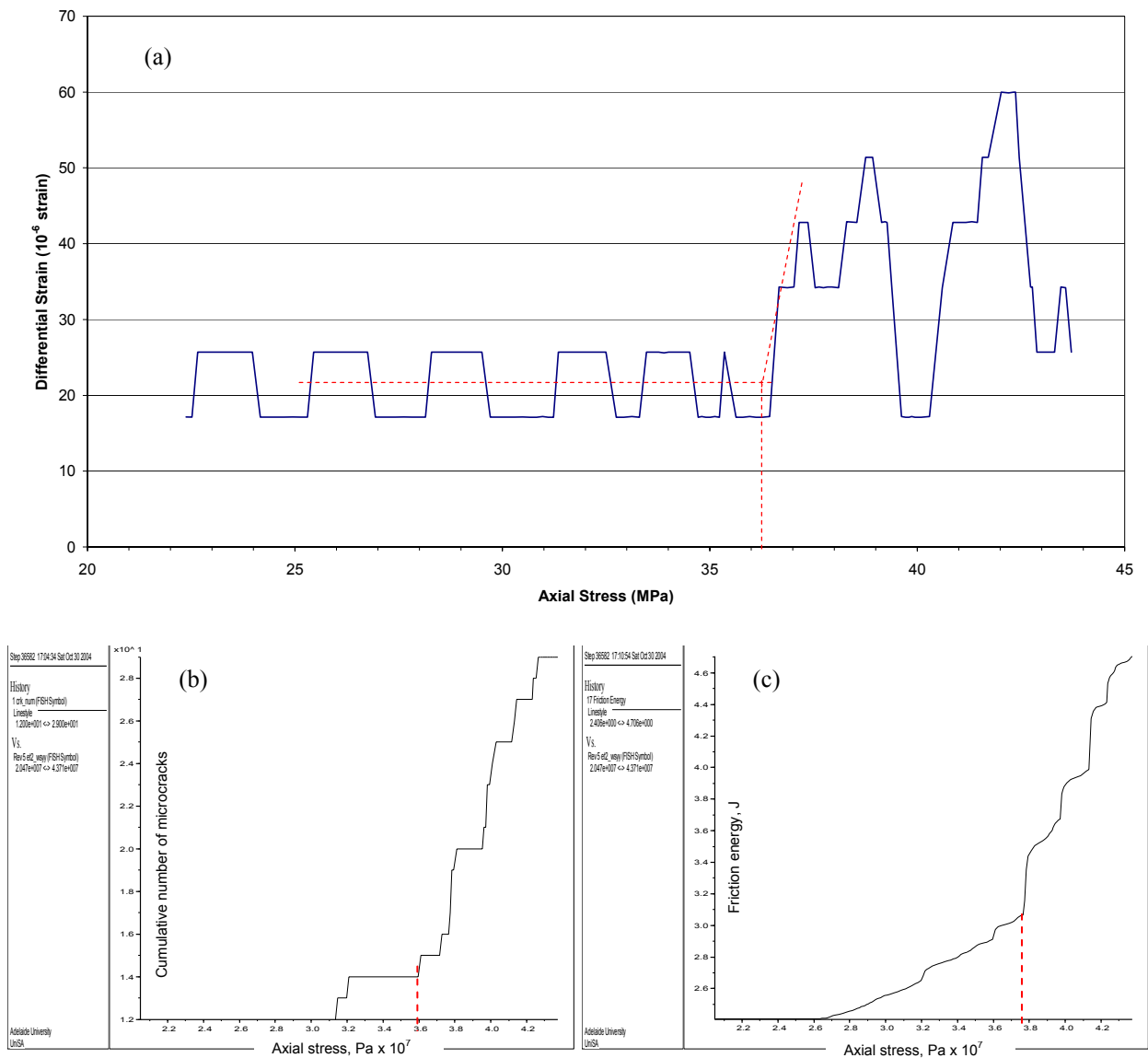


Figure 5.61. Test No.2: (a) DRA curve; (b) cumulative number of microcracks; (c) friction energy.

Table 5.19. Results of Test No.2.

Pre-load stress, MPa	35.9
DME from DRA curve, MPa	36.3
FR	0.99
DME from cum. No. of microcracks, MPa	35.9
FR	1.00
DME from friction energy, MPa	37.6
FR	0.95

Intact rock specimen:  $s_1 = 35.9$  MPa,  $s_3 = 28.0$  MPa.

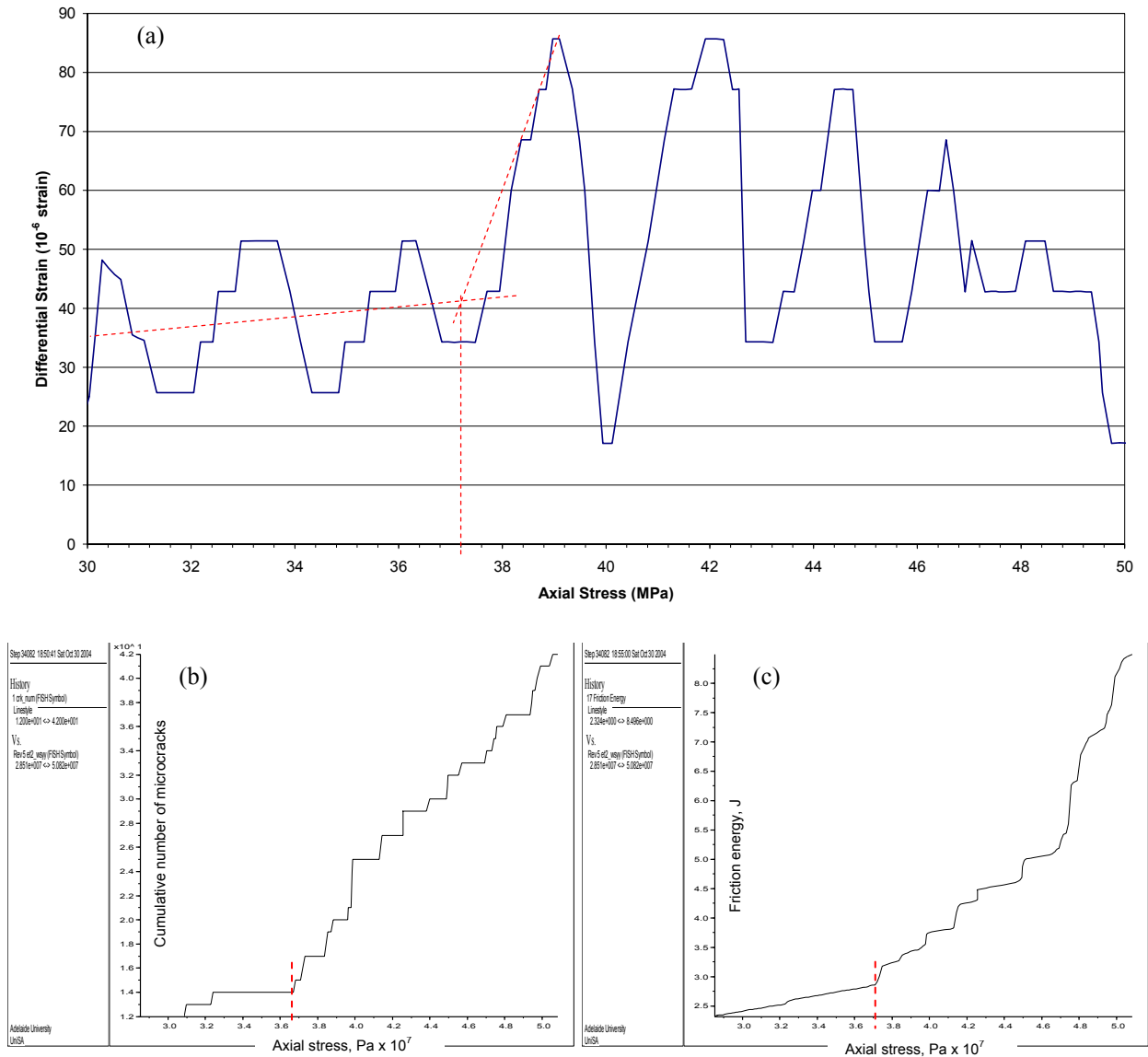


Figure 5.62. Test No.3: (a) DRA curve; (b) cumulative number of microcracks; (c) friction energy.

Table 5.20. Results of Test No.3.

Pre-load stress, MPa	<b>35.9</b>
DME from DRA curve, MPa	37.2
FR	0.97
DME from cum. No. of microcracks, MPa	36.7
FR	0.98
DME from friction energy, MPa	37.2
FR	0.97

Fine-grained rock specimen:  $s1 = 35.6$  MPa,  $s3 = 12.0$  MPa.

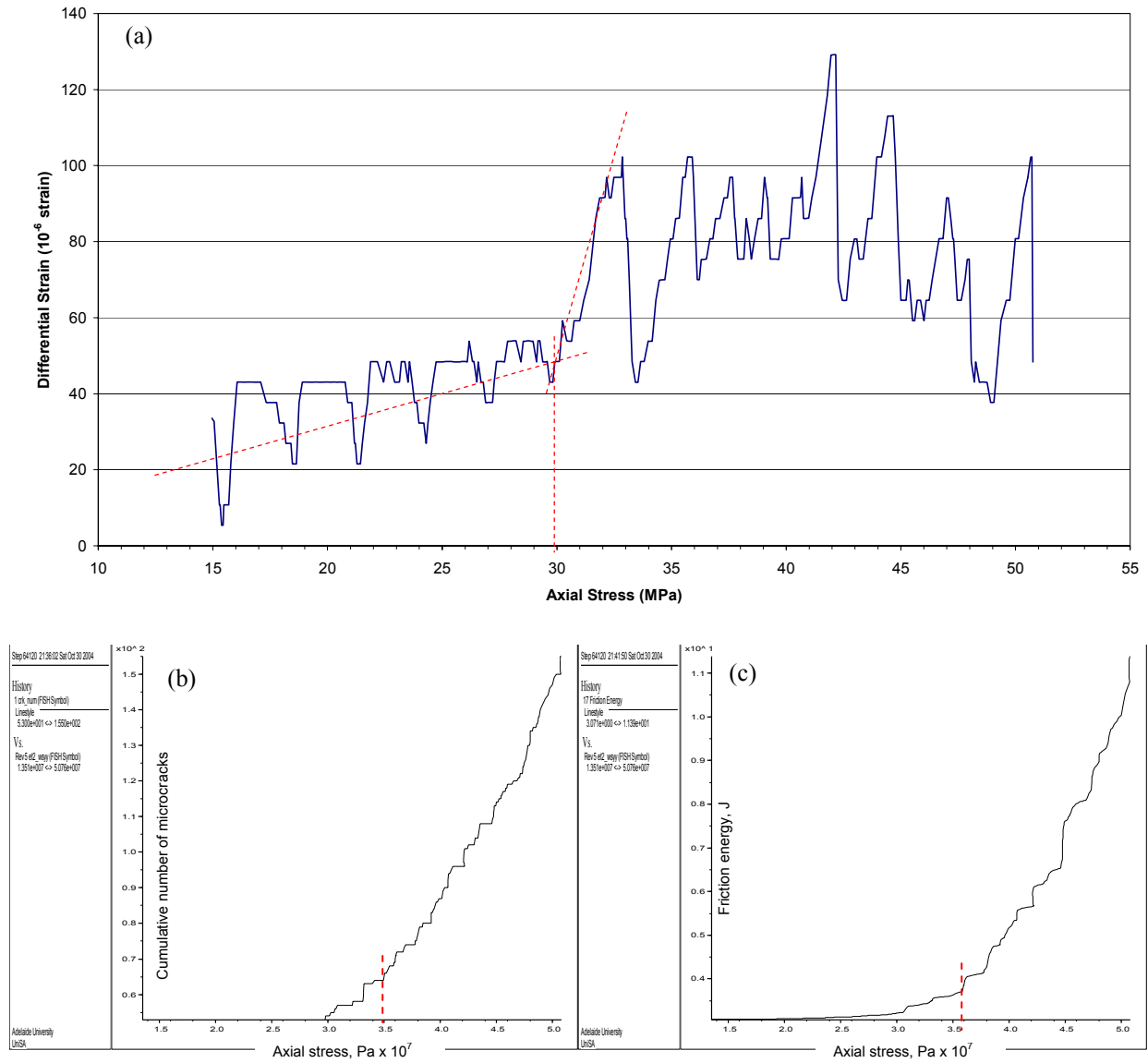


Figure 5.63. Test No.4: (a) DRA curve; (b) cumulative number of microcracks; (c) friction energy.

Table 5.21. Results of Test No.4.

Pre-load stress, MPa	<b>35.6</b>
DME from DRA curve, MPa	30.0
FR	0.84
DME from cum. No. of microcracks, MPa	35.0
FR	1.02
DME from friction energy, MPa	35.9
FR	0.99

Fine-grained rock specimen:  $s_1 = 35.6$  MPa,  $s_3 = 20.0$  MPa.

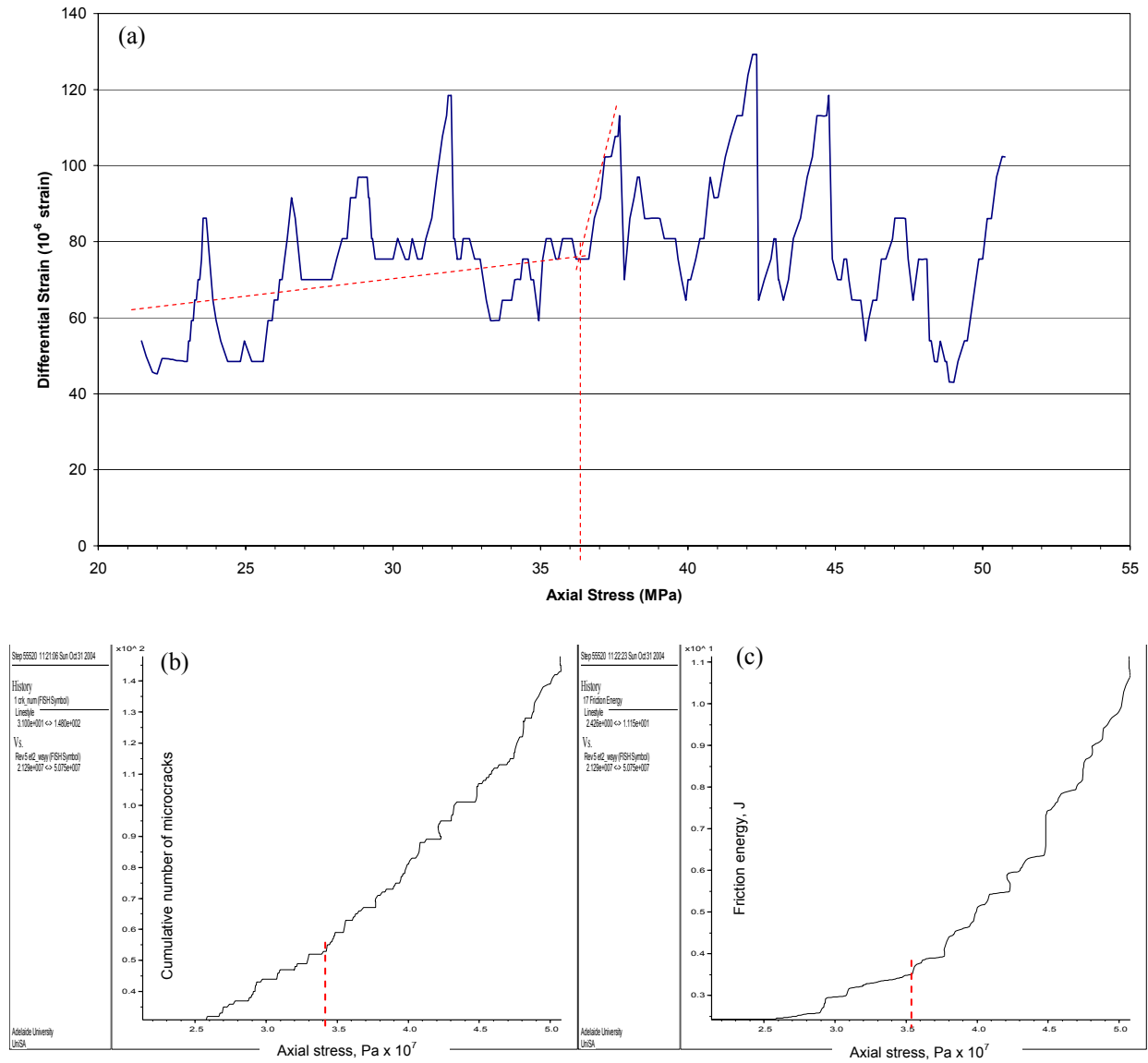


Figure 5.64. Test No.5: (a) DRA curve; (b) cumulative number of microcracks; (c) friction energy.

Table 5.22. Results of Test No.5.

Pre-load stress, MPa	<b>35.6</b>
DME from DRA curve, MPa	36.3
FR	0.98
DME from cum. No. of microcracks, MPa	34.1
FR	1.05
DME from friction energy, MPa	35.3
FR	1.01

Intact rock specimen:  $\sigma_1' = 26.1$  MPa,  $\sigma_1'' = 35.4$  MPa,  $\sigma_3 = 12.0$  MPa.

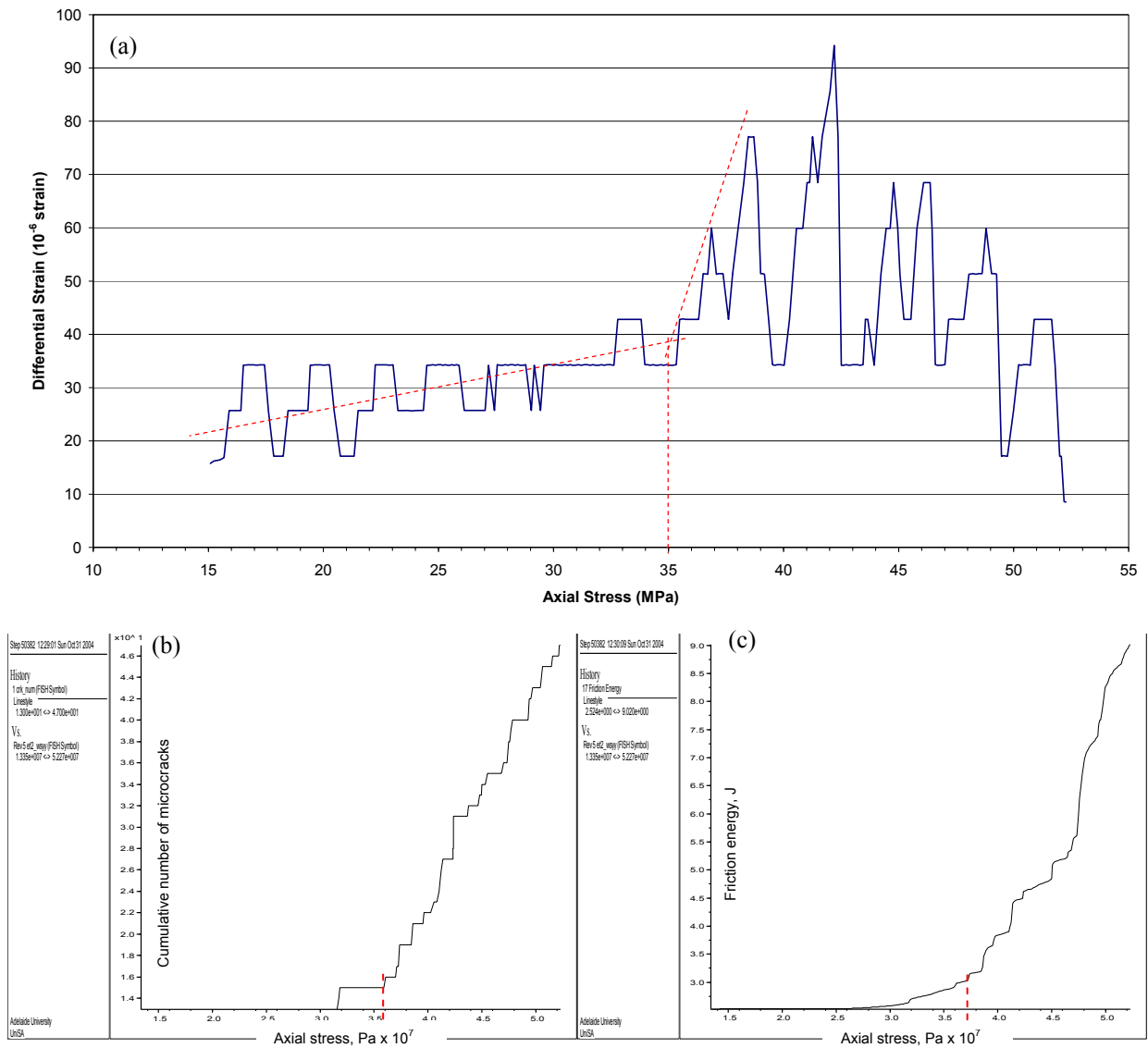


Figure 5.65. Test No.6: (a) DRA curve; (b) cumulative number of microcracks; (c) friction energy.

Table 5.23. Results of Test No.6.

1 <sup>st</sup> pre-load $\sigma_1'$ , MPa	26.1
DME for $\sigma_1'$ from DRA curve, MPa	—
FR	—
DME for $\sigma_1'$ from cum. No. of microcracks, MPa	—
FR	—
2 <sup>nd</sup> pre-load $\sigma_1''$ , MPa	35.4
DME for $\sigma_1''$ from DRA curve, MPa	35.5
FR	1.00
DME for $\sigma_1''$ from cum. No. of microcracks, MPa	35.8
FR	0.99

Intact rock specimen:  $\sigma_1' = 35.4$  MPa,  $\sigma_1'' = 26.0$  MPa,  $\sigma_3 = 12.0$  MPa.

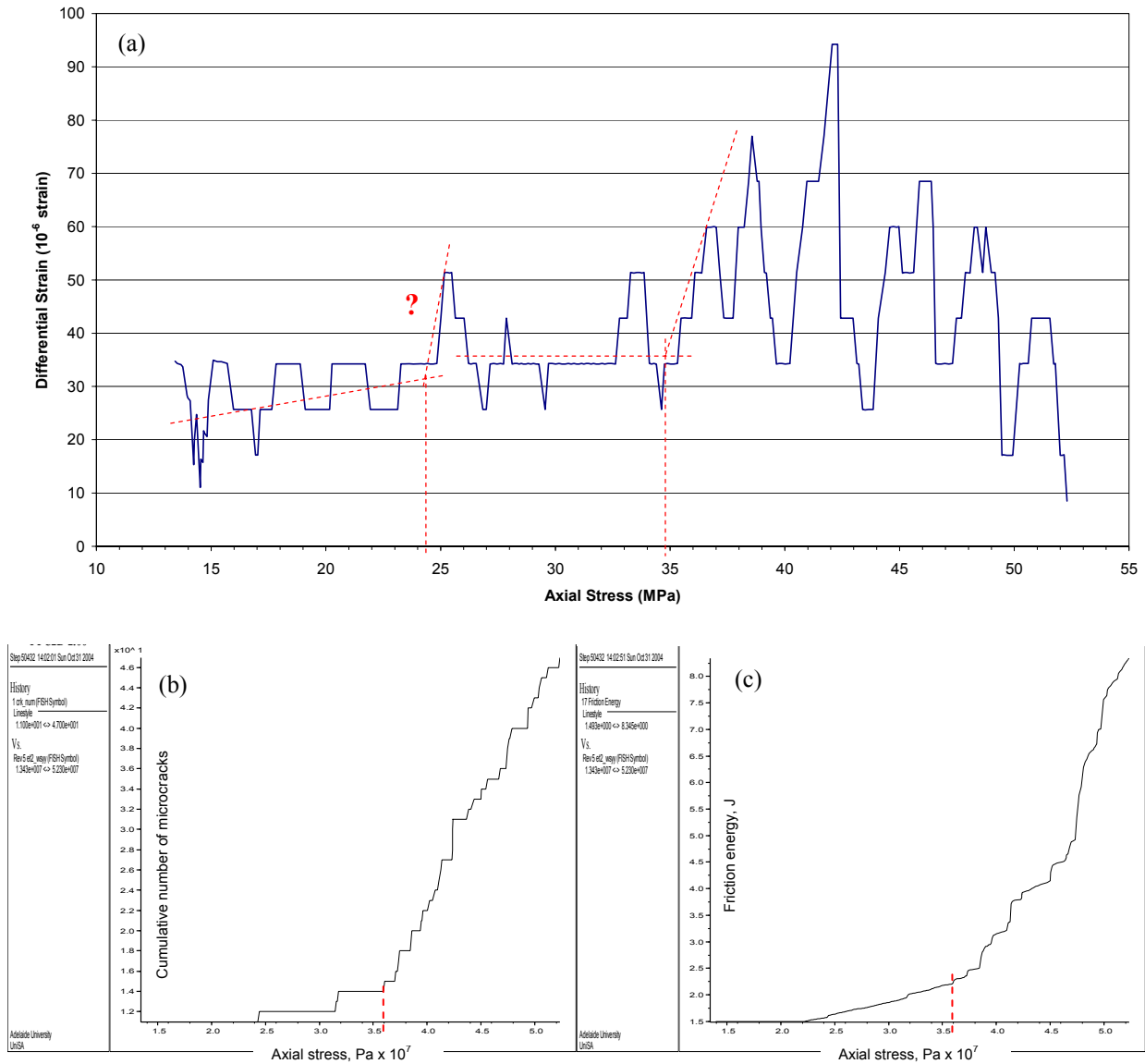


Figure 5.66. Test No.7: (a) DRA curve; (b) cumulative number of microcracks; (c) friction energy.

Table 5.24. Results of Test No.7.

1 <sup>st</sup> pre-load $\sigma_1'$ , MPa	35.4
DME for $\sigma_1'$ from DRA curve, MPa	34.7
FR	1.02
DME for $\sigma_1'$ from cum. No. of microcracks, MPa	35.9
FR	0.99
2 <sup>nd</sup> pre-load $\sigma_1''$ , MPa	26.0
DME for $\sigma_1''$ from DRA curve, MPa	24.3
FR	1.07
DME for $\sigma_1''$ from cum. No. of microcracks, MPa	—
FR	—

Fine-grained specimen:  $\sigma_1' = 26.5$  MPa,  $\sigma_1'' = 36.2$  MPa,  $\sigma_3 = 12.0$  MPa.

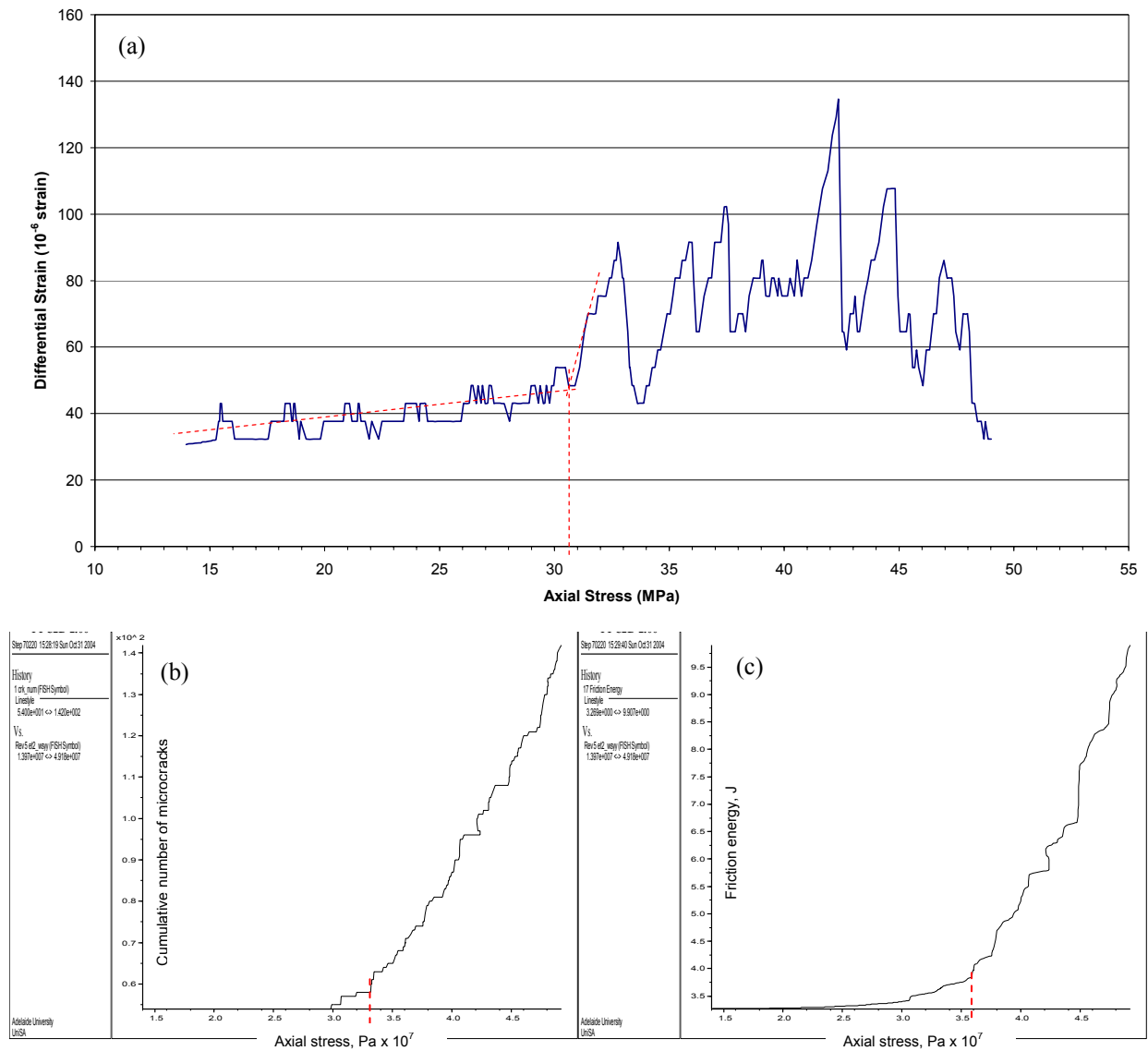


Figure 5.67. Test No.8: (a) DRA curve; (b) cumulative number of microcracks; (c) friction energy.

Table 5.25. Results of Test No.8.

1 <sup>st</sup> Pre-load $\sigma_1'$ , MPa	26.5
DME for $\sigma_1'$ from DRA curve, MPa	—
FR	—
DME for $\sigma_1'$ from cum. No. of microcracks, MPa	—
FR	—
2 <sup>nd</sup> Pre-load $\sigma_1''$ , MPa	36.2
DME for $\sigma_1''$ from DRA curve, MPa	30.6
FR	1.18
DME for $\sigma_1''$ from cum. No. of microcracks, MPa	33.0
FR	1.10

Fine-grained specimen:  $\sigma_1' = 36.4$  MPa,  $\sigma_1'' = 26.9$  MPa,  $\sigma_3 = 12.0$  MPa.

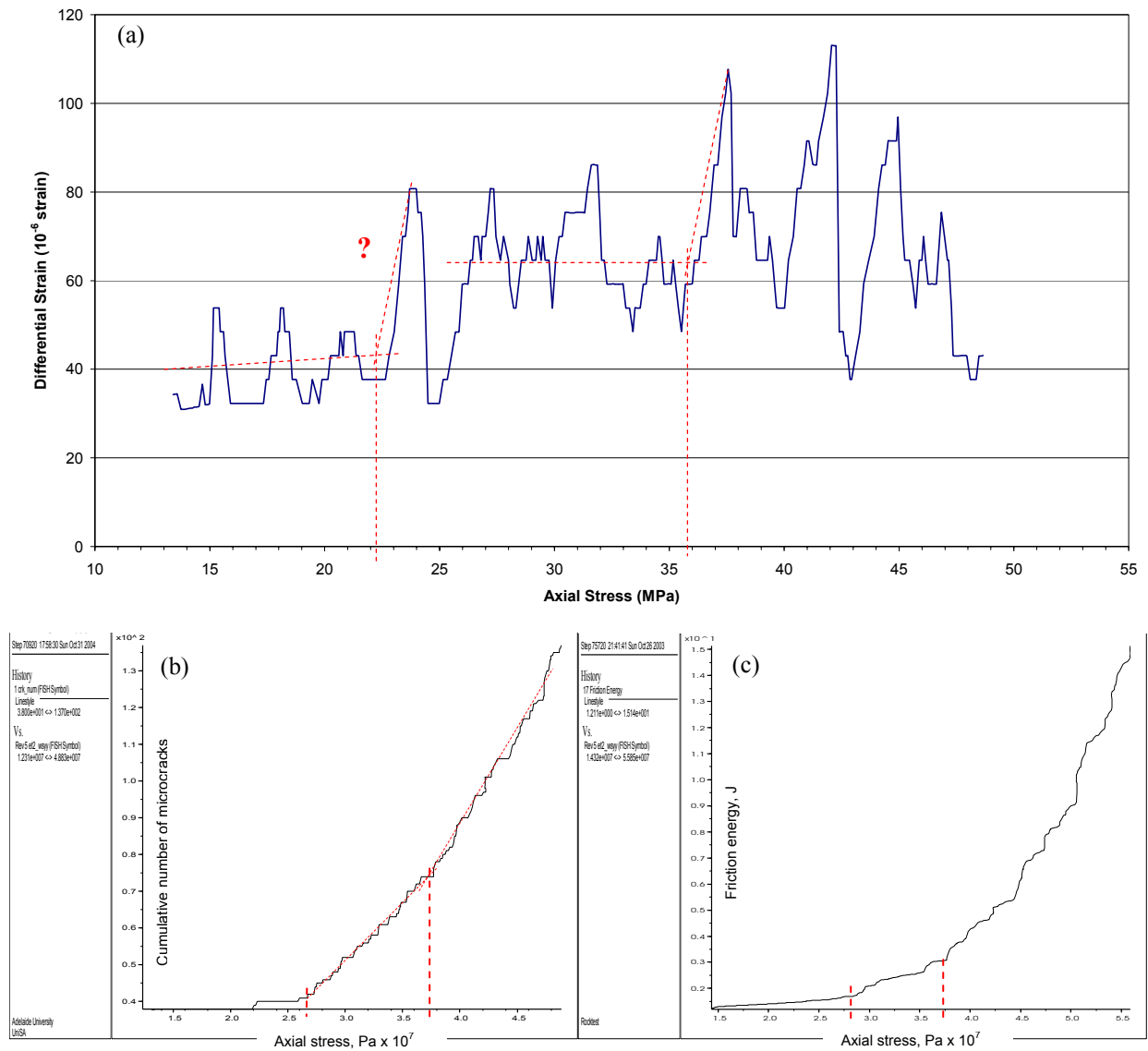


Figure 5.68. Test No.9: (a) DRA curve; (b) cumulative number of microcracks; (c) friction energy.

Table 5.26. Results of Test No.9.

1 <sup>st</sup> pre-load $\sigma_1'$ , MPa	36.4
DME for $\sigma_1'$ from DRA curve, MPa	35.7
FR	1.02
DME for $\sigma_1'$ from cum. No. of microcracks, MPa	37.5
FR	0.97
2 <sup>nd</sup> pre-load $\sigma_1''$ , MPa	26.9
DME for $\sigma_1''$ from DRA curve, MPa	22.2
FR	1.18
DME for $\sigma_1''$ from cum. No. of microcracks, MPa	26.7
FR	1.00

## 6 DISCUSSION

In general, the shapes of the DRA curves obtained from the numerical simulations resemble those applicable to real rock (Figures 3.7 and 4.3). However, the points with the positive gradients obtained when testing the simulated models are not present in the diagrams for the real rocks. This discrepancy may be the result of the low sensitivity of the data recorder used when testing the physical specimens. This feature is not a problem for the numerical tests as they can be considered to replicate ‘closed physical systems’, in which the equations of motion and deformation are calculated with a high degree of precision.

The action of microcrack development, so fundamental to the deformation memory effect in a DEM environment, can be analysed by detailing the micromechanical processes in the two distinctive phases of a DRA diagram, the pre-DME and the post-DME stages (Figure 6.1).

### 1. *Pre-DME stage.*

The strain difference function steadily and linearly increases up to the pre-load value due to the continuous dissipation of the strain energy. This action results from frictional sliding between particles adjacent to the locations where the contact bonds are broken by the pre-loading stress (Note the moderate increase in the friction energy up to the pre-load value, Figure 5.30). The fact that no new contact bond breakage occur can be confirmed by monitoring the cumulative number of microcracks (Figure 5.29). A general strain softening effect is observed in the model: the stiffness in the 1<sup>st</sup> reloading cycle being lower than it is during the pre-load (Note the difference in the slope of these two curves, Figure 5.27).

### 2. *Post-DME stage.*

Evidence that the pre-loading stress has been exceeded, is the inception of broken contact bonds in the model, which represents the onset of nucleation of the microcracks (Figure 5.29). This process is rather chaotic as indicated by the zigzag shape of the post-DME curve in Figure 6.1. With continued axial loading, more microcracks nucleate; the strain energy dissipates at increasing rate through frictional sliding of particles with broken contact bonds. The general trend of the differential strain rate decreases as the stiffness of the model reduces (Note the decreasing slope in the 1<sup>st</sup> reloading cycle, Figure 5.27). The characteristic point of the DME is clearly defined by a ‘spike’ in the curve at the stress at which the pre-load is reached. This spike is not considered to be a strain-hardening effect. It can be explained by the intermittent nature of the contact bond breakage: the bonds in the model do not break continuously, but only after the

axial load reaches a certain value at which a number of bonds break instantaneously. This occurrence can be verified by studying any graph presenting the cumulative number of microcracks (e.g. Figure 5.29). Therefore it can be said, the unstable crack development resulting in the disordered damage in the model is responsible for the irregular shape of the post-DME curve. The intermittent bond breakage also causes the low-amplitude ‘waviness’ seen in all stress-strain curves. In this curve a sporadic localised strain hardening-softening effect is observed during the whole process of axial loading.

Summarising observations made from the analysis of the two parts of the strain difference function, it can be concluded that the DME point is located in the DRA curve on the boundary between the steady positive increase and the chaotic decrease of the differential strain rate curve. The irregular shape of the curve can be idealised as a convex curve with its apex corresponding to the deformation memory effect (Figure 6.1).

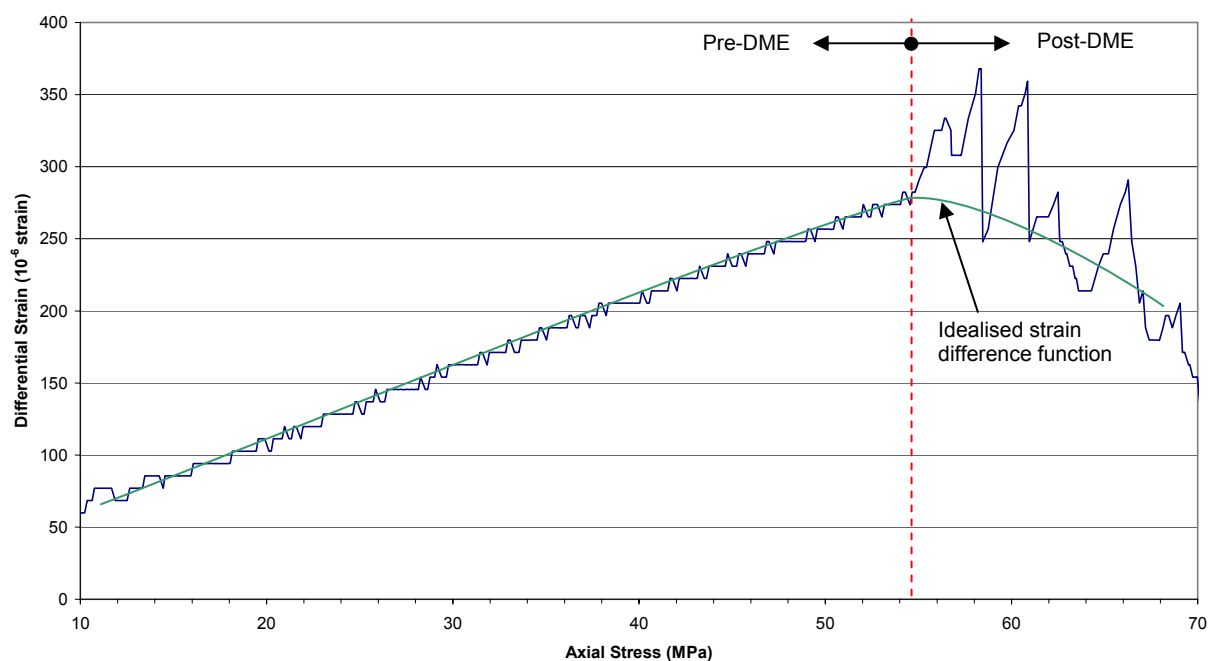


Figure 6.1. Strain difference function broken into two stages (DRA curve borrowed from Figure 5.28d).

The fine-grained model displayed similar characteristics with the inflection point yet more obvious than that in the intact rock model simulations (e.g. Figure 5.32). This feature is due to the comparatively higher number of broken bonds (directly related to the number of ‘balls’ in the model), which results in the more disordered nature of the post-DME damage in the model. No fundamental differences were observed in the complex lithology and discontinuous rock models, where the DME was also well pronounced.

The DME was shown to be sensitive to the orientation of a discontinuity within a model; in all simulations involving a single joint, the DME was detected reasonably accurately (Appendix 2, Tables A2.5 to A2.13). It was however observed that the inflection points in the DRA curves are not well defined when a joint plane is oriented at an angle between  $10^\circ$  and  $30^\circ$  to the direction of the maximum principal stress. Figures A2.17, A2.20, A2.22 & A2.24 demonstrate that at these orientations the model fails preferentially along the joint plane. The DME is not obvious because the model is significantly and prematurely damaged by the pre-load. As can be seen from Figures A2.19c, A2.21c, A2.23c & A2.25c, the failure is accompanied by intensive dissipation of friction energy due to continuous sliding of particles on a joint plane.

In the biaxial LRR tests, microcrack development was detected before the 1<sup>st</sup> reloading cycle reached the pre-load value (e.g. Figure 5.60b). This development occurred because the damage during the pre-loading cycle was induced by the differential stress ( $\sigma_1 - \sigma_3$ ), which was lower than the differential stress in the case of the uniaxial reloading cycle ( $\sigma_1 - 0 = \sigma_1$ ) for a particular value of axial stress. Hence new bond breakage could be expected from the beginning of the uniaxial reloading cycle (subject to the crack initiation threshold being exceeded), although at a lower rate. Apart from this observation, the shapes of the strain difference function are similar to those obtained from the uniaxial cyclic tests.

It was found that the confining stress had an effect on the DME; however the effect tended to be qualitative rather than quantitative. In all biaxial tests the pre-load could be determined accurately from the DRA curve yet the inflection point was difficult to detect in the tests conducted at higher confining stresses. The DME was found to be sensitive to the major-to-minor stress ratio  $k$ : the lower the ratio, the less obvious is the DRA inflection point. The induced pre-load was not easy to discern in the simulations carried out on the models of intact rock and fine-grained rock with confining stresses exceeding  $0.5\sigma_1$ , i.e. when  $k$  was less than 2. The effect that confining stress has on the DME is apparently related to the quantity of microcracks contributing to the stress memory phenomenon. This contribution can be examined by referring to plots showing the cumulative number of microcracks developed during the complete pre-loading (including loading and unloading) cycle (Figure 6.2 and Table 6.1). Pre-load can be seen to be ‘memorised’ by a significantly lower number of microcracks in the tests in which a confining stress is applied. It has to be noted, the microcrack quantity is directly related to the crack initiation threshold: the higher the threshold, the lower is the number of microcracks for a given pre-load value (Table 6.1).

Table 6.1. Microcrack quantity determining the deformation memory effect.

Cumulative number of microcracks at pre-load cycle	Test			
	Uniaxial	Biaxial $\sigma_3=12$ MPa	Biaxial $\sigma_3=20$ MPa	Biaxial $\sigma_3=28$ MPa
During loading	18	9	3	3
During unloading	1	4	9	4
Crack initiation threshold, MPa	3.5	22.0	25.1	33.2

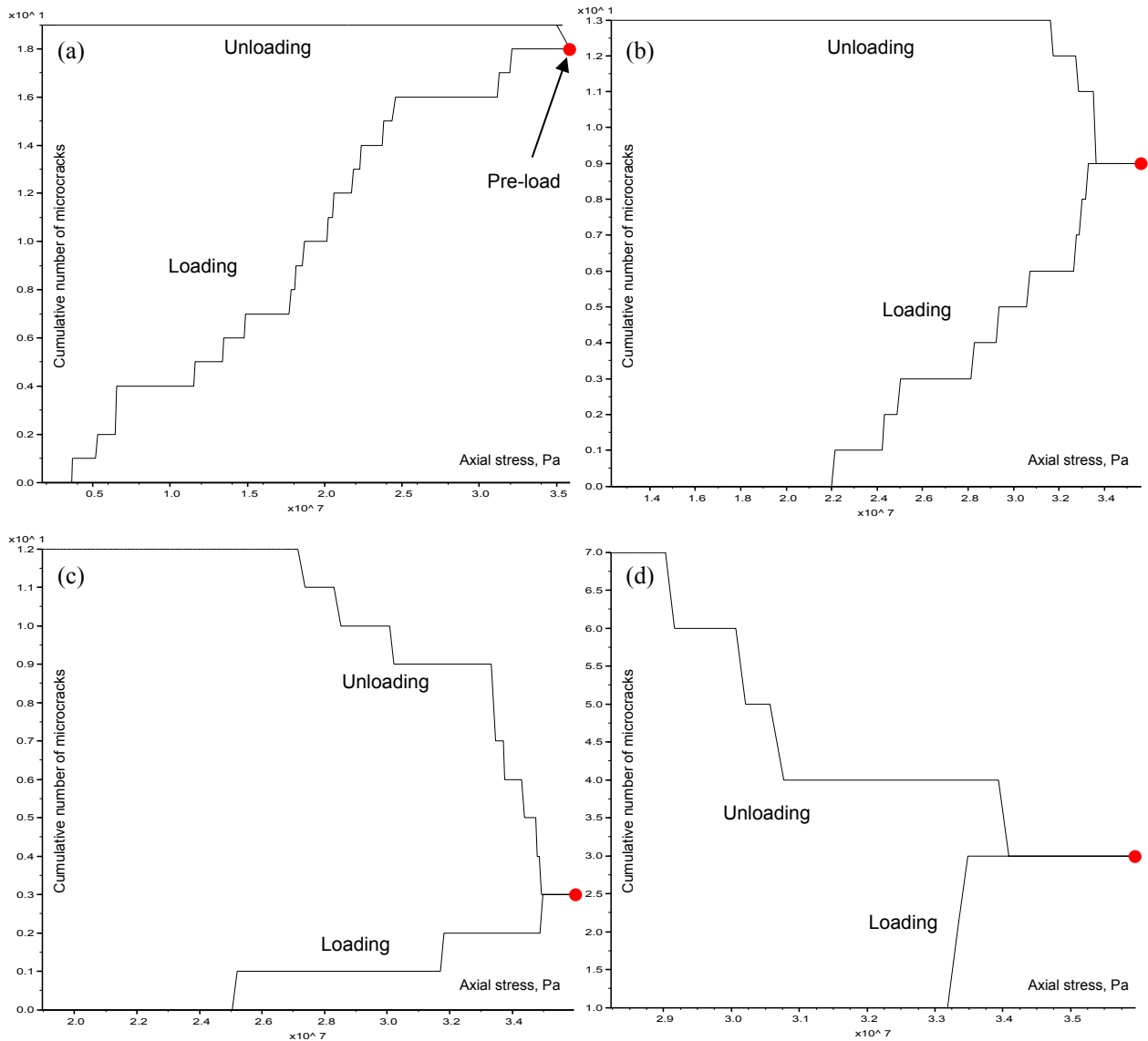


Figure 6.2. Complete pre-loading cycle on the intact rock specimen: (a) uniaxial simulation; (b) biaxial test at  $\sigma_3=12$  MPa; (c) biaxial test at  $\sigma_3=20$  MPa; (d) biaxial test at  $\sigma_3=28$  MPa.

In all biaxial tests, the DME was found to correspond to the absolute axial, but not the differential stress. This result occurred because, once the confining stress was instantaneously removed, the model was still subjected to the axial load which caused the bonds to break. As mentioned, this does not accurately replicate the real rock coring from in-situ, in which case all stresses are removed relatively instantaneously. A typical process of microcrack formation

throughout the pre-loading and 1<sup>st</sup> reloading cycles is presented in Figure 6.3. It can be seen that four microcracks developed after the confining stress had been relieved.

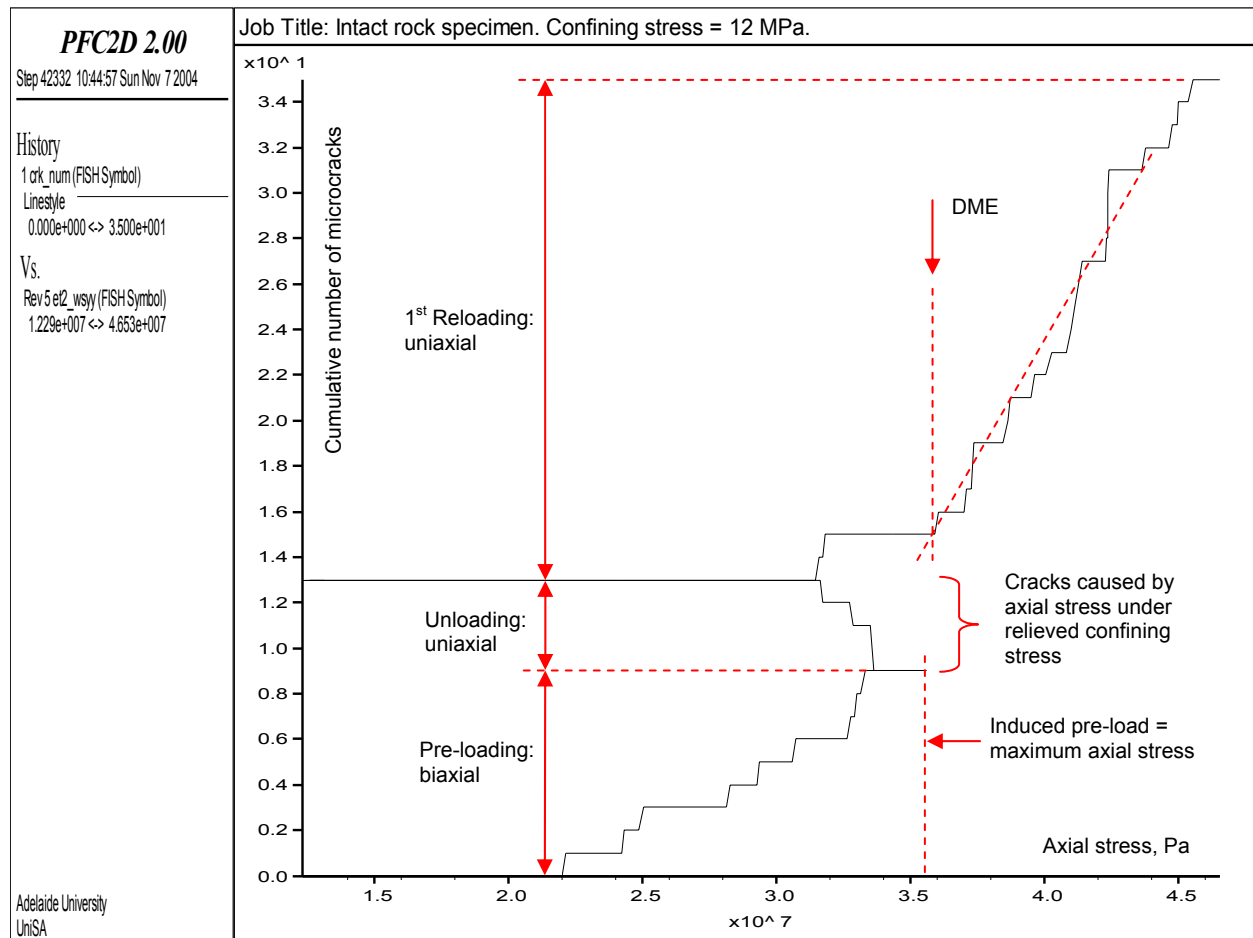


Figure 6.3. History of microcrack development throughout the pre-loading and 1<sup>st</sup> reloading cycles.

A solution was obtained to the question of which stress is detected by the DME, paleo- or present-day stress. The results suggest that the DME detects the highest historical stress that the rock has experienced, which is determined by the DRA stress measurement technique. The LLRR tests on the intact rock and fine-grained models (Figures 5.65 to 5.68) clearly showed that the DME was related to  $\sigma_{\max}(\sigma_1', \sigma_1'')$ . It is however not possible to say whether it was the youngest or the oldest historical stress, the inflection point being related to the highest pre-load in each case. In the simulations, where the consecutive pre-loads were induced at progressively decreasing values, the lower pre-load was also supposedly detected by the strain difference function, as illustrated in Figures 5.66a and 5.68a, albeit with a lower accuracy. The curve of cumulative number of microcracks was also slightly inflected at the lower pre-load value in the case of the fine-grained model (Figure 5.68b). It is however premature to say that all historical stresses can be determined by the DRA technique: the inflection related to the lower pre-load is indistinct and more tests are required to prove or disprove this hypothesis.

## 7 CONCLUSIONS

A numerical model was produced that reasonably replicated the mechanical properties and general behaviour of a physical rock during axial loading. This study showed that the deformation memory effect could be simulated in this model successfully using the distinct element modelling code *PFC<sup>2D</sup>*. By doing so the following conclusions were reached:

- The DME is able to provide an indication as to the stress history a model had been subjected to.
- The link between the DME and microcrack development was confirmed by investigating the breakage that occurs to interparticle bonds. It would not however be necessarily correct to explain the complex nature of the KE/DME in real rocks in terms of interparticle bond breakage occurring in a numerical model. Nonetheless, simulations did provide an insight into the essence of the KE/DME, which has been proved to be related to microcrack development.
- The DME was observed in models involving varying lithologies.
- The DME was observed in models intersected by discontinuities having variable orientations. The phenomenon was found to be affected by the orientation of the discontinuities.
- The confining stress was found to have a considerable effect on the DME.

Although it would be improper to draw a direct parallel between the deformation memory effect in real rocks and that indicated in numerical models, it was considered appropriate to present a number of observations, which may also be applicable when using the DRA technique for stress measurement in real rocks:

- The stress determined by the DRA method is the absolute maximum present-day stress, not the differential stress.
- The DME can be detected effectively only in specimens obtained from depths where the coefficient  $k$ , the major-to-minor principal stress ratio, is greater than 2 (assuming re-loading is conducted in the direction of the major principal stress, which in most cases is the horizontal stress). Referring to Figure 1.2, this could imply that under the typical in-situ stress conditions the DRA technique might be applicable for stress measurements only at relatively shallow depths, maximum 700m, depending on the rock stiffness. This observation possibly explains the varying degree of success in application of the AE/DRA techniques among practitioners.
- Reloadings should be in the range of  $0.6\sigma_c$  to  $0.7\sigma_c$ .

- The DME might not be obvious when testing rocks containing a weak discontinuity oriented at  $10^\circ$  to  $30^\circ$  to the direction of the major principal stress.

There is still much research possible involving DME simulation. Potential future work includes the following:

- Investigate non-coaxial loading of induced stress and subsequent re-loads, i.e. pre-load applied in one direction, while re-loadings are conducted normally or at an angle to the induced stress;
- Model the DME in *PFC<sup>3D</sup>*, a three-dimensional particle flow code, to study the influence of the intermediate principal stress when the model is subjected to polyaxial loading conditions;
- Obtain a ‘damage surface’ (Pestman et al., 2002) in the three-dimensional model and compare stresses obtained using this method to those measured by the DRA technique;
- Simulate Griffith’s crack development by introducing a bondless slot into a fine-grained rock model. Intention is to relate the potential DME to the initiation of tensile wing cracks;
- Investigate the DME retention span, i.e. time dependence effect;
- Study the DME on a model created using the ‘parallel bonds’ concept, which is a more realistic algorithm for modelling solid bodies;
- Investigate the influence of porosity and pore-water pressure on the DME;
- Study the effect of the loading/unloading rate on the DME;
- Use clumped logic algorithm (Itasca, 1999) to study dilatancy and the DME further.

## REFERENCES

- Barr, S.P & Hunt D.P. 1999, 'Anelastic strain recovery and the Kaiser Effect retention span in the Carnmenellis granite, UK', *Rock Mech. Rock Eng.* 32 169-193.
- Barton, C.A. & Zoback, M.D. 1994, 'Stress perturbations associated with active faults penetrated by boreholes: possible evidence for near-complete stress drop and a new technique for stress magnitude measurement', *J. Geophys. Res.*, vol. 99/B5, pp. 9373-9390.
- Billings, M.P. 1942, *Structural geology*, Prentice-Hall, New York, 473 p.
- Brace, W.F. & Byerlee, J.D. 1967, 'Experimental studies of brittle fracture of rocks', in *Proc. 8<sup>th</sup> Symp. on Rock Mechanics*, University of Minnesota, September 15-17, 1966, pp. 58-81.
- Costin, L.S. 1983, 'Microcrack model for the deformation and failure of brittle rock', *J. Geophys. Res.*, 88, pp. 9485-9492.
- Courtillot, V. & Vink, G.E. 1983, 'How continents break up', *Scientific American*, New York, July 1983, 249, no. 1, pp. 40-47.
- Cundall, P.A. & Strack, O.D.L. 1979, 'A discrete numerical model for granular assemblies', *Geotechnique*, 29(1), pp. 47-65.
- Dewey, J.F. 1972, 'Plate Tectonics'. *Readings from Scientific American, Planet Earth*, 1974, Frank Press, pp. 124-135.
- Fairhurst, C. 1965, 'Measurement of in-situ stresses with particular reference to hydraulic fracturing', *Felsmech. Ingenieurgeol.*, II, 3-4, pp. 129-147.
- Fjær, E., Holt, R.M., Hosrud, P., Raaen, A.M. & Risnes, R. 1992, *Petroleum related rock mechanics*, Elsevier, 338 p.
- Friedel, M.J. & Thill, R.E. 1990, 'Stress determination in rock using the Kaiser effect', *US Dept. of the Interior, Bureau of Mines, Report of Investigations RI-9286*.
- Fujii, N. & Hamano, Y. 1977, 'Anisotropic changes in resistivity and velocity during rock deformation', in *High pressure research: applications in geophysics*. London, Academic Press, pp. 53-64.
- Griffith, A.A. 1924. 'The theory of rupture', in *Proc. 1<sup>st</sup> Int. Congress of applied mechanics*, Delft, pp. 55-63.
- Griggs, D.T. 1936, 'Deformation of rocks under high confining pressures', *J. of Geol.*, 44, pp. 541-577.
- Goodman, R.E. 1963, 'Subaudible noise during compression in rocks', *Geol. Soc. of Amer. Bull.*, 74, pp. 487-490.

- Goodman, R.E. 1980, *Introduction to rock mechanics*, New York, John Wiley & Sons, 478 p.
- Haimson B.C. & Lee C.F. 1995, 'Estimating in situ stress conditions from borehole breakouts and coredisking – experiment results in granite', in *Proc. of the Int. Workshop on Rock Stress Measurement at Great Depth*, Tokyo, Japan, 8<sup>th</sup> ISRM Congress, pp. 19–24.
- Haimson, B.C. & Cornet, F.H. 2003, 'ISRM Suggested Methods for rock stress estimation – Part 3: hydraulic fracturing (HF) and/or hydraulic testing on pre-existing fractures (HTPF)', *Int. J. Rock Mech. Min. Sci.*, 40, pp. 1011-1020.
- Harrison, J.P. & Hudson, J.A. 2000, *Engineering rock mechanics. Part 2: illustrative workable examples*, Pergamon.
- Hast, N. 1958, *The measurement of rock pressure in mines*, Swedish Geol. Surv., Ser. C560, 183 p.
- Heim, A. 1878, *Untersuchungen über den Mechanismus der Gebirgsbildung*, im Anschlusse an die geol. Mon. der Tödi-Windgällen-Gruppe, Basel, C.f.Hoernes, p. 337.
- Hoek, E. 2000, 'Practical Rock Engineering Course Notes', *Rocscience* [Online, accessed 22 Feb. 2004]. URL: <http://www.rocscience.com>.
- Holcomb, D.J. 1983, 'Using Acoustic Emissions to determine in-situ stress: problems and promise', *Geomechanics*, AMD, v. 57, pp. 11-21.
- Holcomb, D.J. 1993, 'General theory of the Kaiser effect', *Int. J. Rock Mech. Min. Sci. & Geomech. Abstr.*, 30 (7), pp. 929-935.
- Holcomb, D.J. & Costin, L.S. 1986, 'Detecting damage surfaces in brittle materials using acoustic emissions', *J. App. Mech.*, 108, pp. 536-544.
- Hudson, J.A. & Harrison, J.P. 1997, *Engineering rock mechanics*, Pergamon, 444 p.
- Hughson, D.R. & Crawford, A.M. 1987, 'Kaiser effect gauging: the influence of confining stress on its response', in *Proc. 6<sup>th</sup> Int. Cong. Int. Soc. Rock Mech.*, Montreal, vol.2, pp. 981-985.
- Itasca 1999, *PFC<sup>2D</sup>: Particle Flow Code in 2 Dimensions*, Itasca Consulting Group, Inc., Minneapolis, Minnesota.
- Jaeger J.C. & Cook, N.G.W. 1979. *Fundamentals of rock mechanics*, Chapman & Hall, London.
- James, D.E. 1973, 'The evolution of the Andes', *Readings from Scientific American, Planet Earth*, 1974, Frank Press, pp. 137-146.
- Jin, G., Patzek, T.W. & Silin, D.B. 2003. 'Physics-based reconstructions of sedimentary rocks', SPE 83587, in *Proc. SPE Western Regional / AAPG Pacific Section Joint Meeting*, Long Beach, USA 19-24 May 2003.

- Jing, L. & Hudson J.A. 2002, 'Numerical methods in rock mechanics', *Int. J. Rock Mech. Min. Sci.*, 39, pp. 409-427.
- Jing, L. 2003, 'A review of techniques, advances and outstanding issues in numerical modelling for rock mechanics and rock engineering' *Int. J. Rock Mech. Min. Sci.*, 40, pp. 283-353.
- Kanagawa, T., Hayashi, M. & Kitahara, Y. 1976, 'Estimation of the spatial geo-stress components in rock samples using the Kaiser effect of acoustic emissions', in *Proc. 3<sup>rd</sup> Acoustic Emission Symp.*, Tokyo, pp. 229-248.
- Kaiser, J. 1950, *An investigation into the occurrence of noises in tensile tests or a study of acoustic phenomena in tensile tests*. Ph.D. Thesis, Tech. Hochsch. München, Munich.
- Kranz, R.L. 1979, 'Crack growth and development during creep of Barre granite', *Int. J. Rock Mech. Min. Sci. & Geomech. Abstr.*, 16, pp. 23-35.
- Kranz, R.L. 1983, 'Microcracks in rocks: a review', *Tectonophysics*, 100, pp. 449-480.
- Kurita, K. & Fujii, N. 1979, 'Stress memory of crystalline rocks in acoustic emissions', *Geophys. Res. Lett.*, 6, pp. 9-12.
- Lama, R.D. & Vutukuri, V.S. 1978, *Handbook on mechanical properties of rock: testing techniques and results*, vol. II, pp. 481, Trans Tech Publications.
- Lee, M.Y. 1984, 'Development of a wireline hydrofracturing technique and its use at a site of induced seismicity', in *Proc. 25<sup>th</sup> US Rock Mech. Symp.*, Soc. Mining Engrs, New York, pp. 194-203.
- Lockner, D. 1993, 'The role of acoustic emission in the study of rock fracture', *Int. J. Rock Mech. Min. Sci. & Geomech. Abstr.*, 30 (7), pp. 883-899.
- Li, C. & Nordlund, E. 1993, 'Assessment of damage in rock using the Kaiser effect of acoustic emissions', *Int. J. Rock Mech. Min. Sci. & Geomech. Abstr.*, 30 (7), pp. 943-946.
- Li, C. 1996, 'A theory for the Kaiser effect and its potential applications', in *Proc. 6<sup>th</sup> Conf. on Acoustic Emission / Microseismic Activity in Geologic Structures and Materials*, Pennsylvania State University, June 11-13, 1996, pp. 171-185.
- Ljunggren, C., Chang, Y., Janson, T. & Christiansson, R. 2003, 'An overview of rock stress measurement methods', *Int. J. Rock Mech. Min. Sci.*, 40(7-8), pp. 975-989.
- Martin, C.D. & Chandler, N.A. 1993, 'Stress heterogeneity and geological structures', *Int. J. Rock Mech. Min. Sci.*; 30(7), pp. 993-999.
- Martin, C.D. & Chandler, N.A. 1994, 'The progressive fracture of Lac du Bonnet granite', *Int. J. Rock Mech. Min. Sci. & Geomech. Abstr.*, 31(6), pp. 643-659.

- Martin, C.D., Kaiser, P.K. & Christiansson, R. 2003, 'Stress, stability and design of underground excavations' *Int. J. Rock Mech. Min. Sci.*; 40(7-8), pp. 1027-1047.
- McKenzie, D.P. & Sclater, J.G. 1973, 'The evolution of the Indian Ocean', *Readings from Scientific American, Planet Earth*, 1974, Frank Press, pp. 147-158.
- Meyers, A.G., Hunt, S.P. & Oliver, K.J. 2002, 'The use of the DRA technique and porosimetry for estimating the maximum in-situ stress in rock from core', *Australian Geomechanics J.*, 37 (1), pp. 17-22.
- Momayez M. & Hassani F.P. 1992, 'Application of Kaiser effect to measure in-situ stresses in underground mines', in *Proc. 33<sup>rd</sup> US Symposium on Rock Mechanics*, eds. Tillerson J.R. & Wawersik W.R., Santa Fe, New Mexico. A.A.Balkema, Rotterdam, pp. 979-987.
- Oliver, K.J. 2001, *Relationship between sample porosity and inelastic strain in reservoir core*. Hon. Thesis, University of South Australia, Adelaide, 140 p., unpublished.
- Pestman, B.J., Holt, R.M., Kenter, C.J. & van Munster, J.G. 2002. 'Application of a novel core-based in-situ stress estimation technique', *SPE/ISRM 78158. SPE/ISRM Rock Mechanics Conference OilRock2002*.
- Qin, S., Wang S., Long, H. & Liu, J. 1999, 'A new approach to estimating geo-stresses from laboratory Kaiser effect measurements', *Int. J. Rock Mech. Min. Sci.*, 36, pp. 1073-1077.
- Read, R.S., Chandler, N.A. & Dzik, E.J. 1998, 'In-situ strength criteria for tunnel design in highly-stressed rock masses', *Int. J. Rock Mech. Min. Sci.*, 35(3), pp. 261-278.
- Reed, L.D. & McDowell, G.M. 1994, 'A fracto-emission memory effect and subharmonic vibrations in rock samples stressed at sonic frequencies', *Rock Mech. Rock Eng.*, 27, pp. 253-261.
- Sakaguchi, K., Iino, W. & Matsuki, K. 2002, 'Damage in a rock core caused by induced tensile stress and its relation to differential strain curve analysis', *Int. J. Rock Mech. Min. Sci.*, 39, pp. 367-380.
- Seto, M. Utagawa, M. & Katsuyama, K. 2002, 'Some fundamental studies on the AE method and its application to in-situ stress measurements in Japan', in *Proc. 5th Int. Workshop on the Applications of Geophysics in Rock Engineering*, July 7, Toronto, pp. 67-71.
- Seto, M. & Villaescusa, E. 1999, 'In situ stress determination by acoustic emission techniques from McArthur River Mine core', in *Proc. 8th Australia New Zealand Conf. on Geomechanics*, Hobart, vol. 2, 15 February, pp. 929-934.

- Seto, M., Nag, D.K. & Vutukuri, V.S. 1996, 'Experimental verification of the Kaiser effect in rock under different environment conditions', in *Proc. Eurock 96.*, ed. Barla, G., Torino, pp. 395-402.
- Seto, M., Nag, D.K. & Vutukuri, V.S. 1999, 'In-situ rock stress measurement from rock cores using the acoustic emissions and deformation rate analysis', *Geotech. & Geol. Eng.*, 17, pp. 241-266.
- Sheorey, P.R. 1994, 'A theory for in-situ stresses in isotropic and transversely isotropic rock', *Int. J. Rock Mech. Min. Sci. & Geomech. Abstr.*, 31(1), pp. 23-34.
- Stevens, J.L. & Holcomb, D.J. 1980, 'A theoretical investigation of the sliding crack model of dilatancy', *J. Geophys. Res.*, 85 (B12), pp. 7091-7100.
- Strickland, F.G. & Ren, N.K. 1980, 'Predicting the in-situ stress for deep wells using differential strain analysis', in *Proc. of the SPE/DOE Symposium on Unconventional Gas Recovery*, pp.251-258.
- Stuart, C.E., Meredith, P.G., Murrell, S.A.F. & van Muster, J.G. 1993, 'Anisotropic crack damage and stress-memory effects in rocks under triaxial loading', *Int. J. Rock Mech. Min. Sci. & Geomech. Abstr.*, 30 (7), pp. 937-941.
- Te Kamp L., Rummel F. & Zoback M.D. 1995, 'Hydrofrac stress profile to 9 km at the German KTB site', in *Proc. of the Workshop on Rock Stresses in the North Sea*, Trondheim, Norway: NTH and SINTEF Publishers, pp. 147–53.
- Terzaghi, K. & Richart, F.E. 1952, 'Stresses in rock about cavities', *Geotechnique*, 3, pp. 57-90.
- Vavra, C., Kaldi, J. & Sneider, R. 1992, 'Geological applications of capillary pressure: a review', *American Assoc. of Pet. Geol. Bull.*, 76(6).
- Villaescusa, E., Li, J., & Seto, M. 2002, 'Stress measurement from oriented core in Australia', in *Proc. 5<sup>th</sup> Int. Workshop on the Applications of Geophysics in Rock Engineering*, July 7, Toronto, pp. 72-77.
- Villaescusa, E. & Li, J. 2004, *Stress measurements from oriented core using the Acoustic Emission method*, Report, Gold Fields Australia – Agnew Gold Mining Company, 20 p., unpublished.
- Wang, F., Watson, J. O. & Vutukuri, V.S. 1999, 'Different approaches to study the Kaiser effect in rocks in triaxial loading', in *Proc. 8<sup>th</sup> Australia New Zealand Conference on Geomechanics*, Hobart, v.2, pp. 935-941.
- Wegener A. 1915, *Die Entstehung der Kontinente und Ozeane*. Sammlung Vieweg-Verlag, Braunschweig, vol. 33, 94 p.

- Warpinski, N.R. & Teufel, L.W. 1989, 'A viscoelastic constitutive model for determining in-situ stress magnitudes from anelastic strain recovery of core', *Society of Petroleum Engineers, Production Engineering*, August, pp. 272-280.
- Wolter K. & Berckhemer H. 1989, 'Estimation of in-situ stress by evaluation of time-dependent strain recovery of KTB drill core', *Tectonophysics*, vol. 178 No. 2/4 June.
- Yamamoto K., Kuwahara Y., Kato N. & Hirasawa T. 1990, 'Deformation rate analysis: a new method for in-situ stress estimation from inelastic deformation of rock samples under uniaxial compression', *Tohoku Geophysical J.*, 33, pp. 1-13.
- Yassir, N., Wang D.F., Enever, J.R. and Davies, P.J. 1998, 'Experimental study of anelastic strain recovery and synthetic sandstone subjected to polyaxial stress', in *Proc. SPE/International Society of Rock Mechanics in Petroleum Engineering Conf.*, vol.1, pp. 161-170.
- Zhang, B., Li, H., Li, F. & Shin, K. 1996, 'Kaiser effect tests on orientated rock core', in *Proc. 6<sup>th</sup> Conf. on Acoustic Emission / Microseismic Activity in Geologic Structures and Materials*, Pennsylvania State University, June 11-13, 1996, pp. 211-224.

## **APPENDIX 1. GLOSSARY**

### **acoustic emissions**

Acoustic signals emanating from material under applied stress.

### **brittle deformation**

Deformation in rock resulted in a complete failure: rapture or fracture.

### **borehole breakouts**

= 'dog earing'. Damage in a circular underground opening characterised by diametrically opposite V-shaped notches, oriented normal to the main principal stress.

### **coefficient of friction**

A constant of proportionality,  $\mu$ , relating the normal stress and the corresponding critical shear stress at which sliding starts between two surfaces.

### **compressive stress**

Normal stress tending to shorten the body in the direction in which it acts.

### **confining stress**

Stress equal to minimum principal stress. Increasing minimum principal stress results in an increase in normal stress acting across potential failure plane.

### **crack initiation stress**

Represents the stress level at which microfracturing starts.

### **deformation**

Body rotation, translation, distortion, and dilation.

### **deformation memory effect**

The phenomenon in which the strain difference function changes its gradient from positive to negative after surpassing the highest stress a rock specimen had been subjected to.

### **deformation rate analysis**

Core-based method of in-situ stress determination utilising deformation memory effect.

**deviatoric stress**

Difference of one of the principal stresses and average value of three principal stresses.

**differential stress**

Difference of maximum principal stress and minimum principal stress.

**disking**

The fracturing of a drill core into doughnut shapes indicative of high stress in the rock.

**elastic deformation**

Deformation in the rock without permanent damage. Removal of stress results in complete recovery of the body.

**elastic limit**

Of rock, yield point; maximum stress from which it can recover apparently unchanged. If stressed beyond this point there is disruption or permanent deformation.

**elastic strain**

Strain recovered when applied stress is removed (no permanent deformation).

**failure plane**

Failure comprising a well-defined rupture in a rock sample.

***FISH***

(FlacISH) - Programming language originally used in FLAC numerical code and subsequently in all other codes developed by Itasca.

**Hooke's law**

Within elastic range stress acting on a body is linearly proportional to the strain induced in the body:  $\sigma = E\varepsilon$ .

**hydrostatic stress**

Stress acting equally in all directions.

**hydraulic fracturing**

A method of in-situ stress measurement, which involves inducing a fracture in rock with subsequent recording of shut-in pressure indicating the magnitude of the major principal stress.

**inelastic strain**

Irreversible component of strain. Loading and unloading result in a permanent deformation induced in the body.

**in-situ stress**

Undisturbed stress in rock mass before excavation.

**inter-crystal/grain cracks**

Microcracks that cross over grain boundaries.

**intra-crystal/grain cracks**

Microcracks that begin and end totally within one grain.

**Kaiser effect**

The phenomenon in which acoustic emission activity in a rock specimen under uniaxial compressive loading is quiet until the previously applied maximum stress level is exceeded.

**lithology**

Mineral composition of rock.

**lithostatic stress field**

Hydrostatic stress field in rock where the horizontal stress field equals the vertical stress field, i.e.  $k = 1$ .

**microcrack**

Any cavity within the rock that cannot be seen without a microscope and that has aspect ratio (cavity width divided by cavity length) less than 0.05 (Kranz, 1979).

**maximum strength**

= ultimate strength. Here: uniaxial compressive strength of a rock sample equal to the axial stress at failure.

**numerical modelling**

Computer aided modelling such as ‘boundary’, ‘finite element’ or ‘discrete element’ analysis. The mathematical simulation is used to study and predict behaviour of real materials.

**overcoring**

A method of measuring stress in the rock by determining the expansion of a piece of core by relieving the stress through drilling a larger diameter core around it.

**plastic deformation**

Deformation which occurs in a body once the yield stress is exceeded.

**Poisson’s ratio**

Ratio of lateral to longitudinal strain.

**pore**

Any cavity within the rock with an aspect ratio greater than 0.05 (Kranz, 1979).

**shear stress**

Deformation under this stress involves sliding within a body causing change in shape but not in volume.

**strain**

Non-rigid body deformation (distortion) caused by stress:  $\varepsilon = (l-l_0)/l_0$ , where  $l_0$  – original length,  $l$  – length after deformation.

**strain energy**

The work done in deforming a body within the elastic limit of the material. Stored strain energy can be an indicator of the energy released when rock fails.

**strain hardening**

Occurs if the rock becomes harder as a result of deformation. Young’s modulus increases.

**strain softening**

Occurs if the rock becomes softer as a result of deformation. Young’s modulus decreases.

**strength**

Stress required to cause a fracture in a specimen at room temperature and atmospheric pressure in short-time tests.

**stress**

A mathematical term used to indicate the amount of load placed on the material, whether it be rock, wood, steel or backfill. Defined as a ration of force acting per unit area ( $\text{Nm}^{-2}$  or Pa).

**stress deformation**

The load imposed on any material results in elongation or compression, which is called stress deformation.

**stress field**

A descriptive term to indicate the pattern of stress existing in a particular area.

**tensile stress**

Deformation under this stress involves pulling a specimen apart resulting in a volume change (evidence of inelastic strain).

**tectonic forces**

Earth forces that act on a continent-wide basis to induce high horizontal stresses which cause earthquakes.

**virgin stress**

The stress in the rock mass before it is disturbed by man-made works.

**yield stress**

= elastic limit. A point, where stress-strain curve diverges from straight line.

**Young's modulus**

Coefficient of proportionality in Hooke's law, modulus of elasticity  $E$ .

## APPENDIX 2. Detailed modelling processes

### A2.1 Conventions

Information presented in this Appendix allows the reader to reproduce all modelling processes used for creation and testing the numerically simulated Specimen #3 (intact rock model) and its more complex derivatives: fine-grained model, complex lithology model and discontinuous rock models. However, it is expected that for the better understanding of the *PFC* environment and built-in programming language *FISH* the reader would consult the relevant Itasca documentation, the '*User's Guide*' and '*FISH in PFC*' in particular.

*PFC*<sup>2D</sup> is a command-driven program, although some menu-driven features are partially employed. In this text, all relevant commands are provided in square brackets, e.g.:

```
[md_strength_histogram]
```

The user can simply type such commands in the command line whenever required. Subroutines (termed here as 'drivers') used to invoke numerous commands essential for running numerical tests, are presented in full-text under headings e.g. *Code A2.1*. Parameters required special attention of the user (e.g. values to be changed), are highlighted with bold font, e.g. `cb_sn_mean=82e6`.

### A2.2 Specimen-genesis codes

The first step in the creation of the model was to install the *Augmented FishTank*<sup>5</sup>. In the Notepad the `FisT_env.DVR` code was created and placed into the `C:\Itasca\Pfc` folder.

*Code A2.1. Augmented FishTank environment driver.*

---

```
;fname: FisT_env.DVR
;
def set_fist_env
  environment('itascaFishTank')='c:\\itasca\\pfc\\FisT_04c\\'
end
set_fist_env
;
;EOF: FisT_env.DVR
```

---

Next the link from the *PFC*<sup>2D</sup> executable (shortcut to the `pfc2dw.exe` on the Desktop) to this file was created as follows:

```
C:\Itasca\Pfc\pfc2d\pfc2dw.exe C:\Itasca\Pfc\FisT_env.dvr
```

---

<sup>5</sup> Refer to '*FISH in PFC*', Section 3.1.1.

The specimen-generation driver file spc3.DVR, responsible for calling all supporting *PFC* functions and commands was created (this file was based on Agc.DVR provided by the *Augmented FishTank*) and saved in the folder:

C:\Itasca\Pfc\FisT\_04c\FishPFC2\Drivers\Specimen

The driver code is presented below.

*Code A2.2. Specimen #3 (intact rock model) generation driver.*

---

```

; Filename: spc3.DVR
;
; PURPOSE: Create the coarse grained sandstone: numerical
;          replica of the physical Specimen #3.
;
;
; INPUT:   none
; OUTPUT:  'md_run_name' 'spc' final specimen (bonded)
;
; Adelaide University.
; =====
new
set safe_conversion on
SET random ; for reproducibility
SET disk on ; model unit-thickness cylinders
;
SET echo off ; load support functions
  call %itascaFishTank%\FishPfc\md\md.FIS
  call %itascaFishTank%\FishPfc2\et2\et2.FIS
  call %itascaFishTank%\FishPfc\md\flt.FIS
SET echo on
; =====
SET md_run_name = 'spc3'
title 'Specimen # 3'
; =====
; Specify parameters that control the specimen-generation
; procedures
SET et2_xlen=61.14e-3 et2_ylen=153.32e-3
SET et2_radius_ratio=1.5 et2_rlo=0.8e-3
SET md_wEcfac=1.1
SET tm_req_isostr=-1.0e6 tm_req_isostr_tol=0.50
SET flt_def=3 flt_remain=0.0
;
; Specify parameters that define a contact-bonded material
SET md_add_cbonds=1
SET md_dens=2397
SET md_Ec=20e9 md_knoverks=1.8
SET md_fric=0.50
SET cb_sn_mean=82e6 cb_sn_sdev=30e6
SET cb_ss_mean=82e6 cb_ss_sdev=30e6
;
SET et2_prep_saveall=1
et2_prep ; invoke the specimen-generation procedures
; =====
return
; END OF Filename: spc3.DVR

```

---

The user-defined parameters controlling the specimen-genesis procedure are shown in the text in bold font and listed in Table A2.1. Refer to Chapter 3 of the '*FISH in PFC<sup>2D</sup>*' for detailed description of the parameters.

*Table A2.1. Parameters controlling the specimen-genesis procedure.*

<b>FISH name</b>	<b>Description</b>	<b>Value</b>
et2_ylen	sample height, m	153.32e-3
et2_xlen	sample width, m	61.14e-3
et2_rlo	minimum ball radius, m	0.8e-3
et2_radius_ratio	ball size ratio	1.5
md_wEcfac	wall normal stiffness multiplier	1.1
tm_req_isostr	locked-in isotropic stress, Pa	-1.0e6
flt_def	min. number of contacts to be a non-floater	3
flt_remain	remaining floaters ratio	0

It was decided to create a contact-bonded material. For simulation of solid bodies there is also another type of bonds that can be used, the parallel bonds. However, for the purposes of this study, a contact-bonded material was considered to be adequate for creation of a sandstone replica and conducting compressive tests. The contact-bonded material can be approximated to a material representing particles attached to each other by a cement-like substance of infinitesimal area. Whenever applied stress exceeds the bond strength, the bond breaks reverting particles to unbonded granules. Parameters defining contact-bonded material are listed in Table A2.2.

*Table A2.2. Parameters defining contact-bonded material.*

<b>FISH name</b>	<b>Description</b>	<b>Value</b>
md_dens	ball density, kg/m <sup>3</sup>	2397
md_Ec	ball-ball contact modulus, GPa	20e9
md_knoverts	ball stiffness ratio	1.8
md_fric	ball friction coefficient	0.5
cb_sn_mean	contact-bond normal strength, mean, MPa	82
cb_sn_sdev	contact-bond normal strength, std. dev., MPa	30
cb_ss_mean	contact-bond shear strength, mean, MPa	82
cb_ss_sdev	contact-bond shear strength, std. dev., MPa	30

Having defined all required parameters, the driver file can now be called:

[call %itascaFishTank%\FishPFC2\Drivers\Specimen\spc3.DVR]

By the end of the running process the file is saved automatically as:

C:\Itasca\Pfc\Pfc2d\spc3-spc.SAV.

The saved model can be restored any time by typing:

[rest spc3-spc]

All information about the created model can be obtained by:

```
[print info]
```

After the generation process is completed, the resulting view of the model can be obtained:

```
[plot show]
```

This assembly is presented in Figure 5.9<sup>6</sup>.

The white background, deleted axes and resized caption window resulted from the following commands:

```
[plot cur 0]
```

```
[plot set back white]
```

```
[plot set capt size 18]
```

```
[plot sub 3]
```

Printing was done through the menu.

The contact forces and contact bonds views can be visualised:

```
[plot add cf]           → print
```

```
[plot sub 3]
```

```
[plot add cb]          → print
```

These plots are presented in Figures 5.9 and 5.10.

The interparticle contact bonds in the model were installed randomly with high value of standard deviation in order to achieve failure of the weakest bonds (consequently the DME detection) at a very early stage of the loading. The plots presented in Figure A2.1 were obtained by the following commands:

```
[md_strength_histogram]
```

```
[plot table @md_ntab both]   → print
```

```
[plot table @md_stab both]   → print
```

Note: to be able to change the settings of the new plot (background and size), the plot first has to be made current:

```
[plot cur 0]
```

---

<sup>6</sup> In this Appendix, references are generally made to figures in Chapter 5.

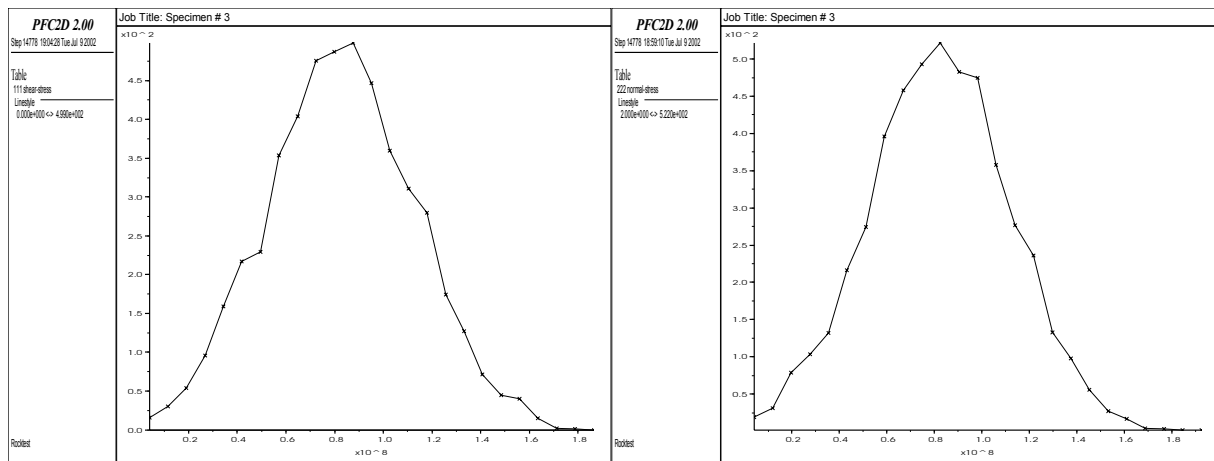


Figure A2.1. Contact-bond strengths distribution: (a) normal strength; (b) shear strength.

A number of tests have shown that the change of the standard deviation of the mean material strength increases or decreases the threshold of the microcracks nucleation (i.e. the crack initiation stress). Consequently, the DME detection is sensitive to this parameter. This however does not affect the essence of the experiment: in any instance, once the interparticle bonds begin failing, the DME may be detected right away. The only objective of selecting the relatively high standard deviation in this study (36% of the mean) was to allow the detection of the DME under a relatively low pre-load value (refer to Section 5.4.1: e.g. the pre-load of 15.4 MPa was only 25% higher than the crack initiation stress of 11.5 MPa).

The specimen generation is now complete. Although this is the final variation of the model in the present study, generally at this stage the simulated specimen would not yet have been finalised, as it would have to undergo a number of iterative modifications of deformability and strength parameters listed in Table A3.2, namely ball contact modulus, ball stiffness ratio, contact-bond strengths and their standard deviations, so as to produce the desired macroresponse (Young's modulus, Poisson's ratio, UCS and general stress-strain behaviour of the sample). These iterations would need to be done after a number of runs of compressive tests. Refer to Section 3.5 of the '*FISH in PFC<sup>2D</sup>*', for details on modelling strategy.

The biaxial environment in *PFC* is a set of a number of various codes written in *FISH* allowing the user to perform a biaxial test upon a model produced by the specimen-generation process. The uniaxial compressive test procedure starts from creating a driver file. This driver (spc3\_bx.DVR) was created and saved in the folder: C:\Itasca\Pfc\FisT\_04c\FishPFC2\Drivers\Specimen.

Parameters controlling the test environment are listed in Table A2-3.

Table A2.3. Parameters controlling the uniaxial compressive test procedure.

FISH name	Description	Value
et2_knxfac	lateral wall stiffness-reduction factor	0.001
et2_knyfac	vertical wall stiffness-reduction factor	1.0
et2_wsxx_req	target confining stress, Pa	1.0e5
et2_wsyy_req	target vertical stress, Pa	1.0e5
et2_ws_tol	wall-servo tolerance	0.01
p_vel	final platen velocity, m/s	0.2
p_cyc	total cycles of platen acceleration	1000
p_stages	accelerate platens in this many stages	20

The biaxial compressive test driver spc3\_bx.DVR is specified below.

Code A2.3. Biaxial compressive test driver.

---

```

; fname: spc3_bx.DVR  Uniaxial test on Specimen #3. Load up to failure.
;
; PURPOSE: 1) restore spc3 specimen,
;          2) perform uniaxial test upon it
;          (variation of biaxial test under confining
;          stress of Pc=0.1 MPa)
; Adelaide University.
; =====
set logfile spc3_bx.log
set log on
; -----
; Execute biaxial test at Pc=0.1 MPa
restore spc3-spc.SAV
set safe_conversion on
SET md_run_name='spc3_00'
title 'spc3_00.Specimen #3. Ax.stress (MPa) vs ax.strain (%)'
SET et2_knxfac=0.001 et2_knyfac=1.0
SET et2_wsxx_req=-1.0e5 et2_wsyy_req=-1.0e5 et2_ws_tol=0.01
SET p_vel=2.0e-1 p_cyc=1000 p_stages=20
call %itascaFishTank%\FishPfc2\et2\_btw2.DVR
; -----
set log off
return
; EOF: spc3_bx.DVR

```

---

Velocity of the horizontal walls was assigned as recommended by Itasca. The number of cycles and number of stages were, however, changed to achieve smoother acceleration of the platens. The spc3-bx.DVR driver calls the \_btw2.DVR, which is a modified version of the provided by PFC \_btw.DVR file. Unlike in the original driver, the termination of the process in the \_btw2.DVR does not occur automatically, but is controlled by the user. This was done to enable an interactive control over the running test. The \_btw2.DVR was saved in the folder: C:\Itasca\Pfc\FisT\_04c\FishPFC2\et2.

*Code A2.4. Driver controlling termination of the test.*

---

```
; Filename: _btw2.DVR (This is a modified _btw.DVR file).
; Termination of the test is controlled by the user (through
; specified No. of cycles: see in bold)
; PURPOSE: Perform biaxial test using existing four walls and
;           extract responses upon test completion.
;
; INPUT:    'md_run_name' 'bnd' bonded assembly
; OUTPUT:   'md_run_name' 'bw0' stage-0, start of test
;           'md_run_name' 'bw1' stage-1, test complete
;
; INPUT(Fish): et2_knxfac, et2_knyfac
;              et2_wsxx_req, et2_wsyy_req, et2_ws_tol
;              p_vel, p_cyc, p_stages
;              md_granular, et2_peakfac, et2_wexx_lim
;              pk_ci_fac
;
; Adelaide University.
; =====
SET echo off ; load support functions
  call %itascaFishTank%\FishPfc\md\fishcall.FIS
  call %itascaFishTank%\FishPfc\md\crk.FIS
SET echo on
; =====
; Specify in calling routine:
; SET et2_knxfac= et2_knyfac=
et2_wallstiff
;
; Specify in calling routine:
; SET et2_wsxx_req= et2_wsyy_req= et2_ws_tol= p_vel=
ini xvel 0.0 yvel 0.0 spin 0.0
  SET fishcall #FC_CYC_MOT et2_servo
  SET et2_servo_xon=1 et2_servo_yon=1
  SET et2_servo_gain_cyc=100 et2_servo_vmax=@p_vel
et2_install_ws
solve ; do it 3 times to assure we are near equil.
et2_install_ws
solve
et2_install_ws
;
et2_sample_dimensions
crk_init
; =====
; Install test monitoring variables and histories
;
history reset
history nstep=20
history id=1 crk_num
history id=50 crk_num_cnf
history id=51 crk_num_csf
history id=52 crk_num_pnf
history id=53 crk_num_psf
;
history id=2 et2_wexx ; wall-derived stresses & strains
history id=3 et2_weyy
history id=4 et2_wsxx
history id=5 et2_wsyy
history id=6 et2_wevol
history id=7 et2_wsm
history id=8 et2_wsd
history id=102 et2_mexx ; averaged stresses & strains
history id=103 et2_meyy ; from 3 measurement circles
```

```

history id=104 et2_msxx
history id=105 et2_msyy
history id=106 et2_mevol
history id=107 et2_msm
history id=108 et2_msd
;
trace energy on ; energy quantities
history id=15 energy boundary
history id=16 energy bond
history id=17 energy frictional
history id=18 energy kinetic
history id=19 energy strain
history id=23 et2_e_delstrain ; increment of strain energy
;
history id=20 et2_n ; wall-derived microstructural quantities
history id=21 et2_e
history id=22 et2_phy_e ; physical void ratio
;
et2_plotviews
prop xdisp=0.0 ydisp=0.0
  SET md_tag_name = '-bw0'
md_save_state
; =====
; Perform the entire test.
; Specify in calling routine:
; SET p_vel= p_cyc= p_stages=
; SET md_granular= et2_peakfac= et2_wexx_lim=
  SET p_close=1 ; load
  SET et2_servo_yon=0
plot hist -5 vs -3
et2_accel_platens
pause
;
;$$$$$$$$$ Here define No. of cycles, e.g. 'cyc 10000'.
;$$$$$$$$$ Monitor the stress-strain curve. If needed
;$$$$$$$$$ add more cycles, e.g. 'cyc 5000' until it is
;$$$$$$$$$ obvious the model fails. Then type 'continue'.
;
et2_gd_biax
;
  SET md_tag_name='-bw1'
md_save_state
; =====
return
; END OF Filename: _btw2.DVR

```

---

Now the uniaxial compressive test could be initiated:

```
[call %itascaFishTank%\FishPFC2\Drivers\Specimen\spc3_bx.DVR]
```

When the run paused, the number of cycles was entered:

```
[cyc 17500]
```

Upon completion of the cycling, the run was allowed to continue to enable the save command:

```
[continue]
```

By now the test was fully completed and the whole process saved as:

```
C:\Itasca\Pfc\Pfc2d\ spc3_00-bw1.sav
```

The stress-strain behaviour of the model is shown in Figure 5.12.

This state can be restored at any time by the command:

```
[rest spc3_00-bw1]
```

The process of execution of all driver files was continually written into a log file. Hence, upon completion of the test, many important parameters could be obtained, such as UCS, elastic modulus, crack initiation stress, number of microcracks formed, etc. The log file of the intact rock model is presented below.

*Code A2.5. Log file: intact rock model.*

---

```
***** Biaxial-test results follow. . .
      md_run_name = spc3_00
      md_numballs = 2505
      Confinement: et2_wsxx_req = -1.000000000000e+005
E (plane stress) = 1.44245766570e+010
nu (plane stress) = 2.13352832879e-001
E (plane strain) = 1.39785860762e+010
nu (plane strain) = 1.75837420986e-001
Fish>   print pk_syy
pk_syy = -8.512257641615e+007
Fish>   print pk_crk_num
pk_crk_num = 2.790000000000e+002
Fish>   print pk_crk_num_cnf, pk_crk_num_csf
pk_crk_num_cnf = 5.800000000000e+001
pk_crk_num_csf = 2.210000000000e+002
Fish>   print pk_crk_num_pnf, pk_crk_num_psf
pk_crk_num_pnf = 0.000000000000e+000
pk_crk_num_psf = 0.000000000000e+000
Fish>   print pk_ci_fac, pk_syy_ci
pk_ci_fac = 2.000000000000e-002
pk_syy_ci = -1.150278598369e+007
Pfc2D>;
Pfc2D> SET md_tag_name='-bw1'
Pfc2D>md_save_state
Fish>   save @_fname
Pfc2D>; =====
Pfc2D>return
Pfc2D>; -----
Pfc2D>set log off
*****
* Log File Ended 20:25:18 Thu Jun 27 2002
*****
*****
```

---

From the results one can see that the Young's modulus is 14.3 GPa and the Poisson's ratio is 0.21. If the model does not closely correspond to the deformability and strength properties of the physical original, the microparameters need to be readjusted (refer to Section 3.5 of the '*FISH in PFC*').

Visualisation of a possible pattern of the specimen failure was obtained by superimposing the view of microcracks developed in the model at failure on the view of displacements of particles:

```
[plot show 1]
[plot cur 1]
[plot sub 3]
[plot sub 1]
[plot add fish crk_item]
[plot add disp]
```

The plots are presented in Figure 5.13.

This finalises the creation of the intact rock model.

The fine-grained model was created by changing the smallest particle diameter from 0.8 mm to 0.5 mm. The ball size ratio was left unchanged,  $et2\_radius\_ratio=1.5$  (refer to Table A2-1).

*Code A2.6. Fine-grained model genesis driver.*

---

```
; Filename: spc3f.DVR
;
; PURPOSE: Create the fine grained sandstone: numerical replica
;         of the physical Specimen #3.
;
; INPUT:   none
; OUTPUT:  'md_run_name' 'spc' final specimen (bonded)
;
; Adelaide University.
; =====
new
set safe_conversion on
SET random ; for reproducibility
SET disk on ; model unit-thickness cylinders
;
SET echo off ; load support functions
call %itascaFishTank%\FishPfc\md\md.FIS
call %itascaFishTank%\FishPfc2\et2\et2.FIS
call %itascaFishTank%\FishPfc\md\flt.FIS
SET echo on
; =====
SET md_run_name = 'spc3f'
title 'Specimen #3'
; =====
; Specify parameters that control the specimen-genesis procedures
;
SET et2_xlen=61.14e-3 et2_ylen=153.32e-3
SET et2_radius_ratio=1.5 et2_rlo=0.5e-3 ;minimum ball size reduced
;
SET md_wEcfac=1.1
SET tm_req_isostr=-1.0e6 tm_req_isostr_tol=0.50
SET flt_def=3 flt_remain=0.0
;
; Specify parameters that define a contact-bonded material
;
```

```

SET md_add_cbonds=1
SET md_dens=2397
SET md_Ec=20e9 md_knoverks=1.8
SET md_fric=0.50
SET cb_sn_mean=82e6 cb_sn_sdev=30e6
SET cb_ss_mean=82e6 cb_ss_sdev=30e6
;
SET et2_prep_saveall=1
et2_prep ; invoke the specimen-genesis procedures
; =====
return
; END OF Filename: spc3f.DVR

```

---

Results of the uniaxial compressive test on the fine-grained model are presented in the log file below.

*Code A2.6. Log file: fine-grained model.*

---

```

***** Biaxial-test results follow. . .
      md_run_name = spc3f_00
      md_numballs = 6415
      Confinement: et2_wsxx_req = -1.000000000000e+005
E (plane stress) = 1.50871673341e+010
nu (plane stress) = 2.10528359346e-001
E (plane strain) = 1.46308373743e+010
nu (plane strain) = 1.73914438039e-001
Fish> print pk_syy
pk_syy = -8.823279327479e+007
Fish> print pk_crk_num
pk_crk_num = 9.230000000000e+002
Fish> print pk_crk_num_cnf, pk_crk_num_csf
pk_crk_num_cnf = 2.250000000000e+002
pk_crk_num_csf = 6.980000000000e+002
Fish> print pk_crk_num_pnf, pk_crk_num_psf
pk_crk_num_pnf = 0.000000000000e+000
pk_crk_num_psf = 0.000000000000e+000
Fish> print pk_ci_fac, pk_syy_ci
pk_ci_fac = 2.000000000000e-002
pk_syy_ci = -1.209804584003e+007
Pfc2D>;
Pfc2D> SET md_tag_name='-bwl'
Pfc2D>md_save_state
Fish> save @_fname
Pfc2D>; =====
Pfc2D>return
Pfc2D>; -----
Pfc2D>set log off
*****
* Log File Ended 06:44:15 Mon Oct 20 2003
*****

```

---

The next model to generate was a complex lithology specimen consisted of two materials of different bond strength. Contact bonds in the top and bottom parts of the sample were left

unchanged, whereas the middle section was assigned weaker value ( $n\_bond=8e4$ ,  $s\_bond=8e4$ ), refer to Figure 5.18. The coefficient of friction was also reduced ( $fric=0.2$ ).

*Code A2.7. Complex lithology model genesis driver.*

---

```
; Filename: spc3t.DVR
;
; PURPOSE: Create the coarse grained sandstone with varying lithology.
;         Referred to as "complex lithology model"
;
; Adelaide University.
;=====
rest spc3-spc                ; restoring Specimen #3 model
; Changing lithology:
group L1 range x= -30.57e-3, 30.57e-3 y= -38.33e-3, 38.33e-3
group L2 range group L1 not
    property n_bond=8e4 s_bond=8e4 fric=0.2 range group L1
plot create litho
plot add ball range group L2 yellow
plot add ball range group L1 cyan
plot add wall
save spc3t-spc.SAV
    ;litho model created and saved
return
; EOF: spc3t.DVR
```

---

Results of the uniaxial compressive test on the complex lithology model are presented in the log file below.

*Code A2.8. Log file: complex lithology model.*

---

```
***** Biaxial-test results follow. . .
md_run_name = spc3t_00
md_numballs = 2505
Confinement: et2_wsxx_req = -1.000000000000e+005
E (plane stress) = 1.44671399698e+010
nu (plane stress) = 2.05311454740e-001
E (plane strain) = 1.40473708604e+010
nu (plane strain) = 1.70338922718e-001
Fish> print pk_syy
pk_syy = -5.679479406243e+007
Fish> print pk_crk_num
pk_crk_num = 1.130000000000e+002
Fish> print pk_crk_num_cnf, pk_crk_num_csf
pk_crk_num_cnf = 2.800000000000e+001
pk_crk_num_csf = 8.500000000000e+001
Fish> print pk_crk_num_pnf, pk_crk_num_psf
pk_crk_num_pnf = 0.000000000000e+000
pk_crk_num_psf = 0.000000000000e+000
Fish> print pk_ci_fac, pk_syy_ci
pk_ci_fac = 2.000000000000e-002
pk_syy_ci = -6.557557447651e+006
Pfc2D>;
Pfc2D> SET md_tag_name='-bw1'
```

```

Pfc2D>md_save_state
Fish>   save @_fname
Pfc2D>; =====
Pfc2D>return
Pfc2D>; -----
Pfc2D>set log off
*****
* Log File Ended 11:35:51 Sun Dec  7 2003
*****

```

---

The discontinuous rock model was created by introduction of two joint sets into the intact rock model. The driver is presented below. As can be seen, the contact bond strength was reduced significantly compared to the ‘intact rock’ inter-particle bond: from 82MPa to 0.01MPa. Coefficient of friction of the balls connected by joint-plane contacts along joint-plane was assigned lower value (fric=0.1), as compared to 0.5 for the intact rock model.

*Code A2.9. Discontinuous rock model genesis driver.*

---

```

; Filename: spc3j.DVR
;
; PURPOSE: Create the coarse grained sandstone with joint sets.
;         Referred to as 'Specimen with joints'.
;
; Adelaide University.
;=====
rest spc3-spc                ; restoring Specimen #3 model
; Adding joint sets:
JSET id=1 dip=40  origin=(0,10e-3) number=3 spacing=45e-3
JSET id=2 dip=-20 origin=(0,0)
  property n_bond=1e4 s_bond=1e4 fric=0.1 range jset=1,2
plot create j_sets
plot add cluster blue cyan lgray lorange white lgreen yellow
save spc3j-spc.SAV
      ;jointed model created and saved
return
; EOF:  spc3j.DVR

```

---

Results of the uniaxial compressive test on the discontinuous rock model are presented in the log file below.

*Code A2.10. Log file: discontinuous rock model.*

---

```

***** Biaxial-test results follow. . .
md_run_name = spc3j_00
md_numballs = 2505
  Confinement: et2_wsxx_req = -1.000000000000e+005
E (plane stress) = 1.28057192930e+010
nu (plane stress) = 4.20272138962e-001
E (plane strain) = 1.16844187229e+010

```

```

nu (plane strain) = 2.95909584813e-001
Fish> print pk_syy
pk_syy = -4.272105997380e+007
Fish> print pk_crk_num
pk_crk_num = 2.310000000000e+002
Fish> print pk_crk_num_cnf, pk_crk_num_csf
pk_crk_num_cnf = 5.400000000000e+001
pk_crk_num_csf = 1.770000000000e+002
Fish> print pk_crk_num_pnf, pk_crk_num_psf
pk_crk_num_pnf = 0.000000000000e+000
pk_crk_num_psf = 0.000000000000e+000
Fish> print pk_ci_fac, pk_syy_ci
pk_ci_fac = 2.000000000000e-002
pk_syy_ci = -6.449773898507e+006
Pfc2D>;
Pfc2D> SET md_tag_name='-bw1'
Pfc2D>md_save_state
Fish> save @_fname
Pfc2D>; =====
Pfc2D>return
Pfc2D>; -----
Pfc2D>set log off
*****
* Log File Ended 08:26:13 Mon Dec 16 2002
*****

```

---

### A2.3 Cyclic test subroutines: all models

Subroutines in this section describe cyclic (LRR) tests to reveal the DME.

To investigate the DME on the intact rock model, four driver files were created for four different pre-load values. Table A2.4 presents number of cycles required for the completion of the test. The LRR tests start from calling the driver file:

```

[call %itascaFishTank%\FishPFC2\Drivers\Specimen\spc3_bx06.DVR]
[call %itascaFishTank%\FishPFC2\Drivers\Specimen\spc3_bx15.DVR]
[call %itascaFishTank%\FishPFC2\Drivers\Specimen\spc3_bx35.DVR]
[call %itascaFishTank%\FishPFC2\Drivers\Specimen\spc3_bx54.DVR]

```

Similar to the biaxial compressive test driver (Code A2.3), this file also calls the driver `_btw2.DVR`, which does not have to be further modified. Once the test execution pauses, a certain number of cycles have to be entered in the command line. These cycles are listed in Table A2.4 for each LRR test. The first set of cycles executes pre-loading stage, the second set controls unloading, then successively 1<sup>st</sup> reloading, unloading and 2<sup>nd</sup> reloading. The whole process can be monitored in an animated stress-strain history window. The command sequence for the test

run is presented below (as an example, for the 15.4 MPa pre-load). After a running process has paused:

```
[cyc 1940]
[set p_close=0]
[et2_accel_platens]
[cyc 1800]
[set p_close=1]
[et2_accel_platens]
[cyc 3500]
[set p_close=0]
[et2_accel_platens]
[cyc 3400]
[set p_close=1]
[et2_accel_platens]
[cyc 3500]
[continue]
```

By now a typical LRR test has been completed. It can be restored any type by typing:

```
[rest spc3_00_15-bw1] – this is the state of the completed test.
```

Another state of the test can also be restored: the status just before cycling. In this case the restoration command is as follows:

```
[rest spc3_00_15-bw0]
```

Table A2.4. Input data for LRR tests.

Pre-load value, MPa	6.0 (elastic region)	15.4	35.9	54.7
File name	spc3_bx06.dvr	spc3_bx15.dvr	spc3_bx35.dvr	spc3_bx54.dvr
No. of cycles				
Pre-load	420	1940	5280	8220
Unload	400	1800	5000	8000
1 <sup>st</sup> Reload	1000	3500	8000	12000
Unload	1000	3400	8000	11500
2 <sup>nd</sup> Reload	1040	3500	8150	11500
Total No. of cycles at the pre-load stress	17600	19120	22460	25400
Total No. of cycles for each reload curve (at the start – at the end):				
1 <sup>st</sup> curve	19500 – 20800	22500 – 26200	30000 – 37300	35500 – 47000
2 <sup>nd</sup> curve	23500 – 25000	31200 – 35300	48000 – 55500	61000 – 72500
Saved test file	spc3_00_06- bw1.sav	spc3_00_15- bw1.sav	spc3_00_35- bw1.sav	spc3_00_54- bw1.sav

Codes A2.11 to A2.14 are the drivers implementing the LRR tests at pre-loads listed in Table A2.4.

Code A2.11. LRR test: intact rock model. Pre-load 6.0 MPa.

---

```

; fname: spc3_bx06.DVR Cyclic test on Specimen #3.
;           Pre-load=6MPa (elastic region).
;
; PURPOSE: 1) restore spc3 specimen,
;           2) perform uniaxial test upon it
;           (variation of biaxial under confining stress of Pc=0.1 MPa)
; Adelaide University.
; =====
set logfile spc3_bx06.log
set log on
; -----
; Execute biaxial test at Pc=0.1 MPa
restore spc3-spc.SAV
set safe_conversion on
SET md_run_name='spc3_00_06'
title 'spc3_00_06. Specimen #3. Pre-load=6.0 MPa'
SET et2_knxfac=0.001 et2_knyfac=1.0
SET et2_wsxx_req=-1.0e5 et2_wsyy_req=-1.0e5 et2_ws_tol=0.01
SET p_vel=2.0e-1 p_cyc=1000 p_stages=20
call %itascaFishTank%\FishPfc2\et2\_btw2.DVR ;=> spc3_00_06-{bw0,bw1}.SAV
; -----
set log off
return
; EOF: spc3_bx06.DVR

```

---

*Code A2.12. LRR test: intact rock model. Pre-load 15.4MPa.*

---

```
; fname: spc3_bx15.DVR  Cyclic test on Specimen #3.
;                               Pre-load=15.4MPa (anelastic region).
;
; PURPOSE: 1) restore spc3 specimen,
;           2) perform uniaxial test upon it
;           (variation of biaxial under confining stress of
;           Pc=0.1 MPa)
; Adelaide University.
; =====
set logfile spc3_bx15.log
set log on
; -----
; Execute biaxial test at Pc=0.1 MPa
restore spc3-spc.SAV
set safe_conversion on
SET md_run_name='spc3_00_15'
title 'spc3_00_15. Specimen #3. Pre-load=15.4MPa'
SET et2_knxfac=0.001  et2_knyfac=1.0
SET et2_wsxx_req=-1.0e5 et2_wsyy_req=-1.0e5 et2_ws_tol=0.01
SET p_vel=2.0e-1  p_cyc=1000  p_stages=20
call %itascaFishTank%\FishPfc2\et2\_btw2.DVR  ;=> spc3_00_15-{bw0,bw1}.SAV
; -----
set log off
return
; EOF: spc3_bx15.DVR
```

---

*Code A2.13. LRR test: intact rock model. Pre-load 35.9 MPa..*

---

```
; fname: spc3_bx35.DVR  Cyclic test on Specimen #3.
;                               Pre-load=35.9MPa (anelastic region).
; PURPOSE: 1) restore spc3 specimen,
;           2) perform uniaxial test upon it
;           (variation of biaxial under confining stress of Pc=0.1 MPa)
; Adelaide University.
; =====
set logfile spc3_bx35.log
set log on
; -----
; Execute biaxial test at Pc=0.1 MPa
restore spc3-spc.SAV
set safe_conversion on
SET md_run_name='spc3_00_35'
title 'spc3_00_35. Specimen #3. Pre-load=35.9MPa'
SET et2_knxfac=0.001  et2_knyfac=1.0
SET et2_wsxx_req=-1.0e5 et2_wsyy_req=-1.0e5 et2_ws_tol=0.01
SET p_vel=2.0e-1  p_cyc=1000  p_stages=20
call %itascaFishTank%\FishPfc2\et2\_btw2.DVR  ;=> spc3_00_35-{bw0,bw1}.SAV
; -----
set log off
return
; EOF: spc3_bx35.DVR
```

---

```
; fname: spc3_bx54.DVR  Cyclic test on Specimen #3.
;                               Pre-load=54.7MPa (anelastic region).
; PURPOSE: 1) restore spc3 specimen,
;           2) perform uniaxial test upon it
;           (variation of biaxial under confining stress of Pc=0.1 MPa)
; Adelaide University.
; =====
set logfile spc3_bx54.log
set log on
; -----
; Execute biaxial test at Pc=0.1 MPa
restore spc3-spc.SAV
set safe_conversion on
SET md_run_name='spc3_00_54'
title 'spc3_00_54. Specimen #3. Pre-load=54.7MPa'
SET et2_knxfac=0.001  et2_knyfac=1.0
SET et2_wsxx_req=-1.0e5  et2_wsyy_req=-1.0e5  et2_ws_tol=0.01
SET p_vel=2.0e-1  p_cyc=1000  p_stages=20
call %itascaFishTank%\FishPfc2\et2\_btw2.DVR  ;=> spc3_00_54-{bw0,bw1}.SAV
; -----
set log off
return
; EOF: spc3_bx54.DVR
```

---

The resulting strain-stress diagrams of all four tests are presented in Figures 5.24-5.27. These plots can be generated any time by typing:

```
[plot hist -5 vs -3]
```

The microcrack snapshots taken at the pre-load and at the completion of each test were obtained by the following steps:

1. The file frag1.DVR located in the folder C:\Itasca\Pfc\pfc2d\Fish\Fishtank was modified and saved as:

C:\Itasca\Pfc\FisT\_04c\FishPFC2\Drivers\Specimen\frag1\_m.DVR.

*FISH* variable *crk\_fil\_cyc\_max* had to be assigned the value in accordance with ‘Total No. of cycles at the pre-load stress’ obtained from Table A2.4. As an example, the microcrack snapshot driver for the 15.4 MPa pre-load is presented below (Code A2.15). For other pre-loads the driver was modified accordingly.

```
;fname: frag1_m.DVR  ====Example for the pre-load 15.4 MPa====
crk_fil_reset
SET crk_fil_cyc_min=0  crk_fil_cyc_max=19120
crk_fil_cyc_interval
crk_makeview
```

```
plot show
plot cur 5
plot add wall black
plot set capt size 18
;EOF: frag1_m.DVR
```

---

2. The following commands were entered into the command line:

```
[set crk_icon=1]
[call %itascaFishTank%\FishPFC2\Drivers\Specimen\frag1_m.DVR]
```

3. Now the microcrack snapshot could be printed. The other snapshots were obtained similarly.

DRA plots illustrating the DME are presented in Figure 5.28. The plots were obtained by the following sequence of steps (example for the pre-load of 15.4 MPa):

1. First it was necessary to transfer the data of stress-strain histories, recorded during the 1<sup>st</sup> and 2<sup>nd</sup> reloading cycles into text files:

```
[rest spc3_00_15-bw1] – if the state of the completed test has not yet been restored
```

```
[hist write -5 vs -3 begin 22500 end 25900 file spc3_15MPa1.HIS] – No. of cycles was
obtained from Table A2.4.
```

```
[hist write -5 vs -3 begin 31200 end 35300 file spc3_15MPa2.HIS]
```

2. The history files were saved in the folder: C:\Itasca\Pfc\pfc2d.

3. The HIS files were opened in MS Excel as delimited by space data CSV files.

4. Next the strain values of the 1<sup>st</sup> reloading cycle were subtracted from the values of the 2<sup>nd</sup> reloading cycle according to Eq. 2.1, Chapter 2.

5. Graph ‘Differential strain vs. axial stress’ was created in Excel.

Plots of histories of cumulative number of microcracks and friction energy (Figures 5.29 and 5.30) were obtained by execution of the following commands (example for the 15.4 MPa pre-load):

```
[plot hist 1 vs -5 begin 22500 end 26200] – cumulative number of microcracks
```

```
[plot hist 17 begin 22500 end 26200] – frictional energy
```

Not only these two, but any history recorded during the test run can also be explored. Total list of all histories tracked by the code can be obtained by the command:

```
[print hist]
```

LRR tests for other models were done similar to the processes described for the intact rock model.

## A2.4 Effect of joint orientation

Codes A2.16 to A2.39 describe creation and uniaxial testing of a number of models with a single joint dipping at a varying angle.

*Code A2.16. Model with single joint at dip=00. Specimen genesis driver.*

---

```
; Filename: spc3j-00d.DVR
;
; PURPOSE: Create the coarse grained sandstone with single joint.
;         Dip=00deg.
;
; Adelaide University.
;=====
rest spc3-spc           ; restoring Specimen #3 model
                        ; Adding joint:
JSET id=1 dip=00 origin=(0,0)
  property n_bond=1e4 s_bond=1e4 fric=0.0 range jset=1
plot create j_sets
plot add cluster blue cyan
save spc3j-00d-spc.SAV           ; jointed model created and saved
return
; EOF:  spc3j-00d.DVR
```

---

*Code A2.17. Model with single joint at dip=00. UCS and LRR tests driver.*

---

```
; fname: spc3j-00d_bx.DVR Uniaxial test on with single joint. Dip=00deg.
;         Load to failure.
;
; PURPOSE: 1) restore spc3j-00d specimen,
;          2) perform uniaxial test upon it
;          (variation of biaxial under confining stress of Pc=0.1 MPa)
;
; Adelaide University.
;=====
set logfile spc3j-00d_bx.log
set log on
; -----
; Execute biaxial test at Pc=0.1 MPa
restore spc3j-00d-spc.SAV
set safe_conversion on
SET md_run_name='spc3j-00d_00'
title 'spc3j-00d_00. Single joint at dip=00deg.'
SET et2_knxfac=0.001 et2_knyfac=1.0
SET et2_wsxx_req=-1.0e5 et2_wsyy_req=-1.0e5 et2_ws_tol=0.01
SET p_vel=2.0e-1 p_cyc=1000 p_stages=20
call %itascaFishTank%\FishPfc2\et2\_btw2.DVR  ;=> spc3j-00d_00-{bw0,bw1}.SAV
; -----
set log off
return
; EOF:  spc3j-00d_bx.DVR
```

---

```
***** Biaxial-test results follow. . .
      md_run_name = spc3j-00d_00
      md_numballs = 2505
      Confinement: et2_wsxx_req = -1.000000000000e+005
E (plane stress) = 1.42240760922e+010
nu (plane stress) = 2.34472620160e-001
E (plane strain) = 1.37109248127e+010
nu (plane strain) = 1.89937481262e-001
Fish>   print pk_syy
pk_syy = -8.552325354950e+007
Fish>   print pk_crk_num
pk_crk_num = 3.270000000000e+002
Fish>   print pk_crk_num_cnf, pk_crk_num_csf
pk_crk_num_cnf = 6.500000000000e+001
pk_crk_num_csf = 2.620000000000e+002
Fish>   print pk_crk_num_pnf, pk_crk_num_psf
pk_crk_num_pnf = 0.000000000000e+000
pk_crk_num_psf = 0.000000000000e+000
Fish>   print pk_ci_fac, pk_syy_ci
pk_ci_fac = 2.000000000000e-002
pk_syy_ci = -1.137771414610e+007
Pfc2D>;
Pfc2D> SET md_tag_name='-bw1'
Pfc2D>md_save_state
Fish>   save @_fname
Pfc2D>; =====
Pfc2D>return
Pfc2D>; -----
Pfc2D>set log off
*****
* Log File Ended 17:23:35 Fri Oct  1 2004
*****
```

---

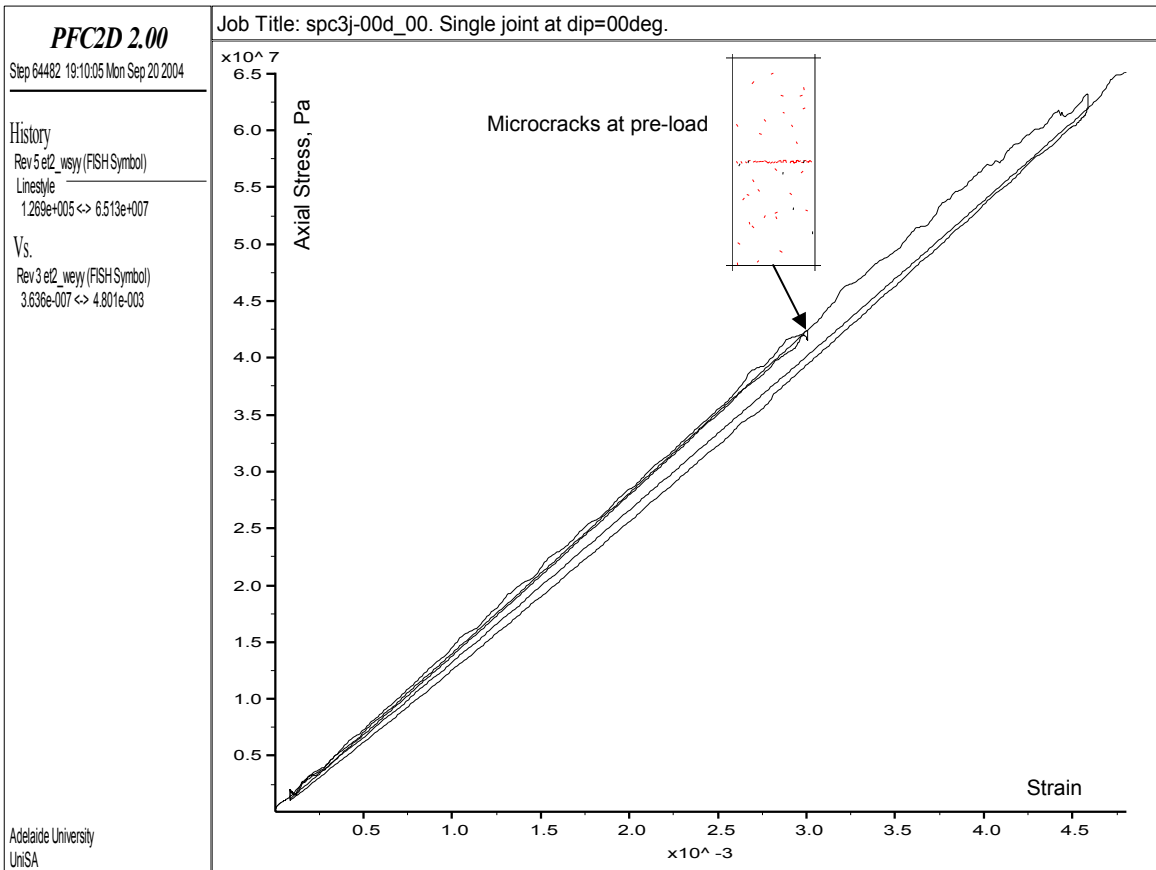


Figure A2.2. LRR test on model with single joint at dip=00.

Code A2.19. Model with single joint at dip=15. Specimen genesis driver.

```

; Filename: spc3j-15d.DVR
;
; PURPOSE: Create the coarse grained sandstone with single joint.
;         Dip=15deg.
;
; Adelaide University.
;=====
rest spc3-spc           ; restoring Specimen #3 model
                       ; Adding joint:
JSET id=1 dip=15 origin=(0,0)
  property n_bond=1e4 s_bond=1e4 fric=0.25 range jset=1
plot create j_sets
plot add cluster blue cyan
save spc3j-15d-spc.SAV           ; jointed model created and saved
return
; EOF: spc3j-15d.DVR

```

Code A2.20. Model with single joint at dip=15. UCS and LRR tests driver.

```

; fname: spc3j-15d_bx.DVR Uniaxial test on with single joint. Dip=15deg.
;
;         Load to failure.
;
; PURPOSE: 1) restore spc3j-15d specimen,

```

```

;          2) perform uniaxial test upon it
;          (variation of biaxial under confining stress of Pc=0.1 MPa)
;
; Adelaide University.
; =====
set logfile spc3j-15d_bx.log
set log on
; -----
; Execute biaxial test at Pc=0.1 MPa
restore spc3j-15d-spc.SAV
set safe_conversion on
SET md_run_name='spc3j-15d_00'
title 'spc3j-15d_00. Single joint at dip=15deg.'
SET et2_knxfac=0.001 et2_knyfac=1.0
SET et2_wsxx_req=-1.0e5 et2_wsyy_req=-1.0e5 et2_ws_tol=0.01
SET p_vel=2.0e-1 p_cyc=1000 p_stages=20
call %itascaFishTank%\FishPfc2\et2\_btw2.DVR ;=> spc3j-15d_00-{bw0,bw1}.SAV
; -----
set log off
return
; EOF: spc3j-15d_bx.DVR

```

---

*Code A2.21. Log file: model with single joint at dip=15.*

---

```

***** Biaxial-test results follow. . .
      md_run_name = spc3j-15d_00
      md_numballs = 2505
      Confinement: et2_wsxx_req = -1.00000000000e+005
E (plane stress) = 1.43062908826e+010
nu (plane stress) = 2.22703602583e-001
E (plane strain) = 1.38316784041e+010
nu (plane strain) = 1.82140301307e-001
Fish> print pk_syy
pk_syy = -8.529392068331e+007
Fish> print pk_crk_num
pk_crk_num = 2.880000000000e+002
Fish> print pk_crk_num_cnf, pk_crk_num_csf
pk_crk_num_cnf = 5.000000000000e+001
pk_crk_num_csf = 2.380000000000e+002
Fish> print pk_crk_num_pnf, pk_crk_num_psf
pk_crk_num_pnf = 0.000000000000e+000
pk_crk_num_psf = 0.000000000000e+000
Fish> print pk_ci_fac, pk_syy_ci
pk_ci_fac = 2.000000000000e-002
pk_syy_ci = -7.235726341198e+006
Pfc2D>;
Pfc2D> SET md_tag_name='-bw1'
Pfc2D>md_save_state
Fish> save @_fname
Pfc2D>; =====
Pfc2D>return
Pfc2D>; -----
Pfc2D>set log off
*****
* Log File Ended 19:50:21 Fri Oct 1 2004
*****

```

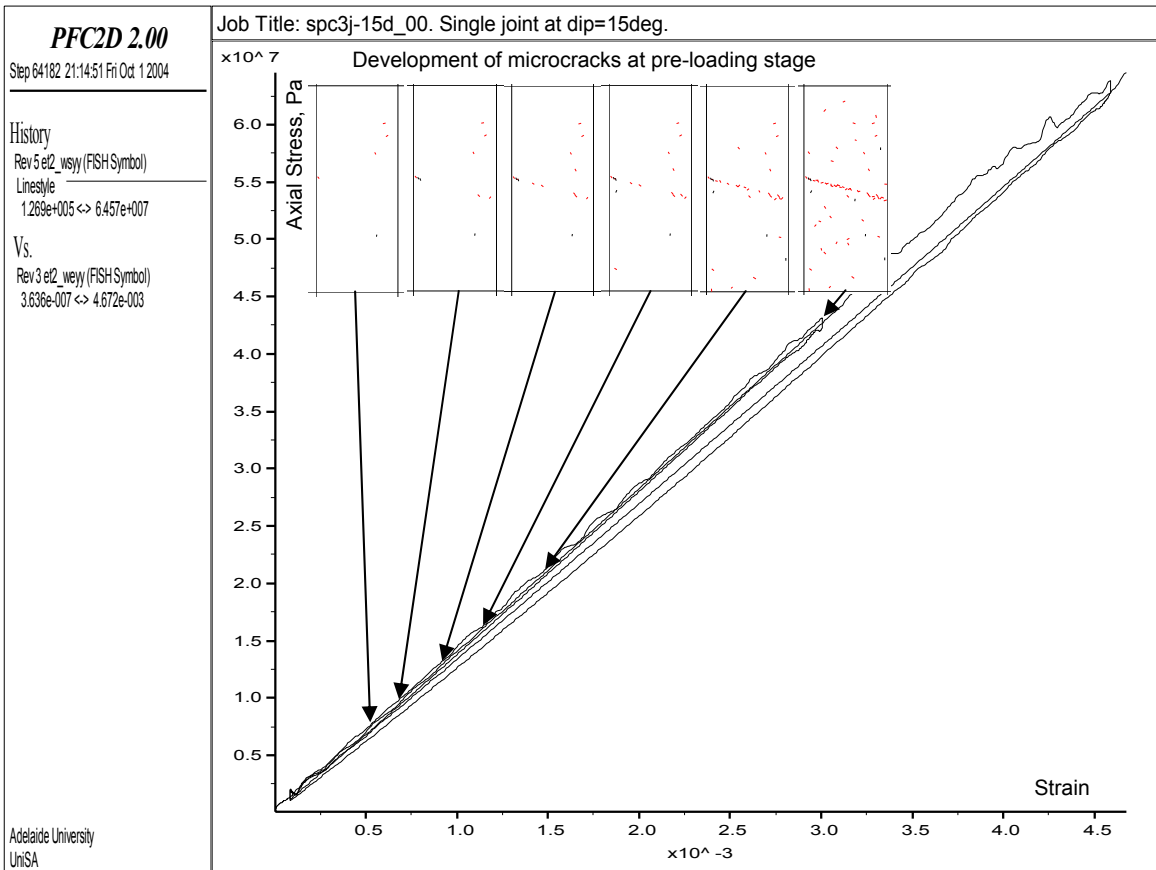


Figure A2.3. LRR test on model with single joint at dip=15.

Code A2.22. Model with single joint at dip=30. Specimen genesis driver.

```

; Filename: spc3j-30d.DVR
;
; PURPOSE: Create the coarse grained sandstone with single joint.
;         Dip=30deg.
;
; Adelaide University.
;=====
rest spc3-spc           ; restoring Specimen #3 model
                       ; Adding joint:
JSET id=1 dip=30 origin=(0,0)
  property n_bond=1e4 s_bond=1e4 fric=0.25 range jset=1
plot create j_sets
plot add cluster blue cyan
save spc3j-30d-spc.SAV           ; jointed model created and saved
return
; EOF: spc3j-30d.DVR

```

Code A2.23. Model with single joint at dip=30. UCS and LRR tests driver.

```

; fname: spc3j-30d_bx.DVR Uniaxial test on with single joint. Dip=30deg.
;
;         Load to failure.
;
; PURPOSE: 1) restore spc3j-30d specimen,

```

```

;          2) perform uniaxial test upon it
;          (variation of biaxial under confining stress of Pc=0.1 MPa)
;
; Adelaide University.
; =====
set logfile spc3j-30d_bx.log
set log on
; -----
; Execute biaxial test at Pc=0.1 MPa
restore spc3j-30d-spc.SAV
set safe_conversion on
SET md_run_name='spc3j-30d_00'
title 'spc3j-30d_00. Single joint at dip=30deg.'
SET et2_knxfac=0.001 et2_knyfac=1.0
SET et2_wsxx_req=-1.0e5 et2_wsyy_req=-1.0e5 et2_ws_tol=0.01
SET p_vel=2.0e-1 p_cyc=1000 p_stages=20
call %itascaFishTank%\FishPfc2\et2\_btw2.DVR ;=> spc3j-30d_00-{bw0,bw1}.SAV
; -----
set log off
return
; EOF: spc3j-30d_bx.DVR

```

---

*Code A2.24. Log file: model with single joint at dip=30.*

---

```

***** Biaxial-test results follow. . .
      md_run_name = spc3j-30d_00
      md_numballs = 2505
      Confinement: et2_wsxx_req = -1.00000000000e+005
E (plane stress) = 1.43487647034e+010
nu (plane stress) = 2.25633000487e-001
E (plane strain) = 1.38624707613e+010
nu (plane strain) = 1.84095076093e-001
Fish> print pk_syy
pk_syy = -8.336505763899e+007
Fish> print pk_crk_num
pk_crk_num = 3.20000000000e+002
Fish> print pk_crk_num_cnf, pk_crk_num_csf
pk_crk_num_cnf = 6.50000000000e+001
pk_crk_num_csf = 2.55000000000e+002
Fish> print pk_crk_num_pnf, pk_crk_num_psf
pk_crk_num_pnf = 0.00000000000e+000
pk_crk_num_psf = 0.00000000000e+000
Fish> print pk_ci_fac, pk_syy_ci
pk_ci_fac = 2.00000000000e-002
pk_syy_ci = -1.150497210065e+007
Pfc2D>;
Pfc2D> SET md_tag_name='-bw1'
Pfc2D>md_save_state
Fish> save @_fname
Pfc2D>; =====
Pfc2D>return
Pfc2D>; -----
Pfc2D>set log off
*****
* Log File Ended 16:44:58 Sat Oct 2 2004
*****

```

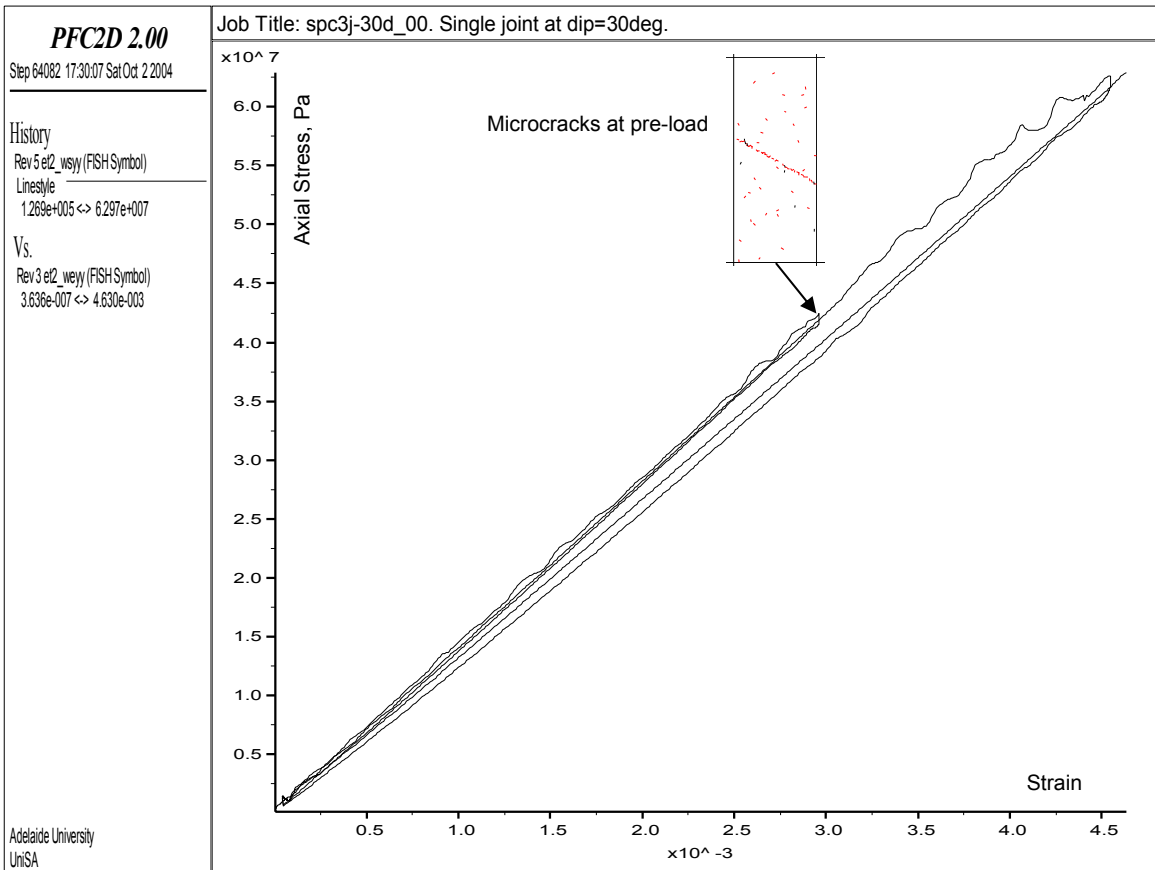


Figure A2.4. LRR test on model with single joint at dip=30.

Code A2.25. Model with single joint at dip=45. Specimen genesis driver.

```

; Filename: spc3j-45d.DVR
;
; PURPOSE: Create the coarse grained sandstone with single joint.
;         Dip=45deg.
;
; Adelaide University.
;=====
rest spc3-spc           ; restoring Specimen #3 model
                       ; Adding joint:
JSET id=1 dip=45 origin=(0,0)
  property n_bond=1e4 s_bond=1e4 fric=0.25 range jset=1
plot create j_sets
plot add cluster blue cyan
save spc3j-45d-spc.SAV           ; jointed model created and saved
return
; EOF: spc3j-45d.DVR

```

Code A2.26. Model with single joint at dip=45. UCS and LRR tests driver.

```

; fname: spc3j-45d_bx.DVR Uniaxial test on with single joint. Dip=45deg.
;
;         Load to failure.
;
; PURPOSE: 1) restore spc3j-45d specimen,

```

```

;          2) perform uniaxial test upon it
;          (variation of biaxial under confining stress of Pc=0.1 MPa)
;
; Adelaide University.
; =====
set logfile spc3j-45d_bx.log
set log on
; -----
; Execute biaxial test at Pc=0.1 MPa
restore spc3j-45d-spc.SAV
set safe_conversion on
SET md_run_name='spc3j-45d_00'
title 'spc3j-45d_00. Single joint at dip=45deg.'
SET et2_knxfac=0.001 et2_knyfac=1.0
SET et2_wsxx_req=-1.0e5 et2_wsyy_req=-1.0e5 et2_ws_tol=0.01
SET p_vel=2.0e-1 p_cyc=1000 p_stages=20
call %itascaFishTank%\FishPfc2\et2\_btw2.DVR ;=> spc3j-45d_00-{bw0,bw1}.SAV
; -----
set log off
return
; EOF: spc3j-45d_bx.DVR

```

---

*Code A2.27. Log file: model with single joint at dip=45.*

---

```

***** Biaxial-test results follow. . .
      md_run_name = spc3j-45d_00
      md_numballs = 2505
      Confinement: et2_wsxx_req = -1.00000000000e+005
E (plane stress) = 1.35535430996e+010
nu (plane stress) = 4.20646679665e-001
E (plane strain) = 1.23652717930e+010
nu (plane strain) = 2.96095211910e-001
Fish> print pk_syy
pk_syy = -6.795286041162e+007
Fish> print pk_crk_num
pk_crk_num = 2.530000000000e+002
Fish> print pk_crk_num_cnf, pk_crk_num_csf
pk_crk_num_cnf = 7.600000000000e+001
pk_crk_num_csf = 1.770000000000e+002
Fish> print pk_crk_num_pnf, pk_crk_num_psf
pk_crk_num_pnf = 0.000000000000e+000
pk_crk_num_psf = 0.000000000000e+000
Fish> print pk_ci_fac, pk_syy_ci
pk_ci_fac = 2.000000000000e-002
pk_syy_ci = -6.865124674344e+006
Pfc2D>;
Pfc2D> SET md_tag_name='-bw1'
Pfc2D>md_save_state
Fish> save @_fname
Pfc2D>; =====
Pfc2D>return
Pfc2D>; -----
Pfc2D>set log off
*****
* Log File Ended 18:12:25 Sat Oct 2 2004
*****

```

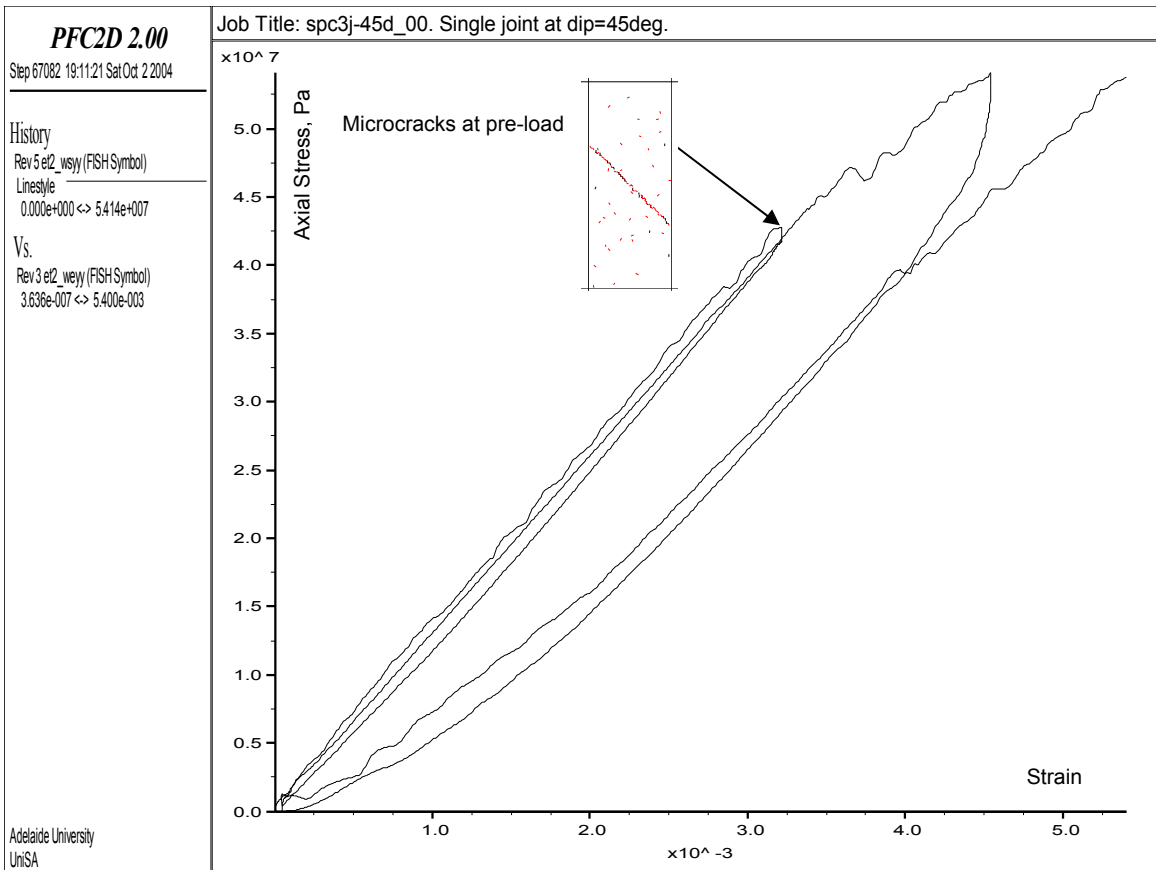


Figure A2.5. LRR test on model with single joint at dip=45. Pre-load=0.63 $\sigma_c$ .

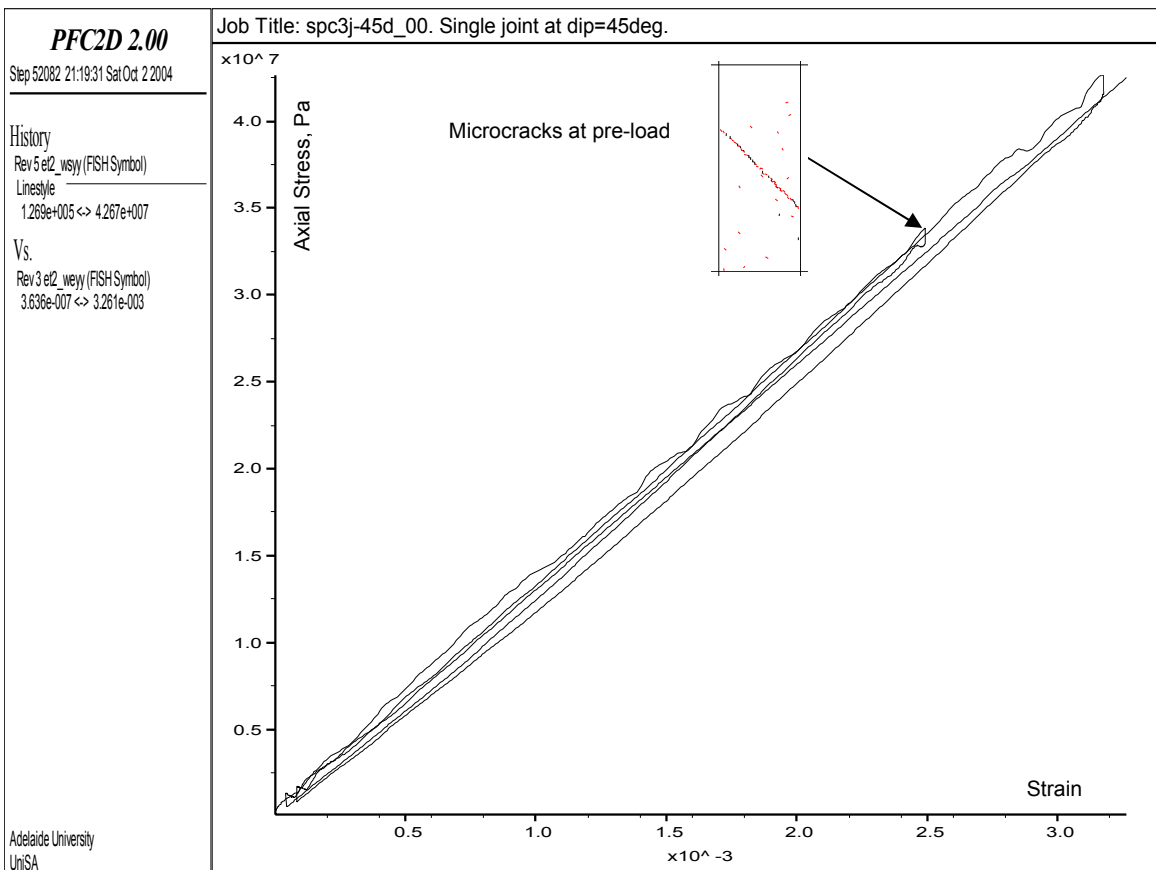


Figure A2.6. LRR test on model with single joint at dip=45. Pre-load=0.5 $\sigma_c$ .

*Code A2.28. Model with single joint at dip=60. Specimen genesis driver.*

---

```
; Filename: spc3j-60d.DVR
;
; PURPOSE: Create the coarse grained sandstone with single joint.
;         Dip=60deg.
;
; Adelaide University.
;=====
rest spc3-spc           ; restoring Specimen #3 model
                        ; Adding joint:
JSET id=1 dip=60 origin=(0,0)
  property n_bond=1e4 s_bond=1e4 fric=0.25 range jset=1
plot create j_sets
plot add cluster blue cyan
save spc3j-60d-spc.SAV           ; jointed model created and saved
return
; EOF:  spc3j-60d.DVR
```

---

*Code A2.29. Model with single joint at dip=60. UCS and LRR tests driver.*

---

```
; fname: spc3j-60d_bx.DVR Uniaxial test on with single joint. Dip=60deg.
;         Load to failure.
;
; PURPOSE: 1) restore spc3j-60d specimen,
;          2) perform uniaxial test upon it
;          (variation of biaxial under confining stress of Pc=0.1 MPa)
;
; Adelaide University.
;=====
set logfile spc3j-60d_bx.log
set log on
; -----
; Execute biaxial test at Pc=0.1 MPa
restore spc3j-60d-spc.SAV
set safe_conversion on
SET md_run_name='spc3j-60d_00'
title 'spc3j-60d_00. Single joint at dip=60deg.'
SET et2_knxfac=0.001 et2_knyfac=1.0
SET et2_wsxx_req=-1.0e5 et2_wsyy_req=-1.0e5 et2_ws_tol=0.01
SET p_vel=2.0e-1 p_cyc=1000 p_stages=20
call %itascaFishTank%\FishPfc2\et2\_btw2.DVR ;=> spc3j-60d_00-{bw0,bw1}.SAV
; -----
set log off
return
; EOF:  spc3j-60d_bx.DVR
```

---

*Code A2.30. Log file: model with single joint at dip=60.*

---

```
***** Biaxial-test results follow. . .
md_run_name = spc3j-60d_00
md_numballs = 2505
Confinement: et2_wsxx_req = -1.0000000000e+005
E (plane stress) = 1.34083261835e+010
```

```

nu (plane stress) = 4.60976755674e-001
E (plane strain) = 1.20734345597e+010
nu (plane strain) = 3.15526413329e-001
Fish> print pk_syy
pk_syy = -5.845698922108e+007
Fish> print pk_crk_num
pk_crk_num = 1.680000000000e+002
Fish> print pk_crk_num_cnf, pk_crk_num_csf
pk_crk_num_cnf = 4.700000000000e+001
pk_crk_num_csf = 1.210000000000e+002
Fish> print pk_crk_num_pnf, pk_crk_num_psf
pk_crk_num_pnf = 0.000000000000e+000
pk_crk_num_psf = 0.000000000000e+000
Fish> print pk_ci_fac, pk_syy_ci
pk_ci_fac = 2.000000000000e-002
pk_syy_ci = -6.546946036263e+006
Pfc2D>;
Pfc2D> SET md_tag_name='-bw1'
Pfc2D>md_save_state
Fish> save @_fname
Pfc2D>; =====
Pfc2D>return
Pfc2D>; -----
Pfc2D>set log off
*****
* Log File Ended 21:58:42 Sat Oct 2 2004
*****

```

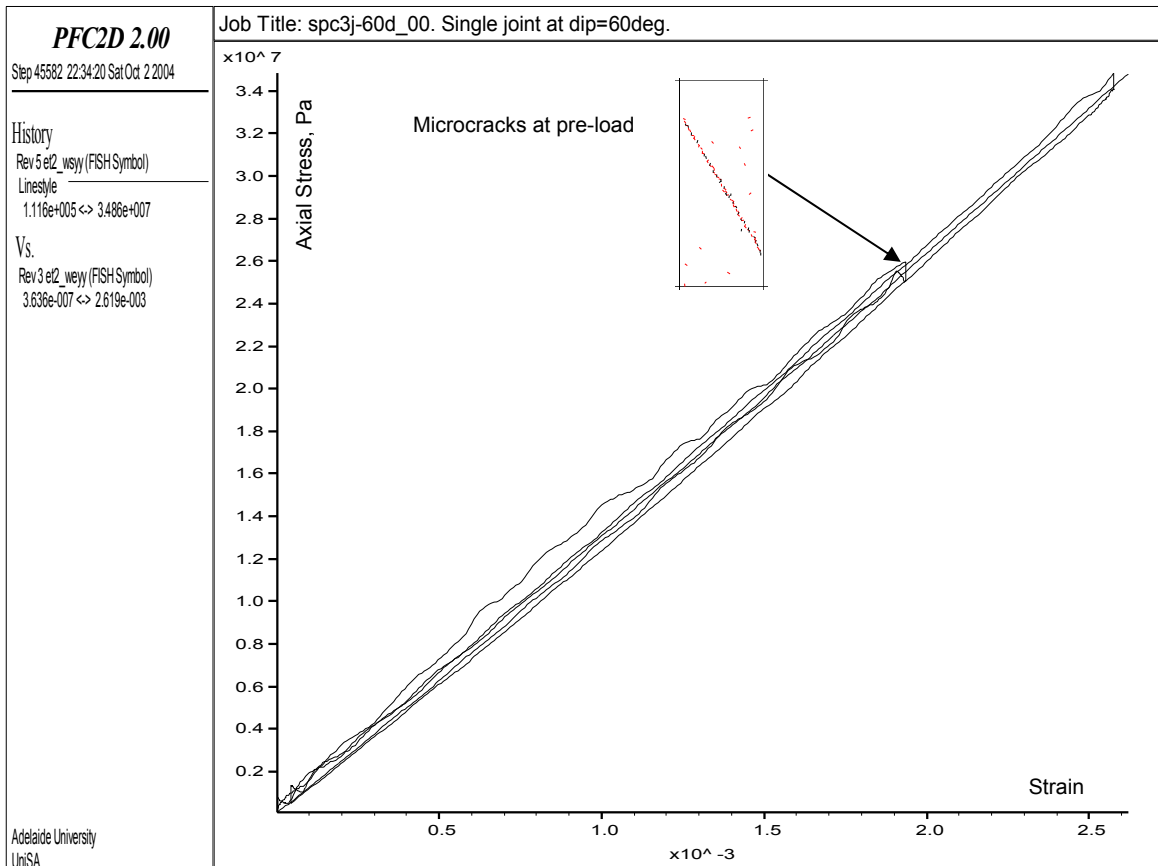


Figure A2.7. LRR test on model with single joint at dip=60.

*Code A2.31. Model with single joint at dip=70. Specimen genesis driver.*

---

```
; Filename: spc3j-70d.DVR
;
; PURPOSE: Create the coarse grained sandstone with single joint.
;         Dip=70deg.
;
; Adelaide University.
;=====
rest spc3-spc           ; restoring Specimen #3 model
                        ; Adding joint:
JSET id=1 dip=70 origin=(0,0)
  property n_bond=1e4 s_bond=1e4 fric=0.25 range jset=1
plot create j_sets
plot add cluster blue cyan lgray lorange white lgreen yellow
save spc3j-70d-spc.SAV           ; jointed model created and saved
return
; EOF:  spc3j-70d.DVR
```

---

*Code A2.32. Model with single joint at dip=70. UCS and LRR tests driver.*

---

```
; fname: spc3j-70d_bx.DVR Uniaxial test on with single joint. Dip=70deg.
;         Load to failure.
;
; PURPOSE: 1) restore spc3j-70d specimen,
;          2) perform uniaxial test upon it
;          (variation of biaxial under confining stress of Pc=0.1 MPa)
;
; Adelaide University.
;=====
set logfile spc3j-70d_bx.log
set log on
; -----
; Execute biaxial test at Pc=0.1 MPa
restore spc3j-70d-spc.SAV
set safe_conversion on
SET md_run_name='spc3j-70d_00'
title 'spc3j-70d_00. Single joint at dip=70deg.'
SET et2_knxfac=0.001 et2_knyfac=1.0
SET et2_wsxx_req=-1.0e5 et2_wsyy_req=-1.0e5 et2_ws_tol=0.01
SET p_vel=2.0e-1 p_cyc=1000 p_stages=20
call %itascaFishTank%\FishPfc2\et2\_btw2.DVR ;=> spc3j-70d_00-{bw0,bw1}.SAV
; -----
set log off
return
; EOF:  spc3j-70d_bx.DVR
```

---

*Code A2.33. Log file: model with single joint at dip=70.*

---

```
***** Biaxial-test results follow. . .
md_run_name = spc3j-70d_00
md_numballs = 2505
Confinement: et2_wsxx_req = -1.0000000000e+005
E (plane stress) = 1.29101630271e+010
```

```

nu (plane stress) = 5.52672023023e-001
E (plane strain) = 1.12744495489e+010
nu (plane strain) = 3.55948980099e-001
Fish> print pk_syy
pk_syy = -4.247340746112e+007
Fish> print pk_crk_num
pk_crk_num = 1.710000000000e+002
Fish> print pk_crk_num_cnf, pk_crk_num_csf
pk_crk_num_cnf = 6.300000000000e+001
pk_crk_num_csf = 1.080000000000e+002
Fish> print pk_crk_num_pnf, pk_crk_num_psf
pk_crk_num_pnf = 0.000000000000e+000
pk_crk_num_psf = 0.000000000000e+000
Fish> print pk_ci_fac, pk_syy_ci
pk_ci_fac = 2.000000000000e-002
pk_syy_ci = -6.547740477830e+006
Pfc2D>;
Pfc2D> SET md_tag_name='-bw1'
Pfc2D>md_save_state
Fish> save @_fname
Pfc2D>; =====
Pfc2D>return
Pfc2D>; -----
Pfc2D>set log off
*****
* Log File Ended 23:19:12 Sat Oct 2 2004
*****

```

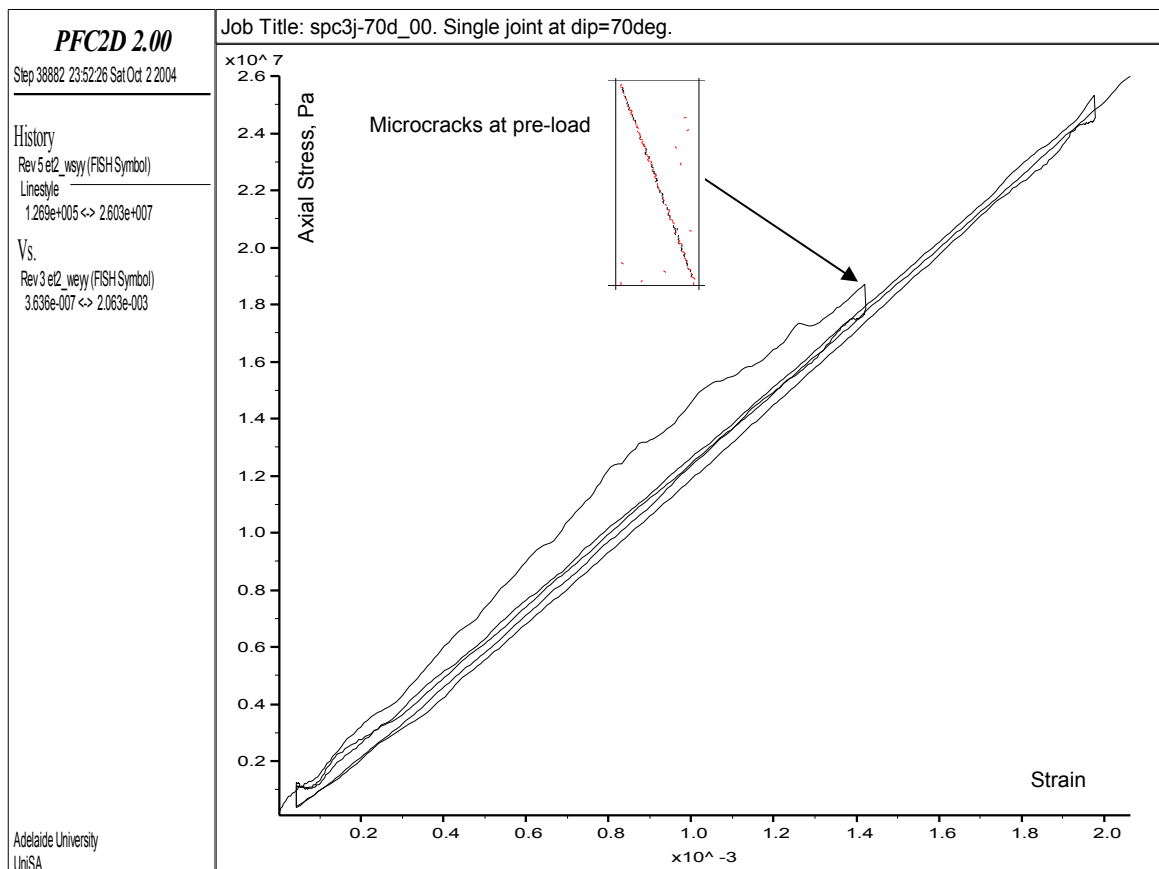


Figure A2.8. LRR test on model with single joint at dip=70.

*Code A2.34. Model with single joint at dip=80. Specimen genesis driver.*

---

```
; Filename: spc3j-80d.DVR
;
; PURPOSE: Create the coarse grained sandstone with single joint.
;         Dip=80deg.
;
; Adelaide University.
;=====
rest spc3-spc           ; restoring Specimen #3 model
                        ; Adding joint:
JSET id=1 dip=80 origin=(0,0)
  property n_bond=1e4 s_bond=1e4 fric=0.25 range jset=1
plot create j_sets
plot add cluster blue cyan
save spc3j-80d-spc.SAV           ; jointed model created and saved
return
; EOF:  spc3j-80d.DVR
```

---

*Code A2.35. Model with single joint at dip=80. UCS and LRR tests driver.*

---

```
; fname: spc3j-80d_bx.DVR Uniaxial test on with single joint. Dip=80deg.
;         Load to failure.
;
; PURPOSE: 1) restore spc3j-80d specimen,
;         2) perform uniaxial test upon it
;         (variation of biaxial under confining stress of Pc=0.1 MPa)
;
; Adelaide University.
;=====
set logfile spc3j-80d_bx.log
set log on
; -----
; Execute biaxial test at Pc=0.1 MPa
restore spc3j-80d-spc.SAV
set safe_conversion on
SET md_run_name='spc3j-80d_00'
title 'spc3j-80d_00. Single joint at dip=80deg.'
SET et2_knxfac=0.001 et2_knyfac=1.0
SET et2_wsxx_req=-1.0e5 et2_wsyy_req=-1.0e5 et2_ws_tol=0.01
SET p_vel=2.0e-1 p_cyc=1000 p_stages=20
call %itascaFishTank%\FishPfc2\et2\_btw2.DVR ;=> spc3j-80d_00-{bw0,bw1}.SAV
; -----
set log off
return
; EOF:  spc3j-80d_bx.DVR
```

---

*Code A2.36. Log file: model with single joint at dip=80.*

---

```
***** Biaxial-test results follow. . .
md_run_name = spc3j-80d_00
md_numballs = 2505
Confinement: et2_wsxx_req = -1.0000000000e+005
E (plane stress) = 1.38260831529e+010
```

```

nu (plane stress) = 3.48970483326e-001
E (plane strain) = 1.29008063798e+010
nu (plane strain) = 2.58693935590e-001
Fish> print pk_syy
pk_syy = -4.520591351630e+007
Fish> print pk_crk_num
pk_crk_num = 1.750000000000e+002
Fish> print pk_crk_num_cnf, pk_crk_num_csf
pk_crk_num_cnf = 6.700000000000e+001
pk_crk_num_csf = 1.080000000000e+002
Fish> print pk_crk_num_pnf, pk_crk_num_psf
pk_crk_num_pnf = 0.000000000000e+000
pk_crk_num_psf = 0.000000000000e+000
Fish> print pk_ci_fac, pk_syy_ci
pk_ci_fac = 2.000000000000e-002
pk_syy_ci = -6.547740477830e+006
Pfc2D>;
Pfc2D> SET md_tag_name='-bw1'
Pfc2D>md_save_state
Fish> save @_fname
Pfc2D>; =====
Pfc2D>return
Pfc2D>; -----
Pfc2D>set log off
*****
* Log File Ended 09:55:59 Sun Oct 3 2004
*****

```

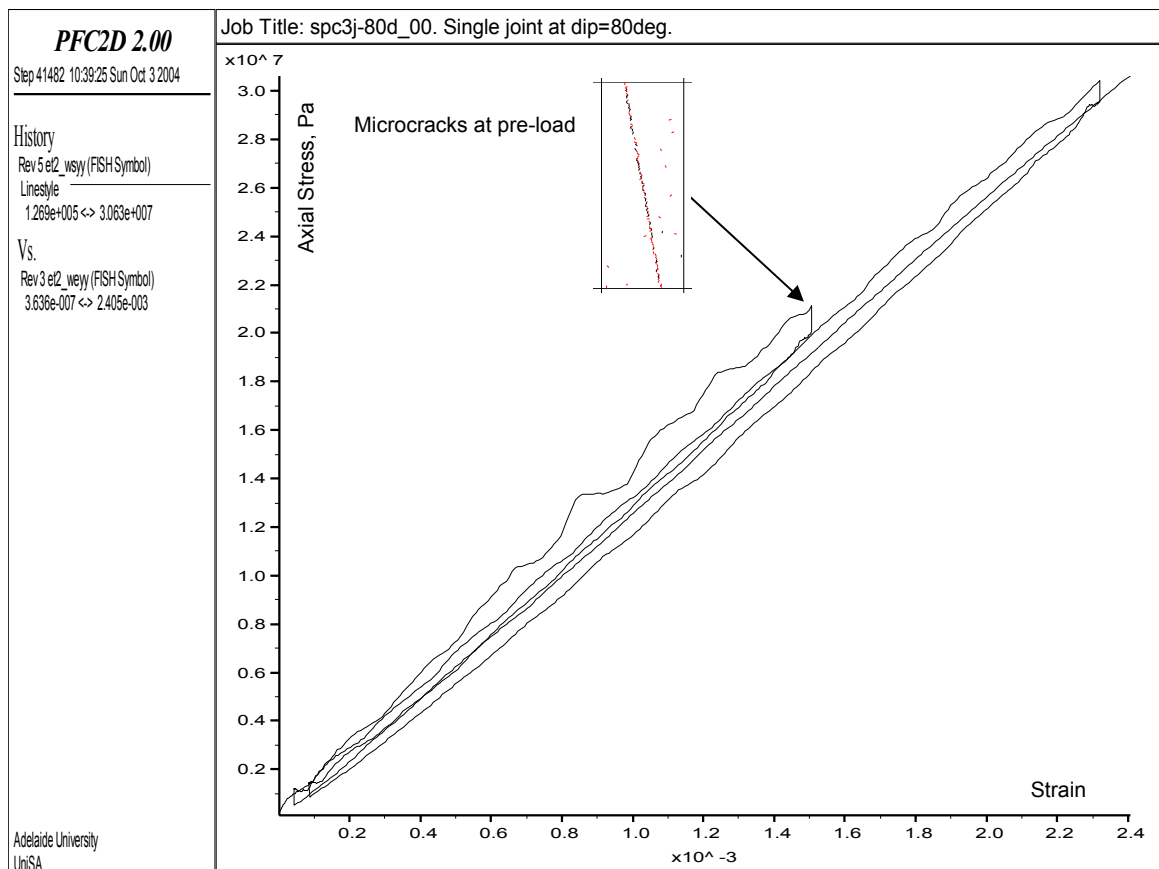


Figure A2.9. LRR test on model with single joint at dip=80.

*Code A2.37. Model with single joint at dip=90. Specimen genesis driver.*

---

```
; Filename: spc3j-90d.DVR
;
; PURPOSE: Create the coarse grained sandstone with single joint.
;         Dip=90deg.
;
; Adelaide University.
;=====
rest spc3-spc           ; restoring Specimen #3 model
                        ; Adding joint:
JSET id=1 dip=90 origin=(0,0)
  property n_bond=1e4 s_bond=1e4 fric=0.25 range jset=1
plot create j_sets
plot add cluster blue cyan
save spc3j-90d-spc.SAV           ; jointed model created and saved
return
; EOF:  spc3j-90d.DVR
```

---

*Code A2.38. Model with single joint at dip=90. UCS and LRR tests driver.*

---

```
; fname: spc3j-90d_bx.DVR Uniaxial test on with single joint. Dip=90deg.
;         Load to failure.
;
; PURPOSE: 1) restore spc3j-90d specimen,
;         2) perform uniaxial test upon it
;         (variation of biaxial under confining stress of Pc=0.1 MPa)
;
; Adelaide University.
;=====
set logfile spc3j-90d_bx.log
set log on
; -----
; Execute biaxial test at Pc=0.1 MPa
restore spc3j-90d-spc.SAV
set safe_conversion on
SET md_run_name='spc3j-90d_00'
title 'spc3j-90d_00. Single joint at dip=90deg.'
SET et2_knxfac=0.001 et2_knyfac=1.0
SET et2_wsxx_req=-1.0e5 et2_wsyy_req=-1.0e5 et2_ws_tol=0.01
SET p_vel=2.0e-1 p_cyc=1000 p_stages=20
call %itascaFishTank%\FishPfc2\et2\_btw2.DVR ;=> spc3j-90d_00-{bw0,bw1}.SAV
; -----
set log off
return
; EOF:  spc3j-90d_bx.DVR
```

---

*Code A2.39. Log file: model with single joint at dip=90.*

---

```
***** Biaxial-test results follow. . .
md_run_name = spc3j-90d_00
md_numballs = 2505
Confinement: et2_wsxx_req = -1.0000000000e+005
E (plane stress) = 1.39618020093e+010
```

```

nu (plane stress) = 3.43832720665e-001
E (plane strain) = 1.30478035584e+010
nu (plane strain) = 2.55859762437e-001
Fish> print pk_syy
pk_syy = -7.860069876641e+007
Fish> print pk_crk_num
pk_crk_num = 4.330000000000e+002
Fish> print pk_crk_num_cnf, pk_crk_num_csf
pk_crk_num_cnf = 1.330000000000e+002
pk_crk_num_csf = 3.000000000000e+002
Fish> print pk_crk_num_pnf, pk_crk_num_psf
pk_crk_num_pnf = 0.000000000000e+000
pk_crk_num_psf = 0.000000000000e+000
Fish> print pk_ci_fac, pk_syy_ci
pk_ci_fac = 2.000000000000e-002
pk_syy_ci = -8.769170875635e+006
Pfc2D>;
Pfc2D> SET md_tag_name='-bw1'
Pfc2D>md_save_state
Fish> save @_fname
Pfc2D>; =====
Pfc2D>return
Pfc2D>; -----
Pfc2D>set log off
*****
* Log File Ended 11:29:33 Sun Oct 3 2004
*****

```

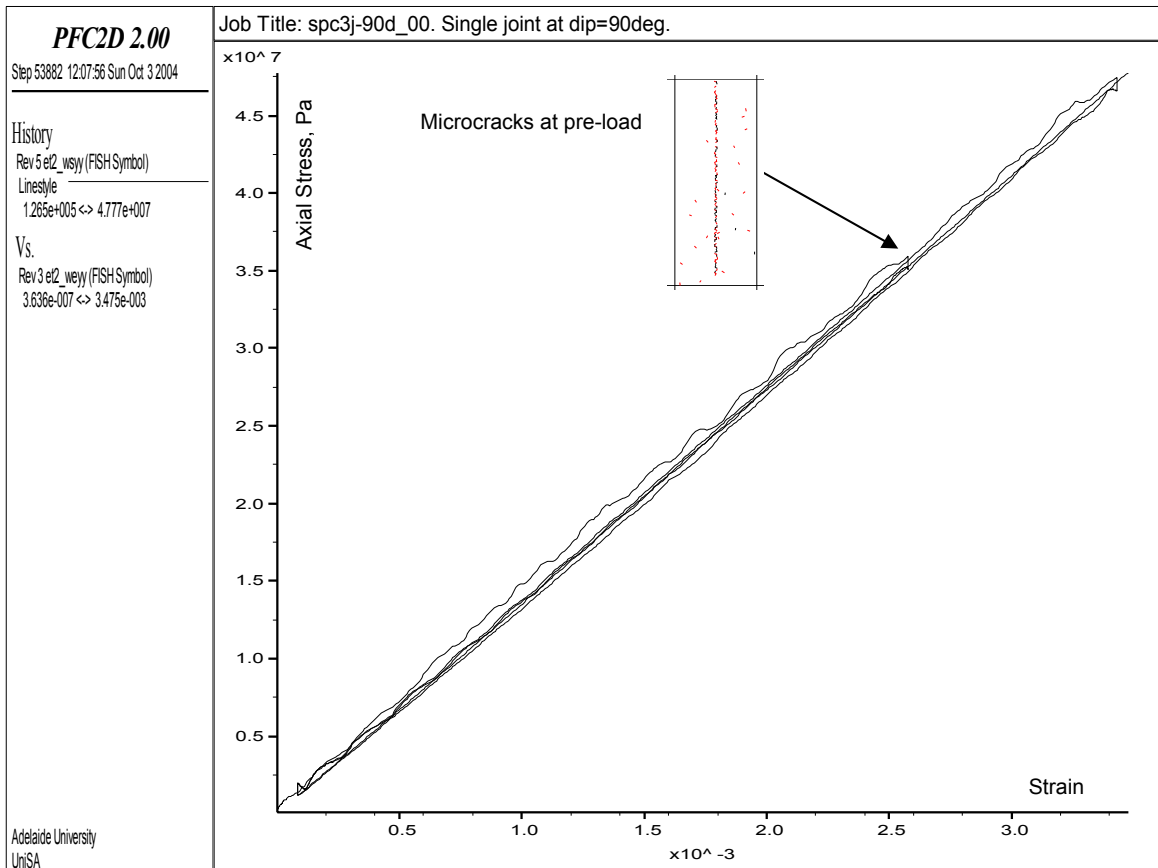


Figure A2.10. LRR test on model with single joint at dip=90.

The DRA on the model with a single joint is detailed in Figures A2.11 to A2.27 and Tables A2.5 to A2.13.

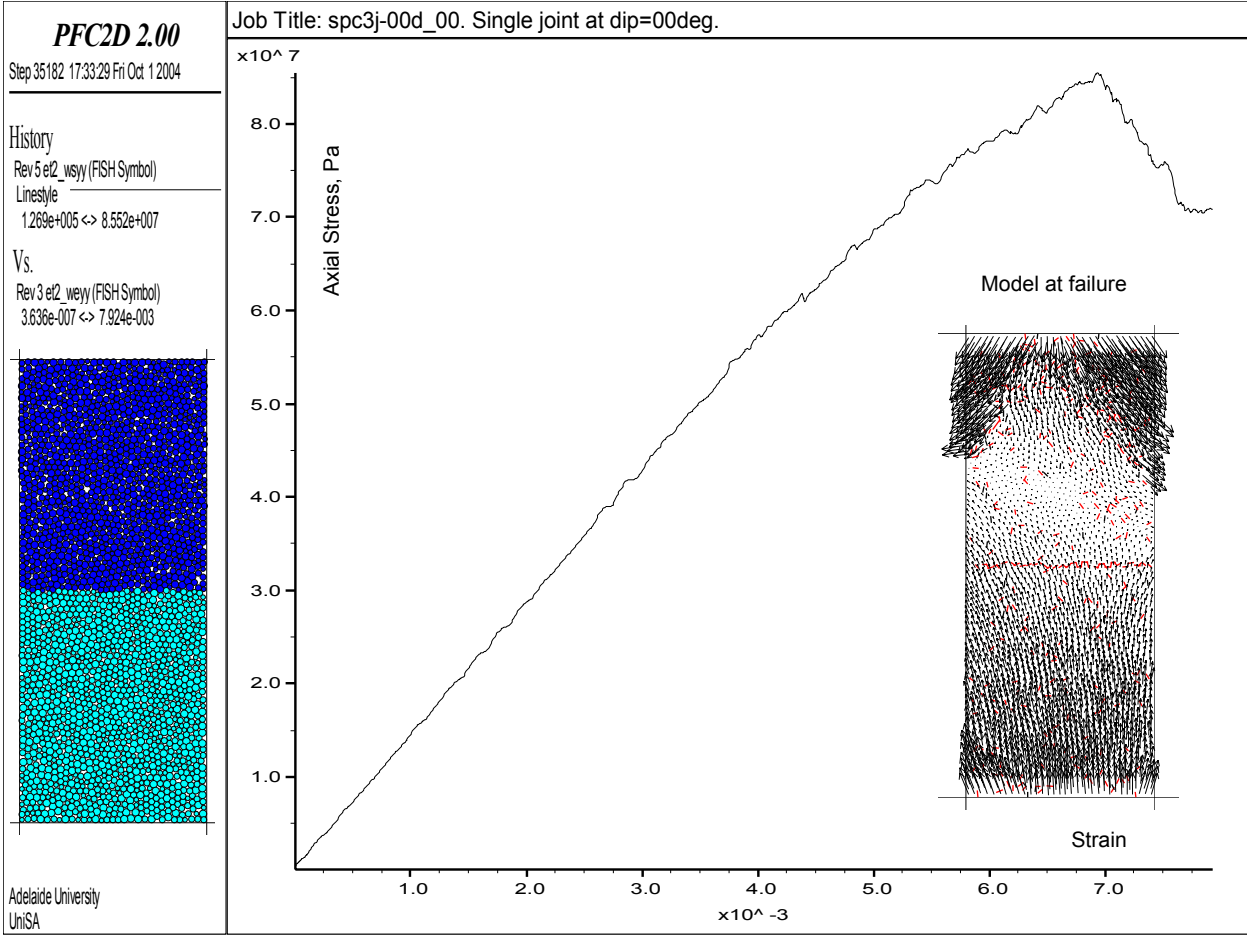


Figure A2.11. UCS test on model with single joint at  $\psi = 90^\circ$ .

Single joint @ dip = 00; s1 = 42.8 MPa.

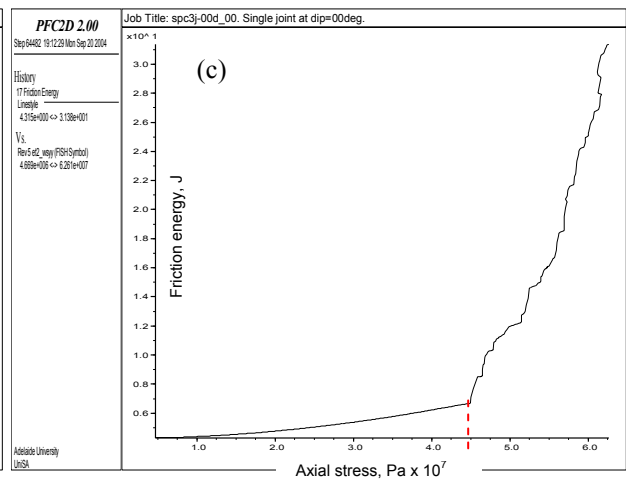
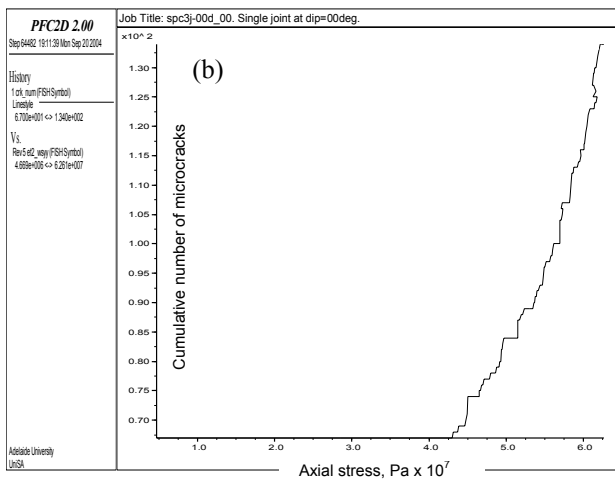
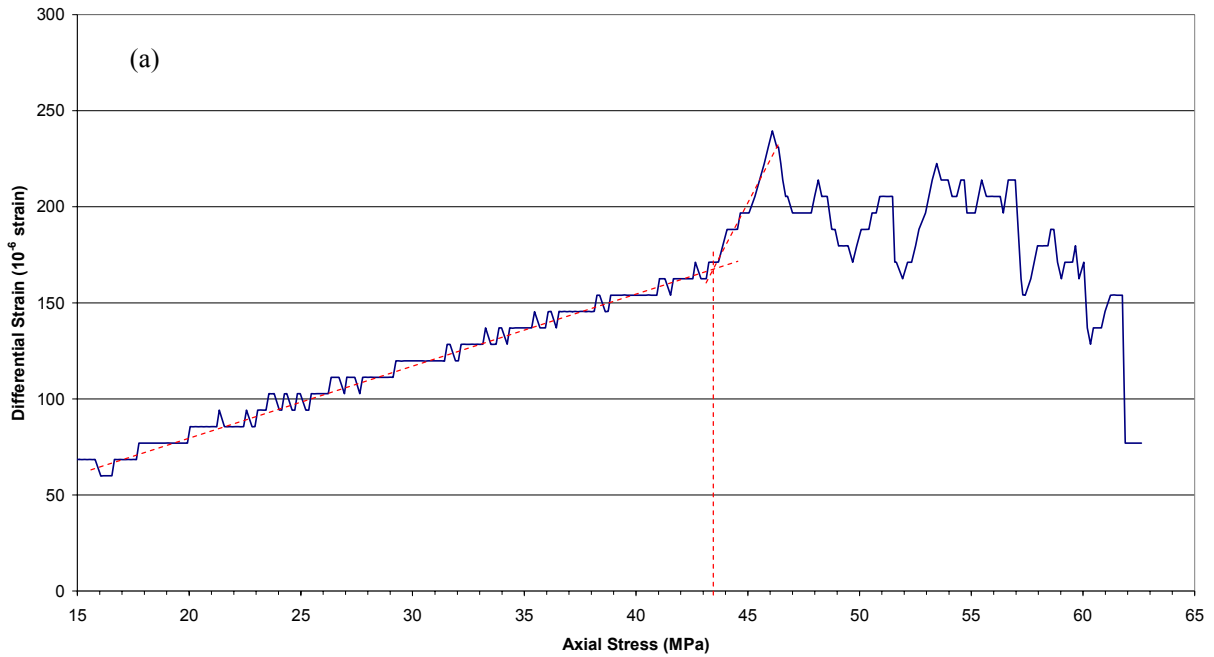


Figure A2.12. LRR test on model with single joint at  $\psi = 90^\circ$ :  
 (a) DRA curve; (b) cumulative number of microcracks; (c) friction energy.

Table A2.5. Results of LRR test on model with single joint at  $\psi = 90^\circ$ .

Pre-load stress, MPa	42.8
DME from DRA curve, MPa	43.5
FR	0.98
DME from cum. No. of microcracks, MPa	42.8
FR	1.00
DME from friction energy, MPa	45.0
FR	0.95

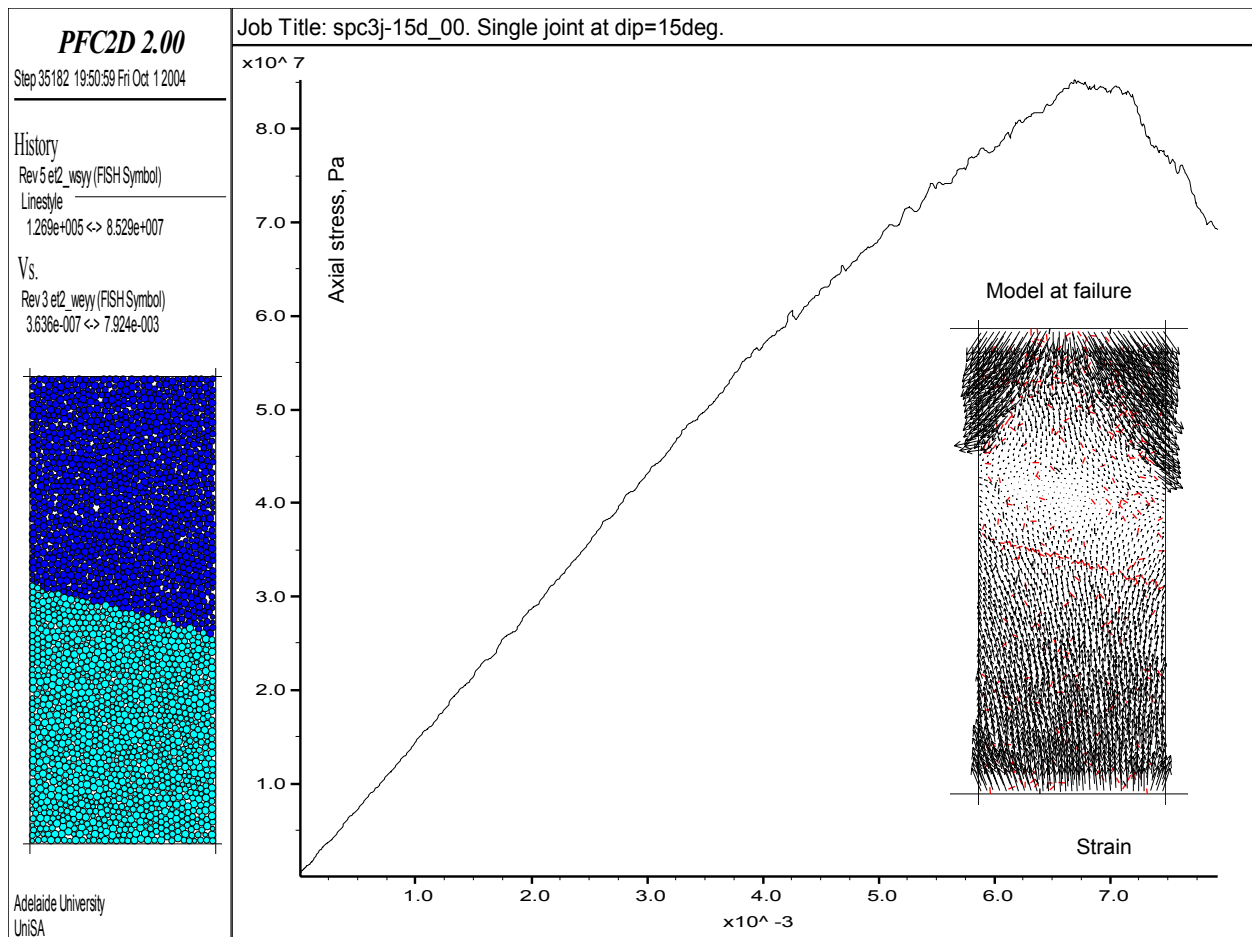


Figure A2.13. UCS test on model with single joint at  $\psi = 75^\circ$ .

Single joint @ dip = 15; s1 = 43.1 MPa.

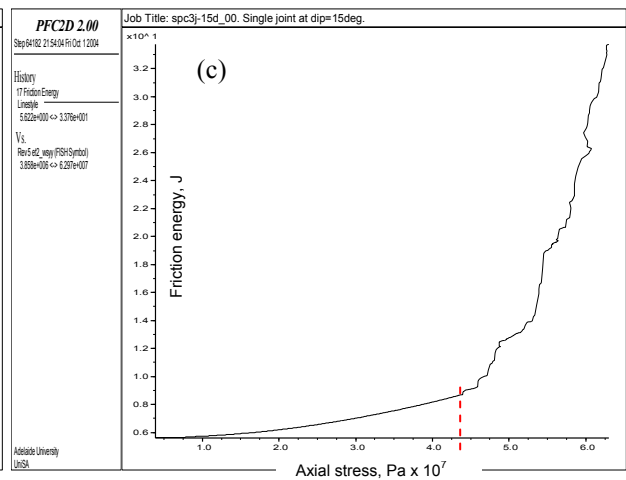
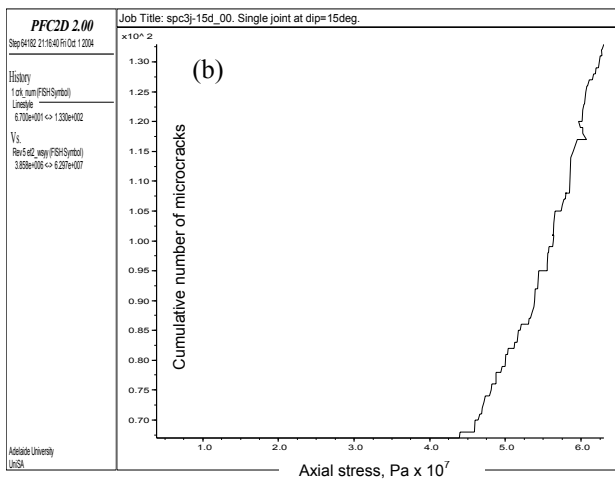
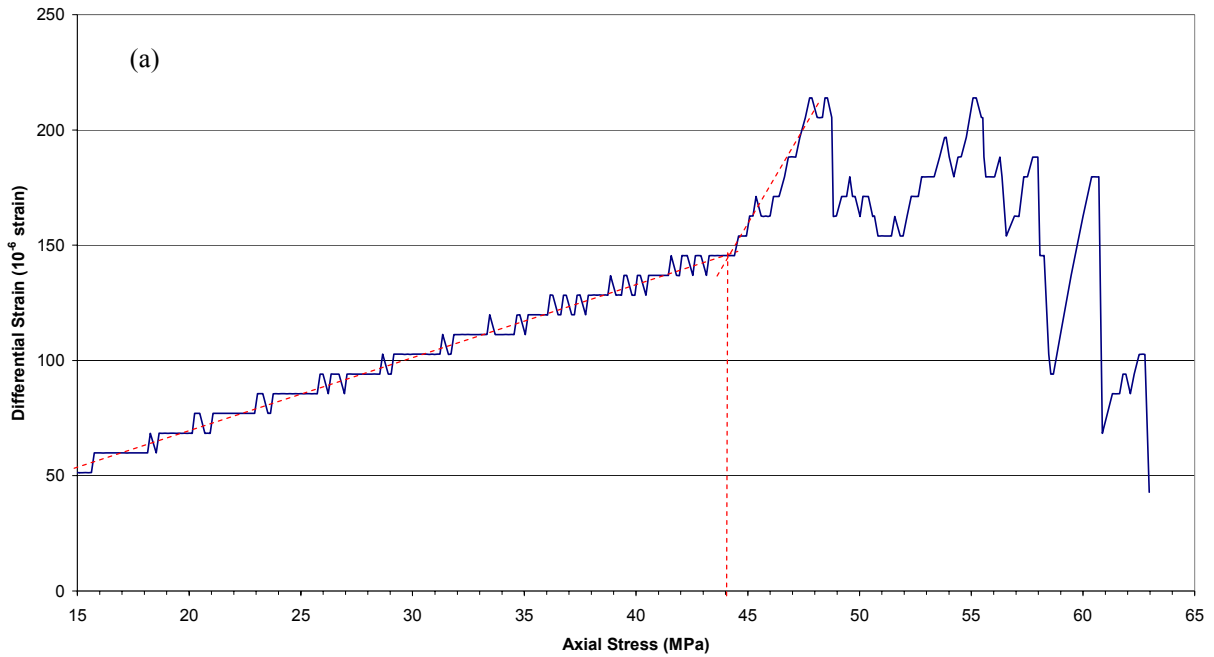


Figure A2.14. LRR test on model with single joint at  $\psi = 75^\circ$ :  
 (a) DRA curve; (b) cumulative number of microcracks; (c) friction energy.

Table A2.6. Results of LRR test on model with single joint at  $\psi = 75^\circ$ .

Pre-load stress, MPa	43.1
DME from DRA curve, MPa	44.0
FR	0.98
DME from cum. No. of microcracks, MPa	43.8
FR	0.98
DME from friction energy, MPa	43.8
FR	0.98

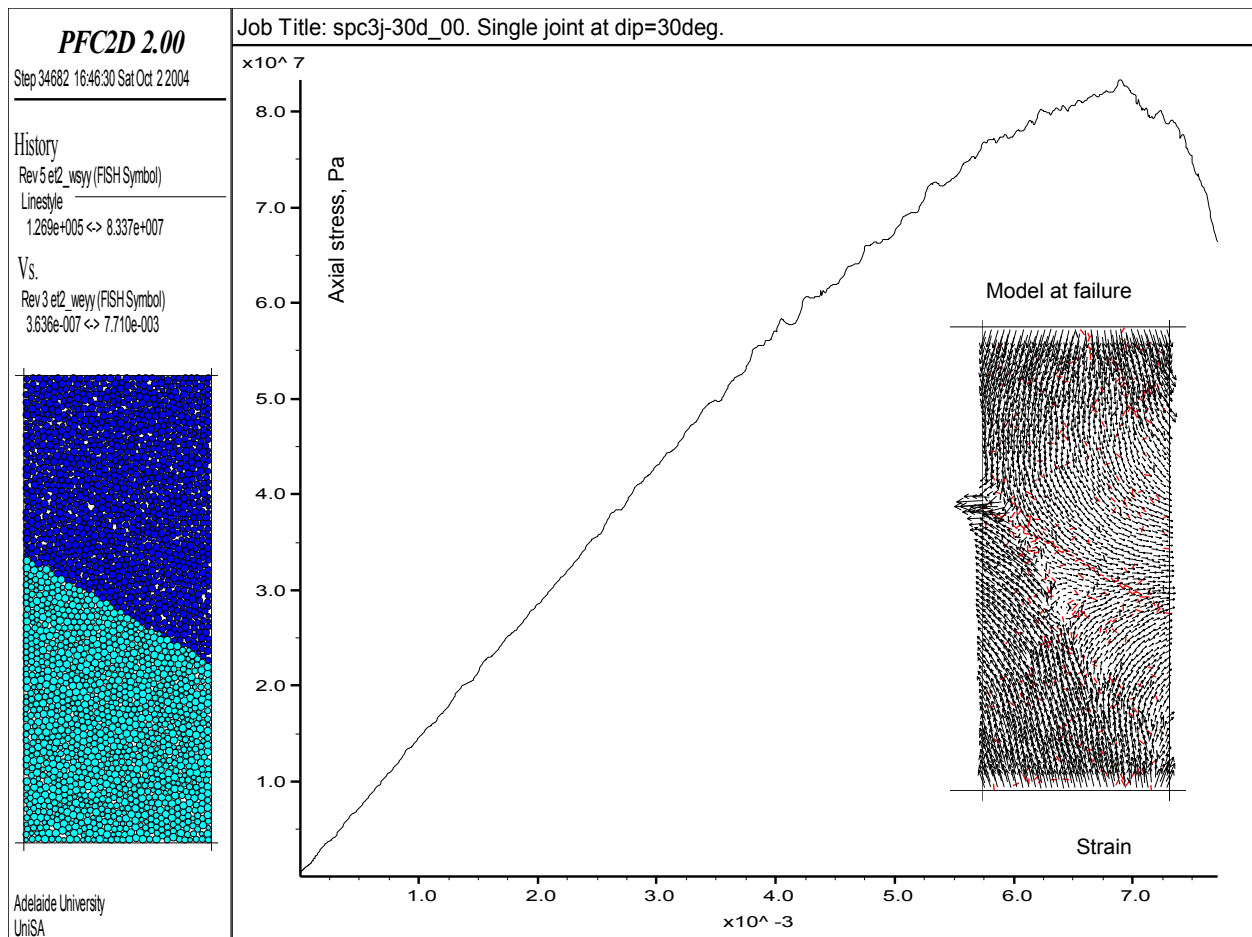


Figure A2.15. UCS test on model with single joint at  $\psi = 60^\circ$ .

Single joint @ dip = 30; s1 = 42.4 MPa.

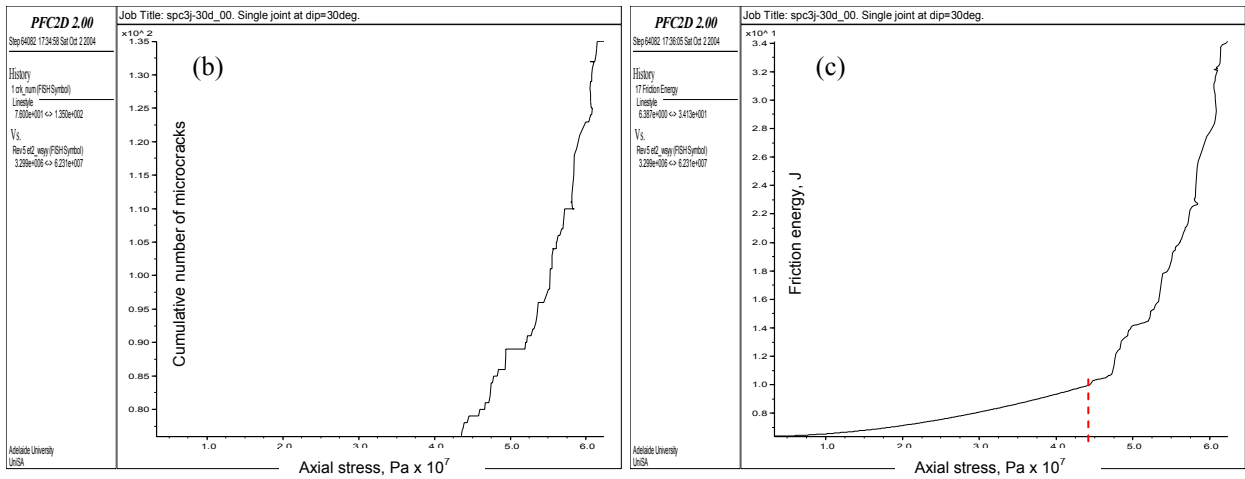
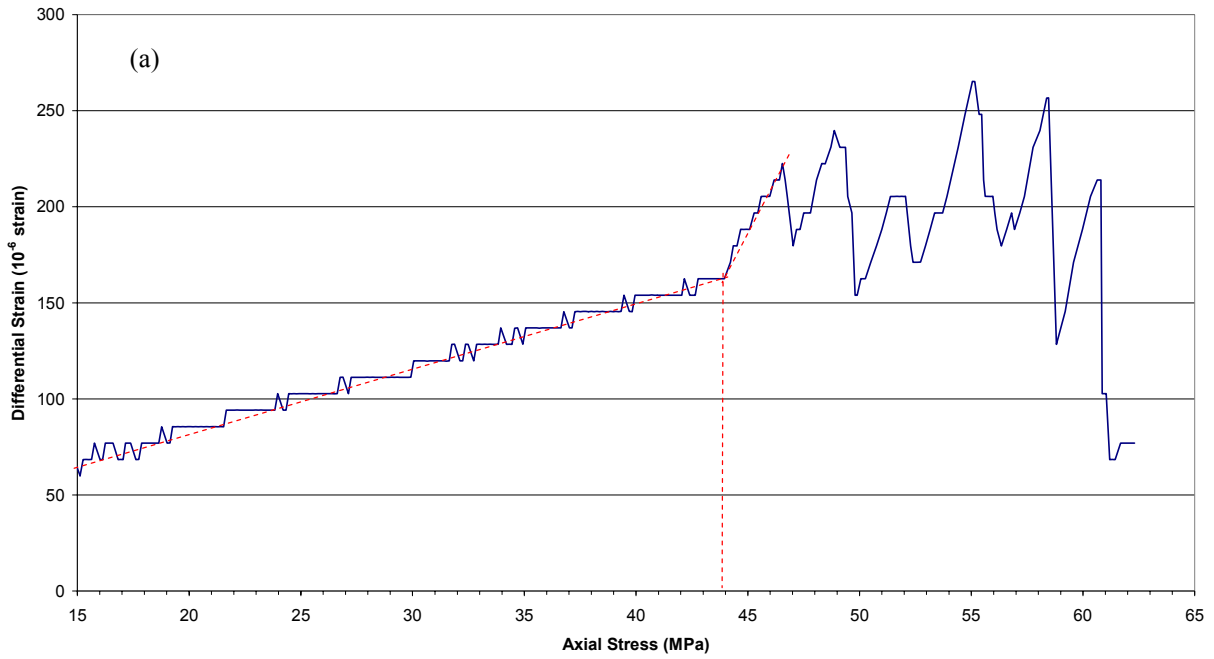


Figure A2.16. LRR test on model with single joint at  $\psi = 60^\circ$ :  
 (a) DRA curve; (b) cumulative number of microcracks; (c) friction energy.

Table A2.7. Results of LRR test on model with single joint at  $\psi = 60^\circ$ .

Pre-load stress, MPa	42.4
DME from DRA curve, MPa	43.8
FR	0.97
DME from cum. No. of microcracks, MPa	43.5
FR	0.97
DME from friction energy, MPa	43.9
FR	0.97

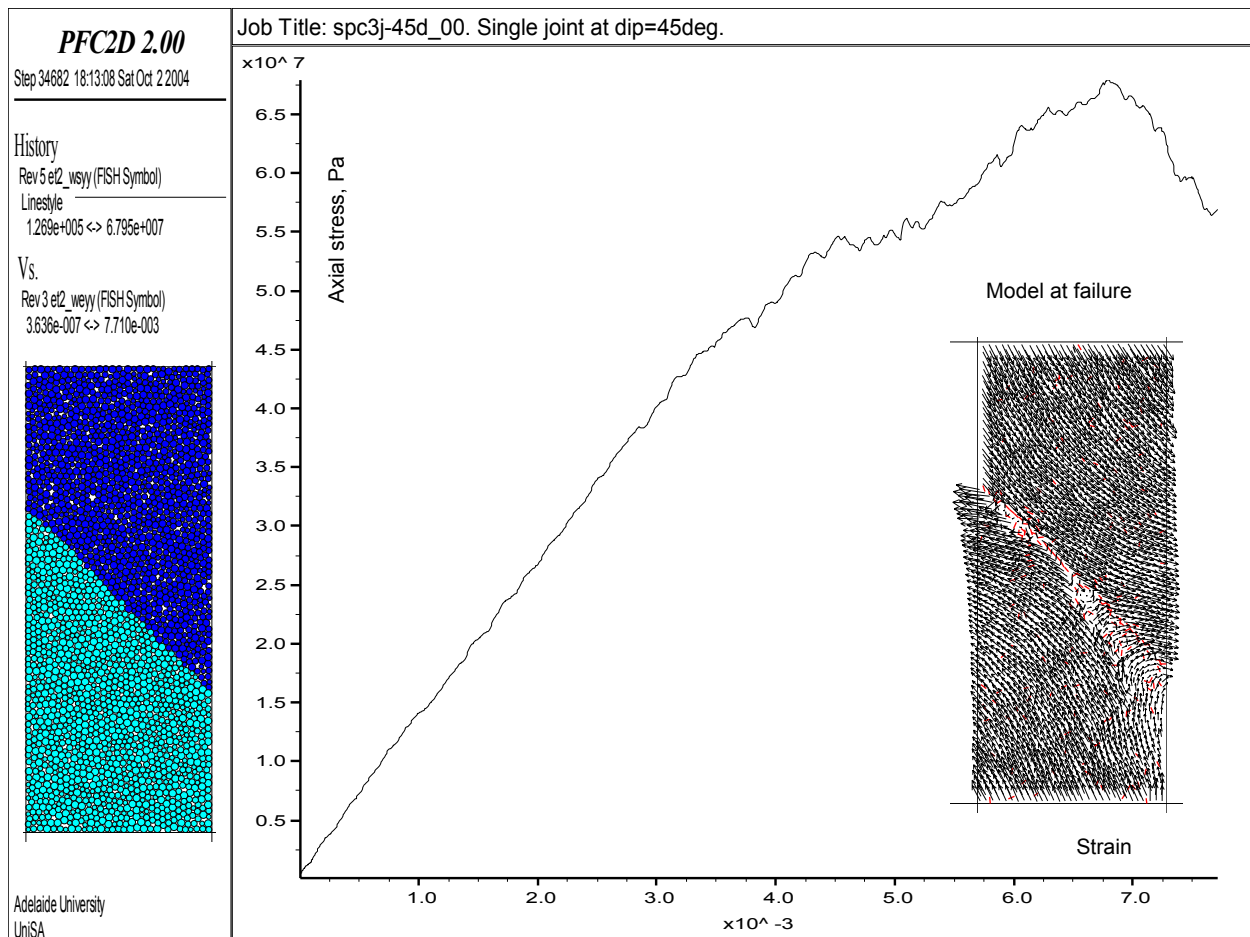


Figure A2.17. UCS test on model with single joint at  $\psi = 45^\circ$ .

Two LRR tests at different pre-load values were run on the model with dip at  $45^\circ$ . In the first test the model was pre-loaded up to  $42.8 \text{ MPa} = 0.63\sigma_c$  (Figure A2.18), in the second test the model was pre-loaded up to  $33.9 \text{ MPa} = 0.5\sigma_c$  (Figure A2.19). As can be seen, the DRA effect is somewhat obscured in the first test: the accuracy is relatively low (Table A2.8). It was resumed, the pre-load was too high, and thus too much damage was induced in the specimen. Since it was anticipated that the following models would also produce low UCS, a decision was made to assign the pre-load values as function of the ultimate strength of the model. After a number of trials, the pre-load was accepted to be in the range of  $0.4\sigma_c$  to  $0.5\sigma_c$ , while subsequent re-loading cycles should not have exceeded  $0.65\sigma_c$ .

Single joint @ dip = 45;  $s_1 = 42.8$  MPa.

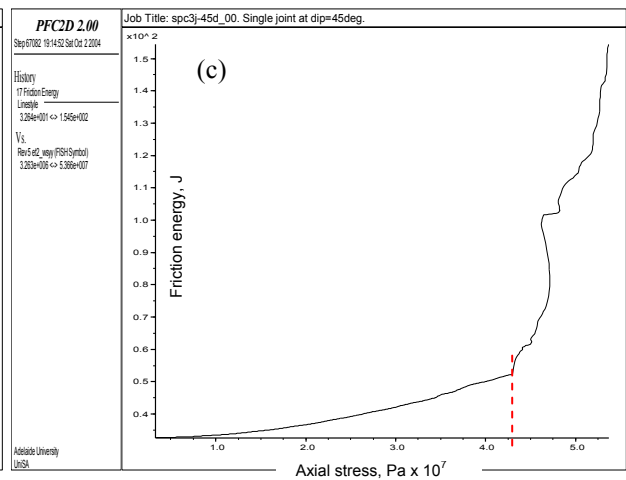
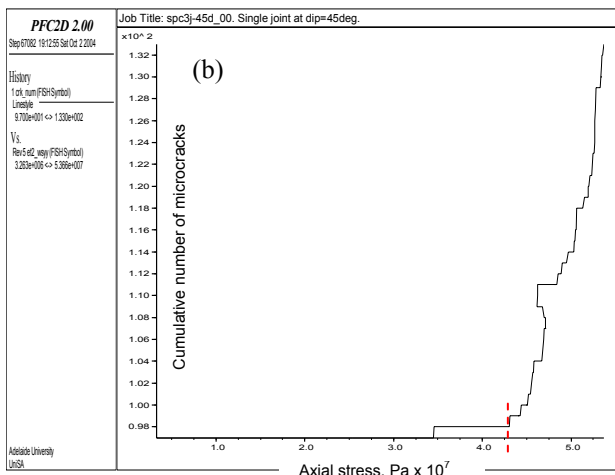
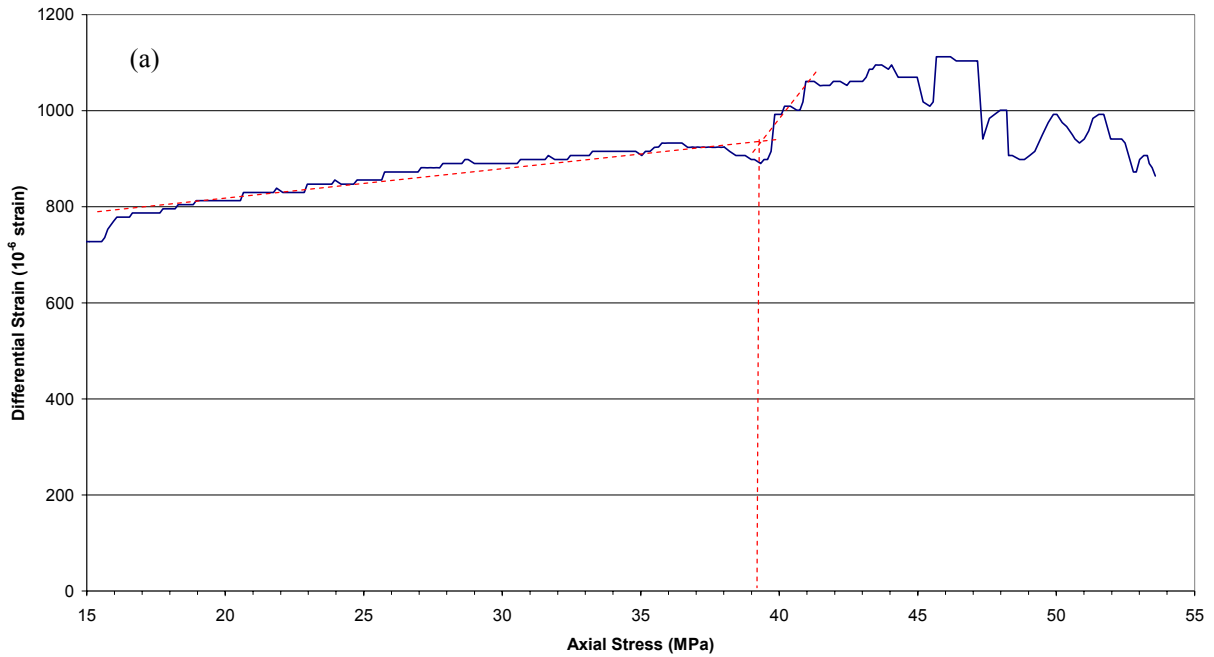


Figure A2.18. LRR test on model with single joint at  $\psi = 45^\circ$ ; pre-load  $= 0.63\sigma_c$ :  
 (a) DRA curve; (b) cumulative number of microcracks; (c) friction energy.

Table A2.8. Results of LRR test on model with single joint  $\psi = 45^\circ$ ; pre-load  $= 0.63\sigma_c$ .

Pre-load stress, MPa	42.8
DME from DRA curve, MPa	39.2
FR	1.09
DME from cum. No. of microcracks, MPa	42.7
FR	1.00
DME from friction energy, MPa	43.2
FR	0.99

Single joint @ dip = 45;  $s_1 = 33.9$  MPa.

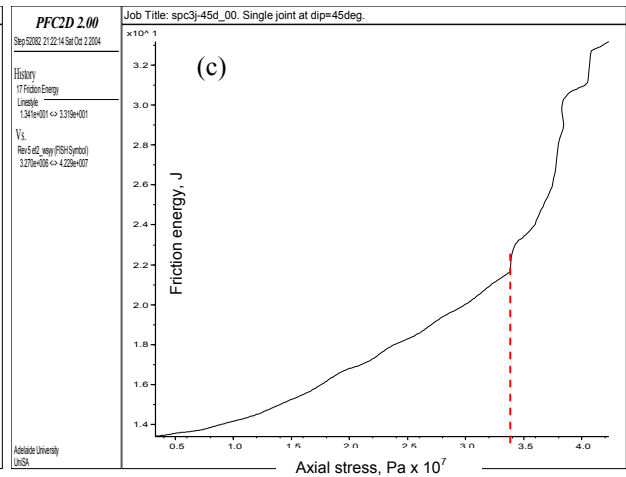
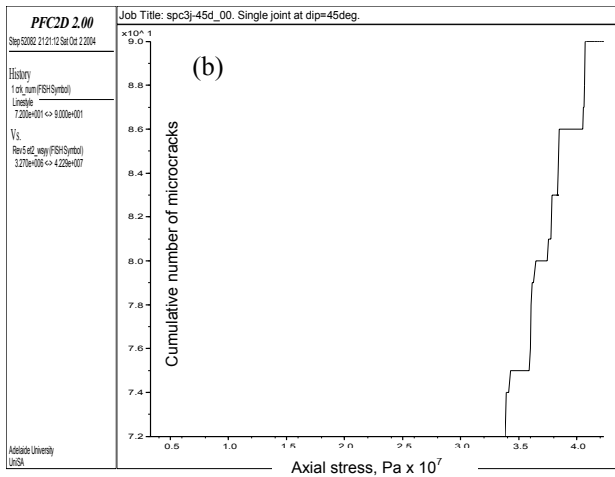
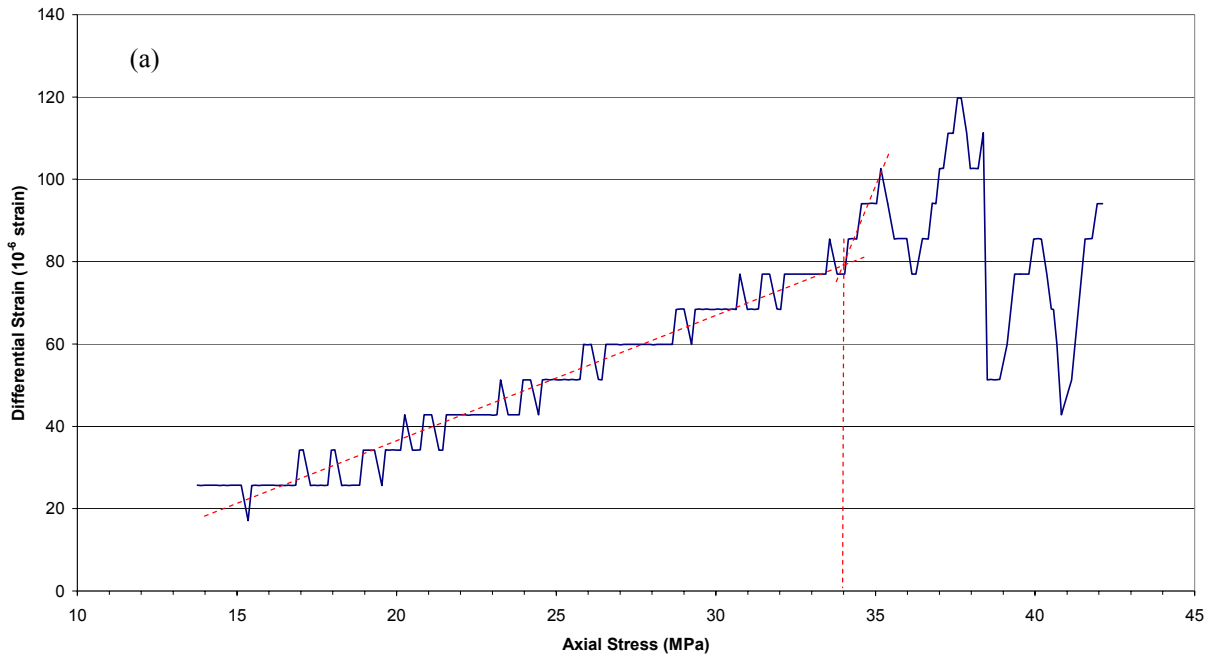


Figure A2.19. LRR test on model with single joint at  $\psi = 45^\circ$ ; pre-load  $= 0.5\sigma_c$ :  
 (a) DRA curve; (b) cumulative number of microcracks; (c) friction energy.

Table A2.9. Results of LRR test on model with single joint at  $\psi = 45^\circ$ ; pre-load  $= 0.5\sigma_c$ .

Pre-load stress, MPa		33.9
DME from DRA curve, MPa		33.9
	FR	1.00
DME from cum. No. of microcracks, MPa		33.9
	FR	1.00
DME from friction energy, MPa		34.1
	FR	0.99

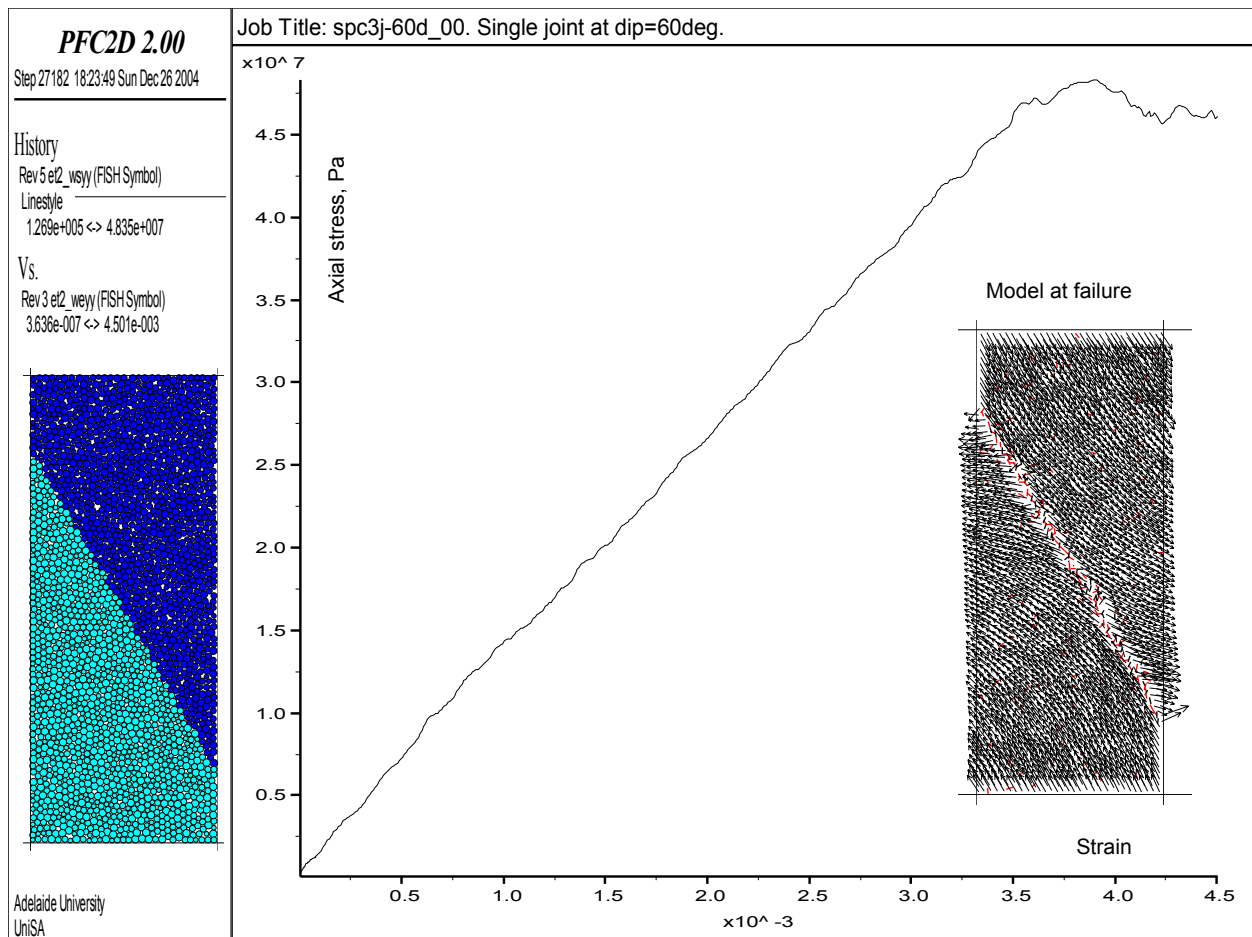


Figure A2.20. UCS test on model with single joint at  $\psi = 30^\circ$ .

Single joint @ dip = 60; s1 = 26.0 MPa.

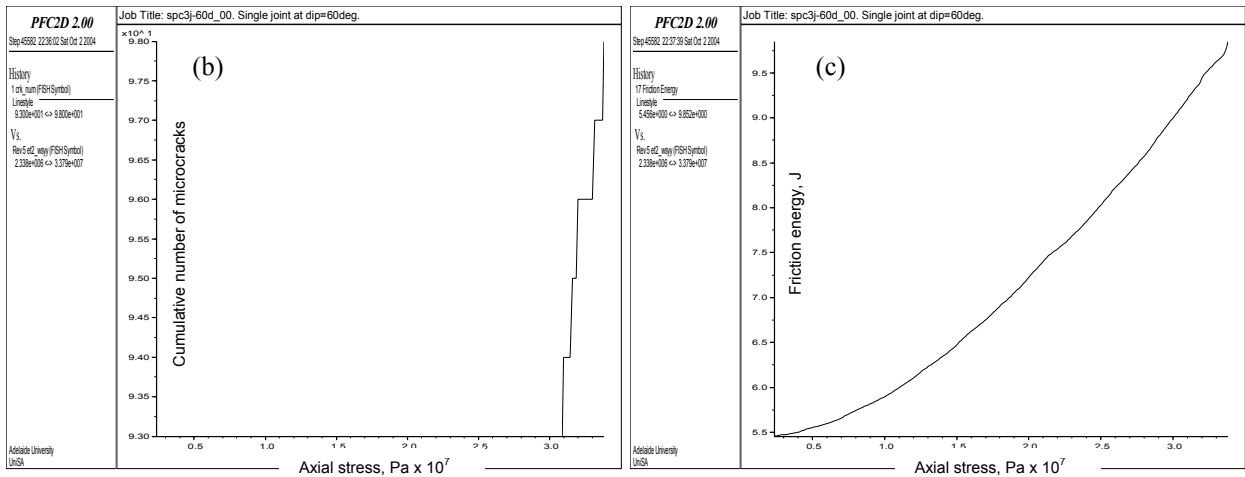
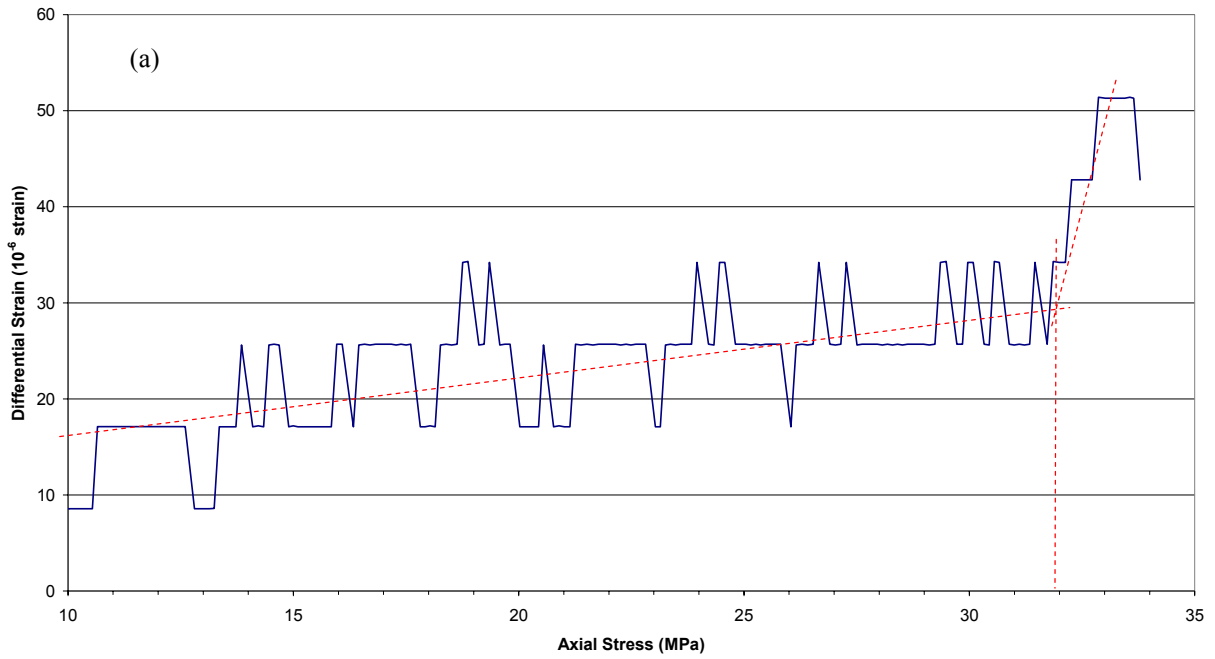


Figure A2.21. LRR test on model with single joint at  $\psi = 30^\circ$ :  
 (a) DRA curve; (b) cumulative number of microcracks; (c) friction energy.

Table A2.10. Results of LRR test on model with single joint at  $\psi = 30^\circ$ .

Pre-load stress, MPa		26.0
DME from DRA curve, MPa		31.8
	FR	0.82
DME from cum. No. of microcracks, MPa		30.8
	FR	0.84
DME from friction energy, MPa		—
	FR	—

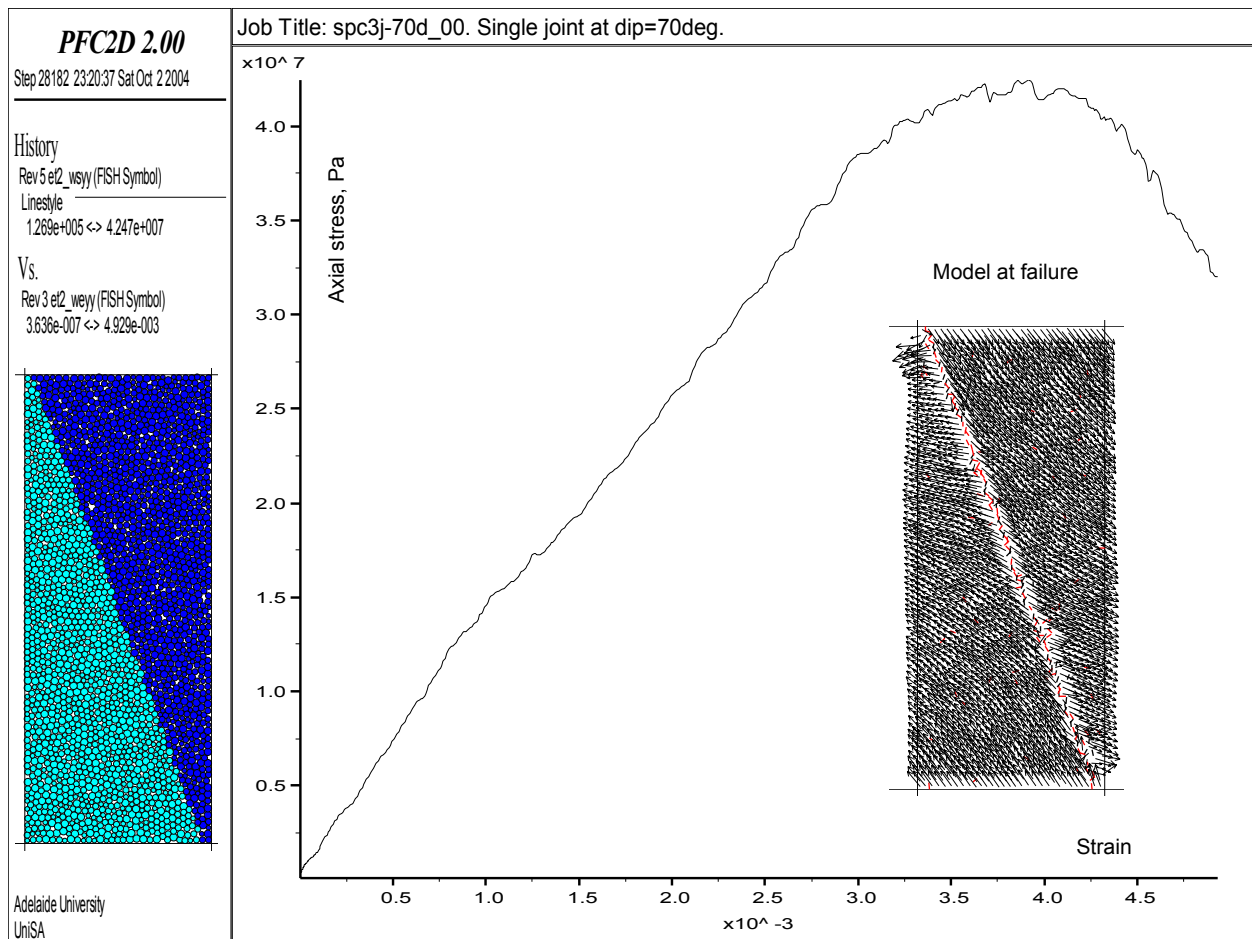


Figure A2.22. UCS test on model with single joint at  $\psi = 20^\circ$ .

Single joint @ dip = 70; s1 = 18.7 MPa.

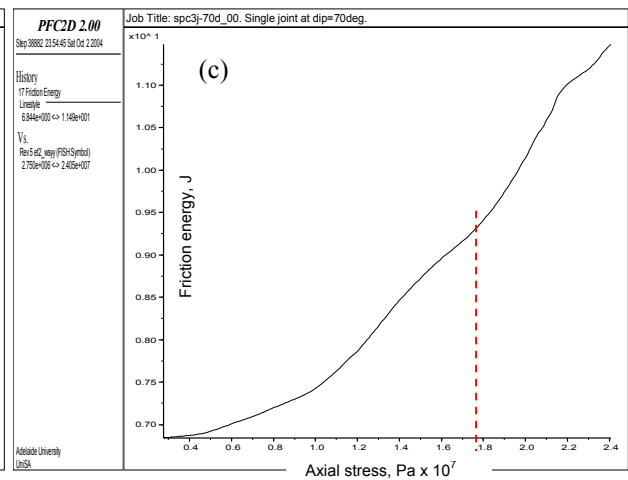
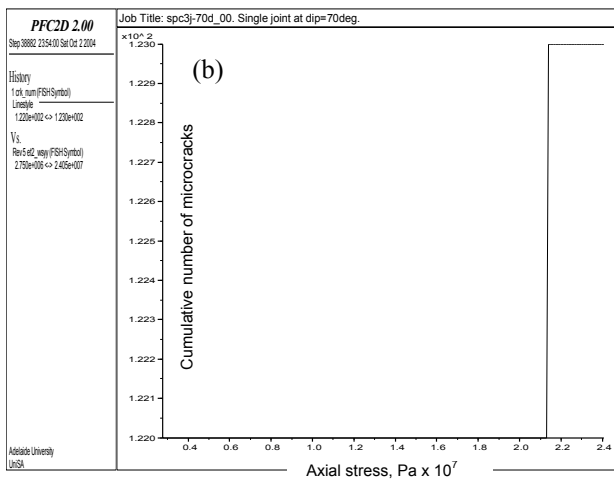
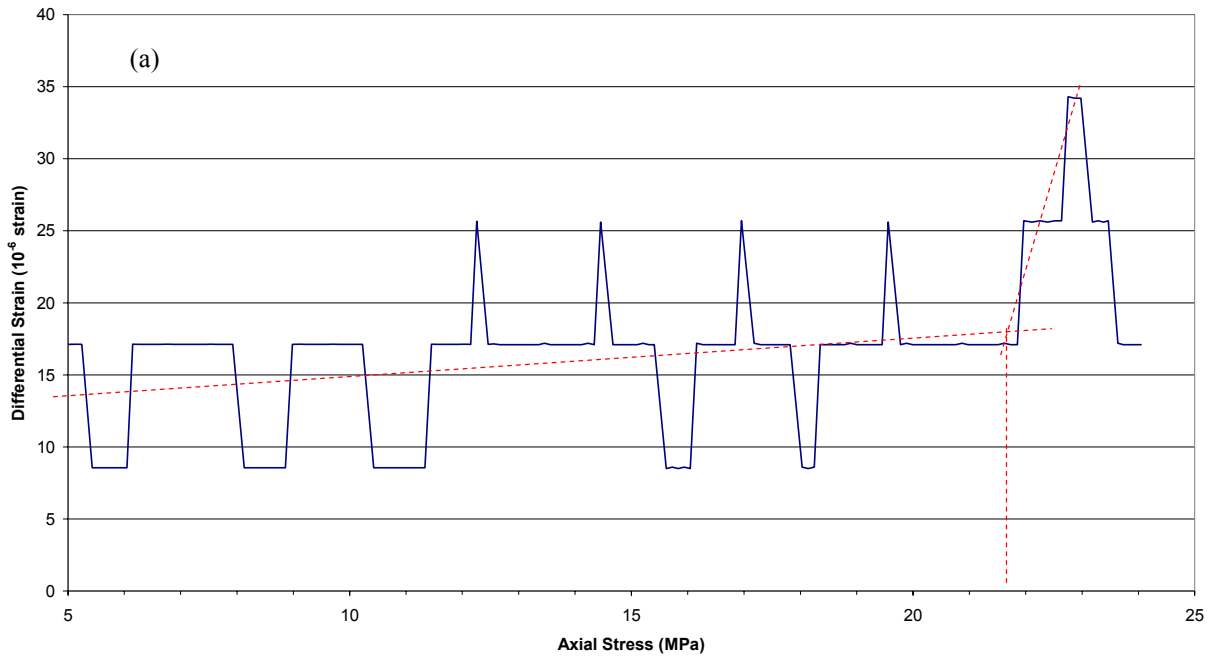


Figure A2.23. LRR test on model with single joint at  $\psi = 20^\circ$ :  
(a) DRA curve; (b) cumulative number of microcracks; (c) friction energy.

Table A2.11. Results of LRR test on model with single joint at  $\psi = 20^\circ$ .

Pre-load stress, MPa	18.7
DME from DRA curve, MPa	21.6
FR	0.87
DME from cum. No. of microcracks, MPa	21.3
FR	0.87
DME from friction energy, MPa	17.7
FR	1.06

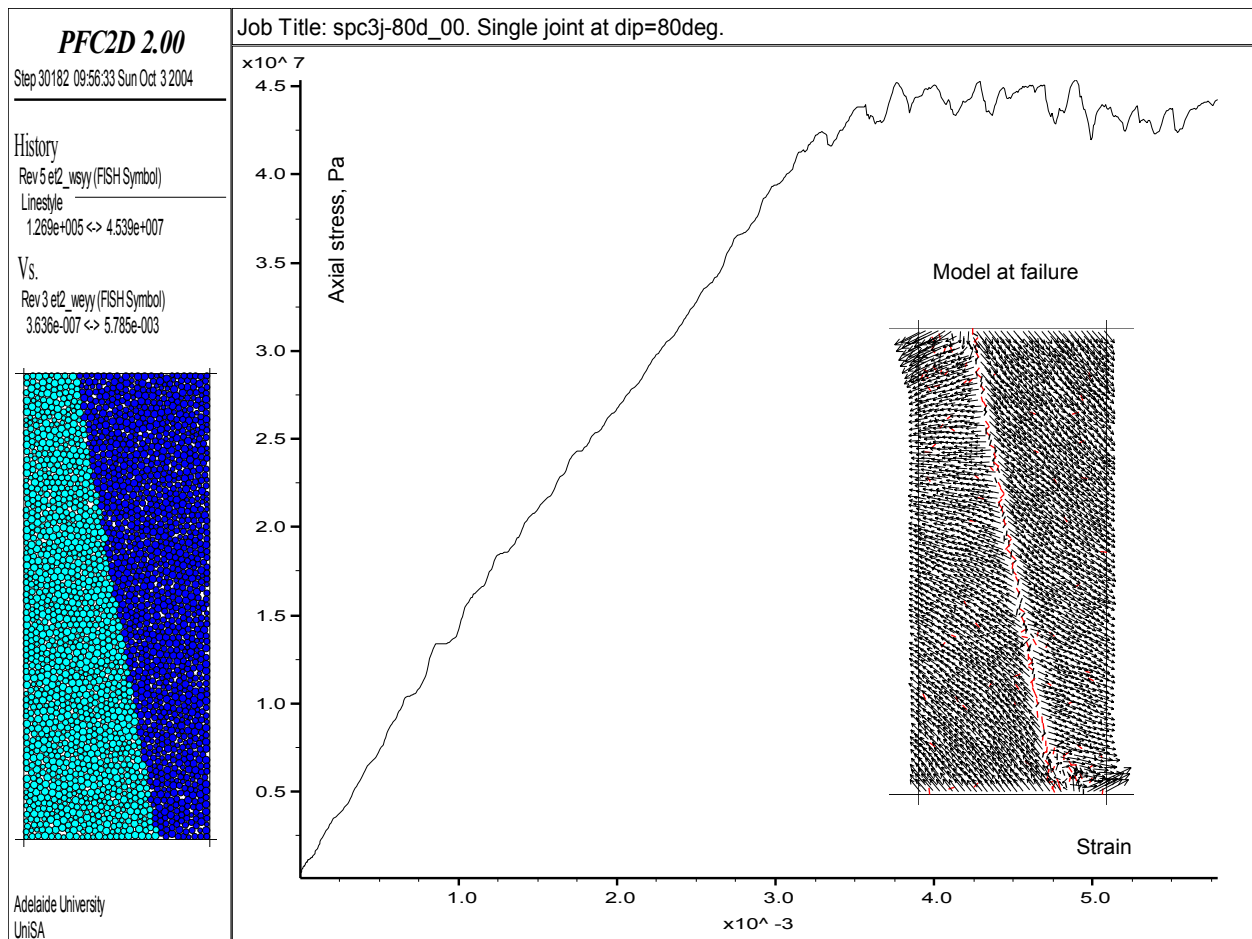


Figure A2.24. UCS test on model with single joint at  $\psi = 10^\circ$ .

Single joint @ dip = 80; s1 = 21.1 MPa.

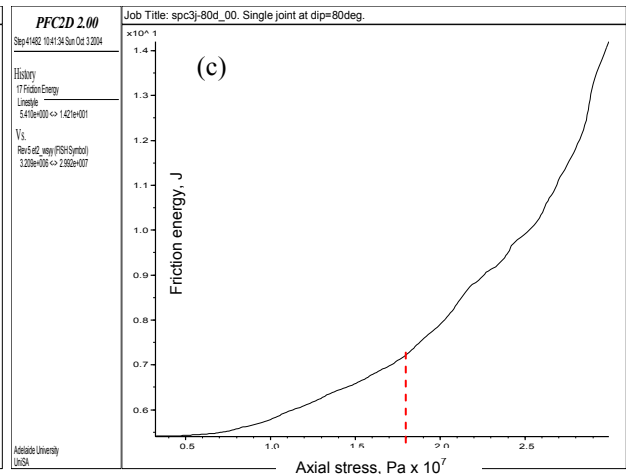
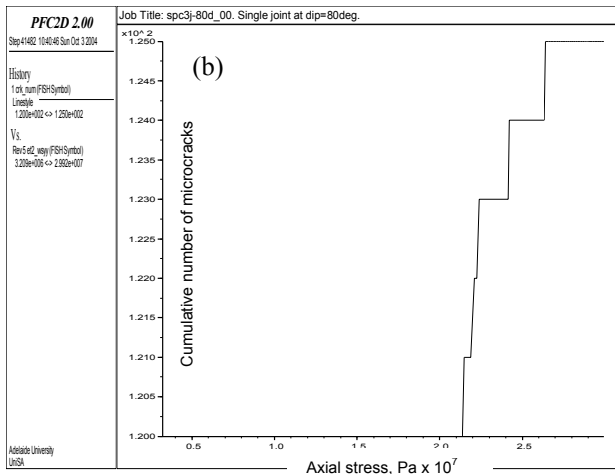
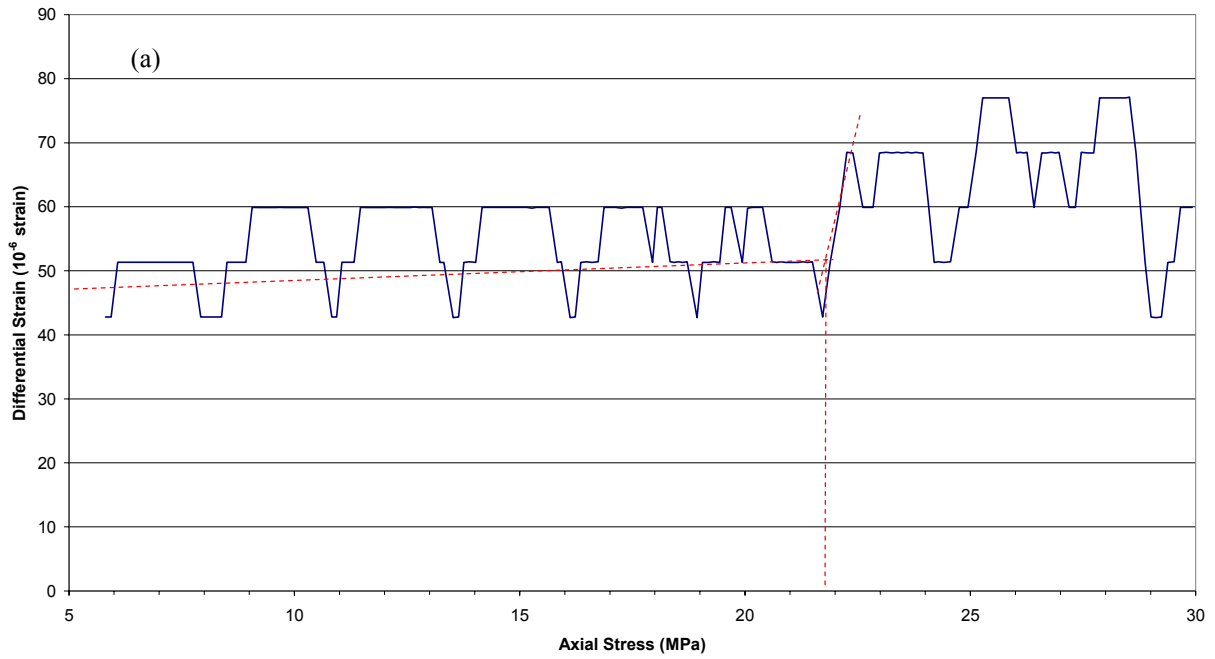


Figure A2.25. LRR test on model with single joint at  $\psi = 10^\circ$ :  
 (a) DRA curve; (b) cumulative number of microcracks; (c) friction energy.

Table A2.12. Results of LRR test on model with single joint at  $\psi = 10^\circ$ .

Pre-load stress, MPa		21.1
DME from DRA curve, MPa		21.8
	FR	0.97
DME from cum. No. of microcracks, MPa		21.4
	FR	0.99
DME from friction energy, MPa		18.0
	FR	1.17

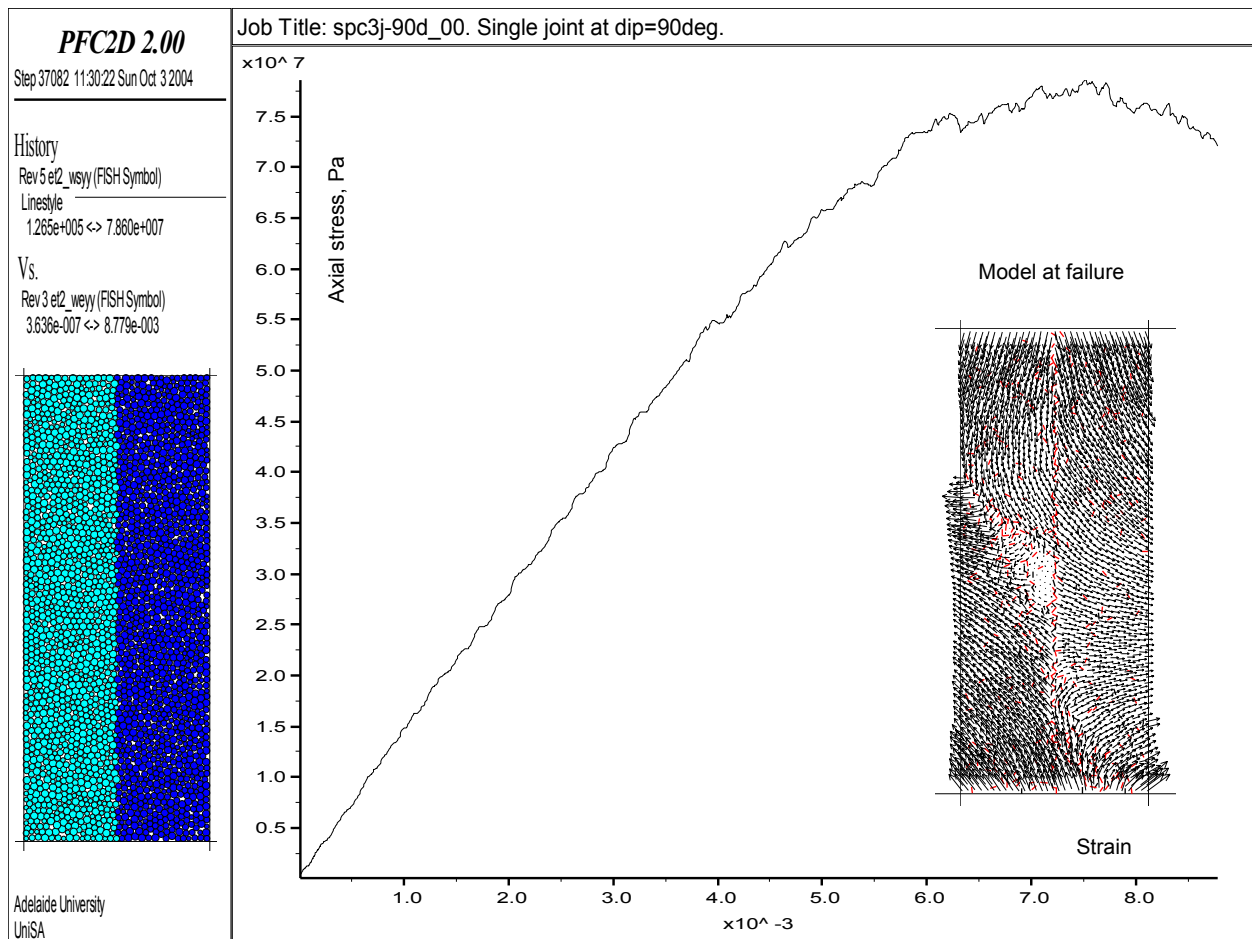


Figure A2.26. UCS test on model with single joint at  $\psi = 0^\circ$ .

Single joint @ dip = 90; s1 = 35.9 MPa.

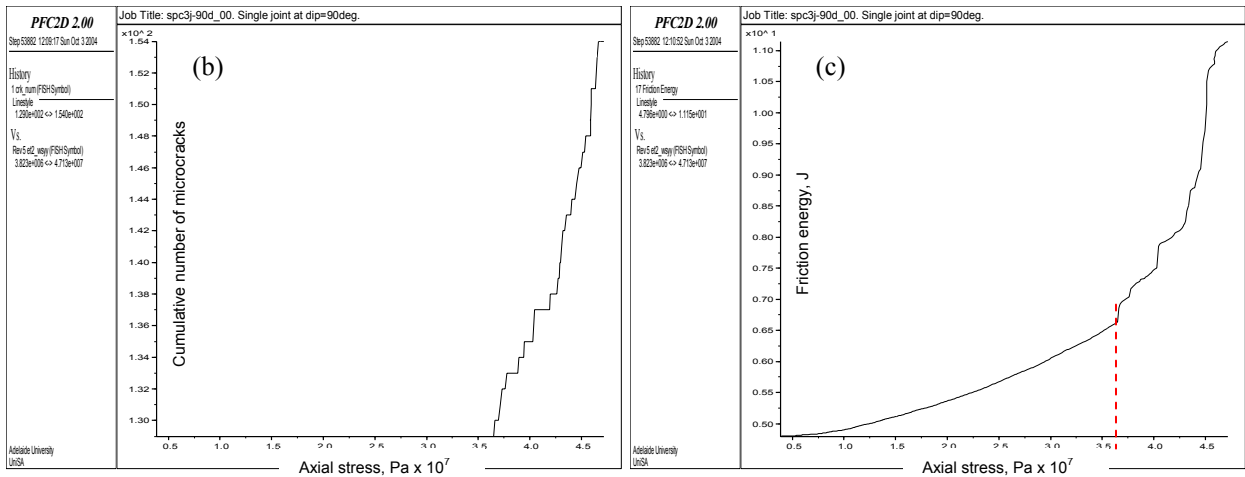
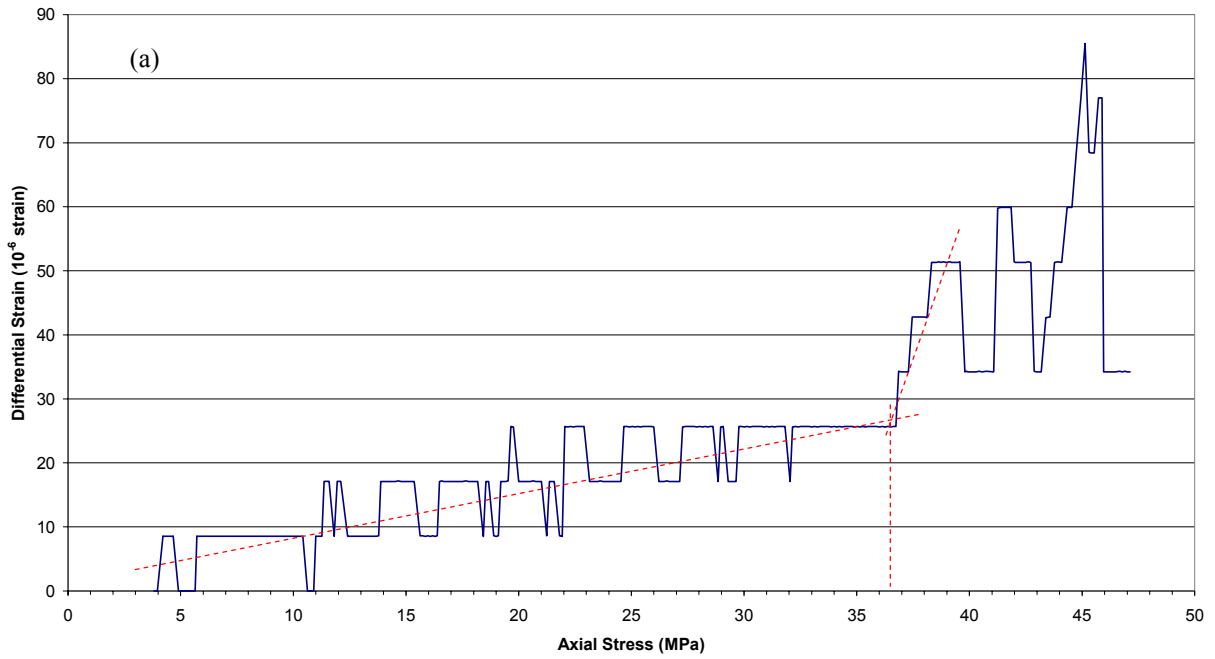


Figure A2.27. LRR test on model with single joint at  $\psi = 0^\circ$ :  
 (a) DRA curve; (b) cumulative number of microcracks; (c) friction energy.

Table A2.13. Results of LRR test on model with single joint at  $\psi = 0^\circ$ .

Pre-load stress, MPa		35.9
DME from DRA curve, MPa		35.5
	FR	1.01
DME from cum. No. of microcracks, MPa		36.6
	FR	0.98
DME from friction energy, MPa		36.6
	FR	0.98

## A2.5 Effect of confining stress

Codes A2.40 to A2.47 describe tests conducted on the intact rock and fine-grained models under biaxial stress conditions.

*Code A2.40. Intact rock model. Biaxial LRR test driver at  $\sigma_1=35.6$  MPa,  $\sigma_3=12$  MPa.*

---

```
; fname: spc3_12_bx.DVR Biaxial test on Specimen #3. Load to failure.
;
; PURPOSE: 1) restore spc3 specimen,
;           2) perform biaxial test upon it under
;           confining stress of Pc=12 MPa.
;
; Adelaide University.
; =====
set logfile spc3_12_bx.log
set log on
; -----
; Execute biaxial test at Pc=12 MPa
restore spc3-spc.SAV
set safe_conversion on
SET md_run_name='spc3_12'
title 'spc3_12. Specimen #3. Axial stress (MPa) vs axial strain (%)'
SET et2_knxfac=1.0 et2_knyfac=1.0
SET et2_wsxx_req=-12e6 et2_wsyy_req=-12e6 et2_ws_tol=0.01
SET p_vel=2.0e-1 p_cyc=1000 p_stages=20
call %itascaFishTank%\FishPfc2\et2\_btw2.DVR ;=> spc3_12-{bw0,bw1}.SAV
; -----
set log off
return
; EOF: spc3_12_bx.DVR
```

---

*Code A2.41. Log file: intact rock model. Biaxial test at  $\sigma_1=35.6$  MPa,  $\sigma_3=12$  MPa.*

---

```
***** Biaxial-test results follow. . .
md_run_name = spc3_12
md_numballs = 2505
Confinement: et2_wsxx_req = -1.000000000000e+005
E (plane stress) = 1.47974466904e+010
nu (plane stress) = 1.90734689593e-001
E (plane strain) = 1.44177680675e+010
nu (plane strain) = 1.60182357380e-001
Fish> print pk_syy
pk_syy = -5.295803809294e+007
Fish> print pk_crk_num
pk_crk_num = 4.900000000000e+001
Fish> print pk_crk_num_cnf, pk_crk_num_csf
pk_crk_num_cnf = 7.000000000000e+000
pk_crk_num_csf = 4.200000000000e+001
Fish> print pk_crk_num_pnf, pk_crk_num_psf
pk_crk_num_pnf = 0.000000000000e+000
pk_crk_num_psf = 0.000000000000e+000
Fish> print pk_ci_fac, pk_syy_ci
pk_ci_fac = 2.000000000000e-002
pk_syy_ci = -1.204572905535e+007
Pfc2D>;
```

```

Pfc2D> SET md_tag_name='-bw1'
Pfc2D>md_save_state
Fish> save @_fname
Pfc2D>; =====
Pfc2D>return
Pfc2D>; -----
Pfc2D>set log off
*****
* Log File Ended 13:38:34 Sun Oct 31 2004
*****

```

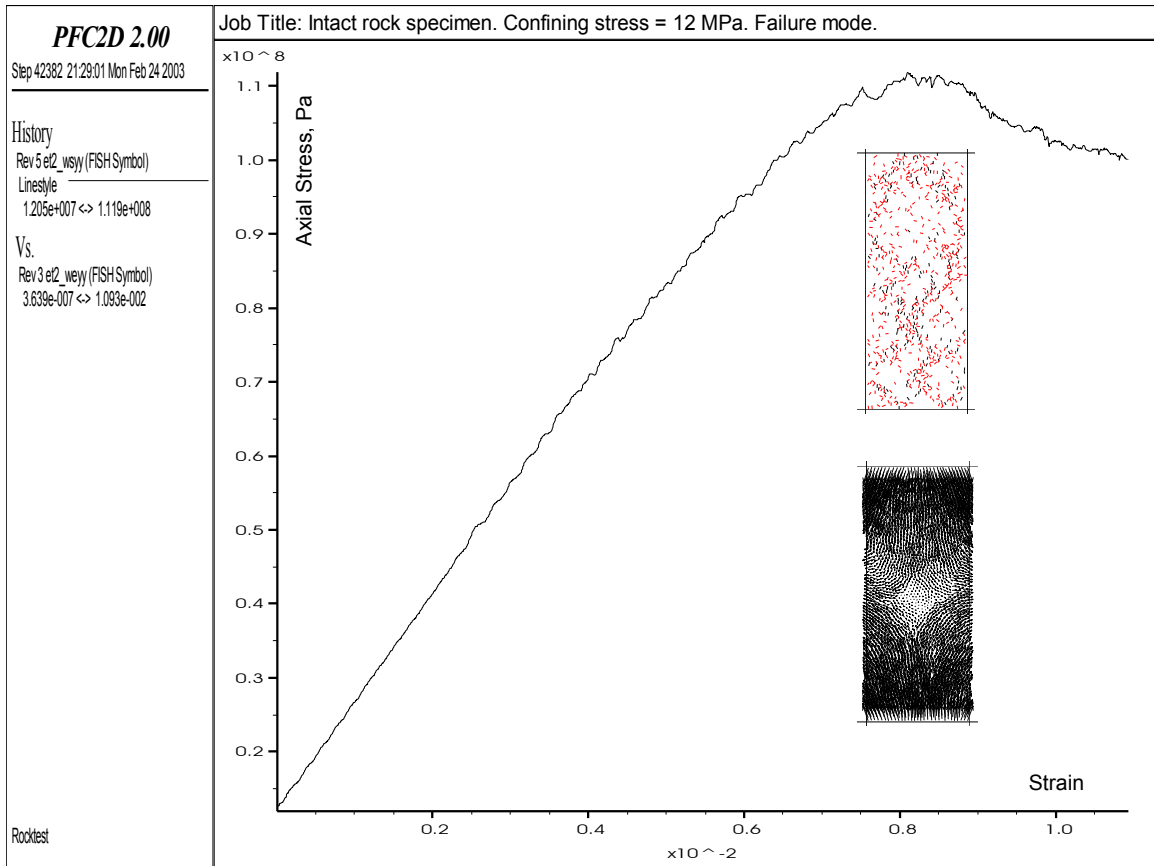


Figure A2.11. Intact rock model. Biaxial test at  $\sigma_1=35.6$  MPa,  $\sigma_3=12$  MPa. Stress-strain curve at failure.

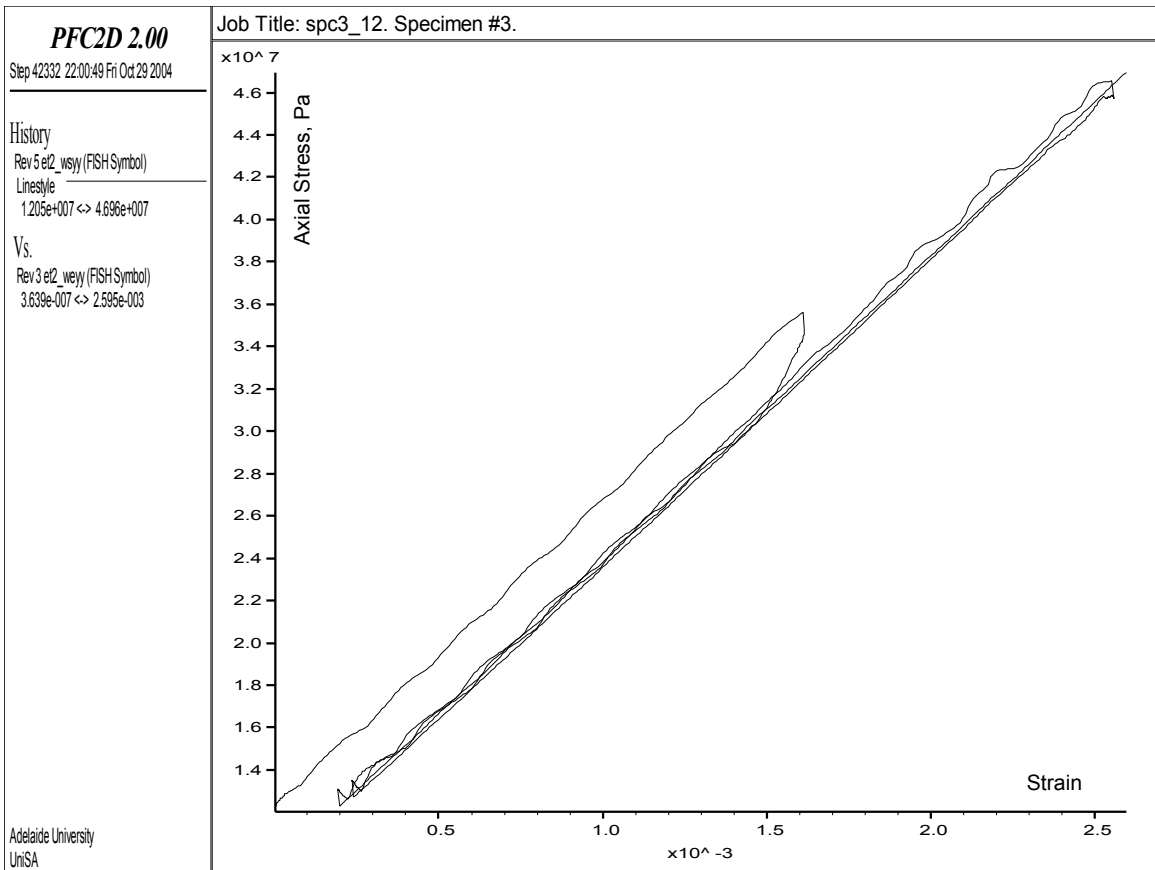


Figure A2.12. Intact rock model. Biaxial LRR test at  $\sigma_3=12$  MPa.

Code A2.42. Intact rock model. Biaxial LRR test driver at  $\sigma_3=20$  MPa.

```

; fname: spc3_20_bx.DVR Biaxial test on Specimen #3. Load to failure.
;           Confining stress 20 MPa
;
; PURPOSE: 1) restore spc3 specimen,
;           2) perform biaxial test upon it
;
; Adelaide University.
; =====
set logfile spc3_20_bx.log
set log on
; -----
; Execute biaxial test at Pc=20 MPa
restore spc3-spc.SAV
set safe_conversion on
SET md_run_name='spc3_20'
title 'spc3_20. Specimen #3. Axial stress (MPa) vs axial strain (%)'
SET et2_knxfac=1.0 et2_knyfac=1.0
SET et2_wsxx_req=-20e6 et2_wsyy_req=-20e6 et2_ws_tol=0.01
SET p_vel=2.0e-1 p_cyc=1000 p_stages=20
call %itascaFishTank%\FishPfc2\et2\_btw2.DVR ;=> spc3_20-{bw0,bw1}.SAV
; -----
set log off
return
; EOF: spc3_20_bx.DVR

```

```
***** Biaxial-test results follow. . .
md_run_name = spc3_20
md_numballs = 2505
Confinement: et2_wsxx_req = -1.00000000000e+005
E (plane stress) = 1.81985627187e+010
nu (plane stress) = 1.83948484647e-001
E (plane strain) = 1.77592599841e+010
nu (plane strain) = 1.55368655843e-001
Fish> print pk_syy
pk_syy = -4.449284496453e+007
Fish> print pk_crk_num
pk_crk_num = 3.20000000000e+001
Fish> print pk_crk_num_cnf, pk_crk_num_csf
pk_crk_num_cnf = 6.00000000000e+000
pk_crk_num_csf = 2.60000000000e+001
Fish> print pk_crk_num_pnf, pk_crk_num_psf
pk_crk_num_pnf = 0.00000000000e+000
pk_crk_num_psf = 0.00000000000e+000
Fish> print pk_ci_fac, pk_syy_ci
pk_ci_fac = 2.00000000000e-002
pk_syy_ci = -1.992020506759e+007
Pfc2D>;
Pfc2D> SET md_tag_name='-bw1'
Pfc2D>md_save_state
Fish> save @_fname
Pfc2D>; =====
Pfc2D>return
Pfc2D>; -----
Pfc2D>set log off
*****
* Log File Ended 16:59:16 Sat Oct 30 2004
*****
```

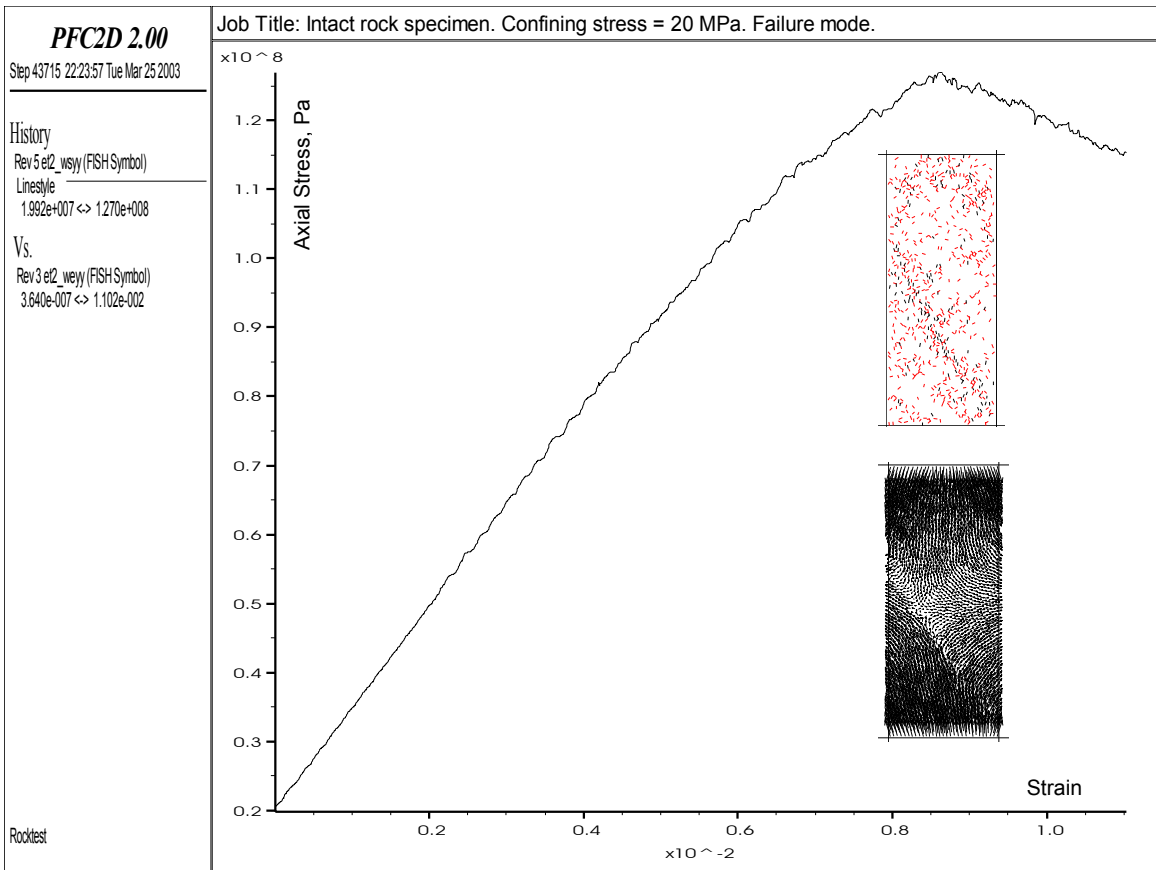


Figure A2.13. Intact rock model. Biaxial test at  $\sigma_3=20$  MPa. Stress-strain curve at failure.

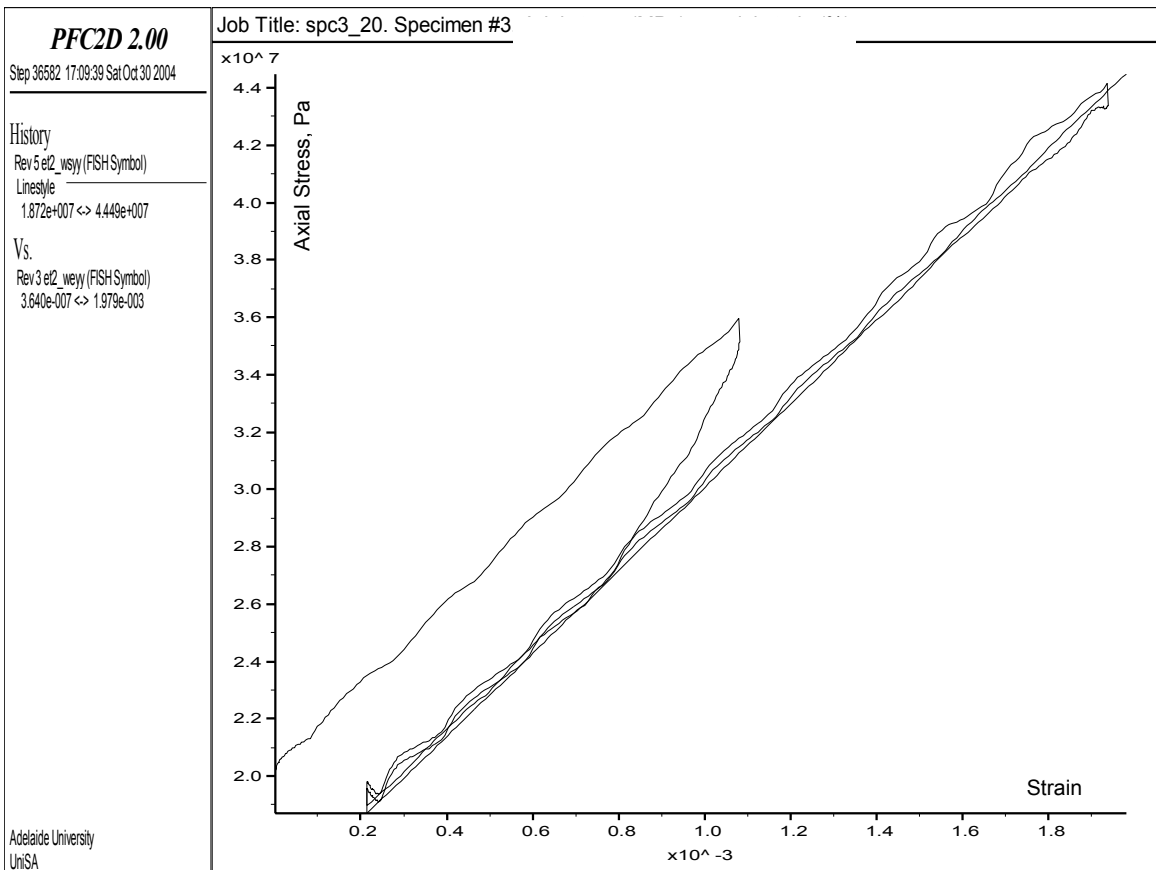


Figure A2.14. Intact rock model. Biaxial LRR test at  $\sigma_3=20$  MPa.

Code A2.44. Intact rock model. Biaxial LRR test driver at  $\sigma_3=28$  MPa.

---

```
; fname: spc3_28_bx.DVR  Biaxial test on Specimen #3. Load to failure.
;                               Confining stress 28 MPa
;
; PURPOSE: 1) restore spc3 specimen,
;           2) perform biaxial test upon it
; Adelaide University.
; =====
set logfile spc3_28_bx.log
set log on
; -----
; Execute biaxial test at Pc=28 MPa
restore spc3-spc.SAV
set safe_conversion on
SET md_run_name='spc3_28'
title 'spc3_28. Specimen #3. Axial stress (MPa) vs axial strain (%)'
SET et2_knxfac=1.0  et2_knyfac=1.0
SET et2_wsxx_req=-28e6  et2_wsyy_req=-28e6  et2_ws_tol=0.01
SET p_vel=2.0e-1  p_cyc=1000  p_stages=20
call %itascaFishTank%\FishPfc2\et2\_btw2.DVR  ;=> spc3_28-{bw0,bw1}.SAV
; -----
set log off
return
; EOF: spc3_28_bx.DVR
```

---

Code A2.45. Log file: intact rock model. Biaxial test at  $\sigma_3=28$  MPa.

---

```
***** Biaxial-test results follow. . .
      md_run_name = spc3_28
      md_numballs = 2505
      Confinement: et2_wsxx_req = -1.000000000000e+005
E (plane stress) = 1.08145098907e+010
nu (plane stress) = 1.68911839764e+000
E (plane strain) = 6.54766182516e+009
nu (plane strain) = 6.28130914252e-001
Fish>   print pk_syy
pk_syy = -8.749908368670e+007
Fish>   print pk_crk_num
pk_crk_num = 2.850000000000e+002
Fish>   print pk_crk_num_cnf, pk_crk_num_csf
pk_crk_num_cnf = 6.500000000000e+001
pk_crk_num_csf = 2.200000000000e+002
Fish>   print pk_crk_num_pnf, pk_crk_num_psf
pk_crk_num_pnf = 0.000000000000e+000
pk_crk_num_psf = 0.000000000000e+000
Fish>   print pk_ci_fac, pk_syy_ci
pk_ci_fac = 2.000000000000e-002
pk_syy_ci = -3.056703554530e+007
Pfc2D>;
Pfc2D> SET md_tag_name='-bw1'
Pfc2D>md_save_state
Fish>   save @_fname
Pfc2D>; =====
Pfc2D>return
Pfc2D>; -----
Pfc2D>set log off
*****
* Log File Ended 19:14:07 Sat Oct 30 2004
*****
```

---

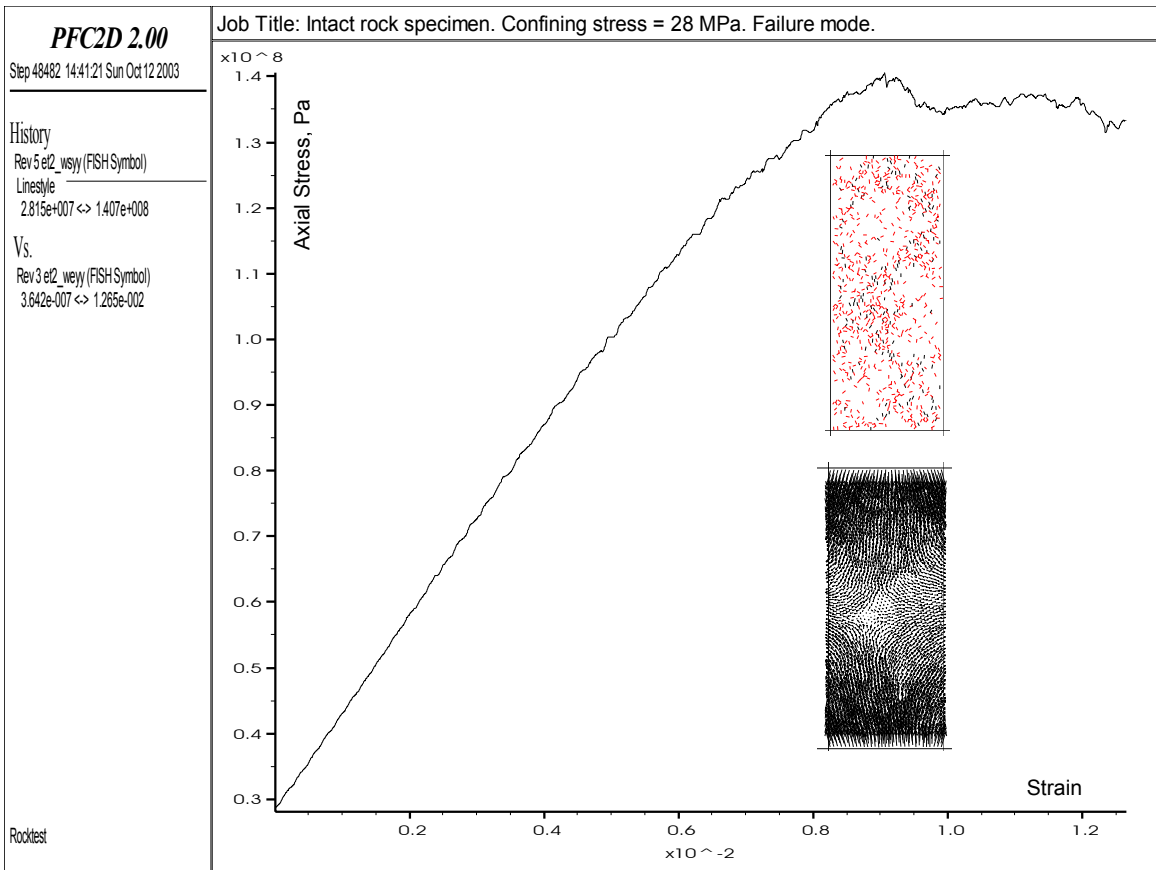


Figure A2.15. Intact rock model. Biaxial test at  $\sigma_3=28$  MPa. Stress-strain curve at failure.

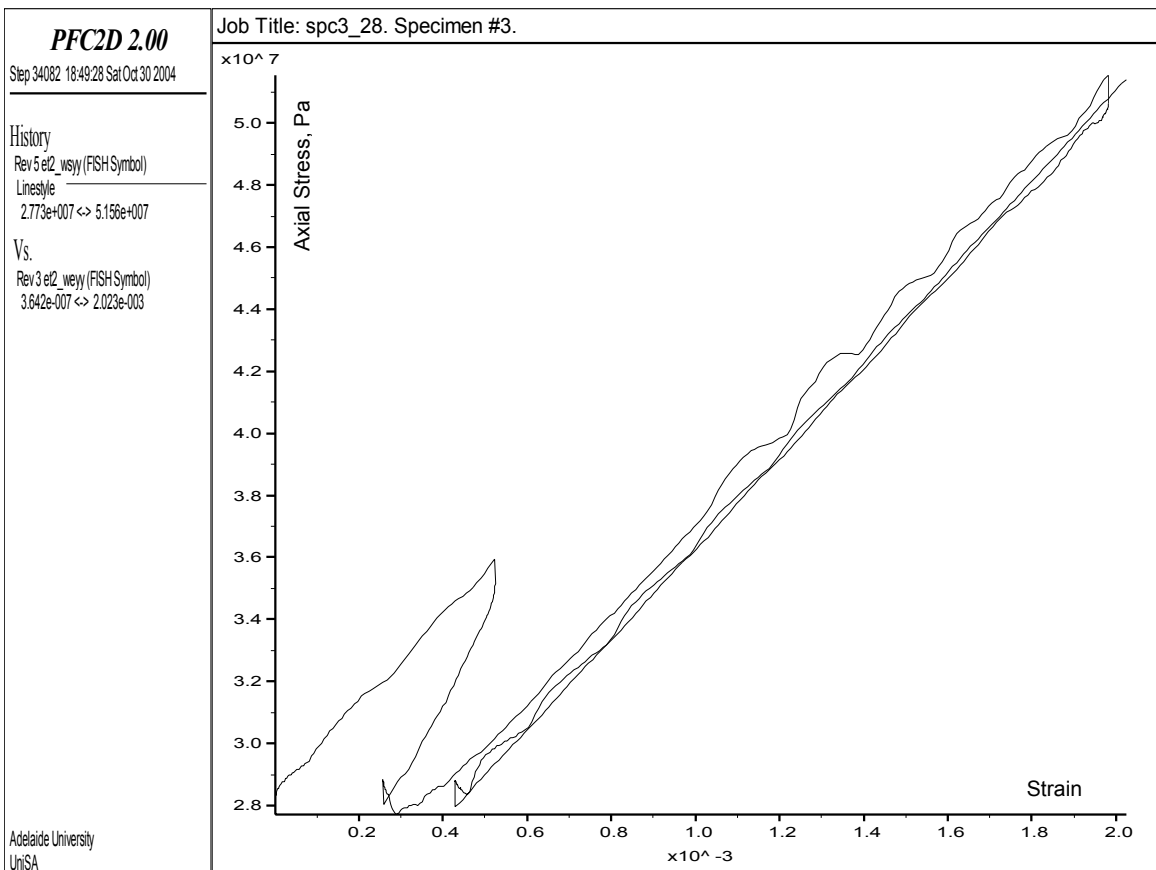


Figure A2.16. Intact rock model. Biaxial LRR test at  $\sigma_3=28$  MPa.

```
***** Biaxial-test results follow. . .
      md_run_name = spc3f_12
      md_numballs = 6415
      Confinement: et2_wsxx_req = -1.00000000000e+005
E (plane stress) = 1.53298869713e+010
nu (plane stress) = 1.87116696750e-001
E (plane strain) = 1.49490165817e+010
nu (plane strain) = 1.57622832921e-001
Fish>   print pk_syy
pk_syy = -4.891188991858e+007
Fish>   print pk_crk_num
pk_crk_num = 1.380000000000e+002
Fish>   print pk_crk_num_cnf, pk_crk_num_csf
pk_crk_num_cnf = 1.900000000000e+001
pk_crk_num_csf = 1.190000000000e+002
Fish>   print pk_crk_num_pnf, pk_crk_num_psf
pk_crk_num_pnf = 0.000000000000e+000
pk_crk_num_psf = 0.000000000000e+000
Fish>   print pk_ci_fac, pk_syy_ci
pk_ci_fac = 2.000000000000e-002
pk_syy_ci = -1.541662945909e+007
Pfc2D>;
Pfc2D> SET md_tag_name='-bw1'
Pfc2D>md_save_state
Fish>   save @_fname
Pfc2D>; =====
Pfc2D>return
Pfc2D>; -----
Pfc2D>set log off
*****
* Log File Ended 16:52:23 Sun Oct 31 2004
*****
```

---

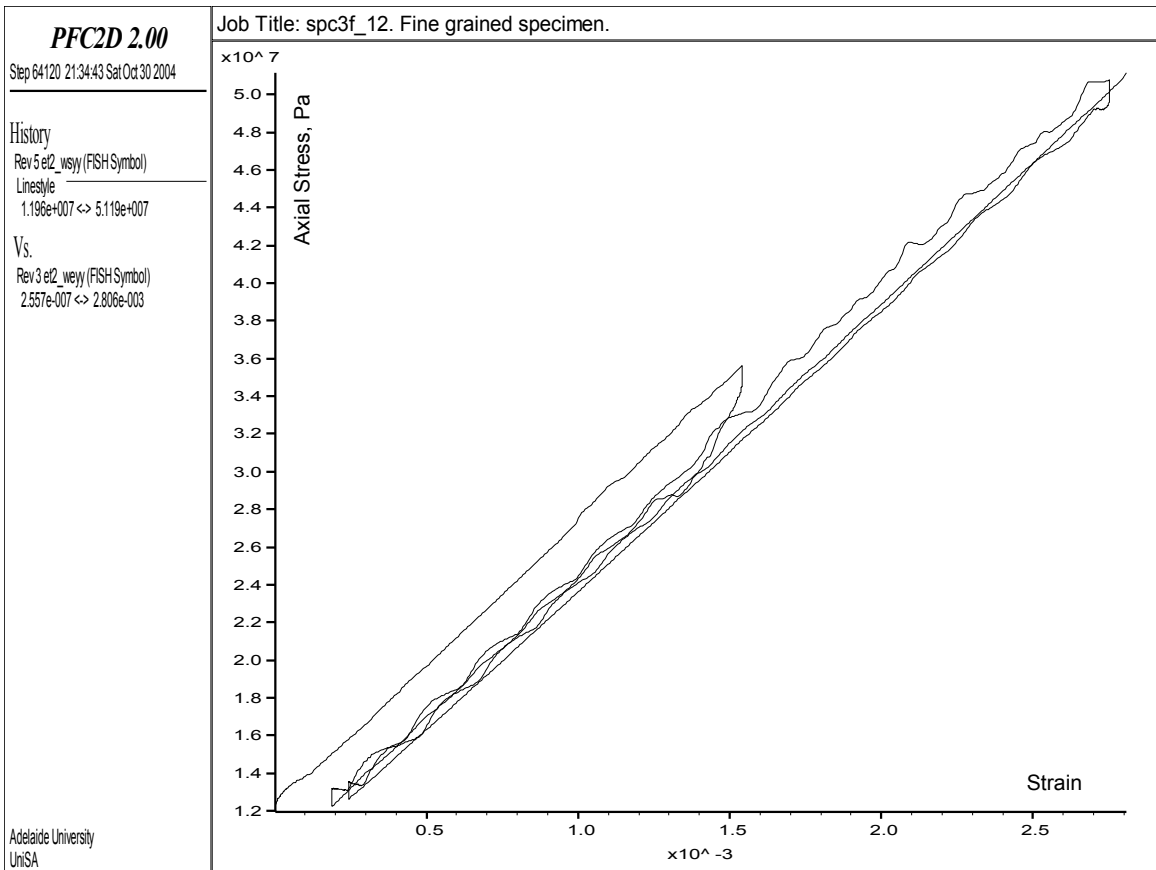


Figure A2.17. LRR test on fine-grained model. Biaxial test at  $\sigma_3=12$  MPa.

Code A2.47. Log file: fine-grained model. Biaxial test at  $\sigma_3=20$  MPa .

```

***** Biaxial-test results follow. . .
      md_run_name = spc3f_20
      md_numballs = 6415
      Confinement: et2_wsxx_req = -1.0000000000e+005
E (plane stress) = 1.61499186562e+010
nu (plane stress) = 1.86249248319e-001
E (plane strain) = 1.57518046141e+010
nu (plane strain) = 1.57006842013e-001
Fish>   print pk_syy
pk_syy = -5.084775004042e+007
Fish>   print pk_crk_num
pk_crk_num = 1.520000000000e+002
Fish>   print pk_crk_num_cnf, pk_crk_num_csf
pk_crk_num_cnf = 2.200000000000e+001
pk_crk_num_csf = 1.300000000000e+002
Fish>   print pk_crk_num_pnf, pk_crk_num_psf
pk_crk_num_pnf = 0.000000000000e+000
pk_crk_num_psf = 0.000000000000e+000
Fish>   print pk_ci_fac, pk_syy_ci
pk_ci_fac = 2.000000000000e-002
pk_syy_ci = -2.608735976798e+007
Pfc2D>;
Pfc2D> SET md_tag_name='-bw1'
Pfc2D>md_save_state
Fish>   save @_fname
Pfc2D>; =====
Pfc2D>return
Pfc2D>; -----

```

```

Pfc2D>set log off
*****
* Log File Ended 10:50:50 Sun Oct 31 2004
*****

```

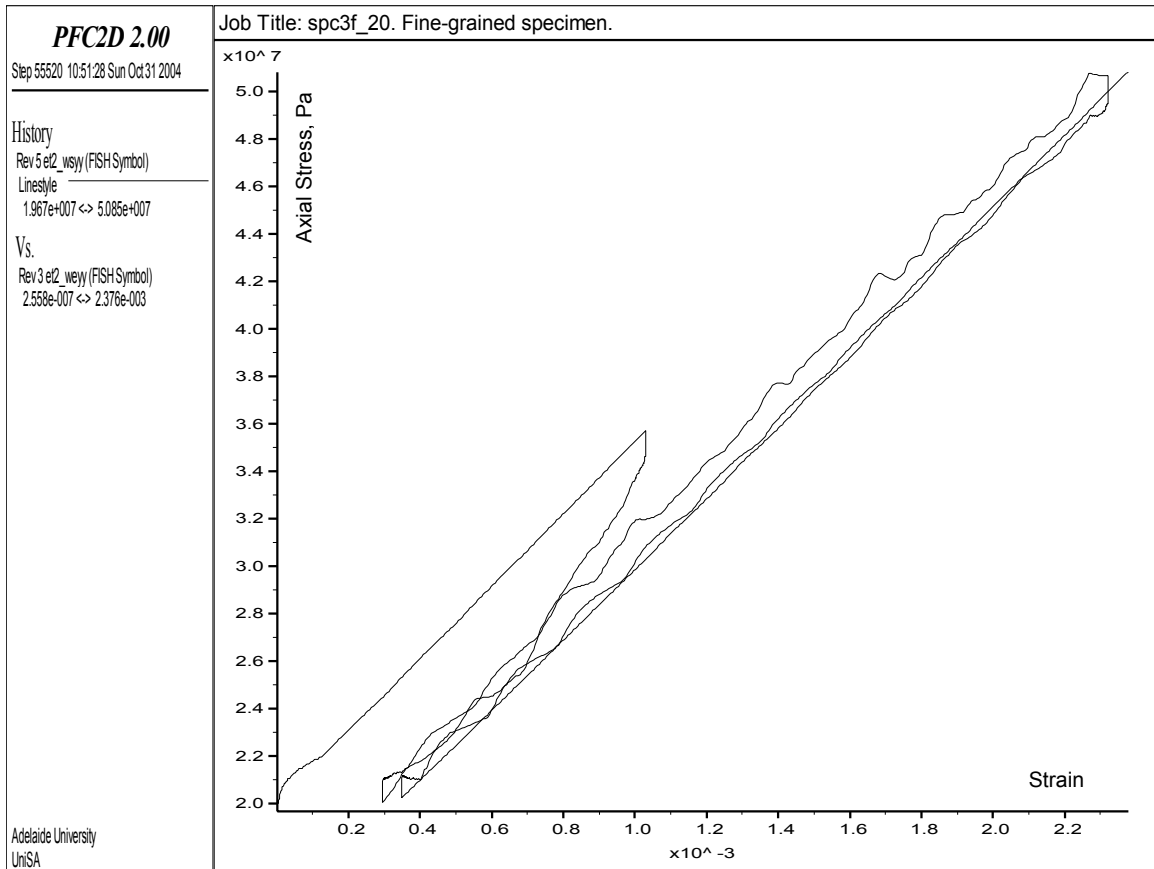


Figure A2.18. LRR test on fine-grained model. Biaxial test at  $\sigma_3=20$  MPa.

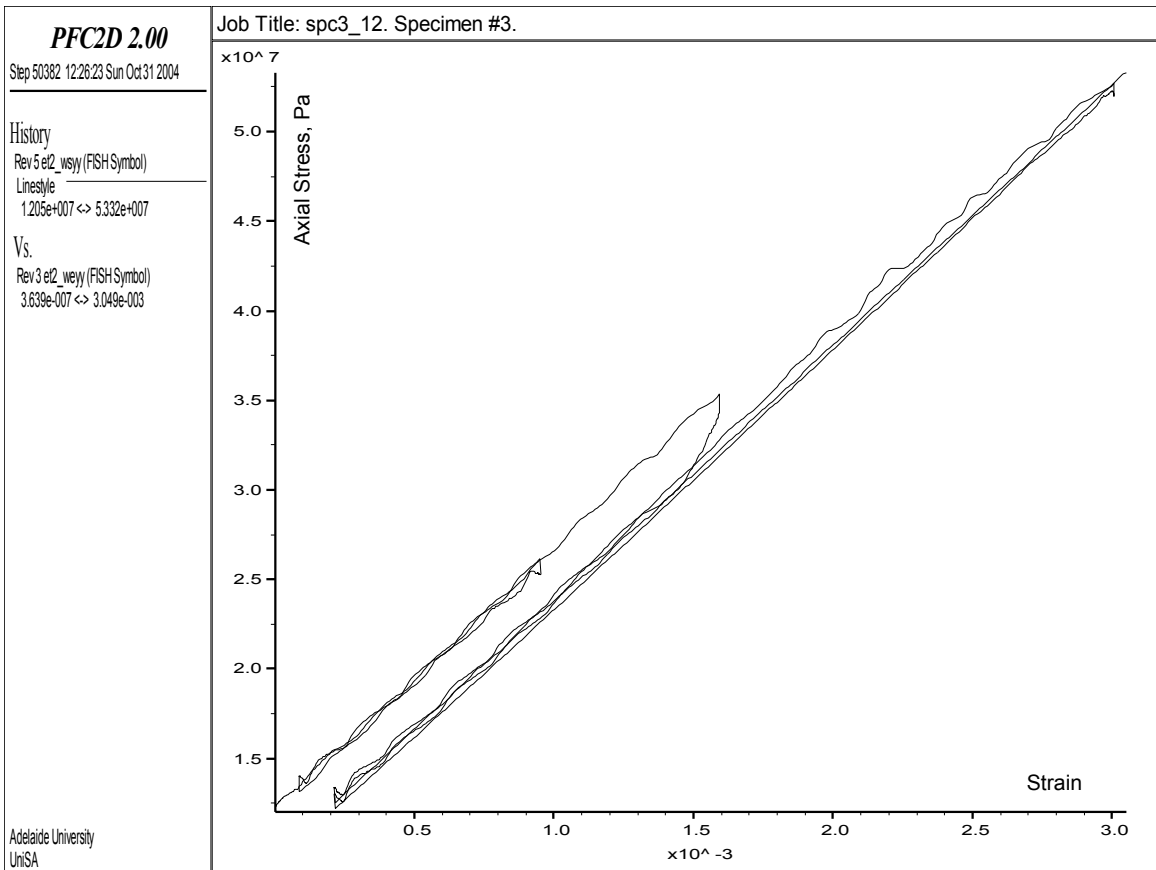


Figure A2.19. LLRR test on intact rock model:  $\sigma_1' = 26.1$  MPa,  $\sigma_1'' = 35.4$  MPa,  $\sigma_3 = 12$  MPa.

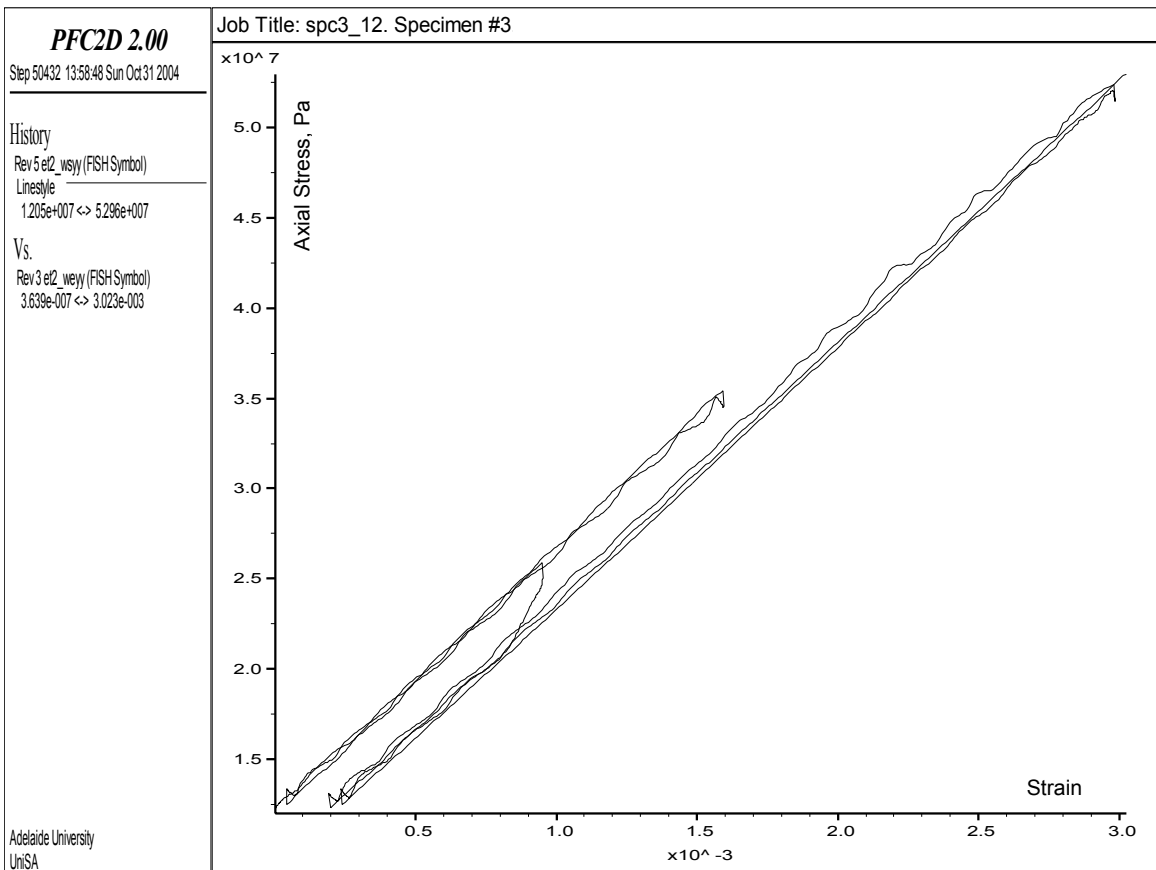


Figure A2.20. LLRR test on intact rock model:  $\sigma_1' = 35.4$  MPa,  $\sigma_1'' = 26.0$  MPa,  $\sigma_3 = 12$  MPa.

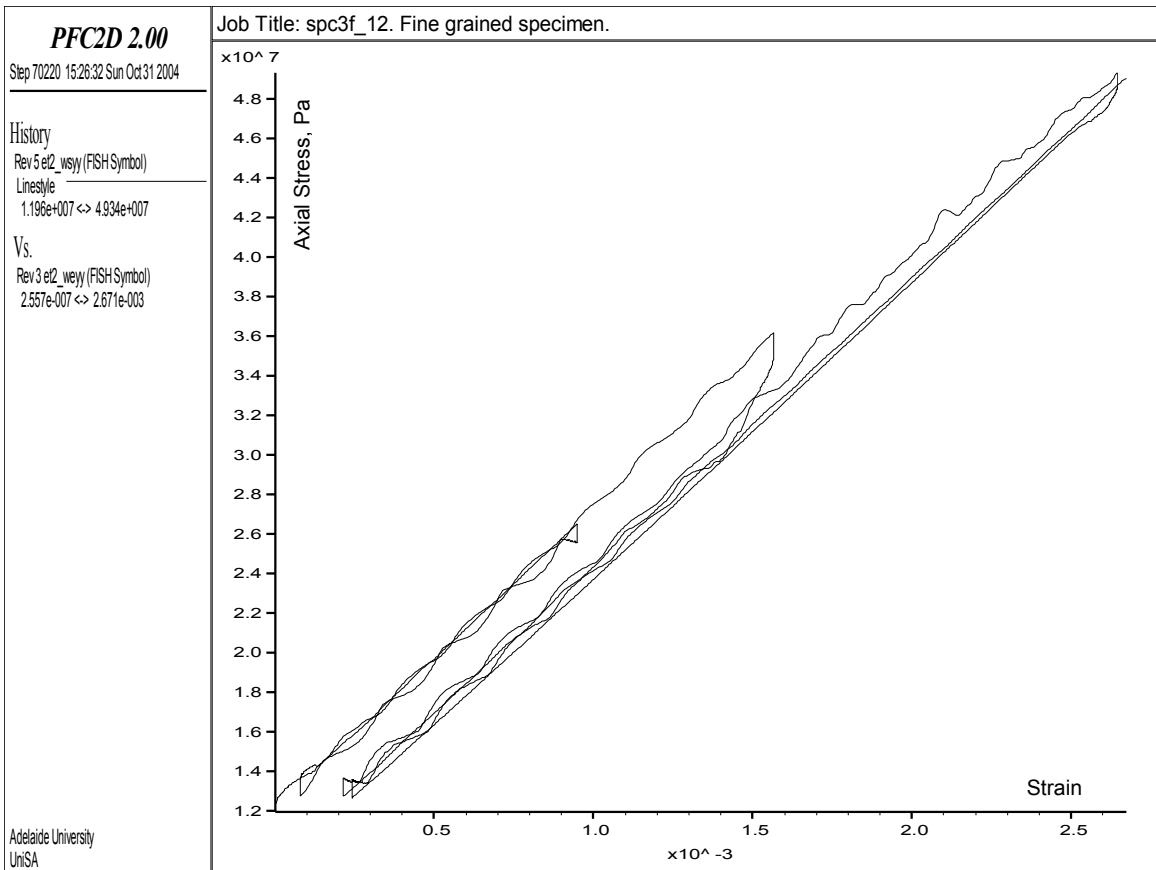


Figure A2.21. LLRR test on fine-grained model:  $\sigma_1' = 26.5 \text{ MPa}$ ,  $\sigma_1'' = 36.2 \text{ MPa}$ ,  $\sigma_3 = 12 \text{ MPa}$ .

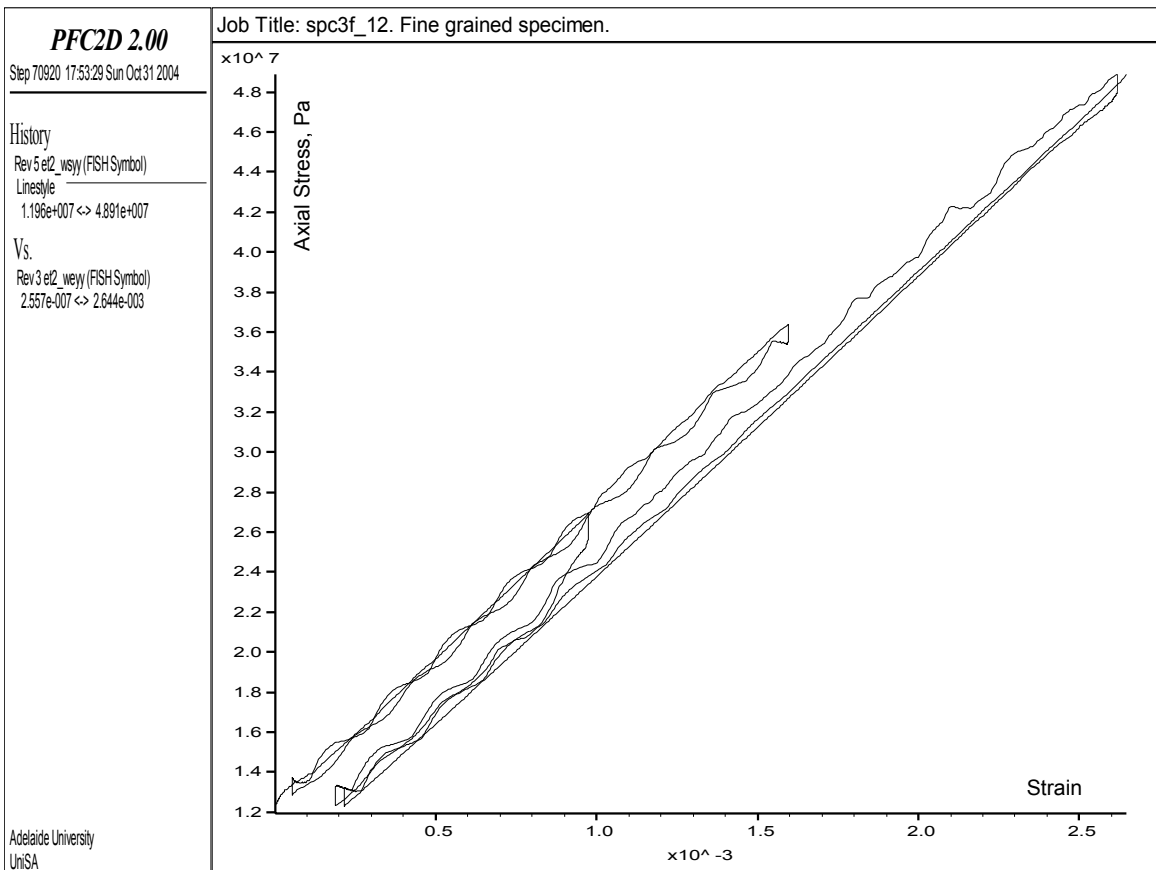


Figure A2.22. LLRR test on fine-grained model:  $\sigma_1' = 36.4 \text{ MPa}$ ,  $\sigma_1'' = 26.9 \text{ MPa}$ ,  $\sigma_3 = 12 \text{ MPa}$ .